LOW TEMPERATURE PHYSICS VOLUME 28, NUMBER 6 JUNE 2002

SUPERCONDUCTIVITY, INCLUDING HIGH-TEMPERATURE SUPERCONDUCTIVITY

Manifestation of two-dimensional behavior of YBCO films in a study of their complex susceptibility

A. V. Khokhlov, A. Yu. Prokhorov,* V. F. Drobotko, and G. G. Levchenko

A. A. Galkin Donetsk Physicotechnical Institute, ul. R. Lyuksemburg 72, 83114 Donetsk, Ukraine

A. V. Klimov

Institute of Physics of the Polish Academy of Sciences, 02-668 Warsaw, Poland

(Submitted January 21, 2002)
Fiz. Nizk. Temp. **28**, 535–542 (June 2002)

The temperature dependence of the complex magnetic susceptibility $\chi' + \chi''$ of various YBCO films is investigated at different amplitudes of the exciting field H_{ac}. It is found that when the temperature T_m at which the maximum is observed on the $\chi''(T)$ curve is plotted as a function of H_{ac}^{α} (the parameter $\alpha=1$, 1/2, or 2/3, depending on the character of the coupling between crystallites), a kink appears at a certain field $H_{ac}=H_1^*$. It is suggested that the temperature T_{c1} obtained by extrapolating the $T_m(H_{ac}^{2/3})$ curve from the high-field region to zero field is the Berezinskii–Kosterlitz–Thouless transition temperature T_{BKT}. This suggestion is based on a comparison of the present results with published data from a study of the complex susceptibility of a $GdBa_2Cu_3O_{6.75}$ single crystal for directions of H_{ac} parallel to the c axis of the single crystal and in its ab plane, and also on the coincidence of the calculated values of certain characteristic temperatures near the BKT transition with our experimental values. © *2002 American Institute of Physics.* [DOI: 10.1063/1.1491175]

INTRODUCTION

Metaloxide high-T_c superconductors (HTSCs) have a quasi-two-dimensional layered structure which is characterized by high anisotropy of a number of their physical properties, and their magnetic properties, in particular. Inherent to such structures is a transition, as $T \rightarrow T_c$, from three-dimensional behavior of the magnetic characteristics to two-dimensional: the Berezinskii–Kosterlitz–Thouless (BKT) transition.[1,2] In the Cu–O layers of YBCO HTSCs the magnetic dipoles arise under the influence of thermal fluctuations only in the form of pairs of two-dimensional (2D) vortices (vortex–antivortex pairs), the magnetic flux of which is closed by two Josephson vortices lying between the superconducting layers. The circulation of the current of the Josephson vortices is what gives HTSC materials superconductivity along the c axis of the crystal. At the temperature T_{BKT} the system of 2D vortices becomes unstable with respect to decoupling of the dipoles, and the critical current in the direction of the c axis falls to zero. At $T > T_{BKT}$ free vortices appear in the layers, and the superconductivity in the ab planes is preserved.

The features of the BKT transition in quasi-2D systems of the HTSC type can be well observed if $\lambda \gg \xi(T_{BKT})$.[2] Here $\lambda = d\sqrt{M/m}$, where d is the interlayer distance between Cu–O planes, m and M are the effective masses in the Cu–O plane and along the c axis, $\xi(T_{BKT})$ is the correlation length $\sim \xi(0)\tau^{-1/2}$, and T_{BKT} is the temperature of the BKT transition. For YBCO one has $(M/m)^{1/2} = 5-7$, $d \simeq 4$ Å, $\xi(0) \simeq 13$ Å, and $\tau = 1 - T_{BKT}/T_{c0} \sim 10^{-2}$ (T_{c0} is the mean-field transition temperature), and the relation $\lambda \gg \xi(T_{BKT})$ is not satisfied. At the same time, the BKT transition is observed in YBCO, both in granular bulk materials[3] and films[4] and in single crystals.[5]

Laser-deposited epitaxial films of YBCO are quite perfect. In them the c axis is to a high degree of accuracy oriented perpendicular to the plane of the film, while at the same time the orientation in the ab plane is textured, and there is incomplete matching of the Cu–O planes in crystallites or domains with a size of 50–100 nm. The presence of this pseudorandom network of nearly perfect crystallites (domains) will probably affect the character of the BKT transition.[6]

The standard procedure for determining the BKT transition temperature T_{BKT} is to measure the current–voltage (I–V) characteristics and plot the temperature dependence of the exponent n in the I–V power law ($V \propto I^n$). At $n \cong 3$ a sharp jump is observed on the I–V curve. The temperature at $n=3$ is taken as T_{BKT}, and the extrapolation of $n(T)$ from the $n>3$ region to $n=1$ gives the mean-field critical temperature T_{c0}, which is practically equal to the temperature of the midpoint of the transition on the $R(T)$ curve.[7] We recall that the temperature difference $\Delta T_c = T_{c0} - T_{BKT}$ depends directly on the value of the effective anisotropy of the material. YBCO compounds have the lowest anisotropy of the HTSCs, because the coherence length along the c axis is comparatively large in them—at low temperatures it is only about a factor of two smaller than the distance between the Cu–O superconducting planes,[8] and these compounds exhibit pronounced three-dimensional behavior. At the same time, YBCO films of poor quality (according to the transport prop-

1063-777X/2002/28(6)/6/$22.00

erties and the value of the critical current density) are found to have large values of ΔT_c.[9]

For YBCO single crystals a value $\Delta T_c = 0.14$ K was found in Ref. 5, and for high-quality YBCO films, Kim *et al.*[4] obtained a value $\Delta T_c = 0.5$ K. The diamagnetic susceptibility of YBCO films was investigated in Ref. 10. The penetration depth λ was calculated from measurements of the complex impedance $Z = R + i\omega L$ for high-quality YBCO films with thicknesses of 500 and 2000 Å. A BKT transition was observed only for the 500-Å thick film.

The diamagnetic response of a $GdBa_2Cu_3O_{6.75}$ single crystal was used to measure the temperature dependence of the dissipative loss χ_1'' and of the real part of the susceptibility χ_1', the latter being responsible for the degree of screening of the external field by the sample.[11] The measurements were made under conditions such that the exciting field H_{ac} was applied along the c axis of the crystal and in the ab plane. It is found that when $\mathbf{H}_{ac}$ is parallel to the ab plane the χ_1' signal appears at a lower temperature than in the case $\mathbf{H}_{ac} \| \mathbf{c}$. It is at this temperature that the true 3D superconductivity sets in. Since the value of the diamagnetic response is proportional to the area of the sample, such measurements are impossible in principle for HTSC films in the case $\mathbf{H}_{ac} \| ab$ because of the extremely small area of the film. However, certain arguments suggest that measurements of the field and temperature dependences of χ_1' and χ_1'' for $\mathbf{H}_{ac} \| \mathbf{c}$ can be used to fix the 2D–3D transition in YBCO films also. This possibility was investigated in the present study.

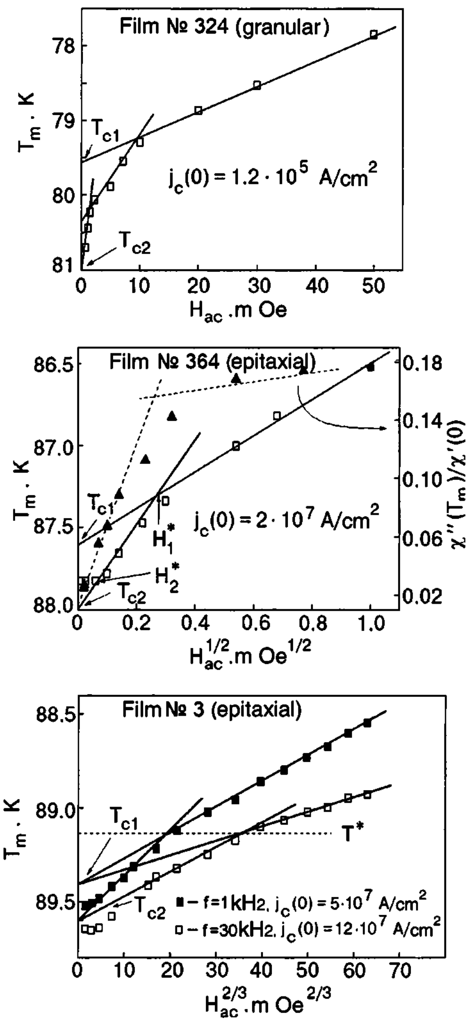

FIG. 1. Temperature T_m at which the maximum of the dissipative part of the magnetic susceptibility occurs, plotted in relation to the amplitude H_{ac} of the exciting field for different YBCO films. As an example, a plot of $\chi_1''/\chi_1'(H_{ac}^{\alpha})$ is shown for film No. 364. The analogous plots for the other films have a similar form.

EXPERIMENTAL RESULTS AND DISCUSSION

Studies of the diamagnetic response of YBCO films were carried out on an inductive apparatus in the range of exciting magnetic fields $H_{ac} = 0.2–1000$ mOe mainly at a frequency of 10 kHz. We recall that χ_1'' reflects the degree of loss to magnetization reversal of the sample and resistive losses. In this study the temperature position T_m of the maximum of χ_1'' is obtained as a function of the amplitude of the exciting field H_{ac} for three samples. Sample No. 324 was deposited by rf magnetron sputtering on a sapphire substrate with a ZrO_2 sublayer stabilized by Y. The polycrystalline film obtained had a thickness $d = 0.8$ μm. Sample No. 364 was grown by laser evaporation on an $SrTiO_3$ substrate and had a thickness of 0.3 μm. The third sample (No. 3) was also grown by laser deposition on a $LaCaO_3$ substrate stabilized by Nd and had a thickness of 0.2 μm. The $T_m(H_{ac}^{\alpha})$ curves for these samples are presented in Fig. 1. The exponent α depends on the character of the weak coupling between crystallites in the sample. It is seen that the curves become linear for different values of α: $\alpha = 1$ for film No. 324, $\alpha = 1/2$ for film No. 364, and $\alpha = 2/3$ for film No. 3.

In the theory of the critical state, the following relation holds at the temperature of the maximum on the $\chi_1''(T)$ curve:[12]

$$j_c(T_m) = \frac{8H_{ac}}{2.474\pi d}, \tag{1}$$

and so the measured $T_m(H_{ac})$ curves are related to $j_c(T)$. When the flux creep, which plays an appreciable role in the investigated temperature interval, is taken into account, relation (1) will be more complicated, but the proportionality between j_c and H_{ac} will remain.

As we see from Fig. 1, all three films, which were grown by different methods in different laboratories and on different substrates, have the same characteristic features.

1. At very low fields there is a certain interval of exciting field amplitudes $[0, H_2^*]$ in which T_m is independent of H_{ac} to within the experimental error. For the granular film No. 324 the value of H_2^* is about 1 mOe, while for film No. 3 it reaches approximately 10 mOe, depending on the frequency of the exciting field.

2. At higher values of H_{ac} the $T_m(H_{ac}^{\alpha})$ plot for each sample becomes linear for a different value of the exponent of the power law, up to a certain field H_1^* at which a kink is observed, the slope of $T_m(H_{ac}^{\alpha})$ becoming smaller than for $H_{ac} < H_1^*$.

3. In the field region $H_2^* \leqslant H_{ac} \leqslant H_1^*$ an appreciable increase of the amplitude of χ_1'' is observed, and in fields $H_{ac} > H_1^*$ the growth of the amplitude of χ_1'' is insignificant or absent altogether, in agreement with the Bean theory of the

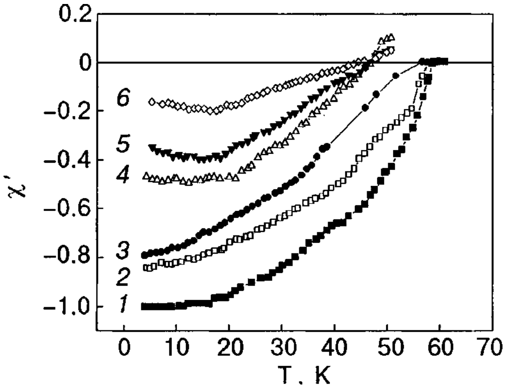

FIG. 2. Temperature dependence of the dissipative part of the magnetic susceptibility χ' for a $GdBa_2Cu_3O_{6.75}$ single crystal at various fields H_{ac} [Oe]: ($H_{ac} \| c$) 0.297 (*1*), 1.11 (*2*), and 4.16 (*3*) for ($\mathbf{H}_{ac} \perp \mathbf{c}$), and 0.22 (*4*), 2.1 (*5*), and 4.16 (*6*) for $\mathbf{H}_{ac} \perp \mathbf{c}$.

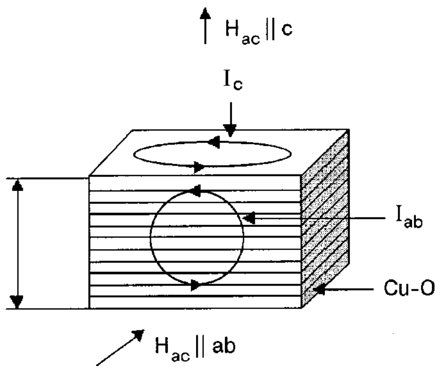

FIG. 3. Diagram of a YBCO film of thickness d containing Cu–O superconducting layers. For $\mathbf{H}_{ac} \| ab$ plane the current I_{ab} vanishes at the temperature where the Josephson couplings between the Cu–O planes vanishes, i.e., at T_{BKT}. The diamagnetic response signal also vanishes in this case.

critical state with flux creep taken into account. In this case the value of χ_1' remains constant.

4. In the region $H_{ac} < H_2^*$ one observes a linear response, in the interval $H_2^* < H_{ac} < H_1^*$ a quasilinear response (the distortions of the response signal χ_1'' from a sinusoidal form are insignificant), and at fields $H_{ac} > H_1^*$ the response is substantially nonlinear.

Extrapolation of the $T_m(H_{ac}^\alpha)$ plots from high fields H_{ac} to zero field gives a certain temperature value T_m which we provisionally call T_{c1}. A similar extrapolation from the field region $H_2^* < H_{ac} < H_1^*$ gives a different temperature, which we call T_{c2}.

It would seem that the behavior of the diamagnetic response in the field region $H_2^* < H_{ac} < H_1^*$ can be described by the Matsushita theory of reversible vortex motion,[13] which is based on the Campbell model[14] and explains the growth of the amplitude of χ_1'' with increasing field H_{ac}. However, this theory is constructed by proceeding from the condition of linear response (the motion of the vortices is reversible, and there is no hysteresis), and with increasing H_{ac} the value of χ_1' should also change; this is not observed experimentally.

It is natural to suppose that the kink on the $T_m(H_{ac}^\alpha)$ plots is due to a BKT transition. To justify this conjecture, we consider the temperature dependence of χ_1' obtained in Ref. 11 for a $GdBa_2Cu_3O_{6.75}$ sample in the form of a plate 0.7 mm thick and having a surface area of $\sim 4\ \mathrm{mm}^2$, with a field orientation $\mathbf{H}_{ac} \| \mathbf{c}$ axis of the crystal and $\mathbf{H}_{ac} \| ab$ plane (see Fig. 2). Figure 2 clearly demonstrates the existence of two-dimensionality in the sample in the temperature interval 48–58 K. Indeed (see Fig. 3), for $\mathbf{H}_{ac} \| \mathbf{c}$ the field H_{ac} induces currents lying in the plane of the sample, and the response signal will exist independently of the dimensionality (2D or 3D) of the structure in the Cu–O layers. For $\mathbf{H}_{ac} \| ab$ plane of the crystal the response signal can arises only when coherent coupling between Cu–O layers appears, i.e., when the sample will be found in a three-dimensional state.

In Fig. 4 the temperatures T_m at which the maxima are observed on the $\chi''(T)$ curves taken for a $GdBa_2Cu_3O_{6.75}$ single crystal at different amplitudes of the exciting field H_{ac} are plotted in relation to the critical current density j_c calculated according to the well-known relation:[11]

$$j_c = \frac{H_{ac}^*}{4\pi d}, \tag{2}$$

where H_{ac}^* is the value of the exciting field with allowance for the demagnetizing factor.

We note that extrapolation of the $T_m(j_c^{2/3})$ curve from large currents to $j_c = 0$ gives a temperature $T_{c1} = 48$ K (the temperature at which the diamagnetic response appears for $\mathbf{H}_{ac} \| ab$), while extrapolation from small currents to $j_c = 0$ gives a temperature $T_{c2} = 58$ K (the temperature at which the χ_1'' and χ_1' signals appear for $\mathbf{H}_{ac} \| \mathbf{c}$).

From the data obtained it can be concluded that the BKT transition temperature in $GdBa_2Cu_3O_{6.75}$ is equal to 48 K.

For YBCO epitaxial films with $\mathbf{H}_{ac} \| \mathbf{c}$ the dependence of T_m on $H_{ac}^{2/3}$ is related to the dependence $T_m(j_c^{2/3})$ by a simple coefficient [in the case when the film is in the critical state; see formula (1)]. By analogy with Ref. 11, it can be assumed that for YBCO films, too, extrapolation from high fields H_{ac} to $H_{ac} = 0$ gives the value $T_{c1} = T_{BKT}$, while extrapolation from fields less than H_1^* gives a value T_{c2}. The width of the $R(T)$ transition in epitaxial film No. 3, according to our data, is around 1 K. The temperature of the midpoint of this transition is usually[7] taken to be equal to the mean-field transition temperature T_{c0}. The temperature at which the diamagnetic response appears ($T_c = 89.8$ K) practically coincides with the temperature at which $R(T)$ goes to zero, to an accuracy of $10^{-3}\ \Omega/\mathrm{cm}$ or better. It follows that the quantity $\Delta T = T_{c0} - T_{BKT}$ should be of the order of $0.5 + |T_c - T_{c1}|$.

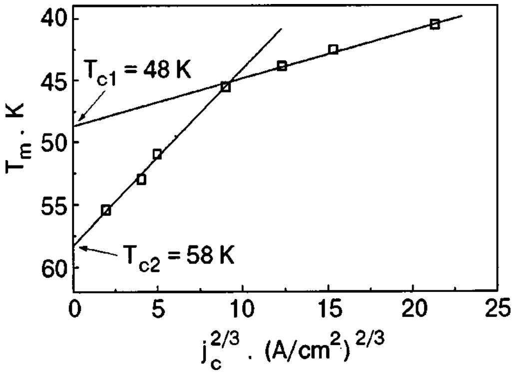

FIG. 4. Temperature T_m at which the maximum occurs on the $\chi''(T)$ curve, in relation to the critical current j_c for a $GdBa_2Cu_3O_{6.75}$ single crystal.

TABLE I. Values of a number of characteristic temperatures near T_c for YBCO epitaxial film No. 3.

T^*. K	τ^*	T_{c1}. K	τ_{c1}	T_{c2}. K	τ_{c2}	T_c. K	τ_c	T_{c0}. K	R_N.Ω
89.12	1.3×10^{-2}	89.4	10^{-2}	89.6	0.77×10^{-2}	89.8	0.55×10^{-2}	90.3	0.7

On the assumption that $T_{c1}=T_{BKT}$, the value of $\Delta T=0.9$ K obtained for film No. 3, with a high current-carrying capacity, is close to the value $\Delta T=0.5$ K found for YBCO films.[5] As we see from Fig. 1, the value of $j_c(0)$ also decreases (the slope of the $T_m(H_{ac}^{\alpha})$ curve increases) with increasing ΔT. A similar picture was also observed in Ref. 9.

Let us analyze the results obtained for the most-studied epitaxial film, No. 3.

As we see in Fig. 1, the $T_m(H_{ac}^{\alpha})$ plot clearly exhibits several characteristic points:

T^*—the temperature at which the kink is observed on $T_m(H_{ac}^{\alpha})$. We note that T^* is the same for exciting-field frequencies of 1 and 30 kHz, even though the emf (and, hence, the current) induced in the film is 30 times greater for $f=30$ kHz than for $f=1$ kHz;

T_{c1}—the temperature value corresponding to $H_{ac}=0$ on the extrapolation of the $T_m(H_{ac}^{\alpha})$ curve plotted for $H_{ac}>H_1^*$.

T_c—the temperature at which an infinite cluster arises in the film and a diamagnetic response appears; T_c coincides with the temperature at which the $R(T)$ curve goes to "zero" ($R\leqslant10^{-3}$ Ω/cm);

T_{c0}—the mean-field transition temperature, which coincides with the midpoint of the $R(T)$ transition.[7]

The values of these temperatures for film No. 3 are given in Table I.

In Ref. 15 a hierarchy of characteristic values of the temperatures (from low to high) is presented for a layered superconductor with weak magnetic coupling [here $\tau=(T-T_{c0})/T_{c0}$]:

τ_f—the temperature below which the fluctuations of the order parameter are significantly less than its mean value;

τ_{BKT}—the temperature of the 3D–2D transition in an individual layer;

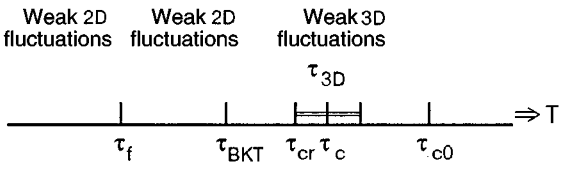

τ_{cr}—the temperature of the crossover from 3D to 2D behavior;

τ_c—the true transition temperature;

τ_{c0}—the mean-field transition temperature.

The shaded region corresponds to the interval of three-dimensional fluctuations.

Comparing the hierarchy given in Ref. 15 with our results, we conjecture that T^* corresponds to T_f, $T_{c1}\rightarrow T_{BKT}$, and $T_{c2}\rightarrow T_{cr}$.

Let us estimate the values of τ_{BKT} and the smearing τ_{3D} of the Kosterlitz–Nelson jump under the influence of thermal fluctuations according to the formulas given in Ref. 15:

$$|\tau_{BKT}|=\frac{|\tau_c|}{\left[1-\dfrac{b}{\ln^2(J/E_{0j}\xi_{ab}^2)}\right]}, \tag{3}$$

$$|\tau_{3D}|=\frac{2|\tau_{BKt}|b}{\ln^3(J/E_{0j}\xi_{ab}^2)}. \tag{4}$$

Here $J=\Phi_0^2d_p/\pi\varepsilon(4\pi\lambda_{ab})^2$ is the "stiffness" characterizing the fluctuations in the ab plane; d_p is the distance between Cu–O planes ($\sim$4 Å), $\lambda_{ab}=\lambda_{ab}(0)/\tau$ is the London penetration depth, $\varepsilon\geqslant1$ is the effective "dielectric constant" describing the reduction of the "stiffness" of the fluctuational vortex pairs;[16] $E_{0j}=\pi h\Delta/4e^2R_N$ is the energy of the Josephson interaction between layers ($E_j=E_{0j}|\tau|$); Δ is the energy gap, $\simeq$20 meV;[17] e is the charge of the electron; R_N is the resistance of the sample near the transition; and b takes on values between 2 and 9.[18] If we assume that $b=9$ and $\xi(0)_{ab}=20$ Å,[17] then estimates give $J=6\times10^{-32}$ J/cm^2 and $E_{0j}=1.5\times10^{-20}$ J. Using Eq. (3), we find $\tau_{BKT}=0.95\times10^{-2}$, from which we get $T_{BKT}=89.44$ K, which is close to the value of T_{c1}. From Eq. (4) we find $\tau_{3\mathrm{D}}=0.41\times10^{-2}$, which corresponds to a temperature interval of width 0.4 K, i.e., ($T_c\pm0.2$) K, and agrees with the value $T_{c2}=89.6$ K. An estimate of τ_f in Ref. 15 gives a temperature several degrees below T_c and is in explicit disagreement with our value of τ^*, and so the physical meaning of the temperature T^* remains unclear.

It is known that the BKT transition is due to two-dimensional vortices in the Cu–O superconducting layers and their interaction both with other vortices within a plane and with vortices in neighboring Cu–O planes. Below T_{BKT} there exist only bound vortex–antivortex pairs, and for $T>T_{BKT}$ the coupling between Cu–O planes is broken, and a fluctuational decay of vortex pairs occurs. When current is present in the sample (measurements of the I–V characteristics and diamagnetic response are made with a transport or induced current) and $T<T_{BKT}$, the Lorentz force acts on the pairs as an effective repulsive interaction and will cause substantial decoupling of the vortices if the current exceeds a threshold value[19,20]:

$$J=J_{GL}\xi_{ab}(E_i/I), \tag{5}$$

where J_{GL} is the Ginzburg–Landau critical current density and I is the specific energy of a 2D vortex. The value of this current estimated in Ref. 6 is approximately equal to 3 μA. From the results of diamagnetic measurements were cannot estimate the current induced in the film for $H_{ac}<H_1^*$, since there is no theory describing the relation between H_{ac} and j_c in this temperature region. However, we assume that the current induced by the exciting field is greater than 3 μA, at least up to fields $H_{ac}=H_2^*$. For $T>T_{BKT}$ the thermal decoupling of vortices is predominant, while below T_{BKT} free vortices arise mainly as a result of the decoupling by the induced current.

Thus, in addition to the fluctuational vortices, at a finite value of the current free vortices arise in the system due to the current-induced decoupling of the dipoles. The presence of two mechanisms governing the resistance of the sample causes the universal Kosterlitz–Nelson jump[21] to be smeared out, and the exponent n in the I–V power law becomes dependent on both the temperature and current. Such a smearing of the jump on the $n(T)$ curve was observed in Refs. 6 and 9, when n began to decrease not from 3 but from $n=5.5$ (Ref. 6) and $n=4.2$ (Ref. 9). We assume that in our case the transition extends from T^* to T_{c2} (a transition width $\Delta T=0.5$ K). A value $\Delta T=0.35$ K was found in Ref. 6, and a value $\Delta T=4$ K in Ref. 9.

Real films, especially those obtained by rapid laser evaporation, begin to grow from ''islands'' formed on the the film–substrate boundary in the initial stage of growth. The substrate itself is not ideally smooth but has depressions and prominances, with a height difference reaching several YBCO lattice constants along the c axis. As the thickness of the film increases, the islands, whose c axes are perpendicular to the plane of the substrate but whose a and b axes are not in a strict mutual orientation, coalesce to form a continuous film. Edge and screw dislocations, enriched with copper,[22] form at the places where coalescence occurs. Thus a real film consists of crystallites, with sizes ranging from a few nanometers to tens of nanometers, separated by dislocations, and the Cu–O planes in adjacent crystallites (domains) may be noncoincident. The transport or induced current flowing along the Cu–O planes passes through the dislocations, which are normal or superconducting but with a lower order parameter. As a result of the mutual misorientation of the Cu–O planes in adjacent crystallites, ''extra'' or ''missing'' partial planes appear. Stacks of Cu–O planes arise which are separated by ''extra'' or ''missing'' Cu–O planes, which do not carry a transport current. Thus effective superconducting layers carrying a transport current appear which are separated from each other by larger distances (and, hence, have a smaller E_j) than in the single crystal. This, in turn, leads to an increase in the ''effective'' anisotropy of the film.

Let us estimate the sizes of these effective layers. In Ref. 23 it was shown that the magnetic penetration depth $L_s=2\lambda_{3D}^2/d_{\text{eff}}$ is related to T_c as $L_s[\text{cm}]=2/T_c[\text{K}]$, where λ_{3D} is the bulk magnetic penetration depth and d_{eff} is the thickness of a superconducting layer. Consequently, one can obtain the effective thickness of each layer, assuming that there is no interaction between layers. Taking $\lambda_{3D}(T)=0.15[\mu\text{m}](1-T_{c1}/T_{c0})^{-0.5}$, where $T_{c1}=89.4$ K, we obtain a value $d_{\text{eff}}\cong 2$ nm. Comparing d_{eff} with the film thickness, which was 200 nm, we can see that quasi-two-dimensional behavior should exist.

The influence of the Josephson interaction on the three-dimensional behavior of YBCO films is manifested in the appearance of an additional attraction between the vortices in a pair, where this attraction depends quadratically on the distance for $r\ll r_c$ and linearly for $r>r_c$.[15,24] Here $r_c=(I/E_j)^{0.5}$ is a certain characteristic distance between vortices in a pair, below which one can neglect the influence of the Josephson interaction between layers in comparison with the intralayer vortex interaction. At distances $r>r_c$ the Josephson contribution is dominant, suppressing the decay of the pairs into free vortices. The decay into free vortices occurs primarily under the influence of the Lorentz force in the presence of current, and also for $T\approx T_{BKT}$, where the Josephson interaction between layers falls to zero. For film No. 3 the characteristic distance $r_c=2\ \mu$m, which is much larger than the size of the crystallites, and therefore the sizes of the boundaries between crystallites should apparently not affect the BKT transition.

Of course, it can be assumed that the transition in YBCO films is not a true BKT transition, which is due to dissipation of vortex–antivortex pairs, but is a transition caused by the breaking up of the Cu–O planes into effective superconducting layers (having a thickness of ~ 2 nm for film No. 3) which do not interact with each other. Such a system will be quasi-two-dimensional. In this case experiments on the I–V characteristics and susceptibility will not detect that the BKT transition is replaced by a quasi-two-dimensional one. However, the observation of a BKT transition in YBCO single crystals, which are free of any mutual misorientation of the Cu–O planes everywhere in the sample, is at odds with the criterion $\lambda\gg\xi(T_{BKT})$ (see Introduction). It is our opinion that the criterion of a BKT transition is in need of refinement.

Thus, by analogy with the results of measurements of the diamagnetic response in a $\text{GdBa}_2\text{Cu}_3\text{O}_{6.75}$ single crystal[11] for $\mathbf{H}_{ac}\|\mathbf{c}$ axis of the crystal and $\mathbf{H}_{ac}\|ab$ plane of the crystal, the good agreement between the calculated and experimentally obtained values of the characteristic temperatures of a sample near the BKT transition and the proximity of our values of the transition width ΔT to the published data give us reason to think that a study of how the temperature of the maximum of χ_1'' depends on the amplitude H_{ac} of the exciting field will afford an opportunity to observe a 2D–3D transition. To confirm the conjecture that we have observed a 2D–3D transition in YBCO films by studying their complex susceptibility, it will be necessary to study the same film simultaneously by the methods of I–V characteristics and diamagnetic response. Such studies are planned for the near future. The physical meaning of the temperature T^* and its independence of the frequency of the exciting field H_{ac} also remain open questions. There is also no explanation for the logarithmic growth of the amplitude of χ_1'' in the field region $H_{ac}<H_1^*$ while the value of χ_1' remains constant.

[*] E-mail: prohorov@levch.fti.ac.donetsk.ua

---

[1] V. A. Berezinskiĭ, Zh. Éksp. Teor. Fiz. **61**, 1144 (1971) [Sov. Phys. JETP **34**, 610 (1972)]; J. M. Kosterlitz and D. J. Thouless, J. Phys. C **6**, 1181 (1973); Progr. Low Temp. Phys. B **7**, 373 (1978).

[2] M. V. Feigelman, V. B. Geshkenbein, and A. I. Larkin, Physica C **167**, 177 (1990).

[3] D. R. Harshman, G. Aeppli, E. J. Ansaldo, B. Batlogg, J. H. Brewer, J. F. Carolan, R. J. Cava, M. Celio, A. C. D. Chaklader, W. N. Hardy, S. R. Kreitzman, G. M. Luke, D. R. Noakes, and M. Senda, Phys. Rev. B **36**, 2386 (1987).

[4] J. Kim, H. Lee, J. Chung, H. J. Shin, and H. J. Lee, Phys. Rev. B **43**, 2962 (1991).

[5] V. Katandella and P. Minnhagen, Physica C **166**, 442 (1990).

[6] Q. Y. Ying and H. S. Kwok, Phys. Rev. B **42**, 2242 (1990).

[7] K. Kadowaki, Y. Songlin, and K. Kitazava, Supercond. Sci. Technol. **7**, 519 (1999).
[8] K. H. Fisher, Physica C **193**, 401 (1992).
[9] P. H. Mikheenko and I. S. Abaliosheva, Physica C **214**, 393 (1993).
[10] A. T. Fiory, A. F. Hebard, P. M. Mankiewich, and R. E. Howard, Phys. Rev. Lett. **61**, 1419 (1988).
[11] G. G. Levchenko, A. V. Pashchenko, V. P. D'yakonov, V. I. Markovich, I. M. Fita, A. A. Pavlyuk, and L. P. Kozeeva, Fiz. Nizk. Temp. **18**, 1332 (1992) [Low Temp. Phys. **18**, 928 (1992)].
[12] E. H. Brandt, Phys. Rev. B **58**, 6506 (1998).
[13] T. Matsushita, E. S. Otabe, and B. Ni, Physica C **182**, 95 (1991).
[14] A. M. Campbell, J. Phys. C **4**, 3186 (1971).
[15] L. I. Glazman and A. E. Koshelev, Zh. Éksp. Teor. Fiz. **97**, 1371 (1990) [Sov. Phys. JETP **70**, 774 (1990)].
[16] P. Minnhagen, Rev. Mod. Phys. **59**, 1001 (1987).
[17] T. Maeno, K. Kagawa, S. Tanda, T. Nakayama, N. Hatakenaka, A. Ohi, T. Matsui, T. Suzuki, and K. Tsuda, Physica C **235–240**, 3321 (1994).
[18] A. T. Fiory, A. F. Hebard, and W. T. Glaberson, Phys. Rev. B **28**, 5075 (1983).
[19] H. J. Jensen and P. Minnhagen, Phys. Rev. Lett. **66**, 1630 (1991).
[20] P. N. Mikheenko, Yu. A. Genenko, Yu. V. Medvedev, A. I. Usoskin, and I. N. Chukanova, Physica C **212**, 332 (1993).
[21] D. R. Nelson and J. M. Kosterlitz, Phys. Rev. Lett. **39**, 1201 (1977).
[22] Y. Gao, K. L. Merkle, G. Bai, H. L. M. Chang, and D. J. Lam, Physica C **174**, 1 (1991).
[23] B. I. Halperin and D. R. Nelsen, J. Low Temp. Phys. **36**, 599 (1970).
[24] L. N. Bulaevskii, S. V. Meshkov, and D. Feinberg, Phys. Rev. B **43**, 3728 (1991).

Translated by Steve Torstveit

Observation of stochastic resonance in percolative Josephson media

A. M. Glukhov* and A. G. Sivakov

B. Verkin Institute for Low Temperature Physics and Engineering of the National Academy of Sciences of Ukraine, 47 Lenin Ave., Kharkov 61103, Ukraine

A. V. Ustinov

Physikalisches Institut III, Universitat Erlangen-Nürnberg, Erwin-Rommel-Str. 1, D-91058 Erlangen, Germany

(Submitted February 27, 2002)
Fiz. Nizk. Temp. **28**, 543–547 (June 2002)

Measurements of the electrical response of granular Sn-Ge thin films below the superconducting transition temperature are reported. The addition of an external noise to the magnetic field applied to the sample is found to increase the sample voltage response to a small externally applied ac signal. The gain coefficient for this signal and the signal-to-noise ratio display clear maxima at particular noise levels. We interpret these observations as a stochastic resonance in the percolative Josephson media which occurs close to the percolation threshold. © *2002 American Institute of Physics.* [DOI: 10.1063/1.1491176]

1. INTRODUCTION

The phenomenon of stochastic resonance has been discussed in relation to diverse problems in nonlinear science, physics, chemistry and biology.[1] Generally speaking, stochastic resonance is the enhancement of the output signal-to-noise ratio by the injection of an optimal amount of noise into a periodically driven nonlinear system. This kind of behavior is often thought as counterintuitive, since here a stochastic force amplifies a small periodic signal. Its mechanism is usually explained in terms of motion of a particle in a double-well potential subjected to noise, in the presence of a time-periodic force. The periodic forcing leads to noise-enhanced transitions between the two wells and thus to an enhanced output of the forcing signal.

A clear example of nonlinear systems with few degrees of freedom is a superconducting loop with a Josephson junction, well known as a superconducting quantum interferometer (SQUID). With a proper choice of the size of the loop, this system undergoes bistable dynamics for magnetic flux trapped in the loop. There have already been experiments that reported operating SQUIDs under stochastic resonance conditions, both with external noise injection[2] and with thermally generated intrinsic noise.[3] The stochastic resonance effect can be considerably enhanced in a system of coupled bistable oscillators (see, e.g., Ref. 4). Therefore, it is interesting to study stochastic amplification for a Josephson media consisting of many superconducting loops with Josephson junctions.

Earlier we observed quantum interference effects in macroscopically inhomogeneous superconducting Sn-Ge thin-film composites near the percolation threshold.[5] This system exhibits a considerable voltage noise under dc current bias and a rectification of ac current, which arise below the superconducting transition temperature. According to Ref. 6, a dc voltage is observed when an ac current larger than the critical current passes through a system of two superconductors weakly connected by an asymmetric double point contact, i.e., the magnetic flux quantization induces critical-current oscillations and the respective voltage oscillations. We have argued[5] that the oscillatory dependence $V_{dc}(H)$ in Sn-Ge thin-film composites is related to quantum interference in randomly distributed asymmetric superconducting loops interrupted by Josephson weak links. In Ref. 5 we reported measurements of the $V_{dc}(H)$ dependence for various orientations of the film relative to the field. The scale of the oscillatory structure in $V_{dc}(H)$ is inversely proportional to the cosine of the angle between the applied magnetic field and the normal to the sample plane. The emergence of the normal magnetic field component alone and also the antisymmetry of the oscillatory structure relative to $H=0$ indicate a quantum-interference origin of $V_{dc}(H)$. Moreover, it appears feasible to relate these active contours to the percolative cluster that has a well-known fractal structure. The existence of a wide and self-similar distribution of Josephson loop areas leads to a fractal character of the dependence $V_{dc}(H)$. We have suggested and verified a model for the origin of the $1/f$ voltage noise by a passive transformation of magnetic field oscillations with a fractal transfer function $V_{dc}(H)$.[5]

In the present paper we study the noise-induced electrical response of granular Sn-Ge thin-film composites. We argue that a distributed network containing many superconducting loops with Josephson junctions may show a cooperative behavior as stochastically resonating media.

2. EXPERIMENTAL DETAILS AND RESULTS

Josephson networks may occur naturally, e.g., in nonuniform superconducting materials such as granular thin films. We prepare granular Sn-Ge thin-film composites having monotonically varying structure by vacuum condensation of Sn on a long (60 mm) substrate along which a temperature gradient is created. Sn is deposited on the previously prepared 50 nm thick Ge layer. The thickness of the Sn layer is 60 nm. The metallic condensate is covered from the top with

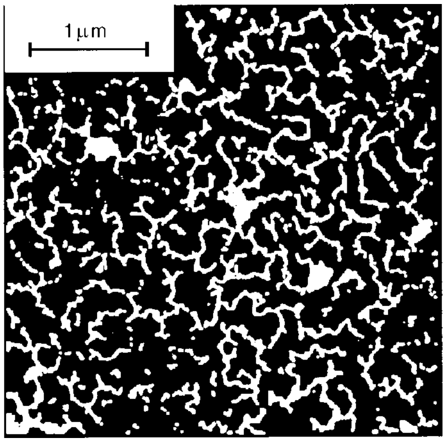

FIG. 1. Electron micrograph of Sn–Ge sample prepared close to the percolation threshold. Black regions correspond to the metallic phase.

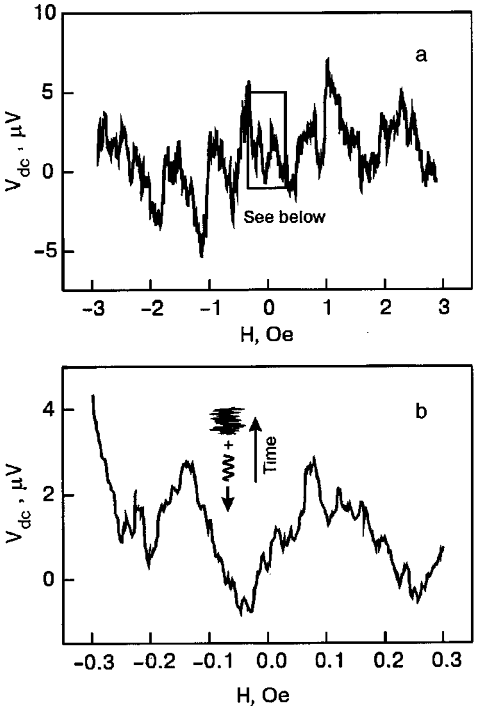

FIG. 2. a—Oscillatory behavior of the rectified voltage across the Sn–Ge sample versus dc magnetic field: $T=3.0$ K, $f_1=100$ kHz, and $I_{\mathrm{ac}}=0.8$ mA. b—Illustration of the stochastic resonance detection scheme. Magnetic field components H_{ac} and H_{noise} are added to the dc magnetic field H.

amorphous Ge. The structural change results in variation of the composite properties from metallic to insulating over the substrate. This crossover in properties is observed on a series consisting of 30 samples cut from different parts of the substrate. For the present investigations, we chose samples with properties near the percolation threshold, with a characteristic structure depicted in Fig. 1.

During the measurements, the samples were kept in exchange gas inside a superconducting solenoid. The electrical measurements were carried out according to the standard four-probe technique. A sinusoidal ac current of frequency $f_1=100$ kHz and amplitude $I_{ac}=0.8$ mA was produced by an HP3245A universal source connected to the current leads through a dc-decoupling transformer. Fast Fourier transformation spectra of the output voltage are measured by using an SR770 spectrum analyzer with a Blackman-Harris window function. We used the signal-to-noise ratio (SNR) as the major characteristic of stochastic resonance. The SNR was measured as the ratio of the voltage amplitude of the spectral line to the voltage noise level below it. The noise background in the signal bin is estimated by performing a linear fit to the peak clipped spectrum. The noise intensity (noise level) denotes the standard deviation σ_N of the Gaussian white noise signal, which was supplied by the internal SR770 generator.

The transition of a sample into the superconducting state is smeared over 1.0 K, with the center of the resistive transition at $T_0=3.8$ K. At temperatures below T_0 and with ac current I_{ac} applied through the sample, we observed a rectified dc voltage V_{dc}, the magnitude of which oscillated as a function of the dc magnetic field H applied perpendicular to the substrate (Fig. 2a). The amplitude and frequency of the current I_{ac} did not significantly affect the general features of the $V_{dc}(H)$ dependence. The results could be always readily reproduced.

To observe the phenomenon of stochastic resonance, we study the rectified voltage dependence on magnetic field. The applied magnetic field consisted of three components: (i) a dc field H, which varied in the range between -300 and $+300$ mOe, (ii) a small ac component with a frequency f_H between 5 and 60 Hz and an amplitude $H_{ac}=20$ mOe, and (iii) Gaussian white noise H_{noise} with an intensity σ_N ranging up to 70 mOe. The Fourier spectra of the voltage response are shown in Fig. 3 together with oscillograms of the input signal $H_{ac}+H_{\mathrm{noise}}$. Figure 4 shows the dependence of the output SNR for the first harmonic of f_H on the intensity of input noise H_{noise}. One can see that increasing the noise amplitude at first increases the SNR and then decreases it. Such maxima are rather characteristic for the phenomenon of stochastic resonance. Similar measurements taken at different magnetic fields and frequencies often showed multiple maxima such as those shown in Fig. 5.

3. DISCUSSION

In summary, our experiments demonstrate the characteristic feature of the phenomenon of stochastic resonance, namely the nonmonotonic behavior of the SNR. At the optimum noise level the SNR increases to 40. The presence of multiple maxima (Figs. 4 and 5) can be due to the effect of different Josephson loops in our structure, which is operated at the border of the percolation threshold.

We suppose that the nonmonotonic dependence of the SNR on frequency f_H (Fig. 5) excludes other possible explanations (such as, e.g., a simple rectification effect due to a nonlinearity of the response) for the observed gain of a small input signal.

Detailed measurements taken at different frequencies, shown in Fig. 5, indicate, at least in some ranges of the dc magnetic field, the existence of parameter regions character-

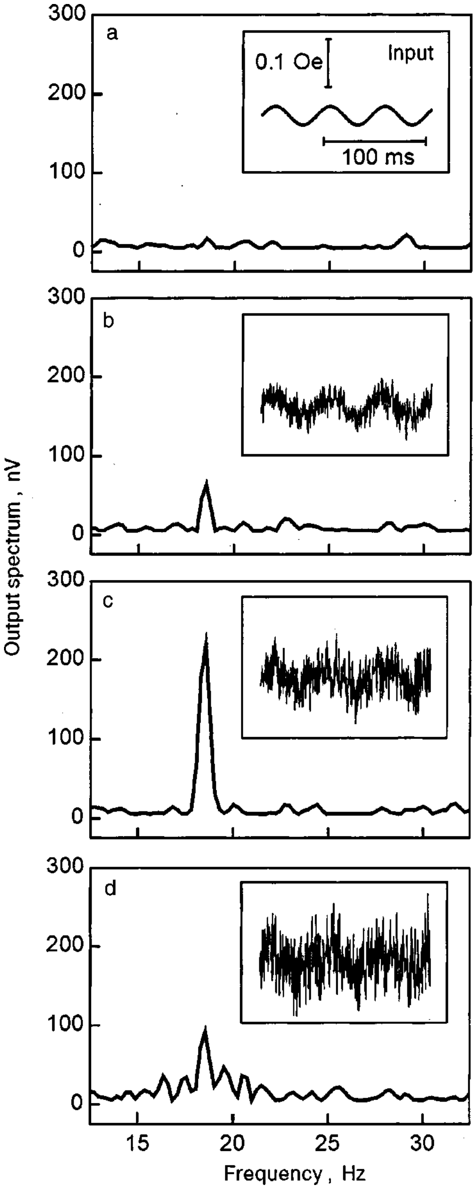

FIG. 3. Input signal $H_{ac}+H_{\mathrm{noise}}$ (insets) and the Fourier spectrum of the output voltage for different levels of input noise H_{noise}: $\sigma_N=0$ (a); $\sigma_N=16$ mOe (b); $\sigma_N=31$ mOe (c); $\sigma_N=47$ mOe (d). The input signal amplitude remains constant at $H_{ac}=20$ mOe. Signal frequency $f_H=18.5$ Hz, dc magnetic field $H=0.17$ Oe.

ized by a significant gain for a relatively broadband signal. We interpret this behavior as a property of percolative Josephson media with a wide range of self-similar loops. The SNR gain in our system can be tuned to a desired operation frequency f_H by changing the dc magnetic field H.

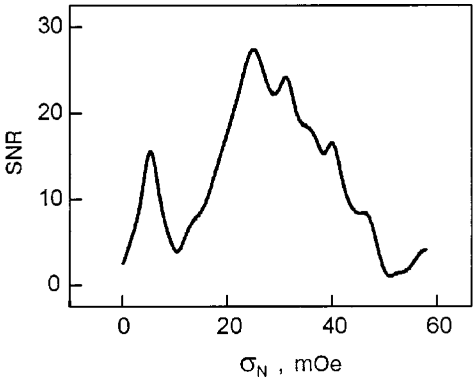

FIG. 4. Output signal-to-noise ratio (SNR) versus input noise level σ_N for the first harmonic of the input signal frequency $f_H=18.5$ Hz. Magnetic field $H=0.17$ Oe.

The nature of the stochastic resonance in the system studied can be related to the commonly known bistable oscillator behavior of the magnetic flux quantization loops. Moreover, in the presence of current bias I_{ac} at relatively high frequency (at f_1 about 100 kHz) with amplitude larger than critical, our samples exhibit dynamical chaos. Such a regime is commonly characterized by a coexistence of multiple attractors in the phase space. Indeed, calculation of Lyapunov exponents from the time evolution of the voltage measured at constant current indicates presence of chaos in our system.[7] In this case, the "phase trajectory" of the system may stay a long time in any of the attractors and perform irregular transitions between them. Synchronization of such

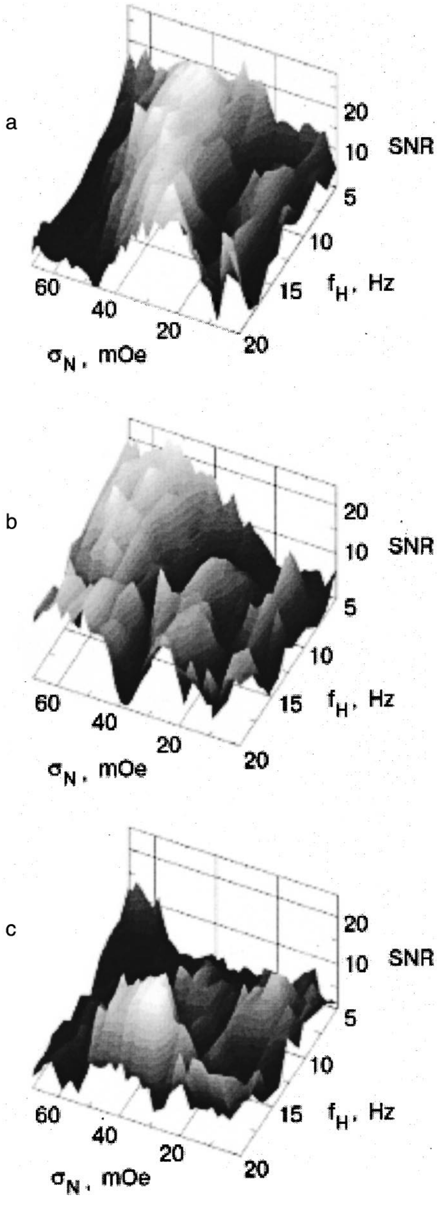

FIG. 5. SNR dependence on input noise level σ_N and input signal frequency f_H at different dc magnetic fields H, Oe: 0.17 (a); 0.18 (b); 0.19 (c).

intermittent transitions by a small input signal may lead to stochastic resonance as well.[8] Yet, these speculations require further investigations to be firmly justified.

This work was supported by the German-Ukrainian collaboration grant of the Bundesministerium für Bildung, Wissenschaft, Forschung und Technologie (BMBF) No. UKR-003-99.

[*] E-mail: glukhov@ilt.kharkov.ua

---

[1] L. Gammaitoni, P. Hanggi, P. Jung, and F. Marchesoni, Rev. Mod. Phys. **70**, 223 (1998).

[2] A. D. Hibbs, A. L. Singsaas, E. W. Jacobs, A. R. Bulsara, J. J. Bekkedahl, and F. Moss, J. Appl. Phys. **77**, 2582 (1995).

[3] R. Rouse, S. Han, and J. E. Lukens, Appl. Phys. Lett. **66**, 108 (1995).

[4] J. F. Lindner, B. K. Meadows, W. L. Ditto, M. E. Ichiosa, and A. R. Bulsara, Phys. Rev. Lett. **75**, 3 (1995).

[5] A. M. Glukhov, A. S. Pokhila, I. M. Dmitrenko, A. E. Kolinko, and A. P. Panchekha, Physica B **24**, 242 (1997).

[6] A. Th. A. M. De Waele and R. De Bruyn Ouboter, Physica **41**, 225 (1969).

[7] A. M. Glukhov, I. M. Dmitrenko, A. E. Kolinko, A. S. Pokhila, and O. G. Turutanov, *XXII International Conference on Low Temperature Physics-1999, Finland*.

[8] V. S. Anischenko, A. B. Neiman, F. Moss, and L. Schimansky-Geier, Usp. Fiz. Nauk **169**, 7 (1999).

This article was published in English in the original Russian journal. Reproduced here with stylistic changes by AIP.

LOW TEMPERATURE PHYSICS VOLUME 28, NUMBER 6 JUNE 2002

Excitation of oscillations of the magnetic induction in a Nb–Ti slab as a result of a thermomagnetic flux avalanche

V. V. Chabanenko*

A. A. Galkin Donetsk Physicotechnical Institute, ul. R. Lyuksemburg 72, 83114 Donetsk, Ukraine

V. F. Rusakov

*Donetsk National University, Ministry of Education and Science of Ukraine, ul. Universitetskaya 24,
83055 Donetsk, Ukraine*

V. A. Yampol'skiĭ

*A. Ya. Usikov Institute of Radio Physics and Electronics, National Academy of Sciences of Ukraine,
ul. Akad. Proskury 12, 61085 Kharkov, Ukraine*

H. Szymczak, S. Piechota, S. Vasiliev, and A. Nabialek

Institute of Physics, Polish Academy of Sciences, al. Lotnikow 32/46, 02-668 Warsaw, Poland

(Submitted February 8, 2002)
Fiz. Nizk. Temp. **28**, 548–552 (June 2002)

Weakly damped oscillations of the magnetic induction with a frequency of $\sim 10^3$ Hz are observed in a hard superconductor. The excitation of oscillations in the mixed state of a Nb–Ti slab is the result of giant magnetic flux avalanches arising in the development of a thermomagnetic instability. The existence time of the oscillatory phenomena is tens of times greater than the duration of the avalanche. These oscillations contain information about the vortex matter of a superconductor. © *2002 American Institute of Physics.* [DOI: 10.1063/1.1491177]

INTRODUCTION

There have been quite a few papers devoted to the study of the response of hard type-II superconductors in a metastable mixed state to a strong external magnetic disturbance.[1–3] Three types of behavior of the critical state of high-T_c superconductor (HTSC) single crystals are observed[1] as the rate of change of the external magnetic field is increased in the range 0–42 T/s: a stable regime of flux entry at low and extremely high rates, and flux entry in the form giant jumps as a result of a thermomagnetic instability at intermediate rates. The stable regime at very high rates of change of the external field arises because of the suppression of the instability of the critical state. The use of higher rates $\sim 10^4$ T/s has permitted the observation[3] of induced unrelaxed shielding currents in HTSC materials, an order of magnitude higher than the typical values of the critical currents under ordinary conditions of low rates of change of the field.

Our previous studies of thermomagnetic instability effects[4] and our Hall-probe study of the structure of the giant flux jumps[5] in Nb–Ti and Nb superconductors revealed a number of curious effects. For example, the surge of the magnetic induction $B_{\text{surf}}(t)$ arising on the surface of the superconductor as a result of a giant avalanche ($\sim 10^{10}$ flux quanta) has a maximum value exceeding the value of the external magnetic field. In other words, the magnetic induction density rises sharply at the surface of the superconductor (compression occurs) as a result of a flux avalanche. The flux compression is followed by oscillations of the magnetic induction which are strongly damped in time. In addition, in the time interval preceding the avalanche the magnetic flux unexpectedly moves in the opposite direction to the avalanche, both during the entry of the flux (the shielding regime) and during its exit (the flux-trapping regime). Here the value of the backward (with respect to the direction of the main flux motion) induction peaks reaches 16% of the total value of the flux jump. Energetically this is already a significant amount, so that one can speak of a certain dynamic potential barrier opposing the change in flux. At present there are no theoretical models that can unequivocally explain the novel dynamical properties of the vortex state of a superconductor.

The present paper is devoted to an experimental study of the dynamical properties of the vortex matter in low-temperature superconductors with strong magnetic flux pinning under extreme conditions by means of induction measurements. These extreme conditions are realized during the breakaway of the vortex matter from the pinning centers and the subsequent giant acceleration (500 km/s^2) as a result of the development of a thermomagnetic instability.[6,7] Under the influence of the Lorentz force the magnetic flux in a fraction of a second acquires a velocity of several tens of meters per second. The goal of the present study is to investigate experimentally the structure of the flux jump in a superconducting slab. The main result of these investigations is the detection of weakly damped oscillatory phenomena, with a frequency of $\sim 10^3$ Hz, in the magnetic induction of the superconductor. The oscillatory process is observed for a time of the order of 0.1 s after completion of the flux avalanche. These oscillatory processes contain information about the vortex state arising in the superconductor after relaxation of the nonuniform mixed state.

The observation of weakly damped oscillations with a

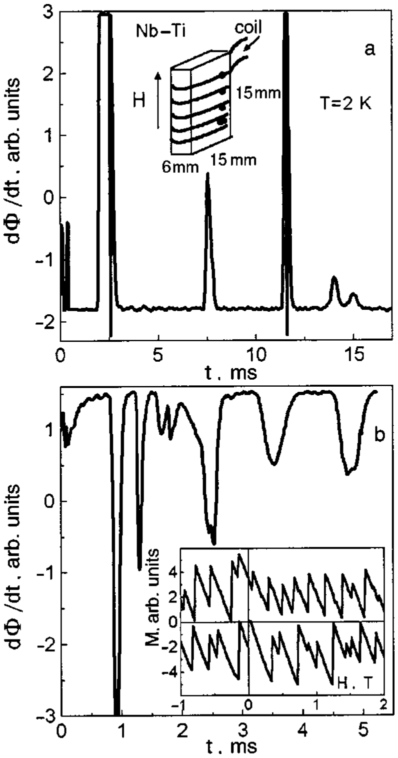

FIG. 1. Voltage across the measuring coil during the development of the thermomagnetic instability: a—an example of discrete avalanches in the flux-trapping regime (the inset shows the geometry of the experiment); b—an example of a practically continuous cascade of avalanches in the magnetic-flux shielding regime (the inset shows how the flux jumps are demonstrated in the magnetization $M(H)$).

rather high frequency in the highly dissipative medium that is the vortex matter of a superconductor in the mixed state is a quite unexpected result. Low-frequency (~ 1 Hz) oscillatory processes in various physical properties of a superconductor prior to the magnetic flux avalanche are well known (see, e.g., Refs. 8–10). They are due to instability of the nonuniform critical state at the instant before the magnetic avalanche. Slow fluctuations of a boundary between normal and superconducting regions as a result of a thermal pulse have been observed in HTSCs.[11] These fluctuations led to oscillations (with frequency ~ 0.05 Hz) of the measured voltages in dc and ac studies.

EXPERIMENTAL TECHNIQUE

The dynamics of the magnetic flux inside a superconductor (Nb–Ti, 50 at.%, $T_c = 9$ K) immersed in liquid helium at $T = 2$ K was investigated by means of an induction coil wound directly on a $6 \times 15 \times 15$ mm superconducting slab (see the inset in Fig. 1a). The coil consisted of several tens of turns. It registered a voltage proportional to the rate of change of the magnetic flux, $d\Phi/dt$. This voltage was fed directly to a Riken Denshi TCC-1000 transient recorder. The structure of each voltage jump across the coil was stored in the memory of this recorder as 1020 experimental points, the coordinates of which were then put into a computer. Loops of the magnetization $\mathbf{M}(H)$ ($\mathbf{M} = \mu_0\mathbf{H} - \mathbf{B}_{\mathrm{surf}}$, where $\mathbf{H}$ is the external magnetic field and μ_0 is the magnetic permeability of free space) were recorded by means of Hall probes, one of which measured the surface induction B_{surf} and the other the external magnetic field H.

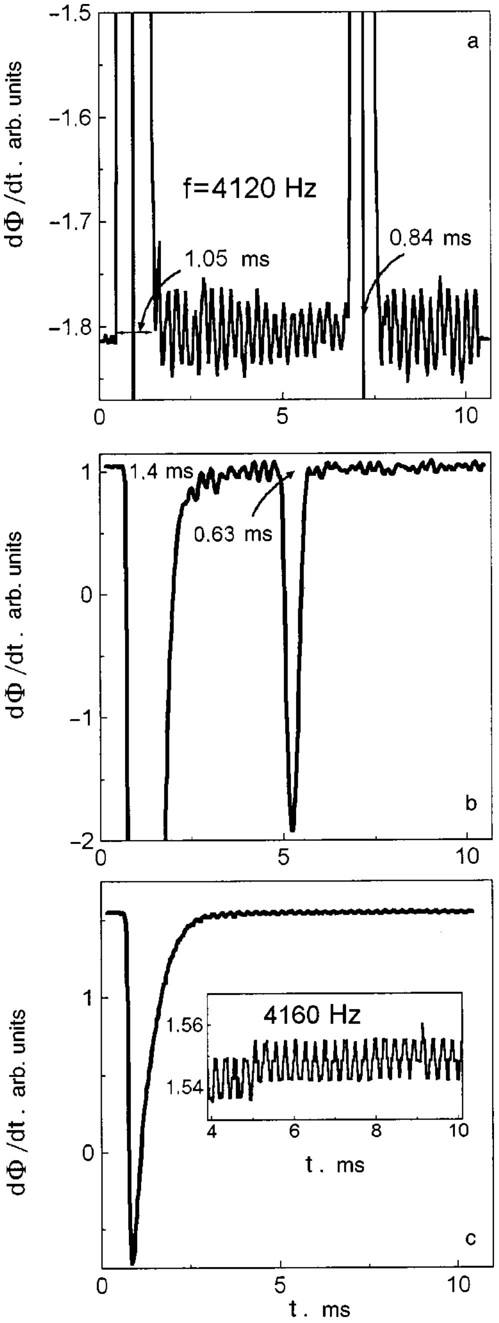

FIG. 2. Oscillatory phenomena at $T = 2$ K in the induction of a superconductor (a Nb–Ti slab): upon the exit (flux-trapping regime) of two successive flux avalanches (a); and upon the entry of flux (flux-shielding regime) in a two-step (b) and a single-step (c) avalanche.

EXPERIMENTAL RESULTS

A study of the signals recorded with the measurement coil and giving the integral characteristic of the process over the entire cross section of the superconducting core showed that during the development of the thermomagnetic instability the magnetic flux enters the sample in a rather complex random manner. Figure 1 shows examples of such signals. We see that the flux can enter both in the form discrete avalanches and in a nearly continuous cascade of jumps (Fig.

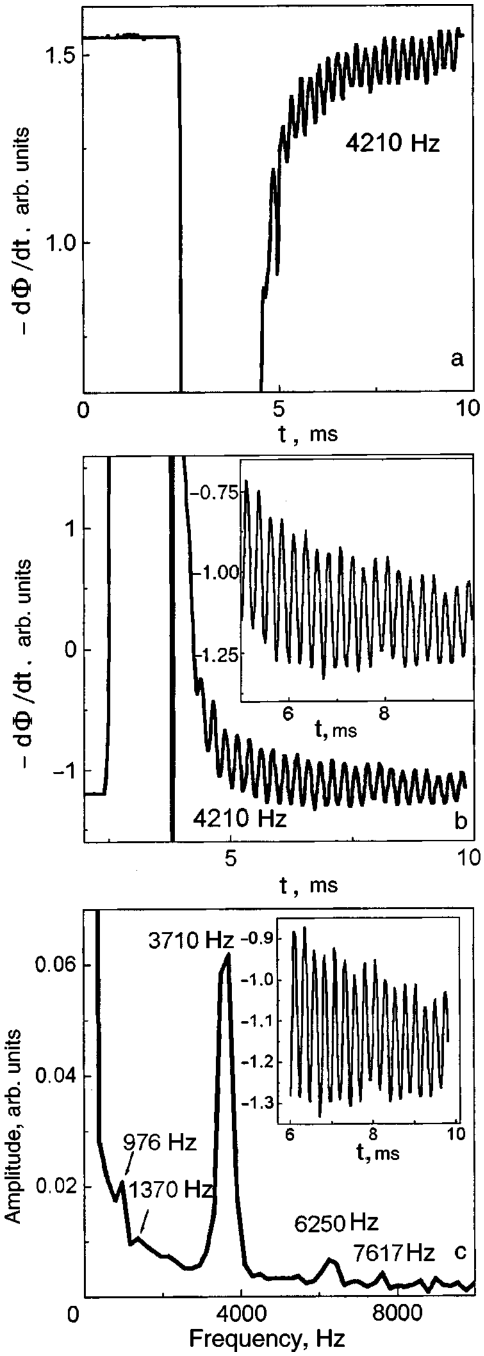

FIG. 3. Detailed picture of the oscillations in a Nb–Ti slab at a temperature of 2 K: a—in the shielding regime, b—in the flux-trapping regime; c—the spectrum of the observed oscillations, constructed by a Fourier transform method.

1b). Both types of pictures are observed during both the entry and exit of the flux. Figure 1 shows randomly chosen examples of the two types of variation of the flux. More rarely double avalanches (Figs. 2a and 2b) and single avalanches (Figs. 2c and 3) are observed.

As the results presented in Figs. 1–3 attest, the avalanches end in an oscillatory process. This oscillatory process contains a certain superposition of oscillations with different frequencies. An estimate of the fundamental frequency of the oscillations shown in Fig. 3b, determined as the quotient of the number of oscillations that have occurred divided by their total duration, gives a value ≈4.2 kHz. An analysis of the frequency spectrum of the oscillations gives a fundamental frequency of 3.71 kHz, which is close to the estimate. Besides the fundamental frequency, the spectrum shown in Fig. 3c contains oscillations with lower amplitudes at frequencies of 976, 1370, 6250, and 7617 Hz.

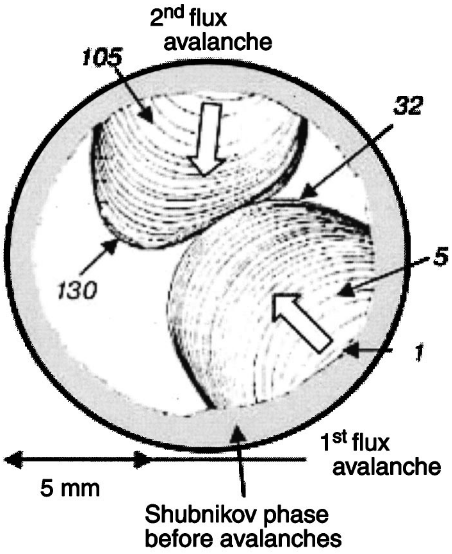

FIG. 4. Visualization of two successive flux jumps in a niobium disk (from Ref. 12).

The observed oscillations of the induction are apparently due to density waves arising in the vortex matter in that part of the superconductor which was entered by the magnetic flux as the result of an avalanche. In the rest of the sample the flux is pinned. Figure 4, which was taken from Ref. 12, shows the result of a magnetooptical visualization (with the use of a fast motion picture camera) of the penetration of the magnetic flux into a niobium disk upon the successive passage of two avalanches. This diagram shows the successive positions of the moving flux front. The time interval between successive frames is 103 μs. The numbers labeling the flux fronts are the frame numbers of the film. Figure 4 reflects an important fact: when the second flux avalanche, which arose near the opposite end of the disk 7 ms after the first, reaches the boundary of the first avalanche after 10 ms, its magnetic flux flows around the already frozen (pinned) profile of the latter. This indicates that the magnetic flux erupting into the sample has properties of ''molten'' matter. This suggests that the induction oscillations detected are due to vortex-matter density waves arising in ''puddles'' of erupting flux. The oscillatory process which we observed is governed by the properties of the molten vortex matter, the most important of which are apparently its mass and viscosity.

CONCLUSION

In this study we have experimentally observed oscillatory phenomena in the magnetic induction of a hard superconductor in the mixed state; they appear after an avalanchelike injection of magnetic flux brought about by a thermomagnetic instability. Further experimental studies of these effects and the construction of a theoretical model of the observed oscillations will make it possible to determine the most important parameters of the vortex matter.

*E-mail: chaban@host.dipt.donetsk.ua

---

[1] A. Gerber, J. N. Li, Z. Tarnawski, J. J. M. Franse, and A. A. Menovsky, Phys. Rev. B **47**, 6047 (1993).
[2] V. Meerovich, M. Sinder, V. Sokolovsky, S. Goren, G. Jung, G. E. Shter, and G. S. Grader, Semicond. Sci. Technol. **9**, 1042 (1996).
[3] K. Rosseel, J. Vanacken, L. Trappeniers, H. H. Wen, W. Boon, F. Herlach, V. V. Moshchalkov, and Y. Bruynseraede, Physica C **337**, 265 (2000).
[4] V. V. Chabanenko, A. I. D'yachenko, M. V. Zalutskii, V. F. Rusakov, H. Szymczak, S. Piechota, and A. Nabialek, J. Appl. Phys. **88**, 5875 (2000).
[5] V. V. Chabanenko, V. Rusakov, V. Yampol'skii, S. Piechota, A. Nabialek, S. Vasiliev, and H. Szymczak, cond-mat/0106379 (June 19, 2001).
[6] S. L. Wipf, Phys. Rev. **161**, 404 (1967).
[7] R. G. Mints and A. L. Rakhmanov, Rev. Mod. Phys. **53**, 551 (1981).
[8] N. H. Zebouni, A. Venkataram, G. N. Rao, C. G. Grenier, and J. M. Reynolds, Phys. Rev. Lett. **13**, 606 (1964).
[9] R. G. Mints, Phys. Rev. B **53**, 12311 (1996).
[10] L. Legrand, I. Rosenman, R. G. Mints, G. Gollin, and E. Janod, Europhys. Lett. **34**, 287 (1996).
[11] I. Kirschner, R. Laiho, A. C. Bodi, and E. Lahderanta, Physica C **290**, 206 (1997).
[12] B. B. Goodman and M. Wertheimer, Phys. Lett. **18**, 236 (1965).

Translated by Steve Torstveit

LOW TEMPERATURE PHYSICS VOLUME 28, NUMBER 6 JUNE 2002

Inelastic electron tunneling across magnetically active interfaces in cuprate and manganite heterostructures modified by electromigration processes

M. A. Belogolovskiĭ,* Yu. F. Revenko, and A. Yu. Gerasimenko

A. Galkin Donetsk Physical and Technical Institute of the National Academy of Sciences of Ukraine,
72 R. Luxemburg Str., Donetsk 83114, Ukraine

V. M. Svistunov

A. Galkin Donetsk Physical and Technical Institute of the National Academy of Sciences of Ukraine,
72 R. Luxemburg Str., Donetsk 83114, Ukraine, Nanoelectronics Laboratory, Faculty of Engineering,
Hokkaido University, Sapporo 060, Japan, and Frostburg State University, Frostburg, MD 21532,
United States

E. Hatta

Nanoelectronics Laboratory, Faculty of Engineering, Hokkaido University, Sapporo 060, Japan

G. Plitnik

Frostburg State University, Frostburg, MD 21532, United States

V. E. Shaternik and E. M. Rudenko

Institute for Metal Physics of the National Academy of Sciences of Ukraine, 36 Vernadsky Blvd.,
Kiev 03142, Ukraine

(Submitted February 11, 2002)
Fiz. Nizk. Temp. **28**, 553–557 (June 2002)

We report a study of the electron tunneling transport in point-contact junctions formed by a sharp Ag tip and two different highly correlated oxides, namely, a magnetoresistive manganite $La_{0.66}Ca_{0.34}MnO_3$ and a superconducting cuprate $LaBa_2Cu_3O_{7-x}$. Strong chemical modifications of the oxide surface (supposedly, oxygen ion displacements) caused by applying high voltages to the junctions have been observed. This effect is believed to be responsible for an enormous growth of inelastic tunneling processes across a transition region that reveals itself in an overall V-shaped conductance background, with a strong temperature impact. The mechanism of the inelastic scattering is ascribed to charge transmission across magnetically active interfaces between two electrodes forming the junction. To support the latter statement, we have fabricated planar junctions between Cr and Ag films with an antiferromagnetic chromium oxide Cr_2O_3 as a potential barrier and at high-bias voltages have found an identical conductance trend with a similar temperature effect.
[DOI: 10.1063/1.1491178]

In the last few years, and mainly due to the progress in nanotechnology, the rapidly emerging field of spin-polarized transport across heterostructures, often called ‘‘spintronics,’’ has become an area of intensive basic and applied studies. Usually, an analysis of spintronic systems ignores interfacial processes which can flip the spin of a conduction electron traveling across a device. But their influence on the magnetic junction transport characteristics may be dramatic and it would be important to study the sensitivity of tunneling transport properties on the magnetic interfacial scattering. This problem was addressed theoretically[1] and experimentally (see Ref. 2 and references therein) in relation to magnetic tunnel junctions showing large magnetoresistance. As it was argued by Guinea,[1] the effect should be particularly enhanced in fully polarized magnets such as doped manganites, where the tendency towards ferromagnetism may be reduced at a surface, leading to antiferromagnetic behavior. Thus to study an effect of spin-flip processes caused by interfacial magnetic excitations on the charge transport in such systems seems to be one of the actual issues.

In this sense, ferromagnets as junction electrodes are not good candidates for investigating the role of the spin-assisted tunneling and simpler devices would be preferable. In our previous paper[3] we presented tunneling measurements on high-temperature superconducting cuprates, another family of perovskites. It was shown that in these materials interactions of tunneling electrons with excitations inside the transitional insulating layer strongly influence the conductance spectra. The system investigated experimentally[3] was a point-contact junction prepared with a sharp Ag tip pressed into the surface of a ceramic superconductor $LaBa_2Cu_3O_{7-x}$ (LBCO). The latter material is known to be one of the most unstable of the superconducting high-T_c cuprates, with a badly degraded layer adjoining the surface. Our interpretation of the data obtained was based on the assumption that oxygen rearrangement caused by an applied electric field re-

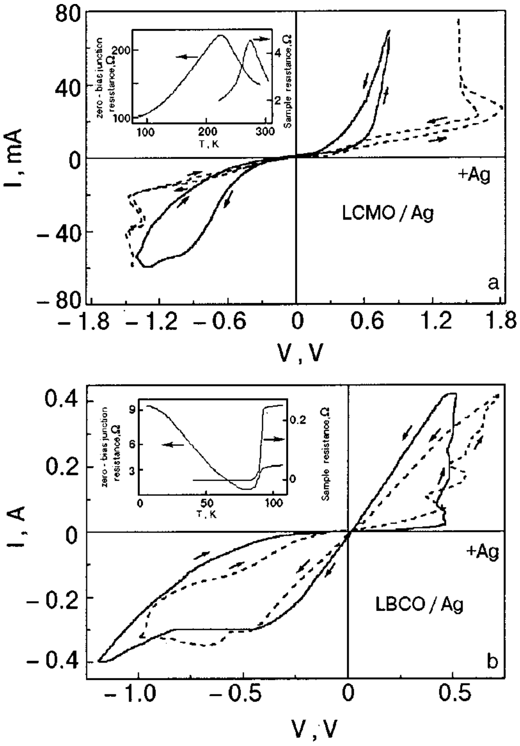

FIG. 1. Switching effect on the current-voltage characteristics of $La_{0.66}Ca_{0.34}MnO_3$/Ag (a) and $LaBa_2Cu_3O_{7-x}$/Ag (b) point contacts at 300 K (solid lines) and 77 K (dashed lines). The insets display the temperature behavior of the zero-bias junction resistance compared with that for a bulk metaloxide sample.

sults in the appearance of an oxygen-deficient region near the interface. In accordance with the 123-compound phase diagram it should be antiferromagnetically ordered, and the related inelastic-scattering processes can contribute strongly to the charge transmission across the junction. In this work, we demonstrate important similarities between background conductance spectra of junctions formed by manganites and cuprates as well as an effect of high bias voltages on them; experimentally demonstrate signs of near-interface chemical modifications (supposedly, oxygen ion displacements that we believe to be a source of the composition changes), and confirm the hypothesis of the existence and strong effect of magnetic correlations in the transition region between Ag and lanthanum-based metal oxides by performing the same measurements on a tunnel junction with a Cr_2O_3 barrier known to be antiferromagnetic in the bulk state.

We start with conductance experiments on the magnetoresistive compound $La_{0.66}Ca_{0.34}MnO_3$ (LCMO). Bulk samples of manganites (as well as cuprates) were sintered by the conventional solid-state method. Appropriate amounts of the corresponding oxides were mixed, pressed, and annealed at 1200 °C for 12 hours. The resulting pellet was ground, sintered, and repelletized before a sample with a high packing density was obtained. The values of the Curie temperature agreed well with known data (the inset in Fig. 1a). Point-contact junctions were prepared with a silver counterelectrode by the same way as those based on high-T_c LBCO compounds (for details see Ref. 3). The corresponding peak in the temperature dependence of the tunnel resistance for LCMO was always shifted to lower T as a result of the suppression of ferromagnetism in the upper layers of the manganites (the inset in Fig. 1a). The related findings for superconducting LBCO contacts with T_c's near 93 K are presented in the inset in Fig. 1b. Together with the overall increase of the junction resistance expected from the conventional tunneling theory,[4] it also displays a minimum below T_c. As was shown in Ref. 5, such a feature appears in the conductance spectra of N-I-S heterostructures for moderate values of the insulating region transparency (the standard theory of tunneling processes[4] assumes the presence of very high potential barriers).

A radical (but reversible) effect of oxygen electromigration processes on the LCMO/Ag contact current–voltage ($I-V$) curves is shown in Fig. 1a in comparison with corresponding data for LBCO/Ag junctions in Fig. 1b. In both cases at 300 K we observed a decrease of the point contact resistance when a positive bias voltage V^* was applied on the Ag tip and an increase for the corresponding negative biases. The values of V^* were different: near 0.8 V for LCMO and about 0.5 V for LBCO. Following previous works on the same subject,[6,7] we explain abrupt changes of the point-contact resistance at activation voltages by modifications of the oxygen stoichiometry near the intrinsic metaloxide surface under the influence of applied electric field. Then the difference in V^* can be ascribed to the fact that in the lanthanum-based cuprate the Cu–O bond is weaker than the Mn–O bond in LCMO. It should be noted that for a parent yttrium-based cuprate (YBCO), where the Cu–O bond is known to be stronger than in LSCO, the bias range where the electromigration effect can be detected is, as a rule, essentially larger.[7] The picture proposed also explains why the activation voltages V^* needed to stimulate the transition from one branch of the conductance spectra to another have increased with decreasing temperature (Fig. 1).

Our results show that after applying high voltages of different polarities not only are the conductance values different but the character of the spectra as well is changed from a parabolic characteristic (the high-resistance characteristic) to a V-shaped behavior in the low-resistance case. Figures 2a–c show typical examples of differential conductance curves $\sigma(V)=dI(V)/dV$, each at a different temperature. It should be emphasized that there is a fundamental difference with conventional metal-insulator-metal junctions, where the background behavior is polynomial for voltages small compared with the barrier height:[4]

$$\sigma(V)=\alpha+\beta V+\gamma V^2. \tag{1}$$

In manganite- and cuprate-based contacts the overall dependence of $\sigma(V)$ does not have the form (1) but rather follows the formula[7]

$$\sigma(V)=a+b|V|+cV^2. \tag{2}$$

To demonstrate it, in the insets in Figs. 2a–c we have plotted the even conductance $\sigma(V)=[\sigma(V)+\sigma(-V)]/2$ for the lowest temperatures studied. It does contain a dominating linear term.

It has been already stressed that the V-shaped background is a common feature of the conductance spectra $\sigma(V)$ of different metallic oxide systems.[8] Here we present some novel results for LBCO/Ag contacts and for Cr-Cr oxide-Ag multilayered structures that, as we hope, may shed light on

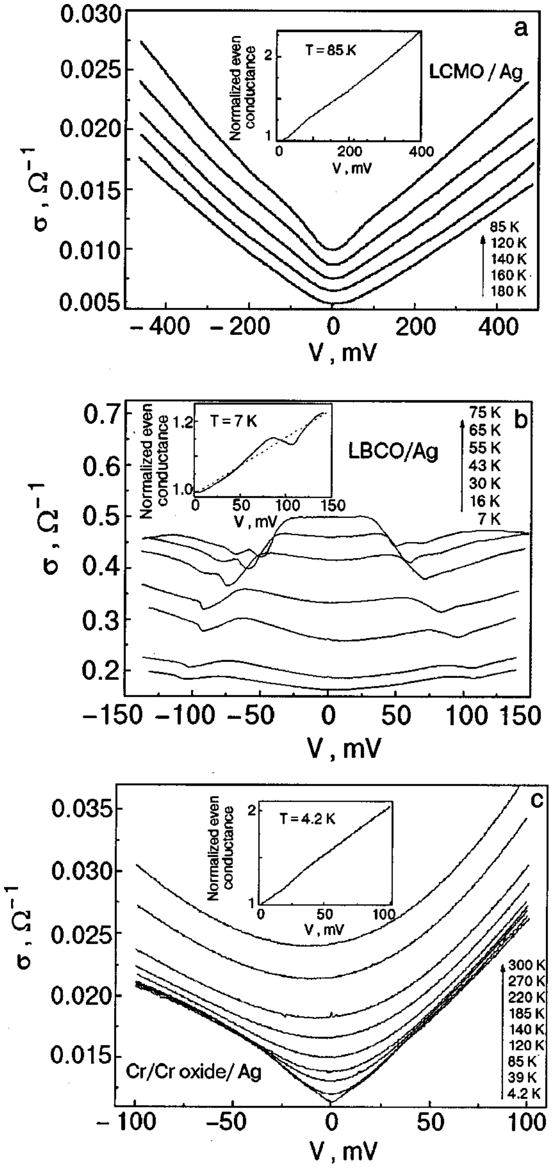

FIG. 2. Temperature effect on the tunneling conductance spectra for a $La_{0.66}Ca_{0.34}MnO_3$/Ag point contact (a), a $LaBa_2Cu_3O_{7-x}$/Ag point contact (b), and a planar junction between Cr and Ag films with a magnetic chromium oxide as a potential barrier (c). Insets show even parts of the differential conductance vs voltage curves at lowest measured temperatures. Note the dominating V-shaped background in all three characteristics.

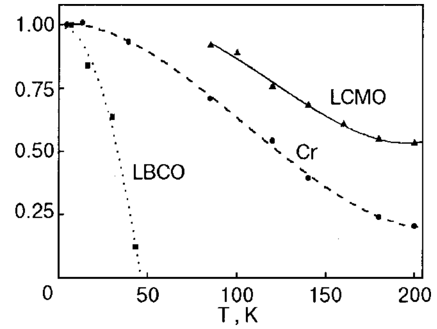

FIG. 3. Temperature behavior of the parameter b characterizing the strength of the inelastic tunneling processes for LCMO and LBCO based point contacts compared with the data for a Cr-Cr_2O_3-Ag junction.

the possible role of inelastic scatterings of a magnetic origin at the injector-oxide interfaces. As is shown in the inset in Fig. 2b, on a large scale the conductance $\sigma(V)$ of the LBCO-based junction exhibits a quasi-linear behavior (2) with a superimposed superconducting gap-like feature. We relate it to chemical composition changes in the near-interface region that are usually attributed to oxygen ion displacement processes at the cuprate surface, leading, in particular, to strong suppression of superconductivity in the upper layers (see the review[9]). The most important thing for our purposes is the correlation between the strength of electromigration processes in LBCO (compared with YBCO and LCMO) and the quasi-linear overall behavior of the differential conductance, which is known to serve as a fingerprint of the inelastic-tunneling effect.[7]

Next, we consider the validity of the assumption of an oxygen-deficient near-interface layer created after application of corresponding high biases to the metallic injector and the existence of a magnetically active interlayer between the two electrodes that strongly influences electron tunneling processes across the transition region. It is believed[7] that the layer appears because of the removal of oxygen in the upper cuprate layers, which modifies the doping of CuO_2 planes and can thus lead to long-range antiferromagnetic correlations between localized Cu spins. An argument for such a supposition comes from Ref. 7, where it was shown that the anomalous $b|V|$ contribution to the conductance spectra of a normal metal/YBCO junction vanishes near the expected Néel temperature T_N. If we are really dealing with a magnetic barrier, the same observation should be true for heterostructures with both pervoskite oxides. For those with LBCO we did not expect the oxygen removal to be as great as in the YBCO/Pb specimens studied in Ref. 7. The reason is that Pb deposited on the metaloxide surface strongly extracts oxygen atoms, forming a PbO_x barrier, but this does not occur for noble metals such as Au or Ag, whose standard reduction potential is known to be higher than that for Cu^{2+}. Hence, T_N for a surface region of LBCO should be somewhat lower than that found before[7] for YBCO-based contacts with Pb. The temperature effect on the linear slope of $\sigma_e(V)$, i.e., on the coefficient b, is shown in Fig. 3 for both structures. As to electromigration effects, the basic behavior of $b(T)$ for LBCO devices is the same as in Ref. 7 for YBCO contacts, but the temperature values at which b decays are considerably lower. It is important that $b(T)$ for manganite samples goes to zero with increasing T as well (Fig. 3).

Why do we interpret the anomalous (proportional to $|V|$) term in the conductance spectra as being a result of inelastic boson-assisted tunneling? The standard theory of tunneling phenomena in metal heterostructures, which takes into account only elastic transmission and the energy dependence of the tunneling matrix element,[4] predicts the quadratic behavior (1). There are several possible reasons why a term proportional to $|V|$ can appear in $\sigma(V)$: the non-Fermi-liquid nature of the oxides (the RVB model, the marginal Fermi-liquid hypothesis, etc.) as well as extrinsic approaches.[10] Following Ref. 7, we reject effects of an intrinsic nature for superconducting cuprates (because of the lack of any correlations between the temperature effect on the superconducting parameters and the coefficient b). The corresponding contribution to the even conductance $\sigma_e(V)$ can appear as a result of inelastic processes.[11] It is equal to $\int_0^{eV}F(\omega)d\omega$ and hence should be a linear function of the bias V for a near-constant density of bosonic states $F(\omega)$ (in the case of magnetic excitations $F(\omega)$ is the dynamic susceptibility integrated over the wave vector). That is precisely the case for a normal YBCO compound[12] or an underdoped high-T_c cuprate $La_{2-x}Sr_xCuO_4$ (Ref. 13), where magnetic inelastic neutron-scattering data reveal spin fluctuations on a large energy scale. We suppose that the broad continuum of these excitations is the origin of the unconventional linear term in $\sigma_e(V)$. Small nonlinearities in $\sigma_e(V)$ for LMCO and Cr oxide at voltages below 100 meV (the insets in Figs. 2a and 2c) reflect fine structures in the corresponding $F(\omega)$.[11]

The last argument for our statement about the magnetic nature of the enormous enhancement of inelastic tunneling processes is provided by a direct experiment with a junction in which an insulating interlayer between metallic electrodes is known to be magnetically ordered. For this purpose we have fabricated planar heterostructures between Cr and Ag thin films with a chromium oxide as a potential barrier. Such junctions were studied thirty years ago by Rochlin and Hansma,[14] who showed that under appropriate oxidation conditions an antiferromagnetic Cr_2O_3 layer grows on the Cr film. At low temperatures, in accordance with our data for LCMO and LBCO, they observed a nearly linear dependence of σ_e (V) on V, with a fine structure that was related to phonon and/or magnon excitations in the Cr_2O_3 barrier. Comparing these findings with those for similar Al-oxide junctions, the authors[14] concluded that the only significant difference between two sets of experiments was the magnetic behavior of Cr_2O_3, which must be responsible for increasing the inelastic tunneling contribution to the conductance of Cr-Cr_2O_3-metal heterostructures. We have followed the preparation procedure described by Rochlin and Hansma[14] and reproduced their data for 4.2 K. Here we present detailed temperature measurements of Cr-Cr oxide-Ag junction characteristics with a special emphasis on the anomalous $|V|$ term in $\sigma(V)$, regarded by us as an indication of inelastic tunneling via magnetic excitations in the oxide layer. As can be seen from Fig. 2c, this contribution is rather strong and determines the overall behavior of the conductance background. We have plotted the strength of the process, i.e., the value of the coefficient b versus temperature, and compared it with analogous curves for perovskite-based junctions. From Fig. 3 one can see a similar behavior of $b(T)$ for all three kinds of heterostructures. The abrupt decrease of the parameter b with increasing temperature can be ascribed to the weakness of the spin fluctuations.

To summarize, we have performed conductance-versus-voltage measurements involving both cuprates and manganites, which we believe are important for deepening our understanding of the charge transport in heterostructures formed by these rather enigmatic materials. In the systems studied a degraded surface layer with enhanced magnetic correlations can play the role of a potential barrier, and in this case spin-assisted inelastic tunneling should strongly contribute to the charge tunneling transmission. To demonstrate this with independent experiments, we have fabricated planar junctions between Cr and Ag films with an insulating Cr_2O_3 layer formed by oxidizing the Cr film. This oxide in the bulk state is known to be antiferromagnetic at low temperatures. Despite different materials, barriers, and preparation methods, the conductance spectra were found to be very similar, with an unusual $|V|$ term in the background dominating at low temperatures. Clearly, the only common feature of the samples studied is a magnetic interface between two metals forming the junction, and it is this that we suppose is responsible for the anomalous experimental findings. The obvious similarities between the three different systems are not surprising because the underlying physics behind the observed phenomena is expected to be the same—an inelastic charge transmission across magnetically active insulating layers.

We thank Prof. M. A. Obolenskii, Prof. A. N. Omelyanchouk, and Prof. Yu. V. Medvedev for stimulating discussions. V.M.S. is grateful to the Ministry of Education, Culture, Science and Technology of Japan for support of his stay at Hokkaido University, and to the Research and Educational Fund of the Frostburg State University for support of his stay in the USA.

*E-mail: vlamis@hsts.fti.ac.donetsk.ua

---

[1] F. Guinea, Phys. Rev. B **58**, 9212 (1998).
[2] P. LeClair, J. T. Kohlhepp, H. J. M. Swagten, and W. J. M. de Jonge, Phys. Rev. Lett. **86**, 1066 (2001).
[3] E. Hatta, V. M. Svistunov, Yu. F. Revenko, M. A. Belogolovskii, N. A. Doroshenko, and G. Plitnik, Mod. Phys. Lett. B **14**, 819 (2000).
[4] E. L. Wolf, *Principles of Electron Tunneling Spectroscopy*, Oxford University Press, New York (1985).
[5] M. Belogolovskii, M. Grajcar, and P. Seidel, Phys. Rev. B **61**, 3259 (2000).
[6] L. F. Rybalchenko, V. V. Fisun, N. L. Bobrov, I. K. Yanson, A. V. Bondarenko, and M. A. Obolenskii, Fiz. Nizk. Temp. **17**, 202 (1991) [Sov. J. Low Temp. Phys. **17**, 105 (1991)]; L. F. Rybalchenko, I. K. Yanson, R. Borowski, and D. Wohlleben, Physica C **224**, 38 (1994).
[7] A. Plecenik, M. Grajcar, P. Seidel, S. Takacs, A. Matthes, M. Zuzcak, and S. Benacka, Physica C **301**, 234 (1998).
[8] Z. Y. Chen, A. Biswas, I. Zutic, T. Wu, S. B. Ogale, R. L. Greene, and T. Venkatesan, Phys. Rev. B (in press).
[9] M. Yu. Kupriyanov and K. K. Likharev, Sov. Phys. Usp. **33**, 340 (1990).
[10] T. Hasegawa, H. Ikuta, and K. Kitazawa, in *Physical Properties of High Temperature Superconductors III*, edited by D. M. Ginsberg, World Scientific, Singapore (1992).
[11] V. M. Svistunov, M. A. Belogolovskii, and A. I. Khachaturov, Phys. Usp. **36**, 65 (1993).
[12] P. Bourges, in *The Gap Symmetry and Fluctuations in High Temperature Superconductors*, Plenum Press (1998).
[13] H. Hiraka, Y. Endoh, M. Fujita, Y. S. Lee, J. Kulda, A. Ivanov, and R. J. Birgeneau, cond-mat/0104087 (2001).
[14] G. I. Rochlin and P. K. Hansma, Phys. Rev. B **2**, 1460 (1970).

This article was published in English in the original Russian journal. Reproduced here with stylistic changes by AIP.

ELECTRONIC PROPERTIES OF METALS AND ALLOYS

Manifestation of Coulomb blockade effects at an arbitrary degeneracy of the levels of a molecular contact

Yu. O. Klymenko*

Institute of Space Research, National Academy of Sciences of Ukraine and National Space Agency of Ukraine, pr. Akad. Glushkova 40, 03680 GSP Kiev-187, Ukraine

(Submitted December 26, 2001; revised February 4, 2002)
Fiz. Nizk. Temp. **28**, 558–568 (June 2002)

The current-voltage (I–V) characteristics of a metal–molecule–metal structure are investigated under the condition that electron tunneling occurs only via a single molecular level of arbitrary degeneracy. A system of kinetic equations taking into account the accumulation of charge on the molecule is solved, and an exact formula for the steady-state current is obtained for the first time. In the low-temperature limit the steps on the I–V characteristic are analyzed and found to be nonequidistant with respect to current. It is shown that with increasing degeneracy of the level the initial current steps tend toward a completely equidistant spacing. In the case when the coupling parameters between the molecule and external electrodes are substantially different, the behavior of the I–V curves on parts with opposite directions of the current is found to be different: either a single current step is formed, with an amplitude proportional to the degeneracy of the level, or equidistant current steps appear in a number equal to the degeneracy of the level. It is shown that for a given polarity of the applied voltage, the matter of which of the two behaviors of the current is realized is completely conditional on whether the level via which the electron transport occurs is occupied or unoccupied by electrons. The results of the theoretical analysis of the I–V characteristics are confirmed by a numerical simulation. © *2002 American Institute of Physics.* [DOI: 10.1063/1.1491179]

1. INTRODUCTION

The Coulomb blockade and related charge effects generally take place in the tunneling of electrons through metal microgranules placed between two metallic electrodes.[1–4] According to the ''orthodox'' theory of one-electron transport, in which the electron–electron interaction effects are described in terms of the capacitance of the microgranules and the change of their electrostatic potential due to the departure or arrival of a single electron on the microgranule, the current–voltage (I–V) characteristics for such a structure should be equidistant with respect to current and voltage, the voltage period being equal to the charging energy of a microgranule, $\delta = e^2/C$ (e is the charge of the electron and C is its charging capacitance).[3,4] To avoid temperature smearing of the charge effects, the energy kT should not exceed the charging energy δ. For typical capacitances of metallic granules $C \sim 10^{-16}$ F we have $\delta \sim 10^{-3}$ eV, and therefore the condition for manifestation of the Coulomb blockade is only that the temperature be low, of the order of 1 K.

In the past decade substantial progress has been made in the miniaturization of the physical objects placed between two external electrodes, now all the way down to molecular size. In particular cases these could be quantum dots,[5,6] cluster molecules,[7] self-assembling molecular nanostructures,[8] self-assembling layers of molecules,[9,10] etc. If the capacitance of molecular contacts on such structures is estimated on the basis of the semiclassical Coulomb blockade model, one obtains values $C \sim 10^{-19}$–10^{-18} F and $\delta \sim 1$ eV,[7–9] which indicate that charging effects should be experimentally observable even at room temperature ($kT = 0.028$ eV). At the same time, the value of the charging energy δ for small molecules is of the same order of magnitude as the distance between molecular levels, thus precluding the possibility of exact solution of the problem.[10]

In this connection it is important to carry out a theoretical study of those cases for which analytical expressions can still be obtained for the I–V characteristic. The simplest of the exactly solvable problems is that of tunneling via a nondegenerate molecular level, which gives rise to a single step at a steady-state current equal to

$$I = e\frac{\Gamma^E \Gamma^C}{\Gamma^E + \Gamma^C}, \tag{1}$$

where Γ^E and Γ^C are the probabilities of electron transitions (per unit time) between the molecule and the emitter E and collector C, respectively.

The problem of electron tunneling via a nondegenerate level of the molecule with twofold spin degeneracy was considered in Ref. 11. In that paper it was shown that spin degeneracy of a level leads to the appearance of two steps on the I–V characteristic. The first current step, with an amplitude

$$I(1) = 2e\frac{\Gamma^E \Gamma^C}{2\Gamma^E + \Gamma^C}, \tag{2}$$

is characteristic for voltages at which only one-electron exchange between the molecule and metallic electrodes is possible. The second current step arises in those regions where two electrons can arrive on the molecule (or depart from it) in succession. This completely opens up the twofold degenerate level for electron transfer and leads to the following formula for the current:

$$I(2)=2e\frac{\Gamma^E\Gamma^C}{\Gamma^E+\Gamma^C}. \tag{3}$$

Formulas (2) and (3) can be interpreted in the following way.[12] In the stage of one-electron exchange the arrival of an electron from the emitter to an unfilled level of the molecule is possible for either spin (i.e., there are two possibilities), while the escape of this electron from the molecule to the collector does not have any spin degree of freedom and is uniquely determined. In comparison with formula (1) this leads to the factor of 2 multiplying Γ^E in formula (2). When the level is completely opened up there are two possible ways for an electron to arrive on the molecule and two ways of leaving it; this is taken into account in formula (3).

It is easy to see that the tunneling of electrons through a molecular level occupied in the ground state must be described by a somewhat different expression than (2), since the departure of an electron from a filled level of degeneracy 2 can occur in two possible ways, while the arrival of a new electron on the level can occur in only one way. As a result, one expects a dependence different from that given above:

$$I'(1)=2e\frac{\Gamma^E\Gamma^C}{\Gamma^E+2\Gamma^C}. \tag{4}$$

The amplitude for the second current step should not change, i.e.,

$$I'(2)=2e\frac{\Gamma^E\Gamma^C}{\Gamma^E+\Gamma^C}=I(2)\,. \tag{5}$$

The difference of the mechanisms for electron tunneling via unoccupied and occupied molecules levels will be manifested with particular clarity in cases when there is strong contact of the molecule with one of the external electrodes (substrate) and a weak coupling of the molecule with the other electron (for specificity, the tip of a scanning tunneling microscope (STM)). One can obtain a preliminary confirmation of this difference by taking limits in relations (2)–(5). For example, for $\Gamma^E \gg \Gamma^C$ we obtain $I(1)=e\Gamma^C$, $I(2)=2e\Gamma^C$ if the molecular level initially does not contain an electron, and $I'(1)=2e\Gamma^C$, $I'(2)=2e\Gamma^C$ in the case of tunneling via a completely filled molecular level. Thus, depending on the occupation of the levels in the initial state of the molecule, either two equidistant (with respect to current) steps or only one step, but of doubled amplitude, can appear.

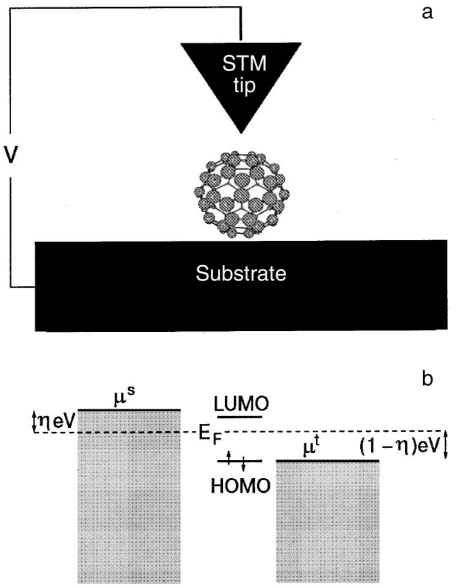

FIG. 1. Schematic view of the metal–molecule–metal structure (a) and the proposed model of the potential distribution on it (b).

The goal of the present study was to investigate the I–V relations for molecular contacts under the condition of electron tunneling via a molecular level of arbitrary degeneracy and to analyze the expressions obtained for the current in cases when this level pertains to a higher occupied molecular orbital (HOMO) or to a lower unoccupied molecular orbital (LUMO). This situation can be realized in the case when the active level of the molecule lies quite close to the Fermi energy, and the applied potential difference is insufficient to ‘‘open up’’ the remaining levels of the molecule. In turn, the degeneracy of the molecular level can come about through the electron spin or a possible high degree of symmetry of the molecule placed between the electrodes. For example, the C_{60} fullerene molecule (Fig. 1a) has 10-fold degeneracy of the HOMO level and 6-fold degeneracy of the LUMO level.

As far as we know, this exactly solvable problem has not been investigated in detail before now. In Sec. 2 we give the main formulas for calculating the current. Unlike Ref. 11, where the method of nonequilibrium Green's functions was used to obtain the I–V characteristics, here we use a direct method (which follows from Refs. 5 and 10) of solving the system of kinetic equations written in terms of the occupation of the given level. In Secs. 3 and 4, respectively, an analytical calculation of the current is carried out for the cases of electron tunneling only via an unoccupied or only via an occupied molecular level. Exact expressions for the current step in the low-temperature limit are obtained for the first time, and their dependence on the degeneracy *K* of the level is traced. It is shown that the I–V steps that appear are periodic with respect to voltage but not with respect to current, but for a high degree of degeneracy of the level the initial current steps are nearly equidistant. On the assumption of strong coupling of the molecule with the substrate and weak coupling with the STM tip, it is predicted that the behavior of the I–V characteristic will be qualitatively different on the parts with opposite directions of the current. For example, at one polarity of the applied potential difference one should observe steps which are equidistant with respect to current and voltage (the number of which should coincide with the degeneracy *K* of the level), while for the opposite potential difference one should observe only one step, with an amplitude proportional to *K*. Moreover, for the same polarity of the applied voltage the behavior of the I–V characteristic depends substantially on which of the molecular levels, LUMO or HOMO, is involved in the electron transport, i.e., one will again observe either a stepwise current growth or a single current step. Since the polarity of the applied voltage is uniquely determined by the conditions of the experiment, analysis of the I–V characteristic in the case of an asymmetric arrangement of the molecule between electrodes will permit an unambiguous determination of which of the levels of the molecule, HOMO or LUMO, is involved in the electron tunneling in the framework of the one-level approximation adopted here. A discussion of the results is presented in Sec. 5, and the findings of this study are summarized briefly in the Conclusion (Sec. 6).

2. SYSTEM OF KINETIC EQUATIONS AND THE FORMULA FOR THE STEADY-STATE CURRENT

To determine the current through a microobject placed between two electrodes it is necessary to know the solution of the system of kinetic equations regulating the electron balance between the microobject and the external electrodes.[5,10] When the value of the charging energy δ becomes comparable to the characteristic distance between energy levels, these equations cannot be solved exactly even for a small number of levels (>2). In this connection it is of interest and importance to find cases with an exact solution of the problem. For example, imposing the condition that the applied potential difference be small compared to kT allows one to find an analytical formula for the current.[5]

We show below that the system of balance equations can be solved exactly if one assumes that the energies of all the levels are identical and that the values of the electron transitions are constant. Then the the analytical solution of the problem becomes possible, owing primarily to the existence of simple recurrence relations between the probabilities of the different level occupations, making it possible to determine the latter without having to solve the initial system of kinetic equations.

Since the assumption that the level via which the electron transport occurs is degenerate greatly simplifies the initial formulas in comparison with those given in Refs. 5 and 10, it will be preferable in the exposition to derive the equations we need without going into the details of the more general theory.

Let us assume that in the ground state of the molecule the electrostatic energy of the electrons in it is equal to zero and that the molecular level via which the electron transport occurs has a degeneracy K. Since, on account of the interaction with the external electrodes the number of electrons on a level can change, we define the instantaneous number of electrons on the level as N $(N=0,\ldots,K)$. Then the expression for the electrostatic energy U as a function of the instantaneous number of electrons N becomes

$$U(N)=\frac{1}{2}N^2\delta, \tag{6}$$

if the given level is unoccupied by electrons, or

$$U(N)=\frac{1}{2}(N-K)^2\delta, \tag{7}$$

if this level is filled in the initial state of the molecule.[10]

Neglecting the potential drop across the molecule, we shall assume that the chemical potential μ^s of the substrate is raised by ηeV in relation to the potential of the molecule, while the chemical potential μ^t of the microscope tip is lowered by an amount $(1-\eta)eV$, as is shown in Fig. 1b, i.e.,

$$\mu^s=E_F+\eta eV, \quad \mu^t=E_F-(1-\eta)eV, \tag{8}$$

where E_F is the energy of the Fermi level, and η is a parameter characterizing the voltage drop across the structure, which can be estimated from the formula $\eta=d^s/(d^s+d^t)$ if the length d_s of the substrate–molecule tunnel barrier and the length d^t of the molecule–STM tip tunnel barrier are known. According to Eq. (8), a positive potential difference $(eV>0)$ leads to the flow of electrons from the substrate (the emitter) toward the microscope tip (the collector). For the opposite potential difference the SMT tip plays the role of electron emitter and the substrate that of the collector.

We introduce the notation

$$\begin{aligned}
&W_{-(+)}(N)=W^S_{-(+)}(N)+W^t_{-(+)}(N),\\
&W^s_-(N)=\Gamma^s[1-f(E_N-\mu^S)],\\
&W^s_+(N)=\Gamma^s f(E_N-\mu^S),\\
&W^t_-(N)=\Gamma^t[1-f(E_N-\mu^t)],\\
&W^t_+(N)=\Gamma^t f(E_N-\mu^t),
\end{aligned} \tag{9}$$

in which $W_-(N)$ has the meaning of the total probability for an electron to depart from a molecule with N electrons on a level, and $W_+(N)$ gives the total probability of arrival of an electron on a level containing $N-1$ electrons. The values of $W^{s(t)}_-$ and $W^{s(t)}_+$, respectively, specify the particular electrode—the substrate or the SMT tip—to which or from which, respectively, the electron transfer occurs. The parameters $\Gamma^{s(t)}$ are defined as the probability of electron transitions (per unit time) between the molecule and the corresponding electrode, $f(x)$ is the Fermi–Dirac distribution function, and

$$E_N=E+U(N)-U(N-1). \tag{10}$$

Here E is the energy of the level, and the difference $U(N)-U(N-1)$ has the meaning of the change in electrostatic energy of the molecule as a result of the tunneling of a single electron.

Assuming that the tunnel barrier between the substrate and molecule (or between the molecule and the STM tip) has a height $\Phi^{s(t)}$ (measured in electron-volts) and a length $d^{s(t)}$ (in angstroms), we can use the WKB approximation for $\Gamma^{s(t)}$ (see Ref. 10 and the discussion in Ref. 13):

$$\begin{aligned}
&\Gamma^s\sim\exp(-1.025d^s\sqrt{\Phi^s-E_F+E}),\\
&\Gamma^t\sim\exp(-1.025d^t\sqrt{\Phi^t-E_F+E}).
\end{aligned} \tag{11}$$

We now write the complete set of kinetic equations for the probabilities P_N of realization of some state with N electrons on the level $(N-0,\ldots,K)$:

$$\begin{aligned}
\frac{d}{dt}P_N=&-P_N[NW_-(N)+(K-N)W_+(N+1)]\\
&+P_{N-1}NW_+(N)+P_{N+1}(K-N)W_-(N+1).
\end{aligned} \tag{12}$$

The structure of these equations is quite clear. A molecule can go from a state with N electrons [a process governed by the negative terms in (12)] only to a state with $N-1$ electrons, through the loss of any of the N electrons, or to a state with $N+1$ electrons, through the acquisition of an additional electron at any of the $K-N$ places available. The positive terms in (12) have an analogous interpretation: they take into account all the ways that the molecule can arrive at a state with N electrons.

To find the current through the molecule we need only take into account, with the corresponding sign, all of the elementary electron-motion events pertaining to some boundary of the molecule, e.g., the molecule–substrate junction. As a result we obtain

$$\begin{aligned} I &= -e\sum_{N=0}^{K} P_N C_K^N [N W_-^s(N) - (K-N) W_+^s(N+1)] \\ &= -e\sum_{N=1}^{K} N C_K^N [P_N W_-^s(N) - P_{N-1} W_+^s(N)], \end{aligned} \tag{13}$$

where we have taken into account that the number of all realizations of a state with N electrons on a K-fold degenerate level is C_K^N (i.e., the number of permutations of K things taken N at a time). The second equation in (13) is obtained with the use of the identity $(K-N)C_K^N = (N+1)C_K^{N+1}$. It is also understood in Eq. (13) that the probability P_N is normalized to unity, i.e.,

$$\sum_{N=0}^{K} C_K^N P_N = 1. \tag{14}$$

To find the steady-state current we need the time-independent solutions of the system of difference equations (12). They are easily found if it is recognized that the solutions of the linear recurrence relations

$$W_+(N) P_{N-1} = W_-(N) P_N, \quad N = 1,\dots,K \tag{15}$$

(see below) satisfy (12) automatically. The dimensionality of the system of equations (12) is one greater than the dimensionality of (15), but the first system is linearly dependent by virtue of the normalization condition (14). Therefore, there exist no steady-state solutions of the linear system (12) which do not satisfy (15). The use of Eq. (15) permits one, first, to simplify the formula for the current (13) significantly:

$$I = e\Gamma^s\Gamma^t \sum_{N=1}^{K} N C_K^N P_N \frac{f(E_N-\mu^s - f(E_N-\mu^t)}{\Gamma^s f(E_N-\mu^s) + \Gamma^t f(E_N-\mu^t)} \tag{16}$$

and, second, to obtain the following expression for all the probabilities of occupation of the level:

$$P_N = Z^{-1} \prod_{p=1}^{N} \frac{W_+(p)}{W_-(p)}, \quad Z = \sum_{N=0}^{K} C_K^N \prod_{p=1}^{N} \frac{W_+(p)}{W_-(p)},$$
$$N = 1,\dots,K. \tag{17}$$

In writing Eq. (16) we have made use of definition (9), and the normalization condition (14) was taken into account in deriving (17).

Finally, the substitution of (17) into (16) leads to an analytical expression for the current, obtained here for the first time. Everywhere below the analysis of the $I(V)$ curve in the low-temperature limit of interest to us is done with the use of the recurrence relations (17) in each of the intervals of constancy of the functions $W_{-(+)}(N)$ from (9), with a subsequent substitution of the normalized solutions into formula (16).

Before turning to the analysis of the I–V characteristics, we note that formulas (12) and (13) can be directly recovered from Refs. 5 and 10 under the condition that all the levels are identical. Formula (16) for the current was obtained on the basis of the recurrence relations (15), and relations of this kind do not have analogs in the case of an arbitrary distribution of levels. It is the existence of the recurrence relations (15) that makes it possible to obtain an analytical solution of the problem addressed in this paper.

3. ELECTRON TRANSPORT VIA THE LOWER UNOCCUPIED LEVEL OF THE MOLECULE

Using (6) together with (8)–(10) in formulas (15) and (16) gives

$$\begin{aligned} & P_{N-1}\{\Gamma^S f(\Delta_L + (N-1/2)\delta - \eta eV) \\ &\quad + \Gamma^t f(\Delta_L + (N-1/2)\delta + (1-\eta)eV)\} \\ &= P_N\{\Gamma^S[1 - f(\Delta_L + (N-1/2)\delta - \eta eV)] \\ &\quad + \Gamma^t[1 - f(\Delta_L + (N-1/2)\delta + (1-\eta)eV)]\}, \\ & N = 1,\dots,K \end{aligned} \tag{18}$$

and

$$I_{\text{LUMO}} = e\Gamma^S\Gamma^t \sum_{N=1}^{K} N C_K^N P_N$$
$$\times \frac{f(\Delta_L + (N-1/2)\delta - \eta eV) - f(\Delta_L(N-1/2)\delta + (1-\eta)eV)}{\Gamma^S f(\Delta_L + (N-1/2)\delta - \eta eV) + \Gamma^t f(\Delta_L + (N-1/2)\delta + (1-\eta)eV)}. \tag{19}$$

Here $\Delta_L = E - E_F > 0$ is the energy distance between the unoccupied level (LUMO) and the Fermi energy. In the low-temperature limit these formulas can be simplified by assuming everywhere below that

$$f(x) = \begin{cases} 0, & x > 0, \\ 1, & x < 0. \end{cases} \tag{20}$$

In the flow of electrons from the substrate to the STM tip $(eV > 0)$ we obtain from (18) and (19)

$$\begin{aligned} & P_{N-1}\Gamma^S f(\Delta_L + (N-1/2)\delta - \eta eV) \\ &= P_N\{\Gamma^S[1 - f(\Delta_L + (N-1/2)\delta - \eta eV)] + \Gamma^t\}, \end{aligned} \tag{21}$$

$$I_{\text{LUMO}}^{>} = e\Gamma^t \sum_{N=1}^{K} N C_K^N P_N. \tag{22}$$

In the initial part $0 < \eta eV < \Delta_L + \delta/2$ relations (21) give the trivial solutions $P_N = \delta_{N,0}$, which upon substitution into (22) lead to zero current. In the next region $\Delta_L + \delta/2 < \eta eV < \Delta_L + 3\delta/2$ the normalized occupation probabilities of the level are given by

$$P_0=\frac{\Gamma^t}{\Gamma^t+K\Gamma^S},\quad P_1=\frac{\Gamma^S}{\Gamma^t+K\Gamma^S},\quad P_N=0,\quad N\geqslant 2. \tag{23}$$

Substituting these probabilities into (22) give an expression for the amplitude of the first current step:

$$I^{>}_{\mathrm{LUMO}}(1)=e\frac{K\Gamma^t\Gamma^S}{\Gamma^t+K\Gamma^S}. \tag{24}$$

Formula (24) agrees with (2) in the case of twofold degeneracy of the level ($K=2$) and generalizes it to the case of arbitrary degeneracy of the unoccupied level. We recall that for the given direction of the electron flow the relations $\Gamma^s=\Gamma^E$ and $\Gamma^t=\Gamma^C$ hold.

In the next interval $\Delta_L+3\delta/2<\eta eV<\Delta_L+5\delta/2$ we have the normalized solutions

$$P_0=\mathcal{D}^{-1},\quad P_1=\gamma^{-1}\mathcal{D}^{-1},\quad P_2=\gamma^{-2}\mathcal{D}^{-1},$$

$$P_N=0,\quad N\geqslant 2. \tag{25}$$

$$\mathcal{D}=1+K\gamma^{-1}+\frac{K(K-1)}{2}\gamma^{-2},\quad \gamma=\Gamma^t/\Gamma^S,$$

which give the following result for the amplitude of the second current step:

$$I^{>}_{\mathrm{LUMO}}(2)=e\Gamma^t\frac{K\gamma^{-1}+K(K-1)\gamma^{-2}}{1+K\gamma^{-1}+[K(K-1)/2]\gamma^{-2}}, \tag{26}$$

which agrees with (3) for $K=2$.

From the induction in the interval $\Delta_L+(2M-1)\delta/2<\eta eV<\Delta_L+(2M+1)\delta/2$ one can obtain expressions for all the nonzero occupation probabilities of the LUMO level:

$$P_N=\frac{\gamma^{-N}}{\Sigma_{p=0}^{M}C_K^p\gamma^{-p}},\quad N=0,\dots,M, \tag{27}$$

which determine the Mth current step

$$I^{>}_{\mathrm{LUMO}}(M)=e\Gamma^t\frac{\Sigma_{N=1}^{M}NC_K^N\gamma^{-N}}{\Sigma_{N=0}^{M}C_K^N\gamma^{-N}}. \tag{28}$$

From the last expression it is easy to see that under the condition $\gamma\ll 1$ (i.e., $\Gamma^s\gg\Gamma^t$) the amplitudes of the steps of the I–V characteristic are determined by the terms with the maximum value of N. Therefore $I^{>}_{\mathrm{LUMO}}(M)=eM\Gamma^t$, i.e., in this limiting case and for $eV>0$ we have equidistant steps with respect to both the voltage and the current.

In the case of negative potential differences eV, when the STM tip is the electron emitter and the substrate is the collector, formulas (18) and (19), with the use of (20), reduce to the form

$$\begin{aligned}P_{N-1}&\Gamma^t f(\Delta_L+(N-1/2)\delta-(1-\eta)|eV|)\\&=P_N\{\Gamma^S+\Gamma^t[1-f(\Delta_L+(N-1/2)\delta-(1-\eta)|eV|)]\},\end{aligned} \tag{29}$$

$$I^{<}_{\mathrm{LUMO}}=-e\Gamma^s\sum_{N=1}^{K}NC_K^NP_N. \tag{30}$$

In view of the formal similarity of Eqs. (29) and (30) with (21) and (22), it is not hard to find expressions for the amplitudes of the current steps. As a result, for the interval $\Delta_L+(2M-1)\delta/2<(1-\eta)|eV|<\Delta_L+(2M+1)\delta/2$ we obtain the nonzero occupation probabilities for the level:

$$P_N=\frac{\gamma^N}{\Sigma_{p=0}^{M}C_K^p\gamma^p},\quad N=0,\dots,M, \tag{31}$$

which lead to the expression

$$I^{<}_{\mathrm{LUMO}}(M)=e\Gamma^t\frac{\Sigma_{N=1}^{M}NC_K^N\gamma^N}{\Sigma_{N=0}^{M}C_K^N\gamma^N}. \tag{32}$$

In the case $\gamma\ll 1$ the main contribution to the current (32) is given by the terms with the minimum value of N, and therefore $I^{<}_{\mathrm{LUMO}}(M)\approx -eK\Gamma^s\gamma=-eK\Gamma^t$ in any interval of variation of the potential difference exceeding $|eV|=(1-\eta)^{-1}(\Delta_L+\delta/2)$. In other words, the I–V characteristic at the given polarity of the voltage will have only a single current step, the amplitude of which is proportional to the degeneracy K of the level.

Thus in the case of a significant difference of the tunneling rates of the junctions, Γ^s and Γ^t, the I–V characteristics of a metal–molecule–metal structure display a pronounced asymmetry of the current. For $\Gamma^s\gg\Gamma^t$ and positive eV one should observe K equidistant current steps, while for negative eV only one step should be observed.

4. ELECTRON TRANSPORT VIA A HIGHER OCCUPIED LEVEL OF THE MOLECULE

For tunneling via a higher occupied molecular level (HOMO) the use of Eq. (7) together with (8)–(10) and (20) leads to the expressions below, which follow from (15) and (16):

$$\begin{aligned}P_{N-1}\{&\Gamma^s f(-\Delta_H+(N-K-1/2)\delta-\eta eV)\\&+\Gamma^t f(-\Delta_H+(N-K-1/2)\delta+(1-\eta)eV)\}\\=P_N\{&\Gamma^s[1-f(-\Delta_H=(N-K-1/2)\delta-\eta eV)]\\&+\Gamma^t[1-f(-\Delta_H+(N-K-1/2)\delta+(1-\eta)eV)]\},\end{aligned} \tag{33}$$

$$I_{\mathrm{HOMO}}=e\Gamma^s\Gamma^t\sum_{N=1}^{K}NC_K^NP_N\frac{f(-\Delta_H+(N-K-1/2)\delta-\eta eV)]-f(-\Delta_H+(N-K-1/2)\delta+(1-\eta)eV)}{\Gamma^s f(-\Delta_H+(N-K-1/2)\delta-\eta eV)]+\Gamma^t f(-\Delta_H+(N-K-1/2)\delta+(1-\eta)eV)}. \tag{34}$$

Here $\Delta_H = E_F - E > 0$ is the energy distance between the Fermi energy and the occupied molecular level.

Again restricting consideration to the low-temperature limit, we obtain for $eV > 0$

$$P_{N-1}\{\Gamma^s + \Gamma^t f(-\Delta_H + (N-K-1/2)\delta + (1-\eta)eV)\}$$
$$= P_N \Gamma^t [1 - f(-\Delta_H + (N-K-1/2)\delta + (1-\eta)eV)], \quad N = 1,\dots,K \tag{35}$$

$$I^{>}_{\mathrm{HOMO}} = e \sum_{N=1}^{K} \Gamma^s \Gamma^t N C_K^N P_N \times \frac{1 - f(-\Delta_H + (N-K-1/2)\delta + (1-\eta)eV)}{\Gamma^s + \Gamma^t f(-\Delta_H + (N-K-1/2)\delta + (1-\eta)eV)}. \tag{36}$$

In the interval $(1-\eta)eV < \Delta_H + \delta/2$ equations (35) give a single nonzero solution $P_K = 1$. According to (20) and (36), this leads to zero current. For $\Delta_H + \delta/2 < (1-\eta)eV < \Delta_H + 3\delta/2$ we have the nonzero solutions of equation (35):

$$P_K = \frac{\Gamma^s}{K\Gamma^t + \Gamma^s}, \quad P_{K-1} = \frac{\Gamma^t}{K\Gamma^t + \Gamma^s}, \tag{37}$$

leading to the following formula for the amplitude of the first current step:

$$I^{>}_{\mathrm{HOMO}}(1) = e\frac{K\Gamma^t\Gamma^s}{KT^t + \Gamma^s}, \tag{38}$$

which agrees with (4) for $K = 2$. In the interval $\Delta_H + 3\delta/2 < (1-\eta)eV < \Delta_H + 5\delta/2$ we obtain for the formation of the second step

$$I^{>}_{\mathrm{HOMO}}(2) = e\Gamma^t \frac{K + K(K-1)\gamma}{1 + K\gamma + [K(K-1)/2]\gamma^2}, \quad \gamma = \Gamma^t/\Gamma^s, \tag{39}$$

which reduces to (5) for the case of twofold degeneracy of the HOMO level.

In the general case for $\Delta_H + (2M-1)\delta/2 < (1-\eta)eV < \Delta_H + (2M+1)\delta/2$ the following formula can be obtained by induction:

$$I^{>}_{\mathrm{HOMO}}(M) = e\Gamma^t \frac{\Sigma_{N=1}^{M} N C_K^N \gamma^{N-1}}{\Sigma_{N=0}^{M} C_K^N \gamma^N} = e\Gamma^S \frac{\Sigma_{N=1}^{M} N C_K^N \gamma^{N}}{\Sigma_{N=0}^{M} C_K^N \gamma^N}. \tag{40}$$

In the case $eV < 0$ the results of the analysis lead to the expression

$$I^{<}_{\mathrm{HOMO}}(M) = -e\Gamma^s \frac{\Sigma_{N=1}^{M} N C_K^N \gamma^{N-1}}{\Sigma_{N=0}^{M} C_K^N \gamma^N} = -e\Gamma^t \frac{\Sigma_{N=1}^{M} N C_K^N \gamma^{-N}}{\Sigma_{N=0}^{M} C_K^N \gamma^{-N}}, \tag{41}$$

which is valid in the interval $\Delta_H + (2M-1)\delta/2 < \eta|eV| < \Delta_H + (2M+1)\delta/2$. In the case $\Gamma^s \gg \Gamma^t$ we see from (40) and (41) that the behavior of the I–V characteristic is substantially different from the analogous curve for tunneling via an unoccupied level. In the case $\Gamma^s \gg \Gamma^t$ for $eV > 0$ one observes a single step, which is proportional to K and arises for $eV = (1-\eta)^{-1}(\Delta_H + \delta/2)$. On the opposite branch of the I–V characteristic there will be K steps which are equidistant with respect to both current and voltage.

5. DISCUSSION OF THE RESULTS AND A NUMERICAL SIMULATION

A comparison of formula (41) with (28) and (40) with (32) shows that the electron transport via molecular levels of different types leads to the same features for the current, but these features are observed on opposite branches of the I–V characteristic. This is unsurprising from the standpoint of solid-state theory, since the electron transport via a level occupied by electrons is similar to the tunneling of holes via a level unoccupied by holes. We shall therefore assume below (unless otherwise stated) that the active level is the lower unoccupied (LUMO) level of the molecule.

As was shown above, the first current step, arising at $eV = \eta^{-1}(\Delta_L + \delta/2)$ if $eV > 0$ or at $|eV| = (1-\eta)^{-1}(\Delta_L + \delta/2)$ if $eV < 0$, is shifted relative to the threshold for the opening up of the level itself, given as $eV = \eta^{-1}\Delta_L$ and $|eV| = (1-\eta)^{-1}\Delta_L$, respectively (see Fig. 1b). An analogous delay of the threshold of the first current step (i.e., the appearance of a region of zero current on the initial part of the I–V characteristic) also takes place in the tunneling of electrons through metal microclusters, which are known to have a quasicontinuous spectrum ($\Delta_L = \Delta_H = 0$). However, the existence of a finite energy gap in the molecule causes the boundaries of the current blockade region to depend, in addition, on the energy distance between the Fermi level and the active level of the molecule. In particular, in the tunneling via an unoccupied level of a molecule there is no current if

$$V \epsilon [-(1-\eta)^{-1}(\Delta_L + \delta/2), \eta^{-1}(\Delta_L + \delta/2)].$$

The tunneling of electrons via a degenerate level leads to an I–V characteristic that is equidistant only with respect to voltage and not with respect to current (see Eqs. (28) and (29)). This distinguishes it from the analogous curve for the case of tunneling through metal microgranules, where equidistance of both types is observed. However, since the quasicontinuous spectrum of microgranules on the initial part of the I–V characteristic is in a certain sense similar to a single level with a large degeneracy, it is useful to find the asymptotic behavior of (28) and (32) for $K \gg 1$ and for initial current steps ($M \ll K$). We see that the main contribution to the asymptotics of these steps is given by terms with the maximum value of N in the numerator and denominator of the aforementioned formulas, and therefore

$$I^{>}_{\mathrm{LUMO}}(M) = -I^{<}_{\mathrm{LUMO}}(M) \approx eM\Gamma^t, \tag{42}$$

i.e., for a high degeneracy of the level the first steps on the I–V characteristic are actually equidistant with respect to current. An illustration of this observation is presented in Fig. 2, which shows the I–V characteristic for different level degeneracies, $K = 2$, 4, and 8.

Let us discuss the case $\Gamma^s \gg \Gamma^t$ in more detail. As was shown above, the significant difference of the tunneling constants leads to substantially different behavior of the I–V

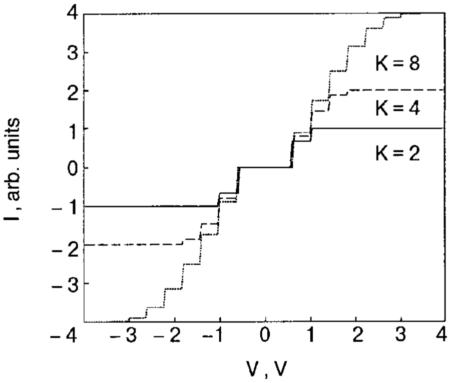

FIG. 2. Current–voltage characteristics of a molecular contact for different degeneracies of the lower unoccupied (LUMO) level of the molecule: $K=2$ (solid curve), $K=4$ (dashed curve), and $K=8$ (dotted curve). The following values of the parameters of the calculation were chosen: $\gamma=1$, $\eta=0.5$, $\delta=0.2$ eV, $E_{\mathrm{LUMO}}-E_F=0.2$ eV. It is seen that the first current steps become increasingly equidistant with increasing degeneracy of the level.

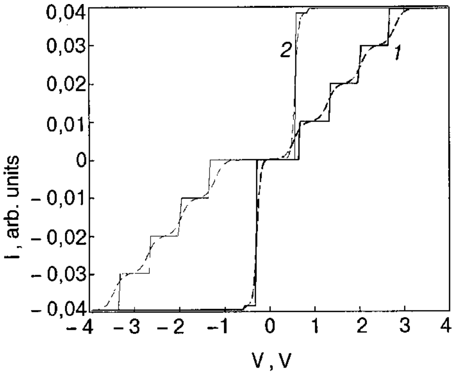

FIG. 3. The current–voltage characteristics of a metal–molecule–metal structure for $\Gamma^t=0.01\Gamma^2$. Curves *1* correspond to the transport of electrons via a higher occupied (HOMO) level of the molecule; curves *2* to transport via a lower unoccupied (LUMO) level. The solid and dashed curves correspond to the cases of zero temperature and room temperature, respectively. The parameters of the simulation are given in the text.

characteristic on parts with opposite directions of the current. The origin of this current asymmetry can be explained as follows.

In the one-level passage of electrons through a molecule the steps on the I–V characteristic can arise only in connection with a change of the total number of electrons on the molecule. For the case $\gamma\ll 1$ formula (27) indeed shows that in the flow of electrons from the substrate via an unoccupied molecular level to the STM tip, the total number of electrons on the molecule varies, and in the interval of formation of the Mth current step the LUMO level of the molecule will in fact be occupied by M electrons.

In the reverse direction of the electron flow $(eV<0)$, i.e., from the STM tip via an unoccupied level of the molecule to the substrate, the total number of electrons in the molecule is practically independent of the applied potential difference and is found from the condition of zero occupancy of the LUMO level (see Eq. (31) in the limit $\gamma\ll 1$). This can be explained as follows. If the coupling of the molecule with the substrate is assumed to be strong and the coupling with the STM tip weak, then the occupation of the level by electrons is completely determined by the position of the chemical potential of the substrate relative to the energy level and is practically independent of the value of the chemical potential at the other electrode. Since the application of a negative potential difference to the structure (see Fig. 1b) decreases the chemical potential of the substrate relative to E_F, this cannot change the occupation of an initially unoccupied molecular level lying above E_F.

An analogous situation with a constant total number of electrons on the molecule is also observed in the tunneling via an electron-filled HOMO level of the molecule if $eV>0$. Because of the strong coupling of the molecule with the substrate the growth of the chemical potential of the substrate cannot change the occupation of the completely filled level lying below E_F. In the case $eV<0$ the decrease of the chemical potential of the substrate leads to a downward jump in the occupation of the level from K to 0 as a result of the leaking of charge from the molecule to the substrate; this is the cause of the steps on the corresponding branch of the I–V characteristic.

As an illustration, in Fig. 3 we present the results of a numerical simulation of the current in the tunneling of electrons via unoccupied and occupied molecular levels of degeneracy 4 for the following values of the parameters: $\Gamma^t=0.01\Gamma^s$, $\eta=0.3$, $\delta=0.2$ eV, and $E_F-E_{\mathrm{HOMO}}=0.3$ eV (curve *1*) or $E_{\mathrm{LUMO}}-E_F=0.1$ eV (curve *2*). The given curves are obtained on the basis of a direct modeling of formulas (16) and (17) for zero temperature and room temperature and exhibit the current asymmetry predicted above.

In the modeling of the I–V characteristic it was assumed that the tunneling constants Γ^s and Γ^t do not depend on the applied potential difference. By virtue of (11) this assumption is valid only if the heights of the tunnel barriers Φ^s and Φ^t are independent of V and can be justified only for not very high voltages applied to the structure. A more detailed discussion of this question is given in Ref. 10.

6. CONCLUSION

In this paper we have presented an analytical calculation of the current in metal–molecule–metal structures under the condition of electron tunneling via only one molecular level with arbitrary degeneracy. The amplitudes of the steps of the I–V characteristics are calculated for the first time in relation to the degeneracy of the level and its occupation by electrons in the ground state of the molecule. It is shown that the steps on the I–V characteristic are equidistant with respect to voltage but not with respect to current, and that an equidistant spacing of the first current steps can be observed only in the case of a large degeneracy of the level. For an asymmetric position of the molecule between electrodes (the typical situation in STM measurements of molecules and one which is often realized under conditions of a mechanically controlled contact with the molecule inside it) it is predicted that the behavior of the I–V characteristic will be substantially different on parts with opposite directions of the current. That is, depending on the sign of the applied potential difference, either a single current step of large amplitude or several small steps, equidistant with respect to both current and voltage, can appear. It follows from the results of this study that the answer as to which of the two types of features will appear on the I–V characteristic depends not only on the current density (which is uniquely determined by the conditions of the experiment) but also on the type of molecular level (occupied or unoccupied) that is involved in the electron transport. This suggests the possibility of experimental determination of the type of level via which the electron tunneling occurs under conditions of the proposed one-level transport.

The author thanks A. I. Onipko and L. I. Malysheva for a helpful discussion of the results.

This study was supported by INTAS Grant No. 99-864.

*phys@space.is.kiev.ua

---

[1] R. I. Shekhter, Zh. Éksp. Teor. Fiz. **63**, 1410 (1972) [Sov. Phys. JETP **36**, 747 (1973)].

[2] I. O. Kulik and R. I. Shekhter, Zh. Éksp. Teor. Fiz. **68**, 623 (1975) [Sov. Phys. JETP **41**, 308 (1975)].

[3] D. V. Averin and K. K. Likharev, in *Mesoscopic Phenomena in Solids*, edited by B. L. Altshuler, P. A. Lee, and R. A. Webb, Elseier, Amsterdam (1991), p. 173.

[4] D. V. Averin and K. K. Likharev, J. Low Temp. Phys. **62**, 345 (1986).

[5] C. W. Beenakker, Phys. Rev. B **44**, 1646 (1991).

[6] D. V. Averin, A. N. Korotkov, and K. K. Likharev, Phys. Rev. B **44**, 6199 (1991).

[7] E. S. Soldatov, V. V. Khanin, A. S. Trifonov, S. P. Gubin, V. V. Kolesov, D. E. Presnov, S. A. Yakovenko, and G. B. Khomutov, JETP Lett. **64**, 556 (1996).

[8] R. P. Andres, T. Bein, M. Dorogi, S. Feng, J. I. Henderson, C. P. Kubiak, W. Mahoney, R. G. Osifchin, and R. Reifenberger, Science **272**, 1323 (1996).

[9] M. A. Reed, C. Zhon, C. J. Muller, T. P. Burgin, and J. M. Tour, Science **278**, 252 (1997).

[10] C. Kergueris, J.-P. Bourgoin, S. Palacin, D. Esteve, C. Urbina, M. Magoga, and C. Joachim, Phys. Rev. B **59**, 12505 (1999).

[11] L. Y. Chen and C. S. Ting, Phys. Rev. B **44**, 5916 (1991).

[12] T. Schmidt, R. J. Haug, R. von Klitzing, A. Förster, and H. Lüth, Phys. Rev. B **55**, 2230 (1997).

[13] A. I. Onipko, R.-F. Bergren, Yu. O. Klymenko, L. I. Malysheva, I. J. W. M. Rosink, L. J. Geerligs, E. van der Drift, and S. Radelaar, Phys. Rev. B **61**, 11118 (2000).

Translated by Steve Torstveit

LOW TEMPERATURE PHYSICS VOLUME 28, NUMBER 6 JUNE 2002

Features of the thermopower of Mo–Re and Mo–Re–Nb alloys and the electronic–topological transition in these systems

T. A. Ignatyeva and A. N. Velikodny

*Kharkov Physicotechnical Institute National Research Center, ul. Akademicheskaya 1, 61108 Kharkov, Ukraine**

(Submitted February 7, 2002; revised March 13, 2002)
Fiz. Nizk. Temp. **28**, 569–579 (June 2002)

The anomalous behavior of the thermopower of $Mo_{1-x}Re_x$ and $Mo_{1-x-y}Re_xNb_y$ alloys is investigated over a wide range of temperatures and concentrations (within the limits of the solid solution). An extremum on the concentration dependence of the thermopower at 10 K, observed for both of these systems at the same electron concentration ≈ 6.1 electrons/atom, attests to the presence of a critical energy E_c in the electronic spectrum of Mo at which an electronic–topological transition occurs in Mo under the influence of impurities. According to the theoretical ideas about the electronic spectrum of Mo, the closest $E_c > E_F^0$ corresponds to the bottom of the band, upon the crossing of which a new electron sheet of the Fermi surface appears. In the binary systems the Re impurity causes a new sheet of the Fermi surface to appear, and in the ternary systems it disappears as the Nb impurity is added. A quantitative comparison of the theory with experiment makes it possible to determine the gap $E_c - E_f^0$ for Mo, which is found to be ≈ 0.02 eV. These results correspond to those obtained previously from the superconducting characteristics. © *2002 American Institute of Physics.* [DOI: 10.1063/1.1491180]

1. INTRODUCTION

Transition metals and alloys have a complex electronic structure and are interesting objects for studying Lifshits transitions of order 2.5.[1] In the literature these transitions have since come to be called electronic–topological transitions (ETTs). Electronic–topological transitions were predicted theoretically[1] for pure metals in the normal state and were analyzed for the case of small elastic stresses. The experimental study of ETTs has been limited to this theoretical framework. The feature arising in the electron density of states at the ETT in this case, $\delta\nu \approx \pm (E_c - E_F)^{1/2}$, appears against the background of the smooth variation of $\nu_0(E)$ for the pure metal and is hard to identify. Here E_F is the Fermi energy, and E_c is the critical energy at which the ETT occurs. After the discovery of these transitions in superconductors[2] the situation changed. For superconductors it has been established experimentally[2] and theoretically[3] that the feature $\delta\nu(E)$ arising at the ETT is related to the features in the superconducting characteristics. It was shown that the derivative $\partial T_c(P,C)/\partial P$ has an extremum related to $\partial\delta\nu(E)/\partial E$ and is an unambiguous criterion of the ETT in superconducting metals and alloys; here T_c is the superconducting transition temperature, P is the pressure, and C is the impurity concentration. Not only was the establishment of a connection between the aforementioned feature and the extremum of the derivative a new finding, but it was also important that a new external parameter by which one could make the Fermi energy approach the singular point of the electronic spectrum had been brought into consideration. For the particular case of superconductors it was first shown experimentally[4,5] and theoretically[3,6] that the changes of the fine structure of the electronic spectrum of a metal as the Fermi level moves can be observed not only under pressure but also under the influence of an impurity. By simultaneously varying the two parameters—the pressure and the concentration of impurities of different valence, which shift the Fermi energy up or down relative to the value E_F^0 for the pure metal—one can always bring about conditions such that $E_F = E_c$ and observe the changes of the topology of the Fermi surface: the appearance or disappearance of a group of carriers (electrons, holes), and the formation or breaking of necks. From the position of the extremum on the electron-concentration or pressure scale one can determine the critical concentration or pressure at which the ETT occurs.

In the 1980s it was pointed out in a number of theoretical papers[7,8] that by studying the concentration dependence of the thermopower $\alpha(C)$ at a fixed temperature, one can observe directly the feature due to the derivative of the electron density of states with respect to energy, $\approx \pm (E_c - E_F)^{-1/2}$, since $\alpha(C) \approx \partial\nu(E)/\partial E$ and has an extremum under the condition $E_F = E_c$. The sign of the extremum depends on the type of carrier (electron or hole sheet).[9,10] Thus it has become clear that the concentration dependence of the thermopower $\alpha(C)$ in a study of the ETT in the normal state of a metal is an analog of the dependence of $\partial T_c(P,C)/\partial P$ in a study of the ETT in the superconducting state and is a test for determining singular points in the electronic spectrum. A general expression for the thermopower can be written in the form

$$\alpha = AT + BT^3, \tag{1}$$

where the first term (the diffusive part of the thermopower) depends on the electron density of states and reflects the features due to the ETT; the second term is due to phonon drag effects.[11]

In this paper we investigate the thermopower of Mo–Re and Mo–Re–Nb superconducting alloys, for which an electronic–topological transition has been observed previously in studies of the behavior of $T_c(C)$, $\partial T_c(P,C)/\partial P$ (Refs. 12 and 13), and $\alpha(C)$ (Ref. 14), and obtain the quantitative parameters of this transition.[13] This makes it possible to compare the manifestation of the ETT in the properties of normal metals and superconductors. We note that a large number of experimental papers have been published on the study of the normal characteristics of Mo and its alloys in relation to the features of the electronic spectrum: the electronic heat capacity,[15] the Hall effect,[16] etc. However, these data are not suitable for comparison with the concrete changes in the fine structure of the electronic spectrum and especially with the concrete changes in the Fermi surface. The present studies of the thermopower of Mo–Re and Mo–Re–Nb alloys make it possible to make an unambiguous determination as to the presence of critical points in the electronic spectrum of Mo and to compare with the changes of the Fermi surface. The temperature dependence of the thermopower anomalies of alloys is investigated over a wide range of temperatures; from those measurements we determine the numerical values of the damping parameter Γ due to scattering of electrons on impurities at the extremal point and the influence of temperature on the value of the anomaly. We carry out a quantitative comparison of the theory[17,18] with experiment, making it possible to determine such parameters of the ETT as the energy gap $E_F^0-E_c$ and the critical concentration C_c. These data can be used to refine the fine structure of the electronic spectrum in those cases when the theoretical calculations, because of their insufficient accuracy (0.1 eV), do not give complete information about the small parts of the Fermi surface and, accordingly, energy gaps of less than 0.1 eV. This is interesting also because these alloys have special physical properties, such as high values of T_c (Ref. 12), etc.,[19] which may be related to the features of the electronic spectrum. In the general case the study of the thermopower is a rather simple method of determining the singular points in the electronic spectrum for both normal and superconducting metals and alloys.

2. SAMPLES AND MEASUREMENT TEMPERATURES

The measurements were made on samples cut from bars prepared by the floating zone method, which had been used previously in Refs. 12 and 13 for studies of the ETT from the superconducting characteristics.

Samples with dimensions of $2\times2\times30$ mm were cut out along the direction of motion of the zone by an electrospark cutter. The samples were etched in a mixture of nitric and fluoric acids and then electropolished to provide a mirror finish and a constant cross section along the entire length. The composition of the samples was determined by activation analysis and correlated with the previously measured dependence of T_c on the concentration of impurities.[12] The maximum possible error of determination of the Re and Nb content was not more than 10%. Manganin foil was spot welded onto the ends of the sample, which were then tinned. Heaters H_1 and H_2 were soldered to the ends (see Fig. 1); one of these heaters was used to produce a temperature gradient ΔT along the sample, and the other to set the average temperature of the sample. The heaters were made from a twisted pair of manganin wires 0.03 mm in diameter, which was wound on copper coils. The resistance of the heaters was 500–1000 Ω.

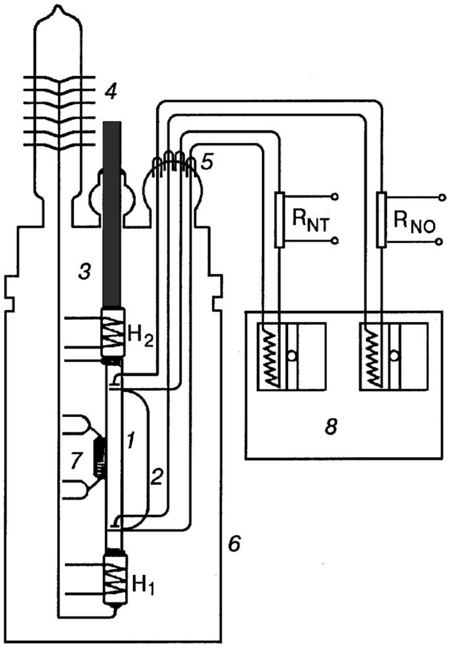

FIG. 1. Layout for the thermopower measurements: *1*—sample, *2*—ZLZh thermocouple, *3*—cold finger, *4*—platinum leads, *5*—platinum capillaries for superconducting wires, *6*—vacuum container, *7*—carbon resistance thermometer, *8*—sensitive element of the SQUID; H_1 and H_2 are heaters.

Measurements of the thermopower were made with a SQUID used as a null indicator. This technique[20] is an ideal instrument for investigating the kinetic properties of metals at low temperatures. The SQUID permits making measurements of small voltages to a rather high accuracy 10^{-13}–10^{-14} V at small temperature gradients. However, the sensitivity of the device is lower for measurements on samples whose resistance can be rather high. In our case the resistance of the samples varied from $\approx 2\times10^{-7}$ Ω for pure Mo to $\approx 10^{-4}$–10^{-3} Ω for alloys; here the sensitivity of the device is lowered to 10^{-13}–10^{-12} V.

A diagram of the thermopower measurements is shown in Fig. 1. The sample *1* was placed in a vacuum container *6*, and the sensitive element of the SQUID *8* was placed next to the container in a helium bath (4.2 K). The measuring circuit of the SQUID was wired with copper-clad Nb–Zr superconducting wires. They were welded on to the sample and the thermocouple *2* and were brought out of the container through platinum capillaries *5* sealed into the glass and were connected to the sensitive element of the SQUID. The temperature gradient ΔT along the sample was 10^{-2} K.

To measure ΔT we used a ZLZh thermocouple, Au–0.03Fe versus superconducting Nb–Zr, of equal diameters 0.1 mm. The temperature dependence of the thermopower for this type of thermocouple is well known. The accuracy to which ΔT was measured was 10^{-5} K. To ensure good thermal contact with the sample the thermocouple was wound several times around the sample together with the Nb–Zr potential leads and was glued down. The average temperature of the sample was set by means of heater H_2, which was soldered between the sample *1* and the cold finger *3*, which was brought out of the container into the helium bath through a "tear drop." The average temperature was measured by a carbon resistance thermometer *7* by a potentiometric method. The thermometer was glued to the center of the sample with BF-2 glue and then, for better thermal contact, was soaked with GKZh oil. The accuracy of the average temperature measurement was 10^{-3} K below 4.2 K and 10^{-2} K at temperatures of 6–10 K. The above scheme was used to measure the concentration dependence of the thermopower in the temperature interval 0–10 K. The temperature dependence of the thermopower were measured in a wide temperature interval (4.2–300 K) by a differential method. The difference of the absolute values of the thermopower of two samples, $\alpha_1-\alpha_2$, one of which was the sample to be studied, while the other had a low value of the thermopower (0.038×10^{-7} V/K^2) at low temperatures, was measured using the vacuum container *6* (Fig. 1) at low temperatures and by a standard potentiometric method at temperatures above 77 K. A diagram of the mounting of the samples is shown in Fig. 2.

Samples *1* and *2* of approximately equal dimensions $2\times2\times30$ mm, were glued at their upper ends to a copper bracket *3*, which was connected to the cold finger *4*. Thermal contact of the remaining parts of the samples was achieved by soaking the "contact" area with GKZh oil.

The samples were electrically isolated from each other and from the copper bracket *3*. Electrical contacts were formed by welding Constantan wires to the samples and soldering these wires to wires *7* consisting of lead ribbons 1 mm wide and 0.05 mm thick, glued together across a layer of cigarette paper. The lead ribbons were soldered to a Nb–Zr superconducting wire *9* which led out of the vacuum container into the helium bath through sealed-in platinum capillaries passing through the glass and was connected to the sensitive element of the SQUID. The places where the wires and ribbons were soldered together were thermally stabilized and had a temperature of 4.2 K. The samples were connected together at the lower end by the same lead ribbon. Carbon thermometers or copper–Constantan thermocouple junctions were mounted on the samples near the places where the Constantan wires were welded on. This mounting arrangement made it possible to create equal temperature gradients on both samples, and so the voltage was proportional to the difference of the absolute values of the thermopowers, $\alpha_1-\alpha_2$. The presence of the "normal" wires above 7 K did not introduce a parasitic emf, since, because of the good thermal contact, the lead ribbons had the same local temperature along the entire length. This was monitored by the absence of voltage jumps upon the transition of the lead to the normal state above 7 K.

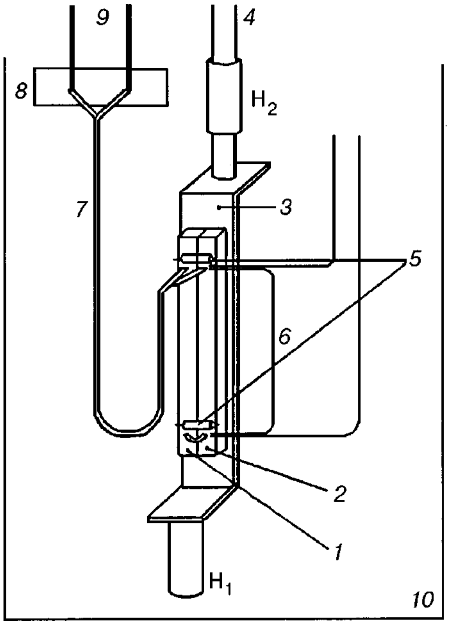

FIG. 2. Diagram of the mounting of the samples for measurement of the temperature dependence of the thermopower of a wide range of temperatures: *1*, *2*—samples, *3*—copper bracket, *4*—cold finger, *5*—resistance thermometers, *6*—thermocouple, *7*—lead ribbons, *8*—block for temperature stabilization, *9*—superconducting wire, *10*—vacuum container; H_1 and H_2 are heaters.

In the temperature interval 4.2–77 K the measurements were done in a helium cryostat with the use of a SQUID. The average temperature of the samples and ΔT were measured by two carbon resistance thermometers. With the appearance of normal resistance of the wires above 7 K the sensitivity of the measuring circuit fell off. For this reason the temperature gradient was gradually increased; a value of 1–6 K was used in the interval from 30 to 77 K.

In the temperature interval 77–300 K the measurements were done in a liquid-nitrogen cryostat, and the difference voltage across the samples was determined by a standard potentiometric method with a sensitivity of 10^{-8} V. The average temperature of the samples was measured by carbon resistance thermometers, and the temperature gradient along the samples was measured by a copper–Constantan thermocouple.

3. RESULTS OF THE MEASUREMENTS

We investigated the temperature and concentration dependence of the thermopower of Mo and of its binary $Mo_{1-x}Re_x$ and ternary $Mo_{1-x-y}Re_xNb_y$ alloys. The indices x and y denote the variable concentrations of Re and Nb, respectively. The samples, which were up to 30 mm long, were quite homogeneous, as was monitored by the width of the superconducting transition, which was ≈0.1 K. Figure 3 shows the results of measurements of the temperature dependence of the thermopower α/T of $Mo_{1-x}Re_x$ alloys in the temperature interval 0–10 K. A cross section of the graphs for $T=\text{const}$ gives the absolute value of α/T, which corresponds to the diffusive part of the thermopower for alloys of different concentrations. At a fixed concentration the slope of the curve of α/T versus T^2 determines the effects due to phonon drag.

It is seen from the data presented that the diffusive part of the thermopower varies under the influence of the impurity by a factor of ≈5, whereas the phonon drag part α/T varies by no more than 15%. However, one cannot fail to notice the features on the curve of α/T versus T^2 in the temperature interval 0–10 K. The slope for samples of different composition twice changes sign. In other words, the coefficient B multiplying T^3 in formula (1) has a singularity as a function of the impurity concentration. This may be due to features of the interaction of electrons with phonons at the

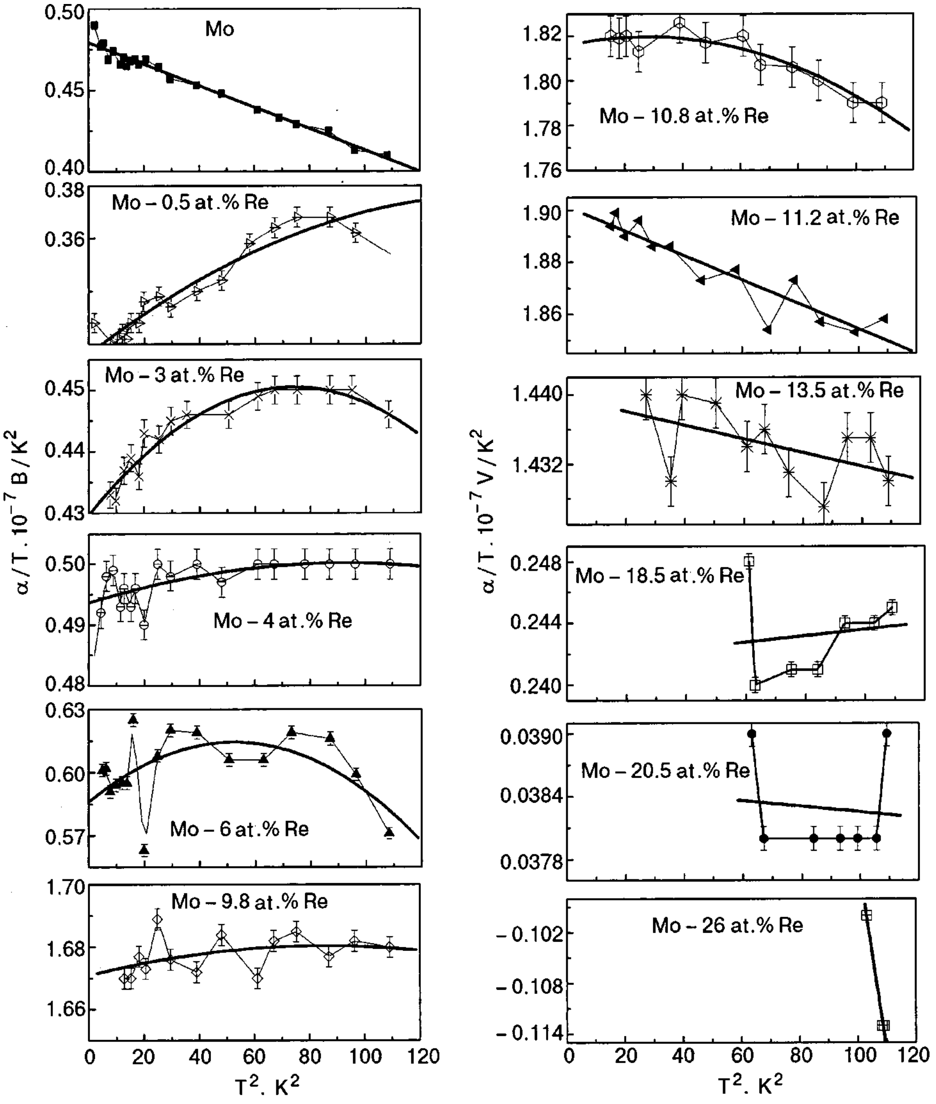

FIG. 3. Dependence of α/T on T^2 for $\mathrm{Mo}_{1-x}\mathrm{Re}_x$ alloys with different concentrations of the Re impurity.

ETT in the alloys. These will be discussed in more detail in a separate paper. In the present paper we will discuss only the features of the diffusive part of the thermopower, $\alpha(C)/T$, assuming that the variations due to phonon drag in the temperature interval 0–10 K are insignificant in comparison with the variations of the thermopower under the influence of impurities. Figure 4 shows the results of measurements of the curves of α/T versus T^2 for different concentrations of the Re impurity and also, on the same scale, a plot of $\alpha(C)/T$ at a temperature of 10 K for $\mathrm{Mo}_{1-x}\mathrm{Re}_x$ alloys.

We see from the plots that in this temperature interval the phonon drag contribution to the thermopower is negligible in comparison with the "giant" variations of the diffusive part of the thermopower as a function of concentration. The diffusive part of the thermopower, $\alpha(C)/T$, is proportional to the derivative $\partial\nu(E)/\partial E$ (Ref. 7) and, as is seen in Fig. 4b, has a maximum. The value of the thermopower α/T increases from 0.4×10^{-7} V/K^2 for pure Mo to 1.8 $\times10^{-7}$ V/K^2 at the maximum for $\mathrm{Mo}_{0.9}\mathrm{Re}_{0.1}$. Analogous curves were obtained for the ternary system $\mathrm{Mo}_{1-x-y}\mathrm{Re}_x\mathrm{Nb}_y$ and are presented in Fig. 5. The ternary systems studied were prepared on the basis of the binary systems with a fixed concentration x of the Re impurity and a variable concentration y of the Nb. The concentration of Re was chosen such that passage through an anomaly (extremum) would occur, and by varying the concentration of the Nb impurity one could return to the electron concentration of pure Mo, passing through the anomaly in the reverse direction. In the alloys studied $x\approx17$ at. % for one system and ≈29 at. % for the other. The composition of the alloy was calculated with allowance for the valence of the impurity relative to pure Mo. It follows from a previous study[13] that the effects of Re and Nb impurities are equal and opposite. Here the efficacy of an impurity was defined as the change in electron concentration of the alloy upon admixture of the impurity: $\Delta n[\text{electrons/atom}]=\Delta Z/100[\%]\Sigma_i C_i[\%]$, where C_i is the atomic concentration of the ith component, ΔZ is the difference of the valences of the impurity and pure Mo, and n is the electron concentration.

For the ternary systems the results are presented as functions of the effective concentrations $C_{\text{eff}}=C_{\text{Re}}+C_{\text{Nb}}$, calculated with allowance for Δn.[13] The $\alpha(C)/T$ curve at 10 K for the ternary systems consists of two segments (two differ-

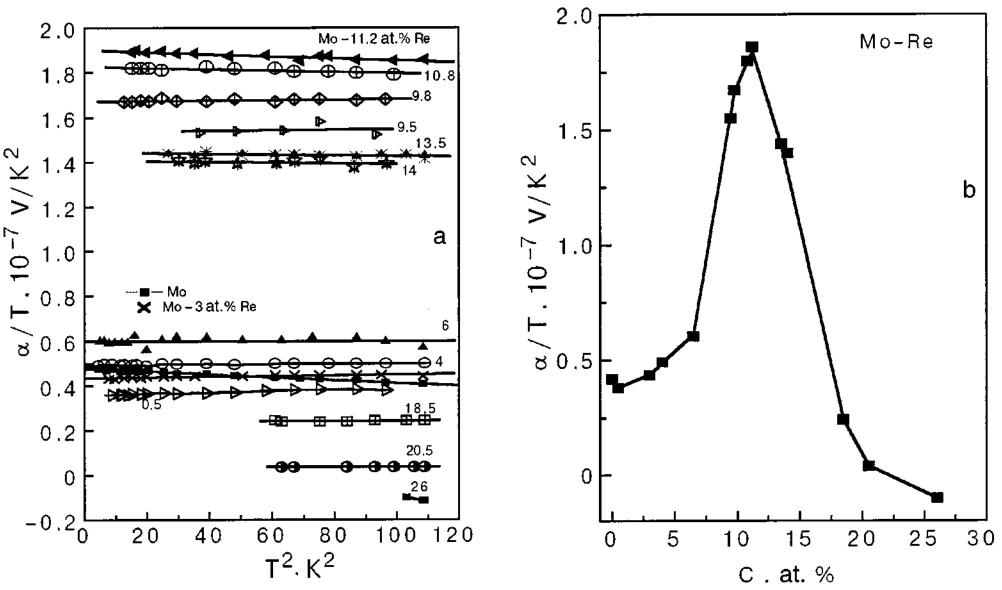

FIG. 4. Dependence of α/T on T^2 (a) and of α/T on C at 10 K (b) for $Mo_{1-x}Re_x$ alloys.

ent values of x) corresponding to a single curve, on which it is seen that the extremum is slightly shifted to higher concentrations in comparison with the binary systems and has a lower numerical value at the extremal point.

The result of a comparison of the thermopower of the binary and ternary systems is presented in Fig. 6. We see that the values of the thermopower at the extremum differ for the binary and ternary systems by a factor of 1.5.

Figure 7 shows a log–log plot of the temperature dependence of α/T for samples with an electron concentration $n \approx 6.098$ electrons/atom for Mo–Re and $n \approx 6.122$ electrons/atom for Mo–Re–Nb in the temperature interval 4.2–300 K. The measurements were made by the differential method. In both cases the difference of the absolute values of the thermopower, $\alpha_1 - \alpha_2$, were measured relative to the same $Mo_{79.5}Re_{20.5}$ sample, which at low temperatures has a close to zero value of the thermopower. From the temperature dependence of the thermopower for the binary and ternary systems measured at the extremal point over a wide temperature interval one can obtain information about the influence of impurities and temperature on the anomaly. In addition, one can find experimentally the values of the damping parameters Γ_1 and Γ_2 for the given samples and determine the respective values of $\partial\Gamma/\partial C$. As we see in Fig. 7, the character of the curves is the same in both cases. The thermopower varies slightly up to a temperature of 30 K for Mo–Re and up to 40 K for Mo–Re–Nb and changes sharply upon further increase in temperature. This is due to the pres-

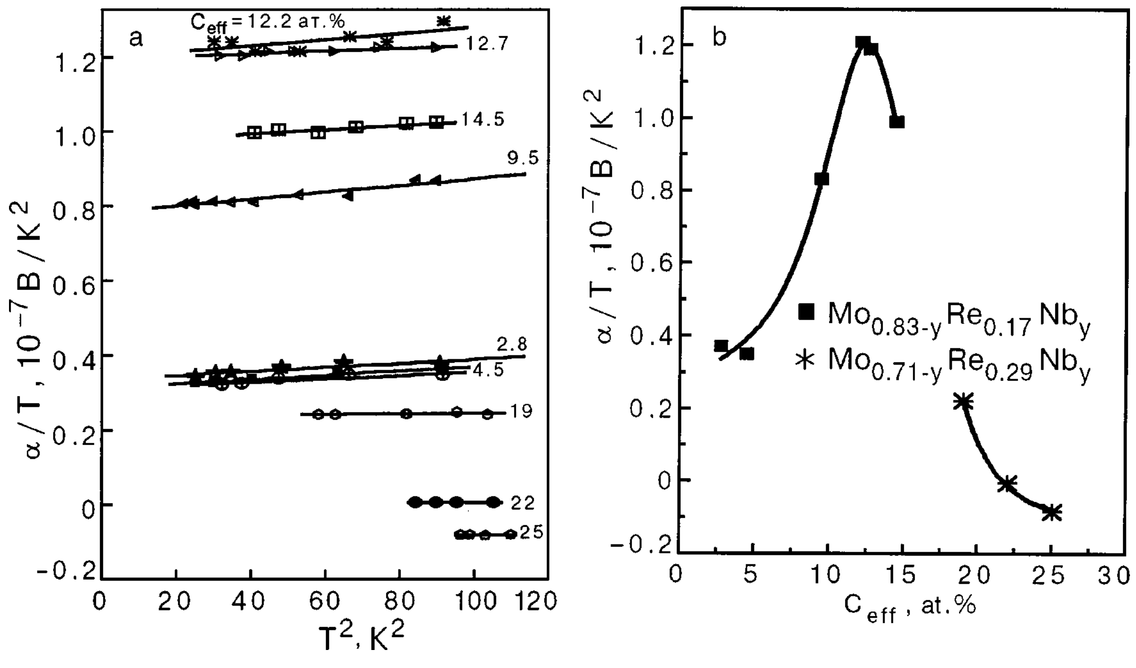

FIG. 5. Dependence of α/T on T^2 (a) and of α/T on C_{eff} at 10 K (b) for $Mo_{1-x-y}Re_x Nb_y$ alloys. The concentrations C_{eff} were calculated with allowance for the valence of the impurities.[13]

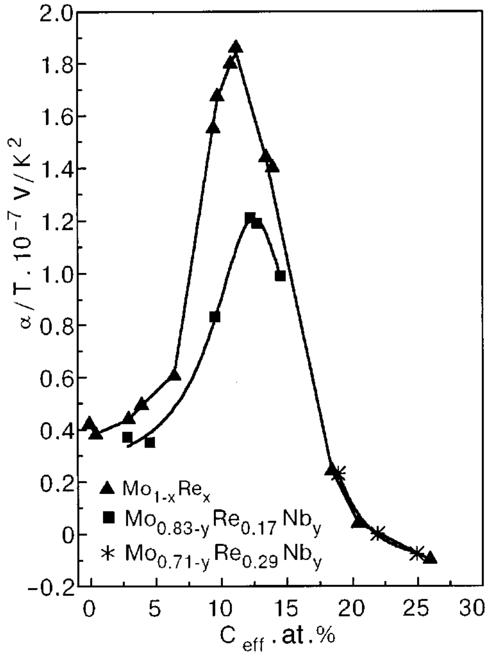

FIG. 6. Concentration dependence of the thermopower for $Mo_{1-x}Re_x$ and $Mo_{1-x-y}Re_x Nb_y$.

ence of two different scattering mechanisms: impurity and phonon.[8,21] The impurity scattering processes are manifested to a larger degree at low temperatures. These mechanisms become comparable in the region of sharp change of the temperature trend. Therefore the value of the temperature at this point corresponds to the value of Γ for the impurity mechanism of scattering and equals 30 K for Mo–Re and 40 K for Mo–Re–Nb. Accordingly, for the binary alloys $\partial\Gamma/\partial C = 3.05$ K/at. %. The ratio of the anomalous values of the thermopower for the binary and ternary systems is $\alpha_{\text{Mo-Re}}/\alpha_{\text{Mo-Re-Nb}} \approx \sqrt{\Gamma_2/\Gamma_1}$ (Ref. 8), where $\Gamma \approx 1/\tau$ is the damping parameter associated with the scattering of electrons on impurities, and τ is the lifetime, on which the residual resistance $r = R_{4.2}/(R_c - R_{4.2})$ and the resistivity ρ also depend. These quantities, measured in the samples in an independent way, are given in Table I. For Mo–Re with $n \approx 6.098$ electrons/atom and for Mo–Re–Nb with $n \approx 6.122$ electrons/atom the ratio $\alpha_1/\alpha_2 = 1.38$ and is proportional to the ratio $\sqrt{\Gamma_2/\Gamma_1} = 1.15$. On the other hand, Γ is proportional to the residual resistance $r = R_{4.2}/(R_c - R_{4.2})$ and to the resistivity ρ, which are measured independently. Their ratios are $\sqrt{r_2/r_1} = 1.43$ and $\sqrt{\rho_2/\rho_1} = 1.4$.

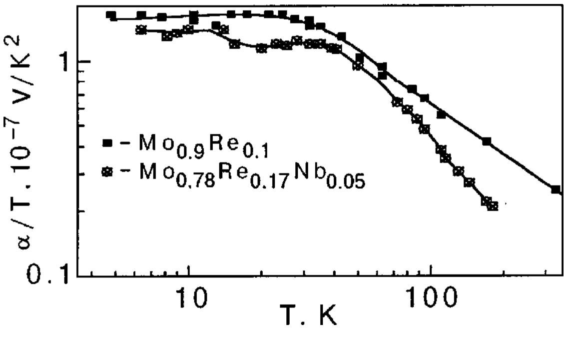

FIG. 7. Temperature dependence of α/T for $Mo_{0.9}Re_{0.1}$ and $Mo_{0.78}Re_{0.17}Nb_{0.05}$ alloys in the temperature range 0–300 K.

TABLE I.

System	α/T, 10^{-7} V/K^2	ρ, 10^{-6} $\Omega\cdot$cm	$\frac{R_{4.2}}{R_c - R_{4.2}}$	Γ, K
$Mo_{0.9}Re_{0.1}$	1.66	3.01	0.36	30
$Mo_{0.78}Re_{0.17}Nb_{0.05}$	1.2	6.09	0.74	40

4. QUANTITATIVE CHARACTERISTICS OF ELECTRONIC–TOPOLOGICAL TRANSITIONS

According to the theory of Refs. 7 and 8, the ETT is manifested as an extremum of the diffusive part of the thermopower as the Fermi energy changes under the influence of an impurity and the condition $E_F = E_c$ is attained. As we see in Fig. 6, for the binary $Mo_{1-x}Re_x$ and ternary $Mo_{1-x-y}Re_xNb_y$ systems the extremum on the $\alpha(C)/T$ curve is observed at the same value of the electron concentration, i.e., the Fermi energies E_F of these systems cross the same critical point of the electronic spectrum. According to theoretical calculations of the band structure of pure Mo,[22] above the Fermi energy E_F^0 along the NH direction there is an unfilled band, the energy of the bottom of which is E_c. Then when E_F rises under the influence of the Re impurity and crosses E_c, a new sheet of the Fermi surface appears at a concentration C_c. If an Nb impurity is added to a binary system having a concentration $C_{\text{Re}} \geqslant C_c$, then as E_F is lowered under the influence of this impurity, the sheet that has appeared will vanish at this same $C_{c\ \text{eff}}$.

Thus, by using impurities with opposing valence differences one can observe two oppositely directed electronic transitions corresponding to the same critical point of the electronic spectrum. These results reflect the electronic nature of the anomalies that we have observed.

Using the theory of Ref. 17, one can carry out a quantitative comparison of the theory with experiment and find numerical values of the parameters of the ETT. According to the formula in Ref. 18, the diffusive part of the thermopower, $\alpha(C)/T$, can be written, with allowance for the anomalous part due to the ETT, in the form of two terms:

$$\frac{\alpha(C)}{T} = \frac{\alpha_0(C)}{T} + \frac{\delta\alpha(C)}{T}, \tag{2}$$

where

$$\frac{\alpha_0(C)}{T} = A_1 + A_2(C - C_0) + A_3(C - C_0)^2;$$

$$\frac{\delta\alpha(C)}{T} = A_4\sqrt{T}\int_{-\infty}^{\infty} Y \cosh^{-2}\frac{Y}{2}\left\{\frac{A_5}{T}(C - C_c) + Y + \left[\left(\frac{A_5}{T}(C - C_c) + Y\right)^2 + \left(\frac{\Gamma^*(C - C_0)}{2T}\right)^2\right]^{1/2}\right\}^{1/2} dY; \tag{A}$$

TABLE II.

System	A_1, V/K^2	A_2, V/K^2·(electrons/atom)	A_3, V/K^2·(electrons/atom)^2	A_4^*, V/K^2	A_5, K/(electrons/atom)	C_c, electrons/atom
$Mo_{1-x}Re_x$	4.79	−7.94	−177.46	14.3	1993.6	6,1004
$Mo_{1-x-y}Re_xNb_y$	5.27	−58.8	24.9	13.69	1702.4	6,1077

$$A_5=\partial(E_F-E_C)/\partial C,\ \ \Gamma^*=\partial\Gamma/\partial n,\ \ A_4\sqrt{T}=A_4^*,$$

and n is the electron concentration.

The first term corresponds to the change in thermopower of Mo under the influence of the impurity with the exclusion of the topological contribution and is represented as a series expansion in $(C-C_0)$, where C_0 is the electron concentration of pure Mo. The second term describes the anomalous component of the thermopower due to the ETT in the alloys.

From a quantitative comparison of the theory with the experimental data on the thermopower by the least-squares method, one can obtain the values of the parameters appearing in expression (2). In the calculations we used the numerical value of the parameter Γ given in Table I. The remaining parameters were determined as adjustable parameters of the fit (see Table II).

The results of the comparison of theory and experiment, corresponding to the values obtained for the parameters in relations (2), are shown graphically in Fig. 8 for the Mo–Re and Mo–Re–Nb alloys.

5. DISCUSSION OF THE RESULTS

Let us compare our results with those published previously.

Figure 9 shows the results of Ref. 13. In the measurements of the thermopower $\alpha(C)/T$ (Fig. 8) and in the ETT studies based on $\partial T_c(P,C)/\partial P$ (Fig. 9), the ratio of the anomalies of the binary and ternary systems have comparable values at the extremum. We see that the experimental and theoretical results agree not only qualitatively but also quantitatively. This again confirms the unified nature of the anomalies observed in the normal and superconducting states.

Using $C_c=6.1$ electrons/atom and the values of the parameter A_5 for the binary and ternary systems from Table II, one can obtain the value of the gap $E_c-E_f^0$ for pure Mo: $E_c-E_F^0=(C_c-C_0)\partial(E_c-E_F^0)/\partial C$ (see Table III).

According to the theory of Makarov and Bar'yakhtar,[3,17] the parameters of the anomalous part of the thermopower, $\alpha(C)/T$ ($A_5=\partial(E_F-E_c)/\partial C$ and C_c) are the same ETT parameters that are determined by the anomalous part of $\partial T_c(P,C)/\partial P$. The values found for these parameters are in agreement with the results of Ref. 13.

The conditions of the experiment for studying the thermopower—low temperatures and high impurity concentrations—permit one to interpret the parameter Γ in the same way for superconductors and normal metals. For

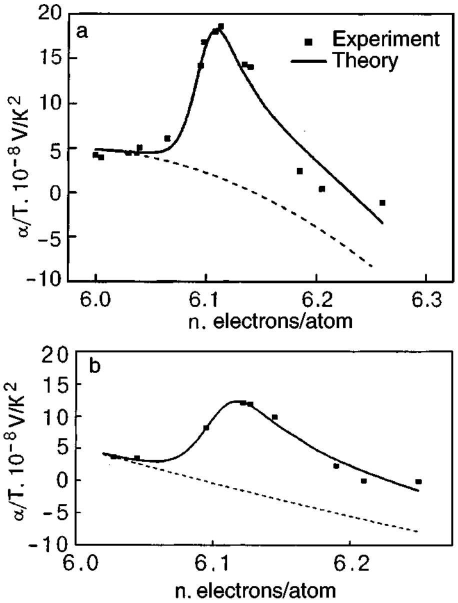

FIG. 8. Dependence of α/T on n for $Mo_{1-x}Re_x$ (a) and $Mo_{1-x-y}Re_x\,Nb_y$ (b) at 10 K. The solid curve corresponds to the anomalous part of the thermopower, $\delta\alpha(C)/\tau$, and the dashed curve to the thermopower without the effect of the ETT, $\alpha_0(C)/T$ (formula (2)).

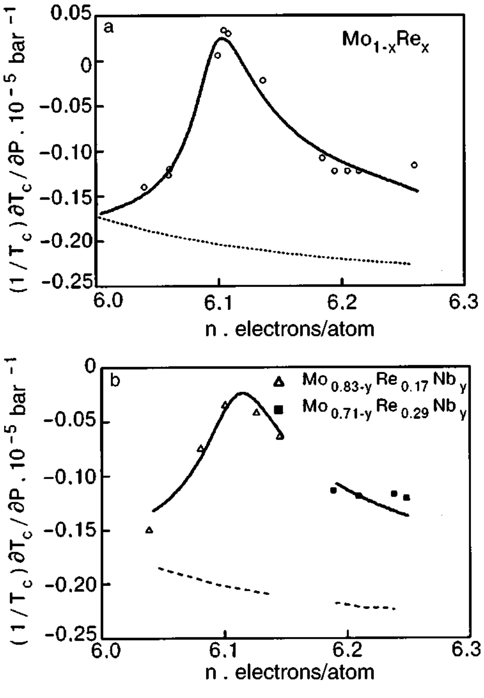

FIG. 9. The functions $[(1/T_c)\partial T_c/\partial P](n)$ for $Mo_{1-x}Re_x$ (a) and $Mo_{1-x-y}Re_x\,Nb_y$ (b). The points are experimental, the solid curves correspond to the anomalous part of the dependence, and the dashed curves to the smooth component.[13]

TABLE III.

System	$E_c - E_F^0$ eV
$Mo_{1-x}Re_x$	0.02
$Mo_{1-x-y}Re_xNb_y$	0.017

superconductors at the concentrations studied, the gap becomes isotropic, and the damping parameter Γ is determined solely by impurity scattering.[23] For the concentration dependence of $\alpha(C)/T$ it is important that at low temperatures the phonon drag is small, and the impurity scattering plays the governing role here as well.[8,21] Therefore, in this case Γ is the same for the superconducting and "normal" states of the alloys. Then the values of the parameters Γ determined from experiment can be used as given values for comparison of theory and experiment in both cases.

An important result is the separation of the smooth and anomalous parts of the thermopower. Better agreement of the experimental data with the theoretical calculation is obtained when the smooth component is nonlinear (Fig. 8). Furthermore, far from the singularity it changes sign. It can be assumed that this is due to a change of the partial contributions to the thermopower from the electron and hole sheets of the Fermi surface or to the proximity of the band top to the Fermi level.

Let us discuss the temperature dependence in Fig. 7. One can discern at least two regions in respect to the influence of scattering processes on the thermopower anomaly: $T < \Gamma$, where the impurity scattering is more important, and $T > \Gamma$, where scattering on phonons predominates. At temperatures $T > \Gamma$ the scattering on phonons becomes larger than the scattering on impurities, and the temperature dependence of α/T for the samples at the anomalous point determines the influence of temperature on the value of the anomaly. In the region $\Gamma < T < 200$ K the log–log plots of $\alpha(T)/T$ are linear. This corresponds to a variation of the anomaly with temperature by a power law T^{-x}, where according to our data $x = 0.5 - 0.6$ and according the theory[8,21] $x = 0.5$. For clarity one can compare the values of α/T for $T_1 = 10$ K and $T_2 = 100$ K, for example, which are 1.7×10^{-7} and 0.6×10^{-7} V/K^2, respectively, for the binary systems and 1.2×10^{-7} and 0.425×10^{-7} V/K^2 for the ternary systems. In this case the ratio $\alpha_{T_1}/\alpha_{T_2} = 2.83$ and 2.82, i.e., proportional to $\sqrt{T_2/T_1} = 3.16$. It is seen that the results agree with the theory to an accuracy of 10%.

Our results can also be compared with the data of Ref. 24, in which the temperature dependence of the thermopower above 10 K was measured for several $Mo_{1-x}Re_x$ alloys and certain other transition-metal alloys, and it was called to attention that the $\alpha(n)/T$ curve has a peak at an electron concentration $n \approx 6.1$ electrons/atom. This agrees with our result. In addition, the value of α/T at the extremal point agrees with the value which we obtained when the $\sim T^{-0.5}$ decrease in the anomaly is taken into account.

6. CONCLUSIONS

1. Two features in the behavior of the thermopower are observed: a maximum on the $\alpha(C)/T$ curve and, as a consequence, anomalous behavior of the coefficient B in formula (1) at low temperatures.

The observed maximum on the diffusive part of the thermopower, $\alpha(C)/T$, is due to the appearance of a new electron sheet under the influence of the Re impurity in the binary systems and the disappearance of this sheet when an Nb impurity is added in the ternary systems. Both transitions occur when the same critical point of the electronic spectrum of Mo is crossed by the Fermi energy as it is shifted in opposite directions. This confirms the electronic nature of the peak in the diffusive part of the thermopower and our interpretation of the phenomenon observed.

2. A quantitative comparison of theory with experiment is carried out. A value of the energy gap $E_c - E_F^0 \approx 0.02$ eV is obtained for Mo at a critical concentration of 6.1 electrons/atom.

3. From the temperature dependence of the thermopower anomaly we have determined the values of the scattering parameter Γ for electron scattering on impurities for the binary and ternary systems. From these same experimental data a power law is established for the decrease of the anomaly of the diffusive part of the thermopower as the temperature is varied in the interval $\Gamma < T < 200$ K: $\alpha/T \sim T^{-x}$, where x, according to our data, is 0.5–0.6, in good agreement with the theory.[8,21]

4. From a comparison of the thermopower anomaly with the anomalies of the superconducting characteristics at the ETT one can conclude that the nature of these anomalies is the same. Therefore, it is possible that this conceptual framework may be used to predict the properties of other systems, including high-T_c superconductors.

*E-mail: xkbm@komeran.com.ua

---

[1] I. M. Lifshits, Zh. Éksp. Teor. Fiz. **38**, 1569 (1960) [Sov. Phys. JETP **11**, 1130 (1960)].

[2] B. G. Lazarev, L. S. Lazareva, V. I. Makarov, and T. A. Ignat'eva, Zh. Éksp. Teor. Fiz. **48**, 1065 (1965) [Sov. Phys. JETP **21**, 711 (1965)].

[3] V. I. Makarov and V. G. Bar'yakhtar, Zh. Éksp. Teor. Fiz. **48**, 1717 (1965) [Sov. Phys. JETP **21**, 1151 (1965)].

[4] T. A. Ignat'eva, V. I. Makarov, and Yu. A. Cherevan', Zh. Éksp. Teor. Fiz. **67**, 994 (1974) [Sov. Phys. JETP **40**, 492 (1975)].

[5] I. Ya. Volynskiĭ, V. I. Makarov, and V. V. Gann, Zh. Eksp. Teor. Fiz. **68**, 1019 () [*sic*].

[6] M. A. Krivoglaz and Tyu-Khao, Fiz. Met. Metalloved. **21**, 817 (1966).

[7] V. G. Vaks, A. V. Trefilov, and S. V. Fomichev, Zh. Éksp. Teor. Fiz. **80**, 1613 (1981) [Sov. Phys. JETP **53**, 830 (1981)].

[8] A. A. Varlamov and A. V. Pantsulaya, Zh. Éksp. Teor. Fiz. **89**, 2188 (1985) [Sov. Phys. JETP **62**, 1263 (1985)].

[9] V. S. Egorov, A. and N. Fedorov, Zh. Éksp. Teor. Fiz. **85**, 1647 (1983) [Sov. Phys. JETP **58**, 959 (1983)].

[10] N. V. Zavaritskiĭ, V. I. Makarov, and A. A. Yurgens, JETP Lett. **42**, 182 (1985).

[11] E. M. Lifshitz and L. P. Pitaevskiĭ, *Physical Kinetics* [in Russian], Nauka, Moscow (1979); A. A. Abrikosov, *Introduction to the Theory of Normal Metals* [in Russian], Nauka, Moscow (1972).

[12] T. A. Ignat'eva and Yu. A. Cherevan', JETP Lett. **31**, 361 (1980).

[13] T. A. Ignat'eva, V. V. Gann, and A. N. Velikodnyĭ, Fiz. Nizk. Temp. **20**, 1133 (1994) [Low Temp. Phys. **20**, 890 (1994)].

[14] A. N. Velikodnyĭ, N. V. Zavaritskiĭ, T. A. Ignat'eva, and A. A. Yurgens, JETP Lett. **43**, 773 (1986).

[15] F. G. Morin and J. P. Maita, Phys. Rev. **129**, 1115 (1963).

[16] W. Royal Cox, D. I. Hayes, and F. R. Brotzen, Phys. Rev. **7**, 3580 (1973).

[17] V. G. Bar'yakhtar, V. V. Gann, and V. I. Makarov, Fiz. Tverd. Tela (Leningrad) **14**, 1715 (1972) [Sov. Phys. Solid State **14**, 1477 (1972)].

[18] N. V. Zavaritskiĭ, A. I. Kopeliovich, V. I. Makarov, and A. A. Yurgens, Zh. Éksp. Teor. Fiz. **94**, 6 (1988) [Sov. Phys. JETP **67**, 1283 (1988)].

[19] D. L. Davidson and F. R. Brotzen, Acta Metalurgica **18**, 463 (1970).

[20] N. V. Zavaritskiĭ and O. E. Omel'yanovskiĭ, Zh. Éksp. Teor. Fiz. **83**, 1182 (1982) [Sov. Phys. JETP **56**, 674 (1982)].

[21] A. A. Abrikosov and A. V. Pantsulaya, Fiz. Tverd. Tela (Leningrad) **28**, 2140 (1986) [Sov. Phys. Solid State **28**, 1195 (1986)].

[22] R. I. Iverson and L. Hodges, Phys. Rev. B **8**, 1429 (1973).

[23] V. I. Makarov, V. G. Bar'yakhtar, and V. V. Gann, Zh. Éksp. Teor. Fiz. **67**, 168 (1974) [Sov. Phys. JETP **40**, 85 (1975)].

[24] A. C. Lin, F. R. Brotzen, and R. B. Liftin, J. Appl. Phys. **51(3)**, 1655 (1980).

Translated by Steve Torstveit

LOW TEMPERATURE PHYSICS VOLUME 28, NUMBER 6 JUNE 2002

LOW-DIMENSIONAL AND DISORDERED SYSTEMS

Two-quantum electron spin–lattice relaxation in amorphous solids

L. G. Zakharov, L. L. Chotorlishvili,[a)] and T. L. Buishvili

Institute of Physics, Academy of Sciences of Georgia, ul. Tamarashvili 6, 380077 Tbilisi, Georgia

(Submitted December 11, 2001; revised February 22, 2002)
Fiz. Nizk. Temp. **28**, 580–583 (June 2002)

A two-quantum process of electron spin–lattice relaxation in amorphous solids is investigated. A relaxation mechanism involving two-level tunneling systems and phonons from the region of the boson peak is considered. It is shown that this mechanism is effective under certain conditions. © *2002 American Institute of Physics.* [DOI: 10.1063/1.1491181]

The study of nuclear and electronic spin–lattice relaxation in amorphous solids at low temperatures is a topical problem in physics. It has been established that the low-temperature ($T<1$ K) properties of amorphous solids are governed by two-level tunneling systems,[1] the main feature of which is that their density of states is nearly constant (it depends weakly on energy), and therefore at low temperatures, when it is mainly low-frequency acoustic phonons that are excited, with a low density, the two-level systems (TLSs) come to play the governing role. The role of the TLSs in the process of nuclear and electronic spin–lattice relaxation was studied in Refs. 2 and 3, respectively.

In addition, it has been established that the density of vibrational states of amorphous solids is characterized by the presence of a low-frequency peak. This peak, also called the boson peak, has a substantial influence on the physical properties of amorphous materials at temperatures of the order of 10 K.[4]

In view of what we have said, the following expression is obtained for the density of vibrational states:[4]

$$g(\omega)=\frac{2N}{\omega_D^3}\left(\omega^2+\mu\omega_m^2\exp\left(-\frac{\ln^2\omega/\omega_m}{2\sigma^2}\right)\right), \tag{1}$$

where ω_D is the Debye frequency, μ is a coefficient taking values from 2 to 10 for different materials, $\sigma=0.48$ is a parameter characterizing the width of the boson peak, N is the number of atoms, and ω_m is the frequency corresponding to the maximum density of states in the peak.[4]

The boson peak also has a substantial influence on the electronic spin–lattice relaxation.[5,6]

In Refs. 2 the process of nuclear spin–lattice relaxation in amorphous materials was studied at low temperatures: processes of the Raman type involving a TLS and a phonon or two TLSs were considered. It was noted that the processes involving a TLS and a phonon gives an expression $1/T_1\approx T^4$ for the nuclear spin–lattice relaxation rate. However, in those papers the Debye model was used, and the features of the density of vibrational states in amorphous systems were not taken into account.

In the present study we investigate the electronic spin–lattice relaxation of the Raman type involving a TLS and a phonon from the region of the boson peak.

As we know, for a paramagnetic impurity of spin 1/2, the spin–lattice interaction is determined by the modulation of the g tensor of the paramagnetic impurity due to the modulation of the intracrystalline field by lattice vibrations.[7] On the other hand, in glasses the interaction of electron spins with the TLS can also occur on account of modulation of the g tensor in response to the tunneling of the paramagnetic center from one equilibrium position to the other (we assume that a part of the paramagnetic center forms a TLS). The part of the Zeeman energy responsible for the electron spin relaxation process has the form

$$H=H_0\int_i[g^{+z}(\mathbf{r}_i)S_i^-+g^{-z}(\mathbf{r}_i)S_i^+], \tag{2}$$

where $S^\pm=S_x\pm iS_y$, S_x and S_y are the projections of the electron spin on the X and Y axes, $g^{\pm z}$ is the symmetric second-rank g tensor, H_0 is the static magnetic field, which is directed along the Z axis, and $\mathbf{r}_i$ is the radius vector of the impurity forming the TLS. We write it in the form

$$\mathbf{r}_i=\mathbf{r}_{i0}+\mathbf{u}_i+\mathbf{d}_il_i^z, \tag{3}$$

where $\mathbf{u}_i$ is the relative displacement of the paramagnetic center and the origin of coordinates during the lattice vibrations, $|\mathbf{d}_i|$ is the distance between minima of the double-well potential, between which the tunneling of the paramagnetic center occurs, $\mathbf{r}_{i0}$ is the radius vector of the midpoint between the two minima of the potential well, and l_i^z is a pseudospin, with spin-1/2 properties, describing the TLS. Taking into account that $|\mathbf{u}_i|,|\mathbf{d}_i|\ll a$ (a is the average distance between atoms) and expanding $g^{\pm z}(\mathbf{r}_i)$ in powers of $|\mathbf{u}_i|/a$ and $|\mathbf{d}_i|/a$, in the eigen-representation of the TLS for the Hamiltonian describing an electron spin relaxation process involving the participation of a TLS and a phonon, we obtain the expression

$$H_{sdp}=\frac{i}{2}H_0\left(\frac{\hbar}{2MV^2}\right)^{1/2}\sum_{iq}(\omega_q)^{1/2}e^{iq\mathbf{r}_i}(a_{\mathbf{q}}-a_{-\mathbf{q}}^+)\times(D_i^{+z}S_i^-+D_i^{-z}S_i^+)(l_i^z\cos\theta_i-l_i^x\sin\theta_i), \tag{4}$$

where

$$D_i^{\pm z}=\sum_{\alpha\beta\gamma}(\lambda_\beta f_\gamma+\lambda_\gamma f_\beta)\frac{1}{2}$$

$$\times\left(\left.\frac{\partial^2 g^{\pm z}(\mathbf{r}_i)}{\partial r_i^\alpha \partial r_i^\beta}\right|_{\mathbf{r}_i=\mathbf{r}_{i0}} r_i^\gamma+\left.\frac{\partial^2 g^{\pm z}(\mathbf{r}_i)}{\partial r_i^\alpha \partial r_i^\gamma}\right|_{\mathbf{r}_i=\mathbf{r}_{i0}} r_i^\beta\right) d_i^\alpha,$$

M is the mass of the crystal, V is the speed of sound in the sample, $a_\mathbf{q}^+$ and $a_\mathbf{q}$ are the creation and annihilation operators for phonons with wave vector **q**, $\omega_\mathbf{q}$ is the phonon frequency, λ_α are the direction cosines of the polarization vector, **f** is a unit vector along the wave vector **q**, $\cos\theta_i=\sqrt{\varepsilon_i^2-\Delta_{0i}^2}/\varepsilon_i$, $\sin\theta_i=\Delta_{0i}/\varepsilon_i$, $\varepsilon_i=\sqrt{\Delta_{0i}^2+\Delta_i^2}$ is the energy of the TLS, and Δ_{0i} is the tunneling energy.[1]

Let us consider the electron spin–lattice relaxation process due to interaction (4). The total Hamiltonian of the system has the form

$$H=H_0+H_{sdp},$$

$$H_0=\hbar\omega_S\sum_i S_i^z+\hbar\sum_n \varepsilon_n l_n^z+\hbar\sum_\mathbf{q}\omega_\mathbf{q} a_\mathbf{q}^+ a_\mathbf{q},$$

where ω_s is the Zeeman frequency. In the case when $\omega_s \ll \omega_m$ and the electron spin–lattice relaxation is governed mainly by the part of the Hamiltonian (4) which is proportional to l_i^x, since in the relaxation process due to the other part of the Hamiltonian (4), proportional to l_i^z, the main role will be played by phonons with a frequency of the order of ω_s+1/τ, where τ is the correlation time.1) Since $\omega_s \gg 1/\tau$, it is essentially only phonons with frequency ω_s that participate in the spin–lattice relaxation process. Consequently, in this case the number of phonons taking part in the process is extremely limited.

Let us calculate the electron spin–lattice relaxation rate using Zubarev's nonequilibrium statistical operator (nonequilibrium density matrix) approach.[9] We assume that the time over which the spin system comes completely to equilibrium is much less than the spin–lattice relaxation time. We construct the nonequilibrium density matrix:

$$\rho=Q^{-1}\exp\left\{-\beta_s\hbar\omega_s\sum_i S_i^z-\beta_l\left(\hbar\sum_n\varepsilon_n l_n^z\right.\right.$$

$$\left.\left.+\hbar\sum_\mathbf{q}\omega_\mathbf{q}a_\mathbf{q}^+a_\mathbf{q}\right)-(\beta_l-\beta_s)\int_{-\infty}^0 \mathrm{e}^{\varepsilon t}K(t)\,dt\right\}, \qquad (5)$$

where $Q^{-1}=\mathrm{Tr}\,\rho$, β_l and β_s are the inverse temperatures of the lattice and spin system, $K(t)=\mathrm{e}^{iHt}K\mathrm{e}^{-iHt}$ is the thermodynamic flux

$$K=\frac{1}{\hbar}\left[H_{sdp},\hbar\omega_s\sum_i S_i^z\right]$$

in the interaction representation. Assuming that the last term in the argument of the exponential function in (5) is small compared to the first two terms, we expand in a series in powers of K, keeping only the linear term. After straightforward manipulations[10] we obtain

$$\frac{d\beta_s}{dt}=-\frac{\beta_s-\beta_l}{T_e},$$

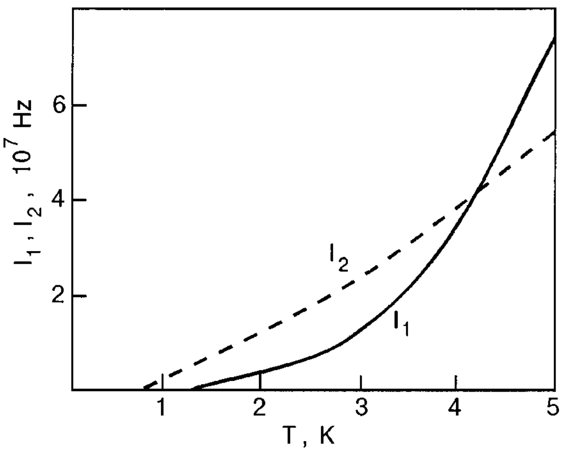

FIG. 1. Temperature dependence of I_1 and I_2.

$$\frac{1}{T_e}=\left(\beta_l\frac{\partial\langle\hbar\omega_s\Sigma_i S_i^z\rangle}{\partial\beta_l}\right)^{-1}$$

$$\times\int_0^{\beta_l}d\lambda\int_{-\infty}^0 \mathrm{e}^{\varepsilon t}\langle K_0(t-i\lambda)K\rangle\,dt, \qquad (6)$$

where

$$K_0(t-i\lambda)=\mathrm{e}^{iH_0(t-i\lambda)}K\,\mathrm{e}^{-iH_0(t-i\lambda)},$$

$$\langle\ldots\rangle=\frac{\mathrm{Tr}(\mathrm{e}^{-\beta_l H}\ldots)}{\mathrm{Tr}\,\mathrm{e}^{-\beta_l H}}.$$

Taking formulas (1) and (6) into account, we finally obtain for the electron spin–lattice relaxation rate in the high-temperature approximation ($\hbar\omega_s \ll k_B T$):

$$\frac{1}{T_e}=\frac{9}{4}\pi\left(\frac{\hbar}{2mV^2}\right)\frac{H_0^2}{\omega_D^3}\overline{P}(I_1+I_2)\frac{\Sigma_i|D_i^{+z}|}{N_s}\frac{1}{\hbar},$$

$$I_1=\int_0^{\omega_D}\frac{\omega^2\sqrt{\omega^2-\Delta_0^2}}{\sinh(\hbar\omega/k_B T)}d\omega, \qquad (7)$$

$$I_2=\mu\omega_m^2\int_0^{\omega_D}\frac{\sqrt{\omega^2-\Delta_0^2}}{\sinh(\hbar\omega/k_B T)}\exp\left(-\frac{\ln^2\omega/\omega_m}{2\sigma^2}\right)d\omega,$$

where m is the mass of the atom, N_s is the density of paramagnetic centers, Δ_0 is the minimum value of the tunneling energy, and $\overline{P}$ is the density of states of the TLS with respect to energy.

One can show by means of a numerical integration that $I_1<I_2$ in the temperature region 1 K$<T<$5 K for $\mu=10$, $\omega_m=5\times10^{11}$ Hz, $\omega_D=1.4\times10^{13}$ Hz, and $\sigma=0.48$. Consequently, in this temperature interval the main role is played by phonons from the region of the boson peak. The temperature dependence of the integrals I_1 and I_2 is shown in Fig. 1. It is easy to verify that $I_1\sim T^4$, while I_2 is proportional to T^2. A similar temperature dependence of the spin–lattice relaxation was observed experimentally in Ref. 11. Let us compare the spin–lattice relaxation rate obtained here (7) with the single-phonon relaxation mechanism, since in the given temperature region the main role is played by one-phonon processes. The one-phonon electron spin–lattice relaxation is described by the Hamiltonian

$$H_{sp}=\frac{i}{2}H_0\frac{1}{2}\left(\frac{\hbar}{2MV^2}\right)^{1/2}\times\sum_i\sum_{\mathbf{q}}(\omega_{\mathbf{q}})^{1/2}e^{i\mathbf{q}\mathbf{r}_i}(a_{\mathbf{q}}-a^{+}_{-\mathbf{q}})(J_i^{+z}S_i^{-}+J_i^{-z}S_i^{+}),$$

where

$$J_i^{\pm z}=\sum_{\alpha\gamma}(\lambda_\alpha f_\gamma+\lambda_\gamma f_\alpha)\left(\left.\frac{\partial g^{\pm z}}{\partial\mathbf{r}_i^{\alpha}}\right|_{\mathbf{r}_i=\mathbf{r}_{i0}}\mathbf{r}_i^{\gamma}+\left.\frac{\partial g^{\pm z}}{\partial\mathbf{r}_i^{\gamma}}\right|_{\mathbf{r}_i=\mathbf{r}_{i0}}\mathbf{r}_i^{\alpha}\right).$$

For the electron spin–lattice relaxation rate in the high-temperature approximation ($\hbar\omega_s<k_BT$) we have

$$\frac{1}{T_{sp}}\approx\frac{9}{4}\pi H_0^2\frac{\Sigma_i|J_i^{+z}|^2}{N_s}\frac{1}{2mV^2\hbar}\frac{k_BT}{\hbar\omega_s}\left(\frac{\omega_s}{\omega_d}\right)^3. \tag{8}$$

For the ratios of the relaxation rates in the temperature region $T<5$ K and with the parameter values indicated above, we obtain, using (8):

$$\frac{1}{T_e}\Big/\frac{1}{T_{sp}}=\frac{\hbar^2}{2}\frac{\overline{P}}{k_BT}\mu\left(\frac{\omega_m}{\omega_s}\right)^2\times\frac{\Sigma_i|D_i^{+z}|^2}{\Sigma_i|J_i^{+z}|^2}\int_0^{\omega_D}\frac{\sqrt{\omega^2-\Delta_0^2}}{\sinh(\hbar\omega/k_BT)}\times\exp\left(-\frac{\ln\omega/\omega_m}{2\sigma^2}\right)d\omega.$$

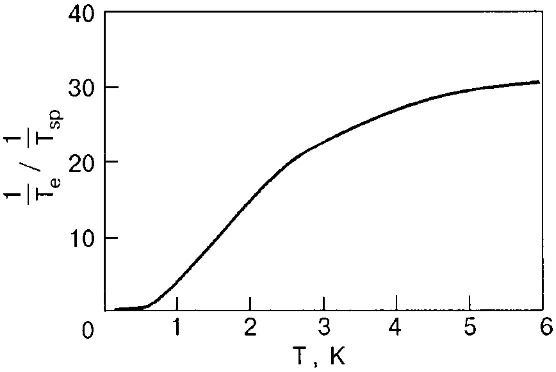

FIG. 2. Temperature dependence of the ratio $(1/T_e)/(1/T_{sp})$.

Figure 2 shows the temperature dependence of the ratio of the relaxation rates $(1/T_e)/(1/T_{sp})$ for the parameters $\overline{P}\approx10^{21}$ J^{-1}, $\omega_m=5\times10^{11}$ Hz, $\omega_D\approx1.4\times10^{13}$ Hz, $\sigma\approx0.48$, $\omega_s\approx10^9$ Hz, $\mu\approx10$, and a ratio

$$\frac{\Sigma_i|D_i^{+z}|^2}{\Sigma_i|J_i^{+z}|^2}\approx\left(\frac{d}{a}\right)^2\approx0.1.$$

It follows from Fig. 2 that in the temperature interval $1\text{K}<T<5$ K the electron spin–lattice relaxation rate is governed mainly by a two-quantum relaxation process involving a two-level system and a phonon from the boson peak region.

[a] E-mail: Lchotor@yahoo.com

[1] The correlation time τ is determined by the correlation function $\langle\delta l_i^z\delta l_i^z(t)\rangle/\langle\delta l_i^z\delta l_i^z\rangle$, where δl_i^z is the fluctuation of l_i^z (Ref. 8).

---

[1] P. Anderson, B. Halperin, and G. Varma, Philos. Mag. **25**, 1 (1972); W. Phillips, J. Low Temp. Phys. **7**, 351 (1972).
[2] T. L. Reinecke and K. L. Ngai, Phys. Rev. B **12**, 3476 (1975); G. Balzer-Jollenbeck, O. Kanert, and J. Steinert, Solid State Commun. **65**, 303 (1988); J. Szeftel and H. Alloul, Phys. Rev. Lett. **34**, 657 (1975).
[3] S. R. Kurtz and H. J. Staplton, Phys. Rev. B **22**, 2195 (1979).
[4] V. K. Malinovskiĭ, V. I. Novikov, and A. P. Sokolov, Sov. Phys. Usp. **163**, 119 (1993) [Sov. Phys. Usp. **36**, 440, 650, 760 (1993)]; V. K. Malinovski and A. P. Sokolov, Solid State Commun. **57**, 757 (1986); A. Fontana and F. Rossi, Phys. Rev. Lett. **78**, 1078 (1997).
[5] N. P. Giorgadze and L. Z. Zakharov, Fiz. Nizk. Temp. **24** 262 (1998) [Low Temp. Phys. **24**, 198 (1998).
[6] A. A. Lebanidze, T. L. Buishvili, and G. R. Kakabadze, Biofizika **42**, 811 (1997).
[7] S. A. Al'tshuler and B. M. Kozyrev, *Electron Paramagnetic Resonance in Compounds of Transition Elements* [Halsted, New York (1975), Nauka, Moscow (1972)].
[8] J. Szeftel and H. Alloul, J. Non-Cryst. Solids **29**, 253 (1978).
[9] D. N. Zubarev, *Nonlinear Statistical Thermodynamics* [Consultants Bureau, New York (1973), Nauka, Moscow (1971)].
[10] I. V. Aleksandrov, *Theory of Magnetic Relaxation* [in Russian], Nauka, Moscow (1975).
[11] G. Grandl and J. Friedrich, Phys. Rev. B **35**, 4915 (1987).

Translated by Steve Torstveit

LOW TEMPERATURE PHYSICS VOLUME 28, NUMBER 6 JUNE 2002

On the correlation of nonperturbative fluctuations of glass-forming liquids and magnetic glasses

A. S. Bakaĭ*

Kharkov Physicotechnical Institute National Research Center, ul. Akademicheskaya 1,
61108 Kharkov, Ukraine

(Submitted February 5, 2002)
Fiz. Nizk. Temp. **28**, 584–594 (June 2002)

Contrary to the established ideas that glasses and glass-forming liquids are homogeneous and isotropic, appreciable structural and compositional heterogeneities are observed in these states. The nature of the heterogeneities in glasses and glass-forming liquids is considered, and the influence of these heterogeneities on the properties of magnetic glasses is examined. Heterophase fluctuations (HPFs), which are nonperturbative disturbances, can play an important role in the thermodynamics of glass-forming liquids, and under certain conditions the liquid has a critical point. The heterogeneities generated in the liquid and glassy states by the HPFs are considered, and the Ginzburg–Landau equations for the HPFs are derived. The order parameter chosen is the fraction of noncrystalline solid-state clusters in the liquid. The correlation length of the order parameter is the characteristic mesoscopic scale of the heterogeneities. The mesoscopic compositional and topological disorder of a glass ‘‘spills over’’ into disorder of its spin system. The phase transitions in the spin system are investigated by well-known approaches with allowance for the mesoscopic heterogeneities. It is shown that correlated domains originating from correlated heterogeneities of the liquid substantially alter the susceptibility and relaxation properties of the paramagnetic state. The phase diagram of a magnetic glass is investigated, and some experimental data are discussed. © *2002 American Institute of Physics.* [DOI: 10.1063/1.1491182]

INTRODUCTION

The topological and compositional disorder of glasses containing magnetic atoms engenders disorder of the spin system. Therefore the theory of the magnetism of glasses is a division of the theory of spin systems with frozen disorder. Because the magnetic interactions are comparatively weak, they have only a slight influence on the glass formation process. Therefore the problem of the magnetism of glasses reduces to two subproblems that can be solved in succession. First one must solve the problem of the formation of a glass from the liquid state. Since a glass inherits the structure of the glass-forming liquid, a theory of the structure of a liquid in the supercooled state is needed. Such a theory should imply a theory of the liquid–glass transition and a description of the structure of the glass. Knowing the structure of the glass, one can set about to solve the second problem—description of its magnetic properties. Clearly the program just outlined is extremely difficult. Essentially one is talking about a theory of phase transitions and phase transformations (with violation of ergodicity) in substantially nonequilibrium and disordered systems. The goal of the present study is to describe a general approach to the solution of the problems and to present the results obtained in the process. We begin in Sec. 1 with a description of the thermodynamics and structure of supercooled liquids and proceed to the properties of disorder in glasses. The theoretical basis for our treatment is provided by the Ginzburg–Landau equations for HPFs, which are a generalization of the equations based on the mean field approximation and presented in Refs. 1–3. Then in Sec. 2, using standard approaches,[4] we consider how the frozen disorder of a glass is manifested in phase transitions of the spin system. We show that a commonality is observed in the approaches to the description of vitrifying liquids and glasses, on the one hand, and disordered spin glasses, on the other. Most importantly, in both cases a governing role is played by heterophase fluctuations (HPFs), which are nonperturbative disturbances of systems with multiple states.

In Sec. 3 we discuss some of the experimental data.

1. HETEROPHASE FLUCTUATIONS IN GLASS-FORMING LIQUIDS

The numerous experimental data have served as a basis for the hypothesis that HPFs (in the form of crystalline and especially noncrystalline solid-state nuclei) play a decisive role in the property of glass-forming liquids and in the liquid–glass transformation process. HPFs are nonperturbative in nature: the ground state of the system, the state of minimum energy, is inhomogeneous. Until recently the theory of HPFs and kinetic processes in which they are involved was based on a droplet approach.[2,3,5,6] Underlying this approach is the assumption that the HPFs exist in the form of compact and noninteracting (mutually isolated) nuclei. In the droplet approach the contribution of HPFs to the free energy near the phase equilibrium line is calculated,[5,7] the kinetics of the evolution of the nuclei is described, and a theory of nucleation and phase transformations is constructed.[8,9] When supplemented with the concept of excluded volume, the droplet approach becomes the Kolmogorov theory of phase transformations.[10] The droplet model is inapplicable for describing the thermodynamics of a heterophase system when the volume fraction of the new phase exceeds about 0.15, and the interaction between ‘‘droplets’’ can no longer be neglected.[3] For states with a large volume fraction of HPFs, a model of interpercolating heterophase clusters has been proposed.[3,11] In those papers the mean field (van der Waals) approximation was used to obtain a criterion for the existence of mesoscopically heterophase states, in which two phases coexist in the form of infinite interpercolating clusters, in the supercritical region. A description of the correlation properties of HPFs can be obtained in the framework of a theory of the Ginzburg–Landau type. Below we present a brief derivation of the Ginzburg–Landau equations for a classical fluctuation field.

As was shown in Refs. 3 and 11, the Gibbs free energy per molecule of a heterophase liquid in the mean field approximation can be written in the form

$$\mu(P,T)=n_s\mu_s(P,T)+(1-n_s)\mu_f(P,T)+n_s(1-n_s)\times\mu_{\text{int}}(P,T)+\frac{k_BT}{k_0}[n_s\ln n_s+(1-n_s)\ln(1-n_s)]. \tag{1}$$

Here n_s is the fraction of molecules belonging to solid-like clusters, μ_s, μ_f, and μ_{int} are the chemical potentials of the molecules in the solid and fluid clusters and in the interphase layer, respectively, k_0 is the associativity parameter, which is approximately equal to the number of molecules in the smallest nucleus, and k_B is Boltzmann's constant (n_s is the order parameter). We note that μ_s and μ_f are the chemical potentials of the ‘‘pure’’ phases with $n_s=1$ and $n_s=0$, respectively.

The phase equilibrium line is determined by the equation

$$\mu_s(P,T)=\mu_f(P,T) \tag{2}$$

Solving this equation for temperature, we find the temperature $T_e(P)$ of phase equilibrium at pressure P. It can be assumed that model (1) is isomorphous to the van der Waals model for a gas–liquid system, and line 2 is analogous to the critical isochore.

It was shown in Refs. 2 and 3 that the position of the critical point on the phase equilibrium line is determined by the equation

$$\mu_{\text{int}}(P,T)=2T_e/k_0 \tag{3}$$

and in the region where

$$0<\mu_{\text{init}}\leqslant 2T_e/k_0 \tag{4}$$

interpercolating solid-like and fluid clusters coexist for $0.15<n_s<0.85$.

For $\mu_{\text{int}}>2T_e/k_0$ a first-order phase transition occurs on the phase coexistence curve (2). If one goes around the critical point through region (4) a continuous transformation of the liquid phase to a noncrystalline solid phase occurs. We stress that a liquid which is heterophase on mesoscopic scales is single-phase and ergodic [with chemical potential (1)] on macroscopic scales.

To obtain an expression for the order-parameter fluctuation field, we introduce a new parameter $\alpha(P,T)$ by the relation

$$\alpha(P,T)=n_s(P,T)-1/2. \tag{5}$$

One can readily see the convenience of the substitution (5) by noting that on the phase equilibrium line the equilibrium value n_s [ensuring the minimum of the free energy (1)] is equal to 1/2.

Treating $\alpha(P,T)$ as a variable that depends on the spatial coordinates and expanding (1) to terms of fourth order in α, we obtain the following expression for the free energy:

$$G(P,T)=v^{-1}\int[a(\nabla\alpha)^2+b\alpha^2+c\alpha^4-h\alpha]dx, \tag{6}$$

where we have taken into account the contribution to the energy from the gradient of the order parameter (v is the specific volume). A standard analysis shows that

$$a=a_0r_0^2(\Delta\rho/\overline{\rho})^2\overline{\varphi}. \tag{7}$$

Here a_0 is a constant of the order of unity, r_0 is the characteristic range of the intermolecular forces ($r_0^3\approx k_0$), $\overline{\varphi}$ is the average binding energy per molecule, $\overline{\rho}$ is the average density, and

$$\Delta\rho=\rho_s-\rho_f \tag{8}$$

is the difference of the densities in the solid and liquid clusters.

Expressions for the remaining coefficients in (6) follow directly from (1):

$$b=2k_0^{-1}T_c-\Delta\mu_{\text{int}}\cong 2k_0^{-1}T_c-\Delta\mu_{\text{int}}(T_e); \tag{9}$$

$$c=2k_0^{-1}T_e/3; \tag{10}$$

$$h=\mu_s-\mu_f\cong(s_f-s_s)(T-T_c). \tag{11}$$

Here s_f and s_s are the entropy per molecule of the liquid and solid fractions.

It is important to note that the ‘‘external’’ field h in the expression for the free energy (6) depends on temperature and goes to zero on the phase equilibrium line. The results of an analysis of the thermodynamic properties of a glass-forming liquid with free energy (6), obtained with the use of the standard approaches in the theory of critical phenomena (see, e.g., Refs. 4 and 12) will be published at a future date. Here we give only the expression for the correlation length R_c, which is the important spatial scale in the critical region:

$$R_c=|b/a|^{-\nu},\quad h\ll h_c(b);$$

$$R_c=|h|^{-\mu},\quad h\gg h_c(b), \tag{12}$$

where

$$h_c(b)=b(b/c)^{1/2}. \tag{13}$$

In spite of the fact that reliable measurements of the thermodynamic quantities have been made only for a comparatively small number of supercooled glass-forming liquids, it can be stated with certainty that the majority of them do not undergo a first- or second-order phase transition upon vitrification, and their glass transition temperature T_g ordinarily lies considerably below the temperature T_e (by 50–80 K). As the temperature is lowered, all of these liquids undergo a continuous phase transformation to the glass, and vitrification sets in when the parameter n_s approaches unity (see Refs. 3 and 13 for more details).

The proximity of the system to the critical point is indicated by the value of the parameter

$$\tau = b/T_e\,. \tag{14}$$

The absence of pronounced features in the behavior of the thermodynamic quantities of the glass-forming liquids above T_g indicates that this parameter is not small for them, e.g., $\tau \approx 10^{-1}$.

To obtain estimates of the remaining coefficients, we set $T_e = 500$ K, $\Delta\rho/\rho = 0.05$, $k_0 = 5$, $\overline{\varphi} = 2$ eV, and $s_f - s_s = 1$. As a result, we find from (13) that $h_c \approx 10^{-1} T_e$. For $(T_e - T_g)/T_e \approx 10^{-1}$, as we see from Eqs. (9)–(11), the following condition is satisfied:

$$h(T_g) \lesssim h_c\,. \tag{15}$$

Therefore, for $T > T_g$ the estimate (12) can be used in the form

$$R_c \approx |b/a|^{-\nu} \approx A r_0. \tag{16}$$

Here the coefficient $A \lesssim 10$. Since r_0 is comparable to the sizes of the molecules, for the chosen numerical values of the parameters the correlation length has a value of up to several nanometers.

The sizes of the solid clusters near T_g are determined by their growth kinetics and growth time. The characteristic sizes of the solid nuclei for $T < T_e$ are greater than or comparable to R_c (i.e., nanometer-sized). As the temperature is lowered, the solid clusters grow, but in view of the slowing of the structural relaxation processes near T_g the system cannot avoid having intercluster boundaries. For this reason glasses inherit a polycluster structure with characteristic cluster sizes $r_{\mathrm{cl}} \sim 10 R_c$. For the values chosen above, r_{cl} has a value of ~ 10 nm.

We see that r_{cl} is genetically related to R_c. Both of these quantities characterize the scales of the structural and compositional heterogeneities of the the glass.

The results of structural studies of metallic glasses with atomic resolution using an ion field microscope[11,14,15] show that all of the glasses studied (of the metal–metal and metal–metalloid types) have structural and compositional heterogeneities with the scales indicated above. Atomically narrow intercluster boundaries are observed, with cluster sizes of ~ 10 nm and with nanometer-size compositional heterogeneities reaching 10%. Evidently, small-radius atoms (e.g., boron in glasses of the Fe–B type) often segregate in the layers near the boundaries.

It can be stated that the notion that the microscopic structure and distribution of the components in glasses is uniform (this is possible for $R_c \to r_0$ and $r_{\mathrm{cl}} \to \infty$) is highly oversimplified and is apparently inapplicable to the overwhelming majority of glasses. The description and analysis of the magnetic properties of glasses should be done with allowance for the structural and compositional heterogeneities discussed above.

2. SPIN ORDERING IN GLASSY MAGNETS

Phase transitions and critical phenomena have been well studied for the case of homogeneous and slightly inhomogeneous crystalline magnets.[12] At the present time substantial progress has been made in understanding the nature of the spin-glass state and paramagnet–spin glass transitions in systems with homogeneous frozen disorder.[16,17] Magnetic glasses, as can be seen from the discussion given above, are spin systems with inhomogeneous frozen disorder. The character of the phase transitions and critical phenomena in such systems can be investigated using the approaches developed in the theory of critical phenomena in spin systems with disorder (see Ref. 4 and the references cited therein). Of particular interest here is the behavior of the system near the paramagnet–ferromagnet (PF) transition point, since here the nonperturbative order-parameter fluctuations engendered by the inhomogeneous disorder play a decisive role both in the order-parameter fluctuations and in the structure of the phase diagram. This state of the spin system above the PF transition temperature is a Griffiths phase.[18,19] As we shall show below, the existence region and the properties of such a state in glasses is determined by the frozen disorder inherited from the liquid phase.

We will be mainly interested in the PF transition, where only one order parameter is important—the average value of the magnetic moment φ. Therefore we can use the mean field approximation (Ising model) and write the free energy in the form

$$F = \int \left[\frac{J}{2} (\nabla \varphi(x))^2 + (T - J)\varphi^2(x) + \frac{1}{4} g \varphi^4(x) - h\varphi(x) \right] d^3x, \tag{17}$$

where

$$g = T/3; \tag{18}$$

J is the value of the spin–spin interactions, and h is the external magnetic field. The average distance between atoms has been set equal to unity.

The frozen disorder is manifested in the fact that the coefficients in the expression for the free energy density are random functions, and because of the compositional and topological heterogeneities their correlation properties are not functions only of the differences of the coordinates.

The value of the interaction J at each site depends on the local topological and compositional disorder, i.e., on the structure of the first coordination sphere. In the clusters the local order is intermediate,[11,20] and that leads to fluctuations of the value of J with a characteristic spatial scale close to the interatomic distance. In addition, as we have said, glasses have an inherent mesoscopic inhomogeneity with a scale of from a few nanometers to tens of nanometers. Because of the significant difference of the scales of the disorder, the random quantity $J(x)$ can be written in the form

$$J(x) = \overline{J}(x) + \tilde{J}(x), \tag{19}$$

where $\tilde{J}(x)$ is a random quantity with zero mean, and

$$\langle \tilde{J}^2 \rangle = \Delta^2(x). \tag{20}$$

The angle brackets here denote averaging over an ensemble of types of local ordering at fixed concentrations of the components. The variation of the composition and character of the local ordering on nanoscales is taken into account by the coordinate dependence of $\overline{J}$ and Δ^2. We note once again that this approach to incorporating the heterogeneities in glasses is justified if the correlation length R_c is much larger than the interatomic distances.

Let us first consider a system with homogeneous microscopic disorder, when $\overline{J}$ and Δ are independent of x. The distribution function of the values of the random interaction parameter is conveniently chosen in the form

$$P(J)=(1-u)\delta(J-J_0)+u\Delta(J+J_0), \tag{21}$$

where

$$u=\frac{1}{2}(1-\sqrt{1-(\Delta/J_0)^2}). \tag{22}$$

It is easy to see that the distribution (21) has a mean value

$$\overline{J}(1-2u)J_0 \tag{23}$$

and a variance Δ^2.

The phase diagram of an Ising magnet with the distribution $P(J)$ of Eq. (21) is described in Ref. 4, for example. If the temperature is measured in units of J_0, then the equation

$$T_c(u)=(1-2u) \tag{24}$$

determines the temperature of the PF transition as a function of u on the segment $0\leqslant u\leqslant u^*$, where u^* is the point at which curve (24) intersects the Nishimori line

$$T_N(u)=\frac{2}{\ln\left(\frac{1-u}{u}\right)}. \tag{25}$$

For $u^*<u\leqslant 1/2$ there is a transition from the paramagnetic phase to the spin glass.

It follows from (24) and (25) that $u^*\approx 0.15$ and $\overline{J}(u^*)/\Delta(u^*)\approx 1$, in good agreement with the phase diagram of a spin system with disorder in the Sherrington–Kirkpatrick model.[16] It is assumed that the point $T_c(u^*)=T_N(u^*)$ is a multicritical point at which the paramagnetic, ferromagnetic, and spin-glass phases are in equilibrium.

Turning to a study of critical phenomena in a spin system with inhomogeneous disorder, we note that as a simplification, J_0 can be assumed constant. In that case $\overline{J}$ and

$$\Delta=2[u(1-u)]^{1/2}=2(u)^{1/2} \tag{26}$$

depend only on u. In Eq. (26) we have taken into account that $u<u^*\ll 1$. It is this quantity that we shall consider random and spatially inhomogeneous.

In view of what we have said, the equation for the equilibrium distribution of the field $\varphi(x)$,

$$\frac{\delta F}{\delta\varphi}=0 \tag{27}$$

takes on the following form (here Δ is the Laplacian operator):

$$(\overline{J}+\tilde{J})\Delta\varphi+(T-\overline{J}-\tilde{J})\varphi+g\varphi^3=h. \tag{28}$$

Here we will be interested mainly in effects associated with the nanoscale heterogeneities inherited from the liquid state. Averaging (28) over the small-scale inhomogeneities, we obtain

$$\overline{J}(x)\Delta\varphi+[T-\overline{J}(x)]+g\varphi^3=h. \tag{29}$$

Separating out in $\overline{J}(x)$ the average value $\langle\overline{J}\rangle$, we find

$$\overline{J}(x)=\langle\overline{J}\rangle+\delta\overline{J}(x)\equiv T_c+\delta\overline{J}, \tag{30}$$

where $\delta\overline{J}(x)$ is a random function with zero mean, and the characteristic scale for variation of r_c is

$$r_{\text{cl}}>r_c\geqslant R_c. \tag{31}$$

The quantity $\delta\overline{J}$ is small compared to $\langle\overline{J}\rangle$, as are the mesoscopic fluctuations of the composition, which, according to available estimates (see the previous Section), is $\leqslant 0.1$. This quantity can be neglected in the first term on the left-hand side of (28) but not in the second term, since we are interested in the temperature region near T_c, where the fluctuations $\delta\overline{J}$ are not small but can exceed $T-T_c$. In view of what we have said, we write (28) in the form

$$\Delta\varphi+[\tau+\delta\tau(x)]\varphi+g_1\varphi^3=h_1. \tag{32}$$

Here

$$\tau=\frac{T-T_c}{T_c};\quad \delta\tau(x)=\frac{\delta\overline{J}(x)}{T_c};$$

$$g_1=g/T_c;\quad h_1=h/T_c. \tag{33}$$

We shall assume that $\delta\tau(x)$ is "coarse-grained" (condition (31) holds) and is described by a Gaussian distribution:

$$P(\delta\tau)=p_0\exp\left\{-\frac{1}{4\overline{\Delta}^2 r_c^3}\int[\delta\tau(x)]^2 d^3x\right\},$$

$$\overline{\Delta}^2=\langle\delta\overline{J}^2\rangle/T_c^2. \tag{34}$$

Formally Eqs. (32)–(34) reproduce the model of critical phenomena in spin systems with disorder, which was considered in Ref. 4, for example. An important difference, however, is the "coarse-grained" nature of the disorder, on account of which, for

$$\tau\leqslant\overline{\Delta}, \tag{35}$$

the mesoscopic disorder plays the dominant role in the critical phenomena.

The fluctuations of the concentrations of the components of a glass ordinarily determine the value of $\delta\overline{J}$. Therefore, for making estimates of $\delta\overline{J}$ one can use the approximate expression

$$\delta\overline{J}=\sum_i \delta c_i\partial\overline{J}/\partial c_i=\sum_i \delta c_i\partial T_c/\partial c_i, \tag{36}$$

where δc_i is the deviation of the concentration of the ith component from the average value.

Essentially, as the temperature is lowered, islands (magnetic clusters) in which

$$\overline{(\varphi^2)}-\overline{\Delta}/g$$

appear in the system and increase in number and size. The islands interact, and at a certain temperature close to T_c, long-range order is established in the spin system, i.e., a PF transition occurs (or a transition to the spin-glass state). The region where $\overline{\varphi^2}$ is nonzero, determined by condition (35), in finite regions has characteristic dimensions of the order of r_{cl}.

The state of the system having the properties described above is called the Griffiths phase. The characteristic properties of this phase are singular behavior of the susceptibility and time correlation function.[18,19] Below we shall follow the description of these quantities given in Ref. 19, with the coarse-grained heterogeneities taken into account.

The time correlation function is known to be well approximated over a wide interval of relaxation times by Kohlrausch's law:

$$C(t)=\langle\varphi(t)\rangle\sim\exp[-(t/\tau_c)^{\alpha}], \tag{37}$$

where τ_c is the characteristic scale of the relaxation time and $\alpha<1$ is the Kohlrausch exponent. We see that for $\alpha\neq 1$ Kohlrausch's law reflects the multiplicity of relaxation times.

The time scale for variations in the orientation of the moment of a compact magnetic island, where $\delta\tau<0$, depends on the size of the island:

$$t_c(L)\sim L^3\overline{\varphi^2}. \tag{38}$$

Here L is the linear dimension of a cluster (we are talking about a three-dimensional system).

Therefore the spectrum of relaxation times is determined by the size distribution function of the clusters, $P(L)$. In a coarse-grained magnet

$$P(L)\propto\exp[-c(p)(L/r_c)^3]. \tag{39}$$

Here p is the volume fraction of clusters in which $\delta\tau<0$, and

$$c(p)\propto\ln(1/p). \tag{40}$$

Equations (38) and (39) imply the following expression for the spectrum of relaxation times:[19]

$$\rho(t_c)\propto\int P(L)\,\delta(t-t_c(L))\,dL\propto\exp(-ct_c/r_c^3\overline{\varphi^2}), \tag{41}$$

and the long-time asymptotics of the correlation function $c(t)$:

$$\begin{aligned} c(t)\big|_{t\to\infty}&\propto\int\rho(t_c)t_c^{-1}\exp(-t/t_c)\,dt_c\\ &\propto\exp[-2(ct/r_c^3\overline{\varphi^2})^{1/2}]. \end{aligned} \tag{42}$$

We see that $\alpha=1/2$ in the model chosen. The value of α depends substantially on the form of the size distribution of the clusters. In particular, for a Gaussian distribution

$$P(L)\propto\exp[-(L-\overline{L})^2/2\lambda^2] \tag{43}$$

and for $\overline{L}\gg\lambda$ it is easy to find that

$$C(t)\propto\begin{cases}\exp(-t/\overline{t_c}) & \overline{t_c}<t<\tau_c\\ \exp[-(t/\tau_c)^{0.4}] & t>\tau_c\end{cases}, \tag{44}$$

where

$$\overline{t_c}\propto\overline{L}^3\varphi^2,\quad \tau_c\propto\left(\frac{\lambda}{L}\right)^2 t_c. \tag{45}$$

It should be noted that the correlation function (44) is of the same form as the pair correlation function proposed in Ref. 19, which describes relaxation in vitrifying liquids and other complex systems having a broad relaxation spectrum.

We see that the model (32), (34), supplemented by the distributions (39) and (43), gives realistic intermediate and long-time asymptotic behavior of the correlation function and reasonable estimates of the Kohlrausch exponent α.

The magnetic susceptibility of a finite cluster, $\chi(L)$, is proportional to $t_c(L)$, so that one may use distribution (39) for elucidating the behavior of this quantity in the existence region of the Griffiths phase. We then find that

$$\chi\propto[c(p)]^{-3}, \tag{46}$$

and, since $c(p)$ goes to zero for $T\to T_c$ (as $\ln p|_{p\to 1}$), the function χ has a singularity at the critical point, but the character of this singularity is not universal (as it is for systems with homogeneous disorder) and depends substantially on the distribution of the heterogeneities.

Magnetized clusters can be treated as supermagnetic particles, and with additional assumptions about the intercluster interactions in the critical region one can calculate the magnetic susceptibility, heat capacity, relaxation spectrum, etc. Here the size distribution of the clusters (in particular, the average size of a cluster) and the average magnetization are the most important quantities. This approach is also widely used in analysis of the properties of amorphous magnets (Ref. 21 and the literature cited therein).

3. DISCUSSION

It is commonly assumed that the physics of glasses and spin systems with disorder, despite the similarity of a number of their properties, e.g., multiplicity of structural states, violation of ergodicity, and the broad spectrum of relaxation times, including extremely long ones, do not share a common constructive basis for the reason that supercoooled liquids have a self-consistent (thermodynamically equilibrium, although metastable) disorder, whereas the disorder of spin systems is frozen in, and in them the problem reduces to one of studying the thermodynamics and dynamics of systems with a stationary disorder, independent of temperature and pressure.

For this reason, despite the great diversity of opinions as to the connection between the vitrification process and phase transitions and critical phenomena,[16] the discussion of the nature of the liquid–glass transition and of the structure and properties inherited by the glass is based on heuristic and phenomenological models whose domains of applicability are unclear.

A theory of heterophase fluctuations in vitrifying liquids, as we have seen, can be formulated in the framework of the Ginzburg–Landau approach. On the one hand, this enables one to establish a constructive connection between the liquid–glass transition and phase transitions and, in particular, the theory of critical phenomena. And, on the other hand, it reveals a connection between the theory of phase transformations and phase transitions in vitrifying liquids and spin systems with disorder. In the self-consistent field approximation the latter can be described in the framework of the Ising model with random coefficients, which, as we know, has much in common with the Ginzburg–Landau equations.

It is clear that HPFs in the region described by Eq. (4) have a nature reminiscent of compact clusters of a Griffiths phase. The fundamental difference is that the HPFs, unlike the heterogeneities of the Griffiths phase, and not "frozen": they appear, change structure, and disappear. It is noteworthy that the heterogeneities of glasses due to heterophase fluctuations of the liquid inevitably leads to the existence of a Griffiths phase in the spin system. We note that the scale and statistical characteristics of the HPFs are inherited by the Griffiths phase of the spin system [see Eqs. (31) and (34)]. Furthermore, the multiplicity of relaxation times in the liquid and Griffiths magnetic phase have the same genetic roots—the structure of HPFs in the liquid.

We note that the manifestation of microscopic disorder in critical phenomena, in particular, in Griffiths effects, is substantially different from the manifestations of large-scale heterogeneities. The temperature region in which the Griffiths phase exists in the presence of microscopic disorder lies between T_0 and T_c (T_0 is the temperature of the PF transition in the absence of disorder), but spin-glass effects engendered by the frozen microscopic disorder are manifested only relatively close to T_c, for[4]

$$\tau \leqslant \tau_d = \exp(-\text{const}/\Delta^2) = \exp(-\text{const}/4u(1-u)). \tag{47}$$

Since the PF transition occurs for $u < u^* \approx 0.15$, we have $\Delta^2 \leqslant 0.45$, so that the microscopic disorder is extremely important only near a multicritical point, i.e., for $u \approx u^*$. The coarse-grained disorder leads to appreciable Griffiths effects even for $\tau \sim \overline{\Delta}$. The value of $\overline{\Delta}$ [which is clearly of order δc_i; see Eq. (39)] can be considerably larger than τ_d on the whole PF transition line, except, possibly, in the neighborhood of the multicritical point. Consequently, it is the coarse-grained disorder that plays the main role in the Griffiths effects, in particular, in the structure of the spectrum of relaxation times and the behavior of the magnetic susceptibility.

Figure 1 shows a schematic illustration of the phase diagram of a glassy magnet on the (T,u) plane. The diagram shows the lines bounding the stability regions of the paramagnetic, ferromagnetic, and spin-glass phases; the Nishimori line $T_N(u)$ (25); and the lines $T_c^*(u) = T_c \times \exp[-\text{const}/u(1-u)]$ and $T_{c,\text{meso}}^*(u) = T_c(1+\overline{\Delta})$. The line $T_c(u)$ defines the region in which there are substantial manifestations of nonperturbative fluctuations in the fine-scale disorder, while the second line, $T_{c,\text{meso}}^*(u)$, is its counterpart for the coarse-grained disorder. We see that the width of the region in which nonperturbative disturbances play the dominant role depends substantially on the character of the distribution of magnetic impurities.

As a useful example of a spin system with disorder in a glass, let us discuss, in the light of the theory developed above, the properties of the magnetic metallic glasses Fe–Zr, which have been studied in some detail in numerous experiments and are widely discussed in the literature.[21–24]

A remarkable property of this family of glasses is that when the Zr concentration x is changed from 0.12 to 0.07, the temperature of the phase transformation from the paramagnetic to the ferromagnetic phase changes from 255 to 105 K, and at $x = 0.07$ and $T = 105$ K there is a paramagnet–spin glass transition.

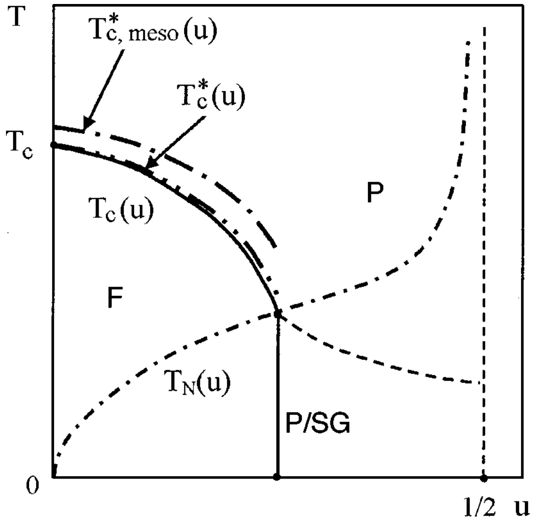

FIG. 1. Phase diagram of a glass-forming magnetic alloy on the (T,u) plane, showing the regions of stability of the paramagnetic phase (P), the paramagnetic and/or spin-glass phase (P/SG), and the ferromagnetic phase (F) and the PF transition line $T_c(u)$ and the Nishimori line $T_N(u)$. Between the lines $T_c^*(u) = T_c \exp[-\text{const}/u(1-u)]$ and $T_c(u)$ there exists a region of strong fine-scale nonperturbative fluctuations with $\overline{\Delta} = 0$, and between the lines $T_c(u)$ and $T_{c,\text{meso}}(u) = T_c(1+\overline{\Delta})$ is a region of coarse-grained nonperturbative fluctuations engendered by the mesoscopic concentrational inhomogeneity of the magnetic impurities.

At $c = 0.1$ the temperature T_c is equal to 225 K, and at $c = 0.08$ one has $T_c = 174$ K. In the light of the above discussion (see Fig. 1) it can be assumed that the multicritical point lies at $c \approx 0.07$. We see that the function T_c is nonlinear even in a comparatively narrow interval of Zr concentrations, and in using formula (23) for the average value of the spin–spin interaction $\overline{J}$ one should therefore take into account the weak dependence of J_0 on c, if it is assumed that u is proportional to c.

To estimate $\overline{\Delta}$ as a function of the zirconium concentration we use expression (36), assuming that $\delta c/c = 0.1$, which is a characteristic measure of the nanoscale heterogeneities in metallic glasses, as has been established in ion microscope studies.[11,14,15] The derivative $\partial T_c/\partial c$ can be determined from the experimental values of $T_c(c)$ given above. As a result, we find that $\overline{\Delta}(0.07) \approx 0.5$ and $\overline{\Delta}(0,1) \approx 0.11$. This means that for $c = 0.07$ the Griffiths effects should be manifested noticeably in a temperature interval 50 K in width above T_c, while for $c = 0.1$ this width would be 25 K.

In Ref. 22 a spin-cluster model was developed for amorphous iron–zirconium alloys. Assuming that compact clusters have a volume distribution, the authors employed the Néel theory, which describes the behavior of the properties of fine magnetic particles, and then, making a comparison with the experimental data, established the temperature dependence of the cluster parameters near T_c for different zirconium concentrations. It was found that near T_c the cluster size is $\leqslant 10^4$ atoms per cluster (this corresponds to $r_c \approx 3-5$ nm), and the cluster effect is observed up to temperatures of 60 K above T_c for $c = 0.07$ and 25 K above T_c for $c = 0.1$. We see that the characteristic scales of the heterogeneities of the liquids and glasses given above are in good agreement with the estimates obtained in Ref. 22.

In studies of the density fluctuations in one-component molecular vitrifying liquids, a number of authors[26–28] have observed the presence of large-scale ($\sim 10^2$ nm) correlations of these fluctuations. The characteristic appearance time of the long correlations (the formation of a Fischer cluster) was found to be many orders of magnitude larger than the characteristic time for rearrangement of the molecular configurations (the α relaxation time). In Ref. 29 a theory of large-scale fluctuations in vitrifying liquids was proposed, according to which the formation of a Fischer cluster occurs in the following way. It has been shown that HPFs have correlations of the short-range topological order on scales $\sim R_c$, i.e., over distances comparable to the correlation length of the order parameter. There exist many types of short-range ordering of molecules. A quantitative measure of the multiplicity of types of short-range order of HPFs is the configurational entropy. Thus the correlated domains of size $\sim R_c$ differ in the type of short-range topological order. It is shown in Ref. 29 that the formation of correlated domains with the same type of short-range order of the fractal agglomerates with large correlation lengths $\sim 10^2 R_c$ is energetically favorable. This is what leads to the formation of a Fischer cluster.

The formation of large-scale Fischer clusters can also occur in multicomponent metallic glass-forming melts. Since the topological and compositional short-range order are intimately related, one expects that in a multicomponent melt the correlated domains will also differ in the short-range compositional order. Therefore, in a multicomponent liquid the Fischer cluster consists of fractal aggregates formed by these correlated domains with different short-range compositional order. These large-scale fractal structures are preserved upon vitrification, and their presence can have a substantial influence on the conductivity and magnetic characteristics of glasses. Since the magnetic properties of a correlated domain are determined by the short-range topological and compositional order, if magnetic ordering occurs in one correlated domain it should spread to the whole fractal aggregate, so that the character, value, and correlation length of the magnetic order depend substantially on the correlation length of the Fischer cluster. Furthermore, the presence of a Fischer cluster in a glass should give rise to slow relaxation modes in the paramagnetic state due to the variation of the orientation of the magnetic moments in those aggregates in which magnetic ordering has occurred.

Because the formation time of a Fischer cluster is very long compared to the characteristic α relaxation time, its structure and size depend substantially on the thermal prehistory of the glass, in particular on the hold time of the melt in the normal or supercooled state and the quenching rate. In a study of the magnetic properties of a Nd–Fe–B–Co–Al alloy in the glassy and crystalline states[30] it was observed that at room temperature the crystalline samples are paramagnetic, whereas the alloy in the glassy state is ferromagnetic, and its magnetic properties depend substantially on the thermal prehistory. The magnetic hardness of the glass is 30 times higher in the case of slow cooling of the melt than for fast cooling. Thus, depending on the cooling rate a glassy alloy of the same composition can be magnetically soft or hard. The authors assume that during slow cooling there is sufficient time for the formation of clusters, which lend magnetic hardness to the glass. Because there are as yet no data on the structure of these clusters, they cannot at present be identified as Fischer clusters.

Similar phenomena have also been observed in other metallic glasses.[31,32]

4. CONCLUSION

The theory developed for the heterophase fluctuations in vitrifying liquids allows one to trace the evolution of their structure during vitrification and to establish the characteristics of the frozen disorder of the spin system of the glass. The most eloquent expression of this disorder is seen in the Griffiths effects in critical phenomena, where the width of the temperature interval in which these effects are important is determined mainly by the large-scale heterogeneities of the glass, which are inherited from the liquid.

The similarity of the formalism used in the description of the HPFs in liquids and critical phenomena in spin systems with disorder reveals the unity of the physics of the both effects.

The width of the region on the (T,u) plane in which nonperturbative fluctuations are dominant, and the relaxation processes that occur in this region, depend substantially on the character of the distribution of concentrational heterogeneities in the glass; because this distribution is inherited from the liquid state, a study of those processes in the glass can yield information about the HPFs in the glass-forming liquid.

The theory developed here can provide an explanation of the experimental data on the magnetic properties of metallic glasses.

This work was supported in part by the STCU, Project 655.

*E-mail: bakai@kipt.kharkov.ua

---

[1] A. S. Bakaĭ, Fiz. Nizk. Temp. **20** 469, 477 (1994) [Low Temp. Phys. **20**, 373, 379 (1994)].

[2] A. S. Bakaĭ, Fiz. Nizk. Temp. **22**, 956 (1996) [Low Temp. Phys. **22**, 733 (1996)].

[3] A. S. Bakaĭ, Fiz. Nizk. Temp. **24**, 27 (1998) [Low Temp. Phys. **24**, 20 (1998)].

[4] V. S. Dotsenko, Usp. Fiz. Nauk **165**, 481 (1995).

[5] Ya. I. Frenkel', Zh. Éksp. Teor. Fiz. **9**, 95 (1939); Ya. J. Frenkel, *Kinetic Theory of Liquids*, Clarendon Press, Oxford (1946).

[6] M. E. Fisher, Physica **3**, 255 (1967).

[7] A. R. Ubbelohde, *Melting and Crystal Structure*, Clarendon Press, Oxford (1965).

[8] M. Volmer and A. Weber, Z. Phys. Chem. **119**, 227 (1925).

[9] Ya. B. Zel'dovich, Zh. Éksp. Teor. Fiz. **12**, 525 (1942)].

[10] A. N. Kolmogorov, Izv. AN SSSR Ser. Mat. **3**, 355 (1937).

[11] A. S. Bakaĭ, *The Polycluster Concept of Amorphous Solids in Glassy Metals III*, edited by H. Beck and H.-J. Güntherodt, Springer, Heidelberg (1994).

[12] A. Z. Patashinskiĭ and V. L. Pokrovskiĭ, *Fluctuation Theory of Phase Transitions* [translation of 1st Russ. ed.], Pergamon Press, Oxford (1979), Nauka, Moscow (1982).

[13] E. W. Fischer and A. S. Bakaĭ, in *Slow Dynamics in Complex Systems*, AIP Conference Proceedings **469**, 325 (1999).

[14] A. S. Bakaĭ, V. V. Kul'ko, I. M. Mikhajlovskij, V. B. Rabukhin, and O. A. Velikodnaya, J. Non-Cryst. Solids **182**, 135 (1995).

[15] A. S. Bakaĭ, N. Vanderka, M. P. Makht, I. M. Mikhaĭlovskiĭ, and T. I. Mazilova, Metallofiz. Nov. Tekhnol. **20**, 58 (1998).
[16] K. Binder and A. P. Young, Rev. Mod. Phys. **58**, 81 (1986).
[17] V. S. Dotsenko, Usp. Fiz. Nauk **163**, 455 (1993).
[18] R. Griffiths, Phys. Rev. Lett. **23**, 17 (1969).
[19] A. J. Bray, Phys. Rev. Lett. **59**, 586 (1987).
[20] A. S. Bakaĭ, *Polycluster Amorphous Solids* [in Russian], Énergoatomizdat, Moscow (1987).
[21] K. L. Ngai, *Disorder Effects on Relaxation Processes*, edited by R. Richert and A. Blumen, Springer-Verlag, Berlin, Heidelberg (1994), p. 89.
[22] L. F. Kiss, T. Kemeney, I. Vincze, and L. Granasy, J. Magn. Magn. Mater. **135**, 161 (1994).
[23] H. Hiroyoshi and K. Fukamichi, Phys. Lett. **85A**, 242 (1981).
[24] D. H. Ryan, J. O. Strom-Olsen, R. Provencher, and M. Towensend, J. Appl. Phys. **64**, 5787 (1988).
[25] D. Kaptas, T. Kemeney, L. F. Kiss, J. Balogh, L. Granasy, and I. Vincze, Phys. Rev. B **46**, 6600 (1992).
[26] E. W. Fischer, Physica A **201**, 183 (1993).
[27] A. Patkowski, E. W. Fischer, W. Steffen, H. Glaeser, M. Baumann, T. Ruths, and G. Meier, Phys. Rev. E **63**, 061503 (2001).
[28] A. Patkowski, Th. Thurn-Albrecht, E. Banachowicz, W. Steffen, T. Narayan, and E. W. Fischer, Phys. Rev. E **61**, 6909 (2000).
[29] A. S. Bakaĭ, J. Non-Cryst. Solids (to be published).
[30] L. Q. Xing, J. Eckert, W. Loeser, S. Roth, and L. Schultz, J. Appl. Phys. **88**, 3565 (2000).
[31] A. Inoue, T. Zhang, A. Takeuchi, and W. Zhang, Mater. Trans., JIM **37**, 636 (1996).
[32] J. Ding, Y. Li, and X. Z. Wang, J. Phys. D **32**, 713 (1999).

Translated by Steve Torstveit

LOW TEMPERATURE PHYSICS VOLUME 28, NUMBER 6 JUNE 2002

Dynamical chaos and low-temperature surface diffusion of small adatom clusters

A. S. Kovalev*

B. Verkin Institute for Low Temperature Physics and Engineering, National Academy of Sciences of Ukraine, pr. Lenina 47, 61103 Kharkov, Ukraine

A. I. Landau

Mivza Berosh 11/24, Beer Sheva 84799, Israel

(Submitted February 13, 2002)
Fiz. Nizk. Temp. **28**, 595–603 (June 2002)

The nonlinear one-dimensional dynamics of diatomic adatom clusters on an atomically grooved crystal surface is investigated by a numerical simulation method. It is shown that for initial conditions such that a given dynamic Hamiltonian of the system possesses chaotic behavior in phase space, the dynamical chaos is manifested in the coordinate space as diffusive motion of the cluster. The process investigated is fundamentally different from ordinary thermal diffusion and can apparently be manifested at low temperatures. © *2002 American Institute of Physics.* [DOI: 10.1063/1.1491183]

INTRODUCTION

The study of the chaotic behavior of dynamical models with a finite number of degrees of freedom and, in particular, nonintegrable Hamiltonian systems, is one of the new fields of theoretical and mathematical physics. It is known[1] that even in the case of conservative nonlinear systems with two degrees of freedom in the absence of a second integral of the motion (besides the energy) the dynamics of a particle for some initial conditions can have a complex, chaotic character.[2] Here, however, one usually studies the dynamics of a system in a finite region of phase space and does not discuss the question of the macroscopic manifestation of that chaotic behavior.

In this paper we investigate the one-dimensional dynamics of a diatomic cluster on the surface of an ideal crystal as an example of a nonlinear dynamical system with two degrees of freedom which admits infinite motion in configuration space, and we consider the question of the possibility of diffusive motion of such a cluster at low temperatures and the connection between the diffusive regime and dynamical chaos in phase space.

Numerous experiments[3,4] on the surface adsorption of atoms of alkali (Li, Na, K, Cs) and alkaline earth (Mg, Sr, Ba) elements on the atomically grooved faces of W, Mo, Re, Ni, and Si and also on surface steps have shown that adsorbed atoms (adatoms) occupy positions in the grooves and around the steps and move mainly along them. That is, the motion (in particular, diffusion) of adatoms carries a predominantly one-dimensional character. At low coverages a gas of isolated adatoms forms on the surface. However, because of the complex character of the interaction of adatoms via a metallic substrate, with increasing density of adatoms on the surface, first (at low coverages) one-dimensional clusters of 2–6 adatoms form, and then whole chains, periodically arranged at large distances from one another. These linear clusters and chains are oriented either perpendicular to the grooves (in the case of W, Mo, and Re substrates) or along the grooves (on the Ni and Si surfaces) and along atomic steps on the surface. However, in all of the cases mentioned, the motion of these objects occurs along the grooves and, regardless of the orientation of the clusters, can be described in the framework of similar one-dimensional models.

The diffusion of adatoms and adatom clusters has a number of unusual features.[5–7] In particular, the diffusion coefficient depends strongly (and nonmonotonically) on the coverage,[4] undoubtedly because of an interaction between adatoms, and can depend substantially on the mechanism for the formation and change in size of the clusters. On the other hand, the experimental observation of rapid (nondiffusive) motion of very large metallic clusters along a graphite surface was reported in Ref. 8. The theoretical study of the structure and dynamics of one-dimensional atomic chains of finite length has been the subject of a large number of papers.[9–11] In particular, a soliton mechanism for the motion of finite-length clusters was proposed in Ref. 9.

Ordinarily the diffusive motion of adatoms and clusters is due to their interaction with the substrate: adatoms suffer random impacts from thermal phonons in the bulk of the substrate. As the temperature is lowered and the bulk excitations are frozen out, the coefficient of ordinary diffusion falls off linearly with the decreasing temperature, and diffusion of this kind ceases. It remains possible to have regular (vibrational or drift) motion of individual adatoms excited in rare collisions with phonons or under the influence of external irradiation.

In this paper we consider the possibility of a fundamentally different mechanism of cluster diffusion, which arises at the transition from isolated adatoms to small adatom complexes as the degree of coverage increases. In the excitation of an isolated atom at $T=0$ in the absence of dissipation, only its regular motion is possible. However, as will be shown below, when atomic complexes are excited, they can undergo stochastic motion, leading to diffusion. This ‘‘anomalous’’ diffusion of complexes, which is nonzero even at zero temperature and which is absent for individual atoms, should be observed as the coverage of the substrate increases.

From the standpoint of the theory of nonlinear regular and stochastic dynamics, this problem is also of fundamental significance. As a rule, fundamental questions of stochastic dynamics of Hamiltonian systems are considered for examples of conservative systems with two degrees of freedom. It is assumed that the stochastic regime arises as a result of instability of the motion of a system in a bounded region of phase space. Our model allows the unbounded displacement of the center of mass (CM) of the adatom complex in coordinate space, and we can consider the fundamental question of the connection between the chaotic character of the dynamics of a mechanical system with diffusional motion of the CM of this complex. We note that for the aforementioned experiments on the surface diffusion of adatom complexes the ideal model is that of coupled mathematical oscillators: the atoms lie along grooves on the surface, and their motion is of a one-dimensional character, and the periodic potential created along the grooves by the atomic structure of the substrate can be modeled by a trigonometric function.

FORMULATION OF THE MODEL

We shall investigate the one-dimensional motion of a diatomic complex. For simplicity we consider the case when the atoms of the cluster move strictly along the grooves on the surface of the crystal, and in equilibrium the cluster is oriented in the direction perpendicular to the grooves (Fig. 1). (The one-dimensional model more realistically describes the situation when the adatom complex is oriented along the grooves. However, then the possible ‘‘jumping’’ of the atoms through each other at high energies becomes a problem. Therefore, in the that case the results which we obtain are applicable only at energies that are not too high. However, was will be shown below, this energy interval is one with several important scenarios of cluster motion.) We denote the coordinates of the atoms as X_1 and X_2 and restrict consideration to a harmonic interatomic interaction and a sinusoidal substrate potential relief for each atom. The total energy of such a system has the form

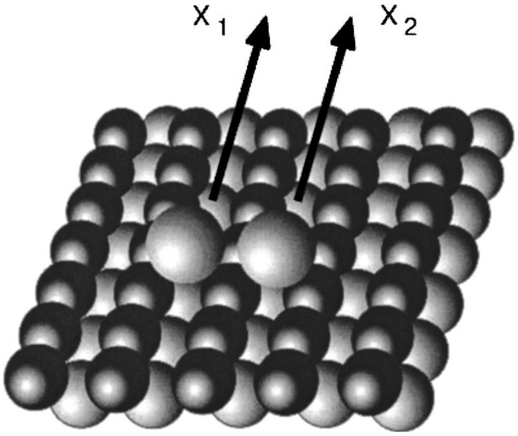

FIG. 1. Diatomic complex on an atomically grooved surface of a crystal.

$$\tilde{E}=\sum_{i=1}^{2}\left\{\frac{m}{2}\left(\frac{dX_i}{dt}\right)^2+U_0\left[1-\cos\frac{2\pi X_i}{a}\right]\right\}+\frac{\alpha}{2}(X_1-X_2)^2, \tag{1}$$

where m is the mass of the atoms, U_0 is the amplitude of the substrate potential, and α is a characteristic of the interatomic interaction in the cluster. The equilibrium state of the diatomic ‘‘molecule’’ corresponds to the values $X_1=X_2=na$. The parameters α and U_0 can be associated with the respective frequencies $\omega_0=\sqrt{2\alpha/m}$ and $\omega_1=\sqrt{U_0/m}$. We shall assume below that the frequencies ω_0 and ω_1 are of the same order of magnitude. The system of dynamical equations has the form

$$m\frac{d^2X_1}{dt^2}+\frac{2\pi U_0}{a}\sin\frac{2\pi X_1}{a}+\alpha(X_1-X_2)=0, \tag{2}$$

$$m\frac{d^2X_2}{dt^2}+\frac{2\pi U_0}{a}\sin\frac{2\pi X_2}{a}+\alpha(X_2-X_1)=0. \tag{3}$$

If the displacements are measured in units of the interatomic distance, $x_i=X_i/a$, and the time in units of $\sqrt{2}/\omega_0$, then the only remaining parameter is the dimensionless quantity $A=(\omega_1/\omega_0)^2/\pi$, which determines the ratio of the energy of interaction with the substrate to the energy of interactions within the cluster. All of our numerical calculations were carried out for a value $A=1$, although the case $A\gg 1$ is very interesting: in that case the dynamics of the system should have traits similar to the stochastic motion in the ‘‘Lorentz gas’’ model. In the case under discussion, Eqs. (2) and (3) can be written in dimensionless form as

$$\frac{d^2x_1}{dt^2}=(x_2-x_1)-\sin(2\pi x_1), \tag{4}$$

$$\frac{d^2x_2}{dt^2}=(x_1-x_2)-\sin(2\pi x_2), \tag{5}$$

and we introduce a dimensionless energy

$$E=\tilde{E}/E_*=\sum_{i=1}^{2}\left\{\frac{1}{2}\left(\frac{dx_i}{dt}\right)^2+\frac{1}{2\pi}[1-\cos(2\pi x_i)]\right\}+\frac{1}{2}(x_1-x_2)^2, \tag{6}$$

where $E_*=\alpha a^2$.

The energy (6) is the only integral of motion of the dynamical system (4), (5), which has two degrees of freedom. Since there is no second integral, the system admits stochastic behavior.[1]

A fragment of the topography of the potential energy surface $U(x_1,x_2)$ corresponding to Eq. (6) is shown in Fig. 2. The simultaneous motion of the diatomic cluster can be represented as two-dimensional motion of a particle with respect to this potential energy surface (PES). The absolute minima of the energy correspond to the points $x_1=x_2=n$ with zero energy. Besides these there exist relative minima of the PES at the points $x_1\approx 1/2\pm 0.368+n$ and $x_2\approx 1/2\mp 0.368+n$, with energy $E_0\approx 0.374$. (The values of all the characteristic energies are given for $E=\tilde{E}/E_*$ [see Eq. (6)].

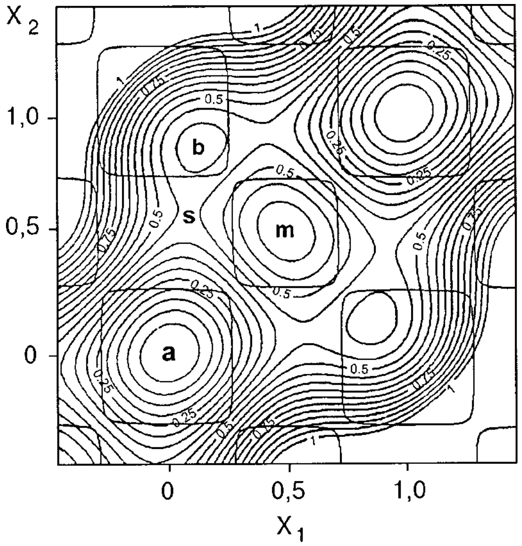

FIG. 2. Topography of the potential energy surface of the system. The singular points correspond to absolute minima (a), relative minima (b), relative maxima (m), and saddles (s). The closed, nearly square contours with sides parallel to the axes correspond to zero Gaussian curvature of the potential energy surface.

The local maxima of the PES correspond to the points $x_1 = x_2 = n + 1/2$, with energy $E_m = 2/\pi \approx 0.637$. When this energy is exceeded, the purely "drift" motion with $x_1 = x_2$, in which internal vibrations of the cluster are not excited, becomes possible. Lying between the minima of the PES are saddle points at $x_1 = 1/12 + n$, $x_2 = 7/12 + n$; $x_1 = 7/12 + n$, $x_2 = 1/12 + n$; $x_1 = 11/12 + n$, $x_2 = 5/12 + n$; and $x_1 = 5/12 + n$, $x_2 = 11/12 + n$, with energy $E_s = 1/\pi + 1/8 \approx 0.443$. This value of the energy plays an important role in the dynamics of a cluster: at energies $E < E_s$ only vibration of the cluster is possible, and it is only for $E > E_s$ that infinite displacement of the dimer becomes possible. When the energy is slightly above E_s the image point executes a zig-zag motion through the saddle points, amounting to a one-dimensional "express" motion of the diatomic complex. Finally, a very important value of the energy is E_t, at which the region in (x_1, x_2) space that is accessible for the motion of the dimer begins to intersect with the region of negative Gaussian curvature of the PES, in which $K = (rt - s^2)(1 + p^2 + q^2)^{-2} < 0$, where $r = \partial^2 U/\partial x_1^2$, $t = \partial^2 U/\partial x_2^2$, $s = \partial^2 U/\partial x_1 \partial x_2$, $p = \partial U/\partial x_1$, and $q = \partial U/\partial x_2$. The lines of zero curvature of the PES in Fig. 2 have a nearly square shape with edges parallel to the x_1 and x_2 axes. (The energy E_t is related to the Toda criterion for the onset of stochastization of the motion in nonintegrable nonlinear dynamical systems.[12,13]) For our choice of parameters, $E_t \approx 0.2$. We have done a numerical simulation of the motion of a diatomic complex with energies $E \geqslant 0.5$. At such energies the infinite displacement of the dimer has become possible, and the trajectory "takes in" the region of negative curvature of the PES, and that can lead to stochastic motion.

At low energies $E \ll E_t$, according to the Kolmogorov–Arnold–Moser theory,[14] the overwhelming majority of initial conditions lead to regular dynamics of the cluster: the only motions that occur are a relative vibrational motion of the atoms in the dimer and a vibrational motion of its CM relative to the potential relief. When the energy E_t is exceeded, the weight of initial conditions that lead to chaotic motion begins to grow rapidly. In the interval $E_t < E < E_s$, however, the motion occurs in a bounded region of coordinate space. Here the average values of the CM coordinate $x = (x_1 + x_2)/2$ and CM velocity $v = (v_1 + v_2)/2$ of the dimer are equal to zero, while the rms deviation of the CM does not exceed the interatomic distance (the unit for the dimensionless variables). The chaotic motion in this situation has been studied widely and in detail by many authors.[1,15]

A more interesting energy region is $E > E_s$, where infinite motion of the dimer is possible. Here its CM moves over distances substantially exceeding the interatomic distances on the surface of the crystal, and one can pose the fundamental question of the influence of stochastization of the motion in a nonintegrable system on the character of the macroscopic displacement of adatom clusters. In particular, one can answer the question of whether this stochastization leads to diffusion of the clusters and what would be the properties of such diffusion. (We stress that we are talking about diffusion in ordinary coordinate space and not Arnold diffusion in phase space.[1])

SETUP OF THE NUMERICAL SIMULATION

The theoretical model described above was investigated by numerical solution of the system of nonlinear equations (4), (5) on a computer. The computer calculations were done by the method of finite differences with a discrete time step Δ. The value of Δ was decreased as the energy increased and was usually chosen in the interval 0.025–0.01. In real time this interval corresponds to a time interval $\tau = \Delta\sqrt{2}/\omega_0$. A fast formula for the Verlet algorithm was used which did not lead to accumulation of round-off error.

All of the calculations were done for the same initial values of the coordinates of the atoms of the dimer, $x_1^{(0)} = x_2^{(0)} = 0$, but the initial values of the particle velocities $v_1^{(0)}$ and $v_2^{(0)}$ and, hence, the total energy of the cluster were varied over wide limits. In practice, instead of the values of $v_1^{(0)}$ and $v_2^{(0)}$, the related "rapidities" $E_i^{(0)} = \mathrm{sgn}(v_i^{(0)}) \times [(v_i^{(0)})^2/2]$ of the two particles were assigned. Here, of course, $E = |E_1^{(0)}| + |E_2^{(0)}|$. Studies were done over a wide energy interval, from $E = 0.5$ to 100. Although in reality our assumption that the motion is of a one-dimensional character

TABLE I.

E_1	E_2	E	Type of dynamics
−0.25	0.25	0.5	Localized vibrations
−0.50	0.50	1.0	chaos
−0.75	0.75	1.5	chaos
−1.00	1.00	2.0	chaos
−1.25	1.25	2.5	chaos
−1.50	1.50	3.0	chaos
−1.75	1.75	3.5	chaos
−2.00	2.00	4.0	Localized vibrations
−2.25	2.25	4.5	Localized vibrations
−2.50	2.50	5.0	chaos
−2.75	2.75	5.5	chaos
−3.00	3.00	6.0	chaos
−5.00	5.00	10.0	chaos
−10.00	10.00	20.0	chaos
−15.00	15.00	30.0	chaos
−20.00	20.00	40.0	chaos

TABLE II.

E_1	E_2	E	Type of dynamics
−5	5	10	chaos
−4	6	10	chaos
−3	7	10	chaos
−2	8	10	Quasiregular
−1	9	10	chaos
0	10	10	Quasiregular
1	9	10	Quasiregular
2	8	10	Regular
3	7	10	Regular
4	6	10	Regular
5	5	10	Regular

is violated at high energies and the cluster breaks up, the investigations at high energies of excitation nevertheless proved useful from a methodological standpoint. The results for the case studies are presented in Tables I–VI. At energies $E=0.5$, 1.0, 1.5, 2.0, 2.5, 3.0, 3.5, 4.0, 4.5, 5.0, 5.5, 6.0, 10.0, 20.0, 30.0, and 40.0 we chose the initial conditions $E_1^{(0)}=-E_2^{(0)}=E/2$, corresponding to the relative internal vibrations of the dimer with a stationary CM at the initial time (Table I). For energies $E=1.125$, 2.0, 4.5, 10.0, 20,0, 30.0, 40.0, 50.0, 60.0, and 100 we chose the initial conditions $E_1^{(0)}=0$, $E_2^{(0)}=E$, corresponding to the motion of only one atom of the dimer at the initial time (Table VI). Finally, for energies of 10, 20, 30, and 40 (Tables II–V, respectively) we chose several initial conditions, ranging from internal vibrations of the dimer to a purely "drift" motion: $E_1^{(0)}=-E/2+n$, $E_2^{(0)}=E-|E_1^{(0)}|$, $n=0,1,\ldots,E$.

Instead of the coordinates x_1 and x_2 of the atoms it is convenient to use the coordinate of the CM of the dimer $x=(x_1+x_2)/2$ and the characteristic relative distance between atoms $y=(x_1-x_2)/2$. In the new variables we have two-dimensional motion of the image point on the (x,y) plane, where the region accessible for motion is a corrugated "corridor" which is open in the direction of the x axis (see Fig. 3). At the initial time a particle with the specified energy starts from the point (0,0) with a velocity $\sqrt{2E}$ in different directions, as is illustrated by the fan of arrows on the left end of Fig. 3. Arrow a corresponds to the condition $E_1^{(0)}=-E_2^{(0)}=E/2$, and arrow b to the condition $E_1^{(0)}=E_2^{(0)}=E/2$. The main types of motion possible are shown schematically in the same figure. First, regular vibrations within a single period of the substrate structure can occur, especially at low energies (curve A in Fig. 3). Second, for initial conditions of type b, a regular "drift" motion, illustrated by curve B in the figure, can exist at high energies. In particular, when the energy is only slightly above E_s this trajectory has the form of curve C, which corresponds to the "express"

TABLE III.

E_1	E_2	E	Type of dynamics
−10	10	20	chaos
−8	12	20	chaos
−6	14	20	chaos
−4	16	20	chaos
−3	17	20	chaos
−2	18	20	Quasiregular
−1	19	20	chaos
0	20	20	Quasiregular
1	19	20	Quasiregular
2	18	20	Regular
4	16	20	Regular
6	14	20	Regular
8	12	20	Regular
10	10	20	Regular

TABLE IV.

E_1	E_2	E	Type of dynamics
−15	15	30	chaos
−14	16	30	Quasiregular
−13	17	30	Regular
−12	18	30	Regular
−11	19	30	Quasiregular
−10	20	30	Quasiregular
−9	21	30	Regular
−8	22	30	Regular
−7	23	30	Quasiregular
−6	24	30	Quasiregular
−5	25	30	Regular
−4	26	30	Regular
−3	27	30	Quasiregular
−2	28	30	Regular
−1	29	30	Quasiregular
0	30	30	Quasiregular
1	29	30	Regular
2	28	30	Regular
3	27	30	Regular
15	15	30	Regular

TABLE V.

E_1	E_2	E	Type of dynamics
−20	20	40	chaos
−18	22	40	chaos
−16	24	40	chaos
−14	26	40	Quasiregular
−12	28	40	Regular
−10	30	40	Quasiregular
−9	31	40	Quasiregular
−8	32	40	Quasiregular
−7	33	40	Regular
−6	34	40	Quasiregular
−5	35	40	chaos
−4	36	40	Quasiregular
−3	37	40	Regular
−2	38	40	Quasiregular
−1	39	40	Quasiregular
0	40	40	chaos
1	39	40	Quasiregular
2	38	40	Regular
3	37	40	Regular
4	36	40	Regular
20	20	40	Regular

TABLE VI.

E_1	E_2	E	Type of dynamics
0	1,125	1,125	chaos
0	2,0	2,0	chaos
0	4,5	4,5	chaos
0	10,0	10,0	Quasiregular
0	20,0	20,0	Quasiregular
0	30,0	30,0	Quasiregular
0	40,0	40,0	chaos
0	50,0	50,0	Quasiregular
0	60,0	60,0	Quasiregular
0	100,0	100,0	chaos

motion of the dimer. Since trajectories of types B and C pass through regions of negative curvature of the PES, apparently they also eventually go over to the stochastic regime, but at very long times (this is especially the case for trajectories of type B, which take in a very small part of the surface with $K<0$). Finally, the most often encountered situation is that of stochastic behavior of the trajectory (curve D).

In the numerical calculation very long trajectories were considered: the number of computational iterations producing them was of the order of 10^8. This number of iterations corresponded to maximum dimensionless times of motion of the dimer (dimensionless physical times) of the order of $t_{\max}\approx 10^6$, which corresponds to 10^5 of the characteristic periods of the vibrations of the atoms in the substrate relief. In the chaotic regime the CM of the dimer moved over distances of up to 4×10^4 periods of this potential relief.

The main computational quantities are the following: the time dependence of the coordinate of the CM of the dimer, $x=x(t)$; the time dependence of the number of reversals of the direction of the velocity of the dimer and the coordinates at which the reversals occur; the time dependence of the standard deviation $D=\sqrt{\langle x^2\rangle-\langle x\rangle^2}$ for the trajectory $x(t)$ of the complexes undergoing chaotic motion; and the parameter $p=\ln D(t)/\ln(t)$, which determines the character of the macroscopic motion of the dimer. In addition, for comparison of the results with those for the conventional methods of studying chaotic dynamics we constructed the Poinaré surface of section for the trajectories found and the one-dimensional point images for the coordinates of the turning points of the CM of the complex.

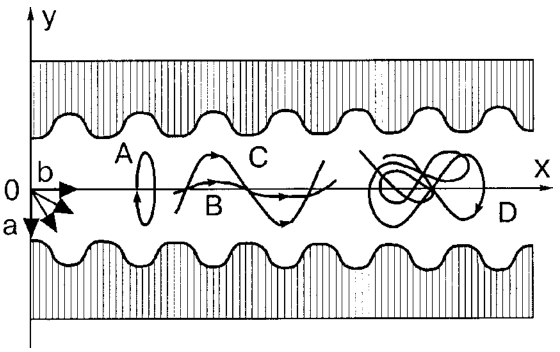

FIG. 3. Schematic illustration of the possible types of motion of the image point. See the text for a description.

Let us discuss in more detail the method of averaging used in the calculation of the standard deviation of a trajectory. This quantity was calculated three ways. In the first case an averaging over the time of motion was done from the initial time $t_0=0$ to a moving time, and the expressions

$$\langle x\rangle=\frac{1}{n}\sum_{k=0}^{n} x(t_k)$$

and

$$\langle x^2\rangle=\frac{1}{n}\sum_{k=0}^{n} x^2(t_k),$$

were used, where $t_k=k\Delta$ and Δ is the iteration step. However, this method of finding the time dependence $D=D(t)$ gives unstable and, hence, insufficiently reliable results even for very long trajectories obtained as a result of $\sim 10^8$ computational iterations. When this method is used, the time dependence $p(t)$ came out to be extremely slow, and it is hard to reach the limiting value of this quantity in a reasonable computation time. Another method was to do a simultaneous averaging over different time series: the trajectory was cut up into six time intervals of identical length, which were then superimposed on one another, and an averaging was done over these six time series. Since this method gave better results, we did the calculations with an averaging over a large number of time series with practically identical initial conditions. To obtain well-convergent and stable results at a reasonable computation time we considered bundles of 400–500 trajectories. In the initial conditions of the motion, i.e., in the originally chosen values of $E_1^{(0)}$ and $E_2^{(0)}$, a random number generator was used to introduce small differences with values of the order of 10^{-8}–10^{-9} times the absolute value of $E_i^{(0)}$ (of course, here the condition $E^{(0)}=\text{const}$ was strictly enforced). Such small differences in the initial conditions of the motion turned out to be sufficient to make the chaotic trajectories diverge rapidly (exponentially) from each other, forming an expanding bundle of trajectories. In this case the averaging of x and x^2 was done over transverse cross sections of the trajectory bundle:

$$\langle x\rangle(t_n)=\frac{1}{m}\sum_{i=1}^{m} x(i,n)$$

and

$$\langle x^2\rangle(t_n)=\frac{1}{m}\sum_{i=1}^{m} x^2(i,n),$$

where $x(i,n)$ is the coordinate of the CM of the ith molecule at the time $t_n=n\Delta$. This method gave more-reliable data for the time dependence $D(t)$.

MAIN RESULTS

A diatomic molecule in the system under discussion can execute four fundamentally different types of motion: localized vibrations of two types, regular translational motion, and, finally, chaotic motion. In the localized vibrations of the first type the molecule pulsates periodically, but its center of mass does not shift (i.e., $x=\text{const}$ and $v=0$). In the localized vibrations of the second type the CM of the molecule executes periodic vibrations, so that $x=\langle x\rangle+x_0\sin\omega t$, while the motion of each atom of the complex can be more complicated. The translational motion is characterized by the absence of changes in the direction of motion of the CM of the molecule, although its velocity v does not necessarily remain constant. If $v=\text{const}$, then one can speak of regular translational motion (or quasiregular, if the velocity changes are small). Finally, in the chaotic motion of the molecule the direction of motion of its CM changes direction many times, and its trajectory $x=x(t)$ has a random character.

Regular translational motion (''drift'' trajectories) is observed, as a rule, at high energies (in particular, at the values $E=10$, 20, 30, 50, and 60). However, a detailed microscopic analysis of the Poincaré section showed that in this case there is a slow enlargement and chaotization of the region of motion in phase space. Curiously, this region pulsates with time, and its volume varies nonmonotonically. The second important observation in the course of the computer simulation was the finding of a ''window of transparency,'' where even at very high energies (in particular, at energies $E=40$ and 100) one observes a rapid transfer of energy from the translational motion of the CM into internal vibrations of the dimer and a rapid stochastization of the motion. This phenomenon is apparently due to an internal parametric resonance in the system: in the ''drift'' of the complex above the periodic relief a periodic force arises which acts on the internal degree of freedom of the dimer in a parametric way.

The most interesting results are those concerning the chaotic motion of the dimer. This is the type of motion that was most often encountered in the numerical simulation. For it, a monotonic change in the parameter $E_i^{(0)}$ corresponds to a nonmonotonic succession of different types of motion of the molecule. For the chaotic motion, calculation of the change of the standard deviation with time in the case of an averaging over 400–500 times series gave a rapid approach to a stationary value of the parameter p. At energy values $E=0.5$ and 1 it was found that the time dependence of the standard deviation satisfies the standard relation $D\sim t^p$ with $p\approx 0.5$, which is characteristic for Brownian motion of a particle.

Thus we have shown that dynamical chaos in phase space leads to spatial diffusion in configuration space and to the onset of Brownian motion of adatom clusters. This result is of exceptional interest, since it demonstrates that under certain conditions cluster diffusion can occur at zero temperature (but finite energy) in the absence of thermal impacts due to the heat bath. In this case the role of the heat bath in a certain sense is played by the internal degree of freedom of the cluster, and its translational motion can exchange energy with the internal vibrations. Here, as a consequence of the nonlinearity of the system, this exchange can occur in a random manner.

In studying the chaotic motion of a cluster along a trajectory $x=x(t)$ we also measured the values of the coordinates of its center of mass, $x^{(1)},x^{(2)},\dots,x^{(N)}$ at successive times $t_k=k\delta$ with a fixed time step δ and determined the change of the coordinates $\Delta x^{(k)}=x^{(k+1)}-x^{(k)}$. The resulting set of values of $\Delta x^{(k)}$ was subjected to further processing by the methods of mathematical statistics with the goal of determining the distribution law of this random quantity. These studies were done for energies $E=1$ and 20, which corresponded to statistical sampling volumes of $N=581$ and 410. It was found that with increasing significance level according to the χ^2 criterion, the $\Delta x^{(k)}$ are distributed according to a normal (Gaussian) law, i.e., they have the same properties as for the trajectories of classical Brownian motion.

In a number of cases, however, the random walk of the dimer at certain times would give way to a rapid ''drift'' regime that lasted a finite length of time. On a larger scale these points in time corresponded to macroscopic jumps of the trajectory. That is, the motion is not so much of the nature of Brownian motion as it is a realization of a Cauchy process. This probably accounts for the following result: it was observed that at energy $E=10$, i.e., in the region of energies high compared to E_m, approximating the time dependence $D(t)$ by a power law $D\sim t^p$ gave an exponent $p\approx 0.65-0.8$, markedly larger than the value 0.5 and typical of a generalized diffusion process. Moreover, if the approximation of $D(t)$ was done for different time intervals, the values of p came out different, and its dependence on the time interval was nonmonotonic. Thus at large values of the energy the process investigated here, being stochastic, does not correspond to classical Brownian motion and possibly not even to a generalized Brownian process.

The authors thank V. I. Belan for assistance in doing the numerical calculations. This study was supported in part by INTAS Grant No. 99-0167.

*E-mail: kovalev@ilt.kharkov.ua

---

[1] A. J. Lichtenberg and M. A. Lieberman, *Regular and Stochastic Motion* [Springer-Verlag, New York (1982); Mir, Moscow (1984)].
[2] M. Henon and C. Heiles, Astron. J. **69**, 73 (1964).
[3] I. F. Lyuksyutov, A. G. Naumovets, and V. L. Pokrovskiĭ, *Two-Dimensional Crystals* [in Russian], Naukova Dumka, Kiev (1988).
[4] A. G. Naumovets, Fiz. Nizk. Temp. **20**, 1091 (1994) [Low Temp. Phys. **20**, 857 (1994)].
[5] A. G. Naumovets and Yu. S. Vedula, Surf. Sci. Rep. **4**, 365 (1984).
[6] R. Kern, G. Le Lay, and J. J. Metois, in *Current Topics in Material Science*, Vol. 3, edited by E. Kaldis, North-Holland, Amsterdam (1979).
[7] D. W. Bassett, in *Surface Mobilities on Solid Materials*, edited by Yu. Thien Binh, Plenum, New York (1983).
[8] G. Honjo, K. Takayanagi, K. Kobayashi, and K. Yagi, Phys. Status Solidi A **55**, 353 (1979).
[9] A. S. Kovalev, Fiz. Tverd. Tela (Leningrad) **21**, 1729 (1979) [Sov. Phys. Solid State **21**, 991 (1979)].
[10] S. Stoyanov and H. Muller-Krumbhaar, Surf. Sci. Rep. **159**, 49 (1985).
[11] O. M. Braun, Surf. Sci. Rep. **230**, 262 (1990).
[12] M. Toda, *Theory of Nonlinear Lattices* [Sprinter-Verlag, New York (1989); Mir, Moscow (1984)].
[13] I. V. Krivoshey, Sov. Sci. Rev. Solid State Chemistry (edited by M. E. Vol'pin) **B11**, 125 (1988).
[14] V. I. Arnold, *Mathematical Methods of Classical Mechanics*, [2nd ed., Springer-Verlag, Berlin (1989); 1st ed., Nauka, Moscow (1974)].
[15] G. M. Zaslavsky, *Chaos in Dynamical Systems* [Harwood, Chur (1985); Nauka, Moscow (1984)].

Translated by Steve Torstveit

LOW TEMPERATURE PHYSICS VOLUME 28, NUMBER 6 JUNE 2002

QUANTUM EFFECTS IN SEMICONDUCTORS AND DIELECTRICS

Self-consistent field model for spatially inhomogeneous Bose systems

Yu. M. Poluéktov*

Kharkov Physicotechnical Institute National Research Center, ul. Akademicheskaya 1, 61108 Kharkov, Ukraine

(Submitted August 27, 2001; revised February 27, 2002)
Fiz. Nizk. Temp. **28**, 604–620 (June 2002)

A self-consistent field (SCF) model is constructed for spatially inhomogeneous Bose systems with broken symmetry. A system of self-consistent equations is obtained for the wave functions of the quasiparticles and the wave function of the condensate particles and another system of equations for the normal and anomalous single-particle density matrices. The many-particle wave function is found. The thermodynamics of multiparticle Bose systems is constructed on the basis of a microscopic treatment in the SCF approximation. It is stressed that Bose condensation in the ideal gas model is substantially different from Bose condensation in a system of interacting Bose particles because a pair condensate is necessarily present as well as the single-particle condensate, even for an arbitrarily weak interaction. The role of single-particle and collective excitations in Bose systems is discussed. *© 2002 American Institute of Physics.* [DOI: 10.1063/1.1491184]

1. INTRODUCTION

The self-consistent field (SCF) model in the quantum mechanics of many-particle systems was introduced by Hartree[1] for describing the states of electrons in atoms. The symmetry of the many-particle wave function in this model with respect to permutations was taken into account by Fock.[2] Nowadays the SCF model is widely used for calculation of atomic shells,[1] nuclear structure,[3] and the properties of molecules and solids.[4] An important feature of the SCF model is that it can be used to describe states with a lower symmetry than that of the initial Hamiltonian. In particular, Bogolyubov generalized the Hartree–Fock model to states with broken symmetry with respect to phase transformations.[5] The Hartree–Fock–Bogolyubov model permits a description of the superconducting states of fermion systems with pairing. The SCF model has mainly been used as a basis for theoretical investigation of the properties of fermions, and only in isolated cases has it been used to study many-particle Bose systems.[6] Interest in the problem of Bose condensation has risen substantially in connection with the experimental observation of Bose condensation in spin-polarized atomic gases by various groups of investigators.[7,8]

In the framework of the SCF model, single-particle excitations arise with nonzero activation energy at zero momentum; the necessity of their existence in Bose systems was pointed out in the book by Bogolyubov and Bogolyubov.[9] The presence of a gap in the spectrum of these quasiparticles is due to the fact that Bose systems with broken phase symmetry contain pairs of particles with opposite momenta, which, as was noted in Ref. 9, must have an energy of dissociation. Excitations with an acoustic dispersion relation, which were predicted by Landau[10] and also exist in systems of interacting Bose particles, may be found from the nonstationary equations for the self-consistent field.

In Sec. 2 of this paper we derive a system of SCF equations for a many-particle system of interacting Bose particles. These equations can be used for a finite-temperature description of spatially inhomogeneous states with broken symmetries with respect to various sorts of transformations. In Sec. 3, thermodynamic relations and expressions for the energy and thermodynamic potential are obtained in the SCF model on the basis of a microscopic approach, and it is thereby shown that the SCF model is in complete agreement with the general principles of thermodynamics. In Sec. 4 a spatially homogeneous Bose system of particles with a short-range repulsive interaction is considered in the nonsuperfluid and superfluid states with a single-particle Bose condensate. The many-particle wave functions are found for a Bose system with a single-particle condensate. The question of the formation of the spectrum of excitations in many-particle Bose systems is discussed in Sec. 5. We note that this question was discussed in Ref. 11 in connection with the experimental data on neutron scattering in ^{4}He.

A generalization of the semi-phenomenological Fermi-liquid approach to the case of a superfluid Bose liquid was made in Ref. 12. The spatially inhomogeneous states of a slightly nonideal Bose gas were considered in the framework of the Bogolyubov approximation in Ref. 13, and in the absence of a single-particle Bose condensate they were considered in the linear approximation in Ref. 14.

In this paper, on the basis of the method developed for Fermi systems in Ref. 15, we construct a general formulation of the SCF method for Bose systems with spontaneously broken symmetry. We show that the state of a system with broken phase invariance—a system of even arbitrarily weakly interacting Bose particles—differs substantially from an ideal Bose gas with a condensate. A many-particle Bose system at low temperatures always undergoes a transition to a state with broken phase symmetry, regardless of the character of the interparticle interaction, and the ideal gas model is oversimplified and does not reflect the essential features of such states of interacting Bose particles. Therefore the SCF model, in which one can describe states with spontaneously broken symmetries, is a more natural choice than the independent-particle model as an initial basis for constructing a microscopic theory of many-particle Bose systems. Among the advantages of the proposed approach is the fact that all particles of the system are treated on a completely equal footing. The separation of a condensate of particles with zero momentum arises in a spatially homogeneous state as a consequence of the general theory.

2. EQUATIONS OF THE SELF-CONSISTENT FIELD

Consider a system of Bose particles with spin zero, interacting by means of a pair potential $U(\mathbf{r},\mathbf{r}')$. The Hamiltonian of such a system has the form

$$H=H_K+H_I, \tag{1}$$

where

$$H_K=\int dxdx'\Psi^+(x)H(x,x')\Psi(x'), \tag{2}$$

$$H_I=\frac{1}{2}\int dxdx'\Psi^+(x)\Psi^+(x')U(x,x')\Psi(x')\Psi(x), \tag{3}$$

and

$$H(x,x')=H_0(x,x')-\mu\delta(x-x'),$$
$$H_0(x,x')=-\frac{\hbar^2}{2m}\Delta\delta(x-x')+U_0(x)\delta(x-x'), \tag{4}$$

where we have used the notation $x=\{\mathbf{r}\}$, and $U_0(x)$ is the external field potential. It is assumed that a many-particle system found in contact with a heat bath can exchange with it both energy and particles, i.e., a grand canonical ensemble is used. For this reason the chemical potential μ is included in the Hamiltonian. The field operators obey the Bose commutation relations and have the form

$$\Psi(x)=\sum_j \varphi_j(x)a_j,\quad \Psi^+(x)=\sum_j \varphi_j^*(x)a_j^+, \tag{5}$$

where a_j^+ and a_j are the creation and annihilation operators for real Bose particles in state j, and the wave functions satisfy the single-particle Schrödinger equation

$$\int dx'H_0(x,x')\varphi_j(x')=\varepsilon_j^{(0)}\varphi_j(x). \tag{6}$$

To pass to the SCF approximation we break the initial Hamiltonian (1) into a sum of two terms:

$$H=H_0+H_C, \tag{7}$$

where the first term is the Hamiltonian of the SCF model, including terms not higher than quadratic in the field operators:

$$\begin{aligned}H_0=\int dxdx'\Big\{&\Psi^+(x)[H(x,x')+W(x,x')]\Psi(x')\\&+\frac{1}{2}\Psi^+(x)\Delta(x,x')\Psi^+(x')+\frac{1}{2}\Psi(x')\Delta^*(x,x')\Psi(x)\Big\}\\&+\int dx[F(x)\Psi^+(x)+F^*(x)\Psi(x)]+E_0',\end{aligned} \tag{8}$$

while the second term is the correlation Hamiltonian, which takes into account particle correlations not included in the SCF approximation:

$$\begin{aligned}H_C=\frac{1}{2}\int dxdx'\{&\Psi^+(x)\Psi^+(x')U(x,x')\Psi(x')\Psi(x)\\&-2\Psi^+(x)W(x,x')\Psi(x')\\&-\Psi^+(x)\Delta(x,x')\Psi^+(x')\\&-\Psi(x')\Delta^*(x,x')\Psi(x)\}\\&-\int dx[F(x)\Psi^+(x)+F^*(x)\Psi(x)]-E_0'.\end{aligned} \tag{9}$$

The Hamiltonian (8) of the SCF model, unlike its counterpart for the case of a Fermi system,[15] also contains terms linear in Ψ and Ψ^+. The self-consistent fields $F(x)$, $W(x,x')$, and $\Delta(x,x')$ appearing in H_0 must be found from the condition that this Hamiltonian be the best approximation to the initial Hamiltonian H; by virtue of the Hermitianity, the following conditions hold:

$$W(x,x')=W^*(x',x),\quad \Delta(x,x')=\Delta(x',x). \tag{10}$$

The choice of the nonoperator term E_0' in (8) and (9) is important for correct formulation of the SCF model. Thus, in the SCF approximation a many-particle system is characterized by a Hamiltonian H_0, while the influence of the correlation Hamiltonian H_C can be taken into account by perturbation theory. In this paper, however, we shall limit the detailed study of the Bose system to the SCF model, neglecting effects due to the correlation Hamiltonian.

Hamiltonian (8) can be reduced to diagonal form. To do this, we first eliminate the terms linear in the Bose operators by introducing "shifted" Bose operators $\Phi(x)$, $\Phi^+(x)$, so that

$$\Psi(x)=\chi(x)+\Phi(x),\quad \Psi^+(x)=\chi^*(x)+\Phi^+(x), \tag{11}$$

and defining the function $\chi(x)$ so that the terms linear in the field operators drop out of H_0. As a result, we obtain the condition

$$\int dx'[\Omega(x,x')\chi(x')+\Delta(x,x')\chi^*(x')]+F(x)=0, \tag{12}$$

where $\Omega(x,x')=H(x,x')+W(x,x')$. With allowance for this last condition the self-consistent Hamiltonian takes the form

$$
\begin{aligned}
H_0 = \int dx dx' \Big\{ & \Phi^+(x)\Omega(x,x')\Phi(x') \\
& + \frac{1}{2}\Phi^+(x)\Delta(x,x')\Phi^+(x') \\
& + \frac{1}{2}\Phi(x')\Delta^*(x,x')\Phi(x)\Big\} \\
- \int dx dx' \Big\{ & \chi^*(x)\Omega(x,x')\chi(x') \\
& + \frac{1}{2}\chi^*(x)\Delta(x,x')\chi^*(x') \\
& + \frac{1}{2}\chi(x')\Delta^*(x,x')\chi(x)\Big\} + E_0'.
\end{aligned} \tag{13}
$$

This Hamiltonian, with the aid of the canonical Bogolyubov transformations

$$
\begin{aligned}
\Phi(x) &= \sum_i [u_i(x)\gamma_i + v_i^*(x)\gamma_i^+], \\
\Phi^+(x) &= \sum_i [v_i(x)\gamma_i + u_i^*(x)\gamma_i^+],
\end{aligned} \tag{14}
$$

is reduced to the diagonal form

$$
H_0 = E_0 + \sum_i \varepsilon_i \gamma_i^+ \gamma_i, \tag{15}
$$

where i is the total set of quantum numbers characterizing the state of the quasiparticle. We see that the SCF approximation leads in a natural way to a quasiparticle representation in Bose systems. The conditions for the transition from Hamiltonian (13) to Hamiltonian (15) are the equations for the coefficients of the Bogolyubov transformation, which have the meaning of components of the quasiparticle wave vector:

$$
\int dx' [\Omega(x,x')u_i(x') + \Delta(x,x')v_i(x')] = \varepsilon_i u_i(x), \tag{16}
$$

$$
\int dx' [\Omega^*(x,x')v_i(x') + \Delta^*(x,x')u_i(x')] = -\varepsilon_i v_i(x). \tag{17}
$$

The requirement that the transformations (14) be canonical leads to the normalization conditions

$$
\begin{aligned}
& \int dx [u_i(x)u_{i'}^*(x) - v_i(x)v_{i'}^*(x)] = \delta_{ii'}, \\
& \int dx [u_i(x)v_{i'}(x) - v_i(x)u_{i'}(x)] = 0
\end{aligned} \tag{18}
$$

and the completeness conditions

$$
\begin{aligned}
& \sum_i [u_i(x)u_i^*(x') - v_i^*(x)v_i(x')] = \delta(x-x'), \\
& \sum_i [u_i(x)v_i^*(x') - v_i^*(x)u_i(x')] = 0
\end{aligned} \tag{19}
$$

for the solutions of the self-consistent equations.

The self-consistent potentials $W(x,x')$ and $\Delta(x,x')$ can be found from the condition of minimality of the functional

$$
I = [\langle (H - H_0)\rangle_0]^2, \tag{20}
$$

where the averaging is done with the density matrix

$$
\rho_0 = \exp \beta(\Omega_0 - H_0), \quad \beta = 1/T, \tag{21}
$$

with T being the temperature. The normalizing constant is determined by the condition $\mathrm{Tr}\,\rho_0 = 1$:

$$
\Omega_0 = -T \ln[\mathrm{Tr}\exp(-\beta H_0)], \tag{22}
$$

and, as we shall show, has the meaning of the thermodynamic potential of the system in the SCF approximation.

Defining the total single-particle density matrix by the relations

$$
\tilde{\rho}(x,x') = \langle \Psi^+(x')\Psi(x)\rangle_0 = \rho(x,x') + \chi^*(x')\chi(x), \tag{23}
$$

$$
\tilde{\tau}(x,x') = \langle \Psi(x')\Psi(x)\rangle_0 = \tau(x,x')\chi(x')\chi(x) \tag{24}
$$

and varying the functional (20) with respect to them, we obtain from the condition $\delta I = 0$ a relation between the self-consistent potentials and the total single-particle density matrices

$$
\begin{aligned}
W(x,x') = {} & U(x,x')\tilde{\rho}(x,x') + \delta(x-x') \\
& \times \int dx'' U(x,x'')\tilde{\rho}(x'',x''),
\end{aligned} \tag{25}
$$

$$
\Delta(x,x') = U(x,x')\tilde{\tau}(x,x'). \tag{26}
$$

The above-condensate density matrices have the form

$$
\begin{aligned}
\rho(x,x') &= \langle \Phi^+(x')\Phi(x)\rangle_0 \\
&= \sum_i [u_i(x)u_i^*(x')f_i + v_i^*(x)v_i(x')(1+f_i)],
\end{aligned} \tag{27}
$$

$$
\begin{aligned}
\tau(x,x') &= \langle \Phi(x')\Phi(x)\rangle_0 \\
&= \sum_i [u_i(x)v_i^*(x')f_i + v_i^*(x)u_i(x')(1+f_i)],
\end{aligned} \tag{28}
$$

where

$$
f_i = \langle \gamma_i^+ \gamma_i\rangle_0 = f(\varepsilon_i) = [\exp(\beta\varepsilon_i) - 1]^{-1} \tag{29}
$$

is the distribution function of the Bose quasiparticles. These matrices, like $\tilde{\rho}(x,x')$ and $\tilde{\tau}(x,x')$, satisfy the conditions

$$
\rho(x,x') = \rho^*(x',x), \quad \tau(x,x') = \tau(x',x). \tag{30}
$$

Since the operators $\Phi(x)$ and $\Phi^+(x)$, according to Eq. (14), are linear in γ and γ^+, while the Hamiltonian H_0 (15) is quadratic, we have

$$
\langle \Phi(x)\rangle_0 = \langle \Phi^+(x)\rangle_0 = 0,
$$

and, hence,

$$
\chi(x) = \langle \Psi(x)\rangle_0, \quad \chi^*(x) = \langle \Psi^+(x)\rangle_0. \tag{31}
$$

Thus $\chi(x)$ can be interpreted as a function that determines the particle number density in the single-particle Bose condensate in the SCF model.

When relations (25) and (26) are taken into account, the self-consistency conditions (16) and (17) take the form

$$\left[-\frac{\hbar^2}{2m}\Delta+U_0(x)-\mu+\int dx'\,U(x,x')\tilde{\rho}(x',x')\right]u_i(x)+\int dx'\,U(x,x')[\tilde{\rho}(x,x')u_i(x')+\tilde{\tau}(x,x')v_i(x')]=\varepsilon_i u_i(x), \tag{32}$$

$$\left[-\frac{\hbar^2}{2m}\Delta+U_0(x)-\mu+\int dx'\,U(x,x')\tilde{\rho}(x',x')\right]v_i(x)+\int dx'\,U(x,x')[\tilde{\rho}^*(x,x')v_i(x')+\tilde{\tau}^*(x,x')u_i(x')]=-\varepsilon_i v_i(x). \tag{33}$$

Besides Eqs. (32) and (33), we must obtain one more equation, since the Bose-condensate function $\chi(x)$ remains undetermined. With this goal, by varying (20) with respect to $\chi(x)$ and setting $\delta I=0$ we find

$$F(x)=-2\chi(x)\int dx'\,U(x,x')|\chi(x')|^2. \tag{34}$$

Ultimately, taking Eq. (12) into account, we arrive at the equation

$$\left\{-\frac{\hbar^2}{2m}\Delta+U_0(x)-\mu+\int dx'\,U(x,x')[\tilde{\rho}(x',x')-2|\chi(x')|^2]\right\}\chi(x)+\int dx'\,U(x,x')[\tilde{\rho}(x,x')\chi(x')+\tilde{\tau}(x,x')\chi^*(x')]=0. \tag{35}$$

Equation (35) together with Eqs. (32) and (33) and relations (18), (19), and (29) completely describe a system of many Bose particles in the SCF approximation. The system of equations obtained has three types of solutions:

I) $\chi(x)=v_i(x)=0,\ u_i(x)\neq 0;$

II) $\chi(x)=0,\ v_i(x)\neq 0,\ u_i(x)\neq 0;$

III) $\chi(x)\neq 0,\ v_i(x)\neq 0,\ u_i(x)\neq 0.$

The first type of solutions (I) describe states in which the symmetry with respect to the phase transformations

$$\Psi(x)\rightarrow\Psi(x)e^{i\xi}, \tag{36}$$

where ξ is an arbitrary phase, is unbroken. In this ''normal'' state the system contains neither a single-particle nor a pair condensate and does not possess the property of superfluidity. The second type of solutions (II) describe states whose symmetry with respect to the transformation (36) is broken on account of the formation of a pair condensate, analogous to that which arises in superfluid Fermi systems.[15] In this case the Bose system possesses the property of superfluidity. Superfluidity of Bose systems due to pair correlations has been studied in Refs. 16 and 17. The solutions of type (III) describe superfluid states with broken phase symmetry, containing both a single-particle and a pair Bose condensate. We note the absence of solutions in which

$$\chi(x)\neq 0,\ v_i(x)=0,\ u_i(x)\neq 0. \tag{37}$$

It is just such a solution that corresponds to the case of an ideal Bose gas below the point of the Bose transition, consisting of a Bose condensate and above-condensate particles. Thus a system of noninteracting particles with a Bose condensate and a system of (even arbitrarily weakly) interacting Bose particles with broken phase symmetry are two essentially different systems. The ideal gas model with a Bose condensate is just as unsuitable for describing the superfluid state of a real system of interacting particles as the ideal Fermi gas model is unsuitable for describing the superfluid state of a Fermi system, for example, and it cannot be used as an initial approximation for constructing a perturbation theory. The use of the ideal gas model with a condensate as a basis is responsible for the various difficulties encountered in constructing a consistent theory of many-particle Bose systems with broken symmetry. This, as we see, is due to the fact that the pair correlations that always exist in superfluid systems of interacting particles cannot be described in the ideal gas model. In real superfluid Bose systems the pair and higher correlations, which break the phase symmetry, play no less important a role than does the single-particle Bose condensate. Thus, according to the estimates of Ref. 18, in superfluid ^{4}He only about 8% of the particles are found in the single-particle Bose condensate, while the remaining contribution to the superfluid density is given by pair and higher correlations.

3. THERMODYNAMIC RELATIONS

To construct a consistent SCF model and obtain the correct thermodynamic relations it is important to make the correct choice of the nonoperator part in Hamiltonian (8). We find it from the condition

$$\partial I/\partial E_0'=0, \tag{38}$$

which ensures that the averages of the exact and self-consistent Hamiltonians are equal:

$$\langle H\rangle_0=\langle H_0\rangle_0. \tag{39}$$

By virtue of this we obtain

$$E_0'=-\frac{1}{2}\int dx\,dx'\,U(x,x')\times\langle\Psi^+(x)\Psi^+(x')\Psi(x')\Psi(x)\rangle_0+2\int dx\,dx'\,U(x,x')|\chi(x)|^2|\chi(x')|^2. \tag{40}$$

The total energy of the system of particles in the SCF approximation has the form

$$E=\int dx\,dx'\,H_0(x,x')\langle\Psi^+(x)\Psi(x')\rangle_0+\frac{1}{2}\int dx\,dx'\,U(x,x')\langle\Psi^+(x)\Psi^+(x')\Psi(x')\Psi(x)\rangle_0 \tag{41}$$

and can be written as a sum of three terms:

$$E=E_1+E_2+E_3, \tag{42}$$

where E_1 is the energy determined by the above-condensate excitations, E_2 is the energy of the single-particle condensate, and E_3 is the "interaction" energy of the condensate and above-condensate particles. The first term can be written in the form of a sum

$$E_1 = T^{(1)} + U_E^{(1)} + U_D^{(1)} + U_{\mathrm{EX}}^{(1)} + U_C^{(1)},$$

where

$$T^{(1)} = -\frac{\hbar^2}{2m}\int dx dx' \, \delta(x-x')\Delta\rho(x,x') \tag{43}$$

is the kinetic energy of the above-condensate subsystem,

$$U_E^{(1)} = \int dx U_0(x) n_Q(x) \tag{44}$$

is the energy of the above-condensate subsystem in the external field,

$$U_D^{(1)} = \frac{1}{2}\int dx dx' \, U(x,x') n_Q(x) n_Q(x') \tag{45}$$

is the energy of the direct interaction of the above-condensate particles,

$$U_{\mathrm{EX}}^{(1)} = \frac{1}{2}\int dx dx' \, U(x,x') |\rho(x,x')|^2 \tag{46}$$

is the energy of the exchange interaction of the above-condensate particles, and

$$U_C^{(1)} = \frac{1}{2}\int dx dx' \, U(x,x') |\tau(x,x')|^2 \tag{47}$$

is the energy of the condensate pairs. In Eqs. (44) and (45) $n_Q(x) = \rho(x,x)$ is the number density of the above-condensate particles. We write the condensate part in the form of a sum:

$$E_2 = T^{(2)} + U_E^{(2)} + U_D^{(2)},$$

where

$$T^{(2)} = -\frac{\hbar^2}{4m}\int dx [\chi^*(x)\Delta\chi(x) + \chi(x)\Delta\chi^*(x)] \tag{48}$$

is the kinetic energy of the single-particle condensate,

$$U_E^{(2)} = \int dx U_0(x) |\chi(x)|^2 \tag{49}$$

is the energy of the condensate in the external field,

$$U_D^{(2)} = \frac{1}{2}\int dx dx' \, U(x,x') |\chi(x)|^2 |\chi(x')|^2 \tag{50}$$

is the interaction energy of the condensate particles. The third contribution to the total energy,

$$\begin{aligned} E_3 = \int dx dx' \, U(x,x') \bigg[& \rho(x,x')\chi^*(x)\chi(x') \\ & + n_Q(x) \left|\chi(x')\right|^2 + \frac{1}{2}\tau(x,x')\chi^*(x)\chi^*(x') \\ & + \frac{1}{2}\tau^*(x,x')\chi(x)\chi(x') \bigg], \end{aligned} \tag{51}$$

is determined by the interaction of the above-condensate particles and the condensate.

We find the thermodynamic potential of a system of Bose particles in the SCF approximation, which, with allowance for (15) and (22), can be written in the form

$$\Omega_0 = E_0 - T \ln\left[\mathrm{Tr} \exp\left(-\beta \sum_i \varepsilon_i \gamma_i^+ \gamma_i \right) \right]. \tag{52}$$

The second term in (52) is calculated in the same way as in the case of an ideal Bose gas. The constant E_0 is found from Eq. (15) with allowance for the relation

$$\langle H_0 \rangle_0 = E - \mu N$$

(N is the total number of particles), so that

$$E_0 = E - \mu N - \sum_i \varepsilon_i f_i . \tag{53}$$

Using Eqs. (32), (33), and (35), we write the kinetic energies $T^{(1)}$ and $T^{(2)}$ in the form

$$\begin{aligned} T^{(1)} = {} & \mu N_Q - U_E^{(1)} - 2(U_D^{(1)} + U_{\mathrm{EX}}^{(1)} + U_C^{(1)}) \\ & + \sum_i \varepsilon_i f_i - \sum_i \varepsilon_i \int dx |v_i(x)|^2 \\ & - \int dx dx' \, U(x,x') \bigg[\rho(x,x')\chi(x)\chi^*(x') \\ & + n_Q(x) \left|\chi(x')\right|^2 + \frac{1}{2}\tau^*(x,x')\chi(x)\chi(x') \\ & + \frac{1}{2}\tau(x,x')\chi^*(x)\chi^*(x') \bigg], \end{aligned} \tag{54}$$

$$\begin{aligned} T^{(2)} = {} & \mu N_B - U_E^{(2)} - \int dx dx' \, U(x,x') \\ & \times \bigg[\rho(x,x')\chi(x)\chi^*(x') + n_Q(x) \left|\chi(x')\right|^2 \\ & + \frac{1}{2}\tau^*(x,x')\chi(x)\chi(x') \\ & + \frac{1}{2}\tau(x,x')\chi^*(x)\chi^*(x') + \left|\chi(x)\right|^2 \left|\chi(x')\right|^2 \bigg], \end{aligned} \tag{55}$$

where $N_Q = \int dx \, n_Q(x)$ and $N_B = \int dx |\chi(x)|^2$ are the numbers of above-condensate and condensate particles.

By virtue of Eqs. (54) and (55) the energy of the system can be written in the form

$$\begin{aligned} E = {} & \mu N - (U_D^{(1)} + U_{\mathrm{EX}}^{(1)} + U_C^{(1)} + U_D^{(2)}) \\ & + \sum_i \varepsilon_i f_i - \sum_i \varepsilon_i \int dx |v_i(x)|^2 - \int dx dx' \, U(x,x') \\ & \times \bigg[\rho(x,x')\chi(x)\chi^*(x') + n_Q(x)|\chi(x')|^2 \\ & + \frac{1}{2}\tau^*(x,x')\chi(x)\chi(x') + \frac{1}{2}\tau(x,x')\chi^*(x)\chi^*(x') \bigg], \end{aligned} \tag{56}$$

from which, by comparison with (53), we determine the expression for E_0 in (15). Ultimately we arrive at the final form of the thermodynamic potential of the Bose system:

$$\begin{aligned}\Omega_0=&-(U_D^{(1)}+U_{\mathrm{EX}}^{(1)}+U_C^{(1)}+U_D^{(2)})-\sum_i \varepsilon_i\int dx|v_i(x)|^2\\&-\int dxdx'U(x,x')\Big[\rho(x,x')\chi(x)\chi^*(x')\\&+n_Q(x)\Big|\chi(x')\Big|^2+\frac{1}{2}\tau^*(x,x')\chi(x)\chi(x')\\&+\frac{1}{2}\tau(x,x')\chi^*(x)\chi^*(x')\Big]+T\sum_i \ln(1-\mathrm{e}^{-\beta\varepsilon_i}).\end{aligned}\tag{57}$$

It can be shown that the variation of the thermodynamic potential given by formula (22) is equal to the average, over the self-consistent state, of the variation of the Hamiltonian:

$$\delta\Omega_0=\langle\delta H_0\rangle_0.\tag{58}$$

Expressing the self-consistent Hamiltonian in terms of $\chi(x)$, $\rho(x,x')$, and $\tau(x,x')$ [or $\tilde\rho(x,x')$ and $\tilde\tau(x,x')$] and varying it with allowance for (58), we obtain

$$\begin{aligned}\frac{\delta\Omega_0}{\delta\chi^*(x)}=\left\langle\frac{\delta H_0}{\delta\chi^*(x)}\right\rangle_0=\frac{\delta\Omega_0}{\delta\rho(x,x')}=\left\langle\frac{\delta H_0}{\delta\rho(x,x')}\right\rangle_0\\=\frac{\delta\Omega_0}{\delta\tau^*(x,x')}=\left\langle\frac{\delta H_0}{\delta\tau^*(x,x')}\right\rangle_0=0.\end{aligned}\tag{59}$$

When the terms of the total density matrices are used in relations (59), the substitutions $\rho(x,x')\rightarrow\tilde\rho(x,x')$ and $\tau(x,x')\rightarrow\tilde\tau(x,x')$ should be made. Thus the relation between the fields $F(x)$, $W(x,x')$, and $\Delta(x,x')$ and the condensate wave function $\chi(x)$ and the single-particle density matrices $\rho(x,x')$ and $\tau(x,x')$ in (25), (26) and (34), which we established with the aid of a variational principle, lead, as we see from Eq. (59), to extremality of the thermodynamic potential in regard to its variations with respect to $\delta\chi$, $\delta\rho$, and $\delta\tau$.

From equations (27), (28), (32), (33), and (35) one can obtain a system of equations for the single-particle density matrices $\rho(x,x')$ and $\tau(x,x')$ [or $\tilde\rho(x,x')$ and $\tilde\tau(x,x')$] and $\chi(x)$. Let us write the system for the total density matrices:

$$\begin{aligned}&-\frac{\hbar^2}{2m}[\Delta-\Delta']\tilde\rho(x,x')+[U_0(x)-U_0(x')]\tilde\rho(x,x')\\&+\int dx''[U(x,x'')-U(x',x'')][\tilde\rho(x,x'')\tilde\rho(x'',x')\\&+\tilde\rho(x,x')\tilde\rho(x'',x'')+\tilde\tau(x,x')\tilde\tau^*(x'',x')\\&-2\chi(x)\chi^*(x')|\chi(x'')|^2]=0,\end{aligned}\tag{60}$$

$$\begin{aligned}&-\frac{\hbar^2}{2m}(\Delta+\Delta')\tilde\tau(x,x')+[U_0(x)+U_0(x')+U(x,x')\\&-2\mu]\tilde\tau(x,x')+\int dx''[U(x,x'')+U(x',x'')]\\&\times[\tilde\rho(x,x'')\tilde\tau(x'',x')+\tilde\rho(x'',x'')\tilde\tau(x,x')\\&+\tilde\rho(x',x'')\tilde\tau(x'',x)-2\chi(x)\chi(x')|\chi(x'')|^2]=0.\end{aligned}\tag{61}$$

To this system of equations we should add Eq. (35). Knowledge of the above-condensate density matrices and condensate wave function is sufficient for calculation of the average of an arbitrary operator O:

$$\begin{aligned}\langle O\rangle_0=&\int dxdx'O(x,x')\tilde\rho(x,x')\\=&\int dxdx'[O(x,x')\rho(x,x')\\&+O(x,x')\chi^*(x)\chi(x')].\end{aligned}\tag{62}$$

We see that the average breaks up into a sum of the above-condensate and condensate contributions.

The correlation Hamiltonian (9) can be written in terms of the above-condensate density matrices in the following form:

$$\begin{aligned}H_C=\frac{1}{2}\int dxdx'U(x,x')[&\Phi^+(x)\Phi^+(x')\Phi(x')\Phi(x)\\&-2\rho(x,x')\Phi^+(x)\Phi(x')-2\rho(x',x')\Phi^+(x)\Phi(x)\\&-\tau(x,x')\Phi^+(x)\Phi^+(x')-\tau^*(x,x')\Phi(x'\Phi(x)\\&+\rho(x,x')\rho(x',\ x)+\rho(x,x)\rho(x',x')\\&+\tau(x',x)\tau^*(x',x)+2\chi^*(x)\Phi^+(x')\Phi(x')\Phi(x)\\&+2\chi(x)\Phi^+(x')\Phi^+(x')\Phi(x)\\&-2\rho(x,x')\chi(x')\Phi^+(x)-2\rho^*(x,x')\chi^*(x')\Phi(x)\\&-2\rho(x',x')\chi(x)\Phi^+(x)-2\rho(x',x')\chi^*(x)\Phi(x)\\&-2\tau(x,x')\chi^*(x')\Phi^+(x)-2\tau^*(x,x')\chi(x')\Phi(x).\end{aligned}\tag{63}$$

This rather unwieldy Hamiltonian can be written more compactly in terms of the normal products of operators and be used to develop a perturbation theory in analogy with the procedure for Fermi systems.[19]

4. SPATIALLY HOMOGENEOUS BOSE SYSTEM

The equations obtained, which are suitable for studying spatially inhomogeneous states, can, of course, also be used for study of a spatially homogeneous system. Let us consider this important particular case. In a spatially homogeneous system the states of the particles are characterized by their momentum, so that here $i=k\equiv\{\mathbf{k}\}$, and the wave functions have the form of plane waves. We shall assume that the interparticle interaction has a δ-function character: $U(x,x')=U_0\delta(x-x')$. In a normal Bose system (the primed quantities) the wave function of a quasiparticle, its dispersion relation, and its distribution function have the forms

$$u'_k(x)=\frac{1}{\sqrt{V}}\mathrm{e}^{-kx},\ \varepsilon'_k=\frac{\hbar^2k^2}{2m}-\tilde{\mu}',\ f'_k=(\mathrm{e}^{\beta\varepsilon'_k}-1)^{-1}, \tag{64}$$

where

$$\tilde{\mu}'=\mu'-2U_0n' \tag{65}$$

is the effective chemical potential, and the single-particle density matrix and particle number density are given by the formulas

$$\rho'(x,x')=\frac{1}{V}\sum_k \mathrm{e}^{-ik(x-x')}f'_k,n'=\frac{1}{V}\sum_k f'_k, \tag{66}$$

where V is the volume occupied by the system. The chemical potential is related to the particle number density by a formula similar to that for an ideal Bose gas above the condensation point, but with the chemical potential μ replaced by the effective chemical potential $\tilde{\mu}'$ (65):

$$n'=\frac{(mT)^{3/2}}{\sqrt{2}\pi^2\hbar^3}\int_0^\infty\frac{d\varepsilon\sqrt{\varepsilon}}{\mathrm{e}^{\varepsilon-\beta\tilde{\mu}'}-1}. \tag{67}$$

Since, according to Eq. (65), the particle number density enters into $\tilde{\mu}'$, Eq. (67) contains n' on both the left and right sides, and therefore formula (67) gives a more complex dependence of the particle number density on the chemical potential than in the ideal gas model. It is obvious that the condition for Bose condensation is $\tilde{\mu}'=0$, i.e., the following relation holds on the phase transition line:

$$\mu'=\mu'_0=2U_0n. \tag{68}$$

The Bose condensation temperature is determined by the same formula as in the case of an ideal Bose gas:

$$T_0=\frac{2\pi\hbar^2}{m}\left[\frac{n'}{\zeta(3/2)}\right]^{2/3}, \tag{69}$$

where $\zeta(3/2)=2.612$ is the Riemann zeta function.

Below the Bose condensation point the self-consistent equations (32), (33), and (35) admit solutions in the form of plane waves:

$$u_k(x)=\frac{u_k}{\sqrt{V}}\mathrm{e}^{-ikx},v_k(x)=\frac{v_k}{\sqrt{V}}\mathrm{e}^{-ikx},\chi=\text{const.} \tag{70}$$

In this case the single-particle density matrices take the form

$$\tilde{\rho}(x,x')=|\chi|^2+\frac{1}{V}\sum_k [|u_k|^2f_k+|v_k|^2(1+f_k)]\mathrm{e}^{-ik(x-x')}, \tag{71}$$

$$\tilde{\tau}(x,x')=\chi^2+\frac{1}{V}\sum_k u_ku_k^*(1+2f_k)\mathrm{e}^{-ik(x-x')}, \tag{72}$$

and the coefficients, according to Eqs. (16) and (17), satisfy the system of algebraic equations

$$(\xi_k-\varepsilon_k)u_k+\Delta v_k=0, \tag{73}$$

$$\Delta^*u_k+(\xi_k+\varepsilon_k)v_k=0, \tag{74}$$

where $\xi_k=\hbar^2k^2/2m-\mu+2U_0n$, $\Delta=U_0\tilde{\tau}(x,x)$, and the total particle number density $n=\tilde{\rho}(x,x)$. Applying the normalization condition (18), i.e., $|u_k|^2-|v_k|^2=1$, we obtain

$$|u_k|^2=\frac{1}{2}\left(\frac{\xi_k}{\varepsilon_k}+1\right),|v_k|^2=\frac{1}{2}\left(\frac{\xi_k}{\varepsilon_k}-1\right),u_kv_k^*=-\frac{\Delta}{2\varepsilon_k}. \tag{75}$$

Equations (73) and (74) imply the quasiparticle dispersion relation

$$\varepsilon_k=\sqrt{\xi_k^2-|\Delta|^2}, \tag{76}$$

and Eq. (35) yields a relation between the chemical potential and the wave function of the Bose-condensate particles:

$$[-\mu+2U_0n_Q]\chi+\Delta\chi^*=0. \tag{77}$$

The total particle number density can be written as

$$n=|\chi|^2+n_q+n_p, \tag{78}$$

where the first term is the particle number density in the Bose condensate, the second term

$$n_q=\frac{1}{V}\sum_k f_k \tag{79}$$

is the number density of the particles forming the quasiparticle excitations, and the last term

$$n_p=\frac{1}{2V}\sum_k\left(\frac{\xi_k}{\varepsilon_k}-1\right)(1+2f_k) \tag{80}$$

is the number density of the particles correlated in Cooper pairs. Thus the number density of particles that do not enter into the single-particle condensate is

$$n_Q=n_q+n_p. \tag{81}$$

The value of Δ is determined by the equation

$$\Delta=\frac{U_0\chi^2}{1+U_0J}=\Theta\chi^2, \tag{82}$$

where

$$J=\frac{1}{2V}\sum_k\frac{1+2f_k}{\varepsilon_k},\quad \Theta=\frac{U_0}{1+U_0J}. \tag{83}$$

We note that when the summation in J is converted to integration, the resulting integral diverges. This is due to the choice of a point interaction. If a potential with a finite interaction radius a_0 were used, the integral would be convergent. Therefore, when calculating J in (83) the integral should be cut off at a wave number $k_0=1/a_0$. In the state with the Bose condensate, the chemical potential, according to Eq. (77), is determined by the formula

$$\mu=2U_0n_Q+\Theta|\chi|^2. \tag{84}$$

Taking Eqs. (82) and (84) into account, we obtain from (76) the final expression for the quasiparticle spectrum:

$$\varepsilon_k=\sqrt{\left(\frac{\hbar^2k^2}{2m}+2(U_0-\Theta)|\chi|^2\right)\left(\frac{\hbar^2k^2}{2m}+2U_0|\chi|^2\right)}. \tag{85}$$

We see that the energy of a quasiparticle at $\mathbf{k}=0$ does not go to zero but takes on a finite value

$$\varepsilon_0 = 2|\chi|^2\sqrt{U_0(U_0-\Theta)} = 2U_0|\chi|^2\sqrt{\frac{U_0 J}{1+U_0 J}}, \qquad (86)$$

i.e., the spectrum has an energy gap. The energy spectrum is clearly stable in the case of repulsion between particles $(U_0>0)$. The energy ε_0 has a clear physical meaning, namely, it is the minimum energy that must be expended to remove a particle from the condensate and thereby create a new quasiparticle. It is entirely natural that in a Bose condensate of interacting particles this energy has a finite value. For a more detailed analysis of the meaning of the expression [Eq. (86)] that determines the energy gap, we use relations (5), (11), and (14) to express the operators of real particles in terms of the amplitude of the Bose condensate and the quasiparticle operators. Since in this case $\varphi_j(x) = \mathrm{e}^{-ikx}/\sqrt{V}$, we have

$$a_k = \chi\sqrt{V}\delta_{k,0} + u_k\gamma_k + v^*_{-k}\gamma^+_{-k},$$

$$a^+_k = \chi^*\sqrt{V}\delta_{k,0} + v_{-k}\gamma_{-k} + u^*_k\gamma^+_k. \qquad (87)$$

These relations permit one to find the momentum distribution of the real particles, $f_k^{(p)} = \langle a_k^+ a_k\rangle$, and the anomalous average $g_k\langle a_k a_{-k}\rangle$:

$$f_k^{(p)} = V|\chi|^2\delta_{k,0} + f_k + \frac{1}{2}\left(\frac{\xi_k}{\varepsilon_k} - 1\right)(1+2f_k), \qquad (88)$$

$$g_k = -\chi^2\Theta\,\frac{(1+2f_k)}{2\varepsilon_k} \quad (\mathbf{k}\neq 0). \qquad (89)$$

These formulas imply the relation

$$\frac{1}{V}\left|\sum_{k\neq 0}\langle a_k a_{-k}\rangle\right| = |\chi|^2\frac{JU_0}{1+JU_0}. \qquad (90)$$

Ultimately, formula (86) can be written in the form

$$\varepsilon_0 = \frac{2U_0|\chi|}{\sqrt{V}}\left|\sum_{k\neq 0}\langle a_k a_{-k}\rangle\right|^{1/2}. \qquad (91)$$

We see that the gap in the quasiparticle spectrum is determined by the interparticle interaction constant, the density of particles in the single-particle Bose condensate, and the anomalous averages describing the pair correlations in a system of interacting Bose particles with broken phase symmetry.

We note that if $U_0-\Theta = U_0^2 J/(1+U_0 J)$ in (86) is formally set equal to zero, then we would obtain the excitation spectrum found by Bogolyubov:[20]

$$\varepsilon_k = \sqrt{\frac{\hbar^2k^2}{2m}\left(\frac{\hbar^2k^2}{2m} + 2U_0|\chi|^2\right)}. \qquad (92)$$

At a finite value of the wave number the difference of the spectrum (85) from the Bogolyubov spectrum (92) can be made arbitrarily small if the interaction is weak enough. The condition for this is

$$U_0^2 J|\chi|^2 \gg \hbar^2k^2/2m.$$

However, right at the point $k=0$, which is a singular point for the spectrum in a perturbation theory in the intensity of the interaction, one is not justified in neglecting the term $2(U_0-\Theta)|\chi|^2$ that leads to the existence of a gap in the spectrum (85). The possibility of the existence of excitations with a nonzero activation energy was discussed long ago, and excitations with a gap have been considered by many authors.[16,21–24] In the Introduction of the Bogolyubovs' book[9] it is mentioned that, because in a Bose gas with interaction there are pairs with opposite momenta, they should have a dissociation energy associated with each pair. "This means that in addition to the phonon branch of the spectrum we have another branch in the excitation spectrum, corresponding to the excitation of pairs" (p. 322 of the Russian edition of Ref. 9). In addition, we note that the single-particle and pair condensates for a single coherent system, and for this reason the gap in the excitation spectrum is determined not only by the pair anomalous average but also by the particle number density in the single-particle condensate (91). A discussion of the solutions which have a gap in the quasiparticle spectrum is given in Ref. 6.

Hugenholtz and Pines[25] used Belyaev's[26] quantum-field perturbation theory for Bose systems with a condensate to show that the quasiparticle spectrum at small momenta obeys a linear law except in possible pathological cases. It should also be kept in mind that the validity of this result, as Pines himself stressed,[27] depends on the validity of the perturbation series expansion. The efficiency of using perturbation theory depends substantially on how well the initial approximation is chosen, i.e., on how close the structure of the state in the zeroth approximation is to the state of the real system. The many-particle wave function of an ideal gas whose particles are all found in the Bose condensate,

$$|\Phi_0\rangle = \frac{(a_0)^N}{\sqrt{N!}}|0\rangle, \qquad (93)$$

is oversimplified and is far from the form of the wave function of a system of interacting Bose particles, as can be seen, for example, from a comparison of (93) with the many-particle wave function obtained below [see Eq. (109)] for a system of interacting Bose particles in the SCF model. Indeed, it appears that responsibility for the difficulties encountered in a quantum-field treatment of many-particle Bose systems (the vanishing of the anomalous self-energy part at zero momentum, which was pointed out in Refs. 28 and 29) rests with the choice of the ideal Bose gas model for the zeroth approximation, as it does not take into account the pair correlations of particles with opposite momenta, and these correlations always exist together with the single-particle condensate. In addition, the result of Hugenholtz and Pines[25] relies substantially on the assumption that the operators for particles with zero momentum can be replaced with C numbers.[23] No such assumption is needed in constructing a theory of many-particle Bose systems on the basis of the SCF model.

The existence of a gap in the spectrum has the consequence that the distribution function f_k of the quasiparticles, both above and below the Bose transition temperature, has a finite value at the point $\mathbf{k}=0$, except at the temperature T_0 itself, where the distribution function diverges for $\mathbf{k}\to 0$ as $f_k \to k^{-2}$.

For a quadratic Hamiltonian such as the Hamiltonian of the SCF model (8), one can find the eigenvectors of the states. In the case when the states of the particle are described by plane waves (70), the self-consistent Hamiltonian has the form

$$H_0=\sum_k\left(\frac{\hbar^2k^2}{2m}-\mu\right)a_k^+a_k+\sum_k\left[W_ka_k^+a_k+\frac{1}{2}\Delta_ka_k^+a_{-k}^+\right.$$
$$\left.+\frac{1}{2}\Delta_k^*a_{-k}a_k\right]+Fa_0^++F^*a_0+E_0',\qquad(94)$$

and the Schrödinger equation corresponding to it is

$$H_0|I\rangle=E_I|I\rangle,\qquad(95)$$

where $|I\rangle$ is the eigenvector of the state with energy E_I. For a delta-function interaction in (94) we have $\Delta_k=\Delta$ [see Eq. (82)], $W_k=W=2U_0n$, and $F=-2\sqrt{V}U_0|\chi|^2\chi$. In the derivation of the equations of the self-consistent field a change to new quasiparticle operators is made with the Hamiltonian remaining unchanged. For finding the state vector it is convenient to go over to a new Hamiltonian expressed in terms of the same particle operators. The new Hamiltonian $\widetilde{H}_0$, related to H_0 by a unitary transformation with U,

$$\widetilde{H}_0=U^+H_0U,\qquad(96)$$

has the same eigenvalues as H_0, but these values correspond to the new eigenvectors

$$|\overline{I}\rangle=U^+|I\rangle.\qquad(97)$$

By applying two successive unitary transformations by U_1 and U_2, we go from the Hamiltonian H_0 to the Hamiltonian

$$\widetilde{H}_0=U_2^+U_1^+H_0U_1U_2=E_0+\sum_k\varepsilon_ka_k^+a_k.\qquad(98)$$

The unitary transformation with

$$U_1=\exp(\sqrt{V}(\chi a_0^+-\chi^*a_0))\qquad(99)$$

eliminates from (94) the terms linear in the particle operators, and the unitary transformation with

$$U_2=\exp\left(\frac{1}{2}\sum_k(\psi_ka_k^+a_{-k}^+-\psi_k^*a_ka_{-k})\right),\quad\psi_k=\psi_{-k}\qquad(100)$$

eliminates the quadratic terms which are noninvariant with respect to phase transformations. The parameter ψ_k in (100) is determined by the relations

$$u_k=\cosh|\psi_k|,\quad v_k^*=\frac{\psi_k}{|\psi_k|}\sinh|\psi_k|.\qquad(101)$$

We note that Hamiltonian (98), unlike (94), is invariant with respect to phase transformations and commutes with the particle number operator. The eigenvectors of $\widetilde{H}_0$ for states with total particle number N have the well-known form

$$|N,\lambda\rangle=(n_1!n_2!\dots n_j!\dots)^{-1/2}(a_1^+)^{n_1}(a_2^+)^{n_2}\dots(a_j^+)^{n_j}\dots|0\rangle,$$
$$N=\sum_j n_j,\qquad(102)$$

where $|0\rangle$ is the vector of the vacuum state of the particles, and the index λ denotes the states with different distributions of N particles over the single-particle states. To each state vector (102) there corresponds an eigenvector of equation (95):

$$|\widetilde{I}\rangle=U_1U_2|N,\lambda\rangle.\qquad(103)$$

The operator (99) can be written in the form

$$U_1=U_1(\chi)=\exp\left(-V\frac{|\chi|^2}{2}+\sqrt{V}\chi a_0^+-\sqrt{V}\chi^*a_0\right).\qquad(104)$$

The action of this operator on the vacuum vector creates a coherent state[28]

$$|\chi\rangle=U_1(\chi)|0\rangle=\mathrm{e}^{-V|\chi|^2/2}\mathrm{e}^{\sqrt{V}\chi a_0^+}|0\rangle,\qquad(105)$$

which is an eigenvector of the annihilation operator: $a_0|\chi\rangle=\sqrt{V}\chi|\chi\rangle$. The operator in (100) contains a sum over momenta in the exponent. Among the terms in it are pairs with equal but opposite momenta, **k** and $-$**k**, and also a term with **k**$=0$. Taking this into account, we write the operator (100) in the form

$$U_2=U_2(\psi_0)\prod_{k\neq-k\neq0}U_2(\psi_k),\qquad(106)$$

where

$$U_2(\psi_0)=\mathrm{e}^{1/2(\psi_0a_0^{+2}-\psi_0^*a_0^2)}$$
$$=\mathrm{e}^{-\Gamma_0/2}\mathrm{e}^{\Lambda_0a_0^{+2}}\mathrm{e}^{-\Gamma_0a_0^+a_0}\mathrm{e}^{-\Lambda_0^*a_0^2},$$
$$U_2(\psi_k)=\mathrm{e}^{(\psi_ka_k^+a_{-k}^+-\psi_k^*a_ka_{-k})}$$
$$=\mathrm{e}^{-\Gamma_k}\mathrm{e}^{\Lambda_ka_k^+a_{-k}^+}\mathrm{e}^{-\Gamma_ka_k^+a_k}\mathrm{e}^{-\Gamma_ka_{-k}^+a_{-k}}\mathrm{e}^{-\Lambda_k^*a_ka_{-k}},$$

and

$$\Lambda_0=\frac{\psi_0}{2|\psi_0|}\tanh|\psi_0|,\quad\Gamma_0=\ln\cosh|\psi_0|;$$

$$\Lambda_k=\frac{\psi_k}{|\psi_k|}\tanh|\psi_k|,\quad\Gamma_k=\ln\cosh|\psi_k|.$$

The action of the operator on the vacuum vector generates a state

$$|\psi_k\rangle=U_2(\psi_k)|0\rangle=\mathrm{e}^{-\Gamma_k}\sum_{n=0}^{\infty}\frac{\Lambda_k^n(a_k^+a_{-k}^+)^n}{n!}|0\rangle,\qquad(107)$$

which is natural to treat as a pair coherent state which is an eigenvector of the operator $u_k^2a_ka_{-k}-v_k^{*2}a_k^+a_{-k}^+$, so that

$$(u_k^2a_ka_{-k}-v_k^{*2}a_k^+a_{-k}^+)|\psi_k\rangle=u_kv_k^*|\psi_k\rangle.\qquad(108)$$

The operators $U_2(\psi_k)$ commute with one another and, for **k**$\neq0$, with $U_1(\chi)$, and only the operators $U_2(\psi_0)$ and $U_1(\chi)$ are noncommutative. The vacuum vector of the self-consistent Hamiltonian H_0 (the vacuum vector for the quasiparticles) is obtained as a result of the action of the operator U_1U_2 on the vacuum vector for the particles:

$$|0_q\rangle=\mathrm{e}^{V\Lambda_0\chi^{*2}-1/2(V|\chi|^2+\Gamma_0)}\mathrm{e}^{\sqrt{V}(\chi-2\Lambda_0\chi^*)a_0^+}\mathrm{e}^{\Lambda_0a_0^{+2}}$$
$$\times\prod_{k\neq-k\neq0}\mathrm{e}^{-\Gamma_k}\mathrm{e}^{\Lambda_ka_k^+a_{-k}^+}|0\rangle.\qquad(109)$$

Taking into account the relation between the particle and quasiparticle operators

$$\gamma = U_1 U_2 a U_2^+ U_1^+ \tag{110}$$

we can easily find an arbitrary eigenvector of the Hamiltonian H_0. These vectors have the form (102) with the particle operators replaced by the quasiparticle operators and with $|0\rangle$ replaced by $|0_q\rangle$, as is obvious from (15). The vector of the state with N quasiparticles is generated from the vector of the state with N particles by operating on it with U_1U_2. The eigenvector (109) and the other eigenvectors of the self-consistent Hamiltonian H_0 (94) are not eigenvectors of the particle number operator and consist of a superposition of vectors describing states with different particle numbers, but they are eigenvectors of the operator $N_q = \Sigma_i \gamma_i^+ \gamma_i$ and describe states with a fixed number of quasiparticles.

From Eqs. (87)–(89), and for $T=0$ from the form of the many-particle wave function (109), we obtain the averages of the operators for particles with zero momentum:

$$\langle a_0 \rangle_0 = \sqrt{V}\chi,$$

$$\langle a_0^2 \rangle_0 = V\chi^2 + u_0 v_0^*(1+2 f_0),$$

$$\langle a_0^+ a_0 \rangle_0 = V|\chi|^2 + |v_0|^2 + (1+2|v_0|^2) f_0. \tag{111}$$

It follows that in the limit $V\to\infty$ we have

$$\langle a_0^+ a_0 \rangle_0 = \langle a_0^+ \rangle_0 \langle a_0 \rangle_0 = \sqrt{\langle a_0^{+2} \rangle_0 \langle a_0^2 \rangle_0}.$$

5. SINGLE-PARTICLE AND COLLECTIVE EXCITATIONS

The concept of quasiparticles arises in the approximate solution of a many-particle problem as a result of the reduction of the Hamiltonian of a system of interacting particles to a form analogous to the Hamiltonian of an ideal gas. Such an operation can be performed in at least two ways, and, accordingly, there are two types of excitations—single-particle (or self-similar) and collective.

A method of constructing the single-particle (self-similar) excitations by proceeding from the many-particle Hamiltonian was developed by Bogolyubov in the theory of the slightly nonideal Bose gas.[20] Essentially, in this approach a microscopic Hamiltonian containing an interaction operator with at least four (in the case of a pair interaction) creation and annihilation operators (3) is approximated by a quadratic operator, which is then diagonalized. This is the approach that was used to construct the SCF model in this paper. On the phenomenological level the concept of single-particle excitations was introduced by Landau in the theory of the Fermi liquid.[31] We note that the Fermi liquid model can be obtained by the Bogolyubov method on the basis of the microscopic approach.[32] The single-particle excitations are essentially individual particles having a dispersion relation that changes on account of the interaction with the surrounding particles and depends on the thermodynamic parameters. In normal (nonsuperfluid) states, where the phase symmetry is not broken, the number of single-particle excitations is fixed and is equal to the number of particles. Asymptotically, at large momenta, the dispersion relation of these quasiparticles is the same as that for free particles. In many-particle systems with broken phase symmetry (superfluid, superconducting) the number of single-particle excitations depends on the thermodynamic parameters (temperature, pressure) and is always less than the total number of particles of the system. This is because only a fraction of the particles take part in the formation of the single-particle excitations, while the rest form condensates (single-particle, pair), which break the phase symmetry. This is just how matters stand in the phenomenological Bose- and Fermi-liquid theories generalized to superfluid systems[12,33] and in the SCF model for Fermi systems with broken symmetry.[15] In particular, in a Bose system at zero temperature the single-particle excitations are absent altogether, and all of the particles are correlated into condensates of different levels, e.g., into a single-particle and a pair condensate if one is using the SCF approximation, and into condensates containing a larger number of particles if the higher approximations are used.

Another way of introducing elementary excitations in a many-particle system dates back to Debye, who developed it in the construction of the theory of the heat capacity of solids.[34] In this approach the many-particle system is treated as a continuous medium, the motion of which is described by classical equations. As a result of quantization we arrive at excitations which are vibrational quanta of the medium. Such excitations are usually called collective. In the case of collective excitations the particles forming the system move coherently and are, as it were, ‘‘frozen’’ into the continuous medium. The number of such excitations, generally speaking, is in no way related to the number of particles in the system. The quanta of the collective oscillations of the density are phonons, which at low momenta have a linear dispersion relation, the energy of which goes to zero with increasing wavelength. In an analogous way one can introduce collective excitations associated with the coherent oscillations of other characteristics of the continuous medium. When the oscillations of the magnetization are quantized, the collective excitations become magnons. In a gas of charged particles, e.g., electrons, the collective excitations are quanta of plasma oscillations—plasmons. A characteristic feature of these excitations is the presence of an energy gap (plasma frequency) in their dispersion relation, which is due to the long-range character of the Coulomb interaction.

Thus the quasiparticle excitations considered in this paper in the framework of the SCF model are single-particle excitations analogous to the excitations with an energy gap in Fermi systems with broken phase symmetry (sometimes called bogolons). A distinctive feature of such excitations in Bose systems with a single-particle condensate is the possibility of creation of solitary excitations. Nonequilibrium solitary excitations contribute to density fluctuations and their dispersion relation can therefore be observed directly in experiments on inelastic neutron scattering.[11]

The static SCF model describes single-particle excitations but does not permit taking into account the contribution of collective excitations to the thermodynamics. It should be emphasized that Bose and normal Fermi systems have an extremely important difference. In normal Fermi systems the contribution of collective excitations to the thermodynamics decreases with increasing temperature. For example, the heat capacity due to single-particle excitations is proportional to the temperature, while the heat capacity due to collective excitations is proportional to the temperature cubed. Because of this, the SCF model, the phenomenological version of which is the Fermi liquid theory, is well applicable for the description of Fermi systems at low temperatures. For Bose systems the situation is contrary. At sufficiently low temperatures, when the Bose system is found in a state with broken phase symmetry, the number of single-particle excitations decreases and, furthermore, by virtue of the presence of the gap in the energy spectrum, their contribution to the thermodynamic properties of the many-particle Bose system decreases. On the other hand, the contribution of collective excitations, which, as we have said, cannot be described in a static SCF model, increases. These same arguments also apply to uncharged Fermi systems with broken phase symmetry. The good agreement with experiment of the modern theory of superconductivity, which is a variant of the SCF theory, is due to the fact that the electron system is charged, resulting in an energy gap (the plasma frequency) in the spectrum of collective excitations, so that one can, to high accuracy, neglect the contribution of collective excitations to the thermodynamics of superconductors. The situation is different in superfluid ^{3}He, which is a neutral Fermi liquid. Here the description of the thermodynamic properties in the SCF approximation is less justified, and the role of collective excitations should be significant. In particular, taking the collective spin-wave excitations into account can explain the stability of the A phase of superfluid ^{3}He.[35]

The collective excitations can be taken into account in two ways. The most consistent from the standpoint of the microscopic description is to calculate the two-particle Green's function or the vertex function in a higher approximation than the SCF approximation. The quantum-field approach, perturbation theory, and the diagram technique for describing many-particle Fermi systems with broken symmetries on the basis of the SCF model as an initial approximation are developed in Ref. 19. This approach can be extended to Bose systems with broken symmetries. The other method of studying collective excitations is based on the use of the SCF equations generalized to the nonstationary case. By studying small oscillations one can establish the dispersion relation of the collective excitations. Such oscillations can be nonequilibrium and excited by an external influence, but the same oscillations are excited by a thermal method utilizing the energy of a heat bath in contact with the many-particle system. Considering the gas of collective excitations as ideal, one can calculate the contribution of collective excitations to the thermodynamics of the many-particle system.

The separation of the excitations of the many-particle system into single-particle and collective, like the concept of quasiparticles in general, is of an approximate character. The problem of separating excitations into collective and single-particle has been elaborated in greatest detail by Bohm and Pines for the case of the electron gas.[36] However, for arbitrary many-particle systems, especially those found in states with spontaneously broken symmetries, a consistent procedure for separating the single-particle and collective motions does not yet exist.

It should also be noted that there is a certain confusion in the terminology, which is reflected in the understanding of the physical essence of the approximations used. This is especially true for Bose systems. The many-particle problem can be reduced to a single-particle problem in only one case—in the ideal gas model with complete neglect of interparticle interactions. Every state in a system of interacting particles is a collective state, in the broad sense that it is determined by the states of all the particles of the system. Therefore, both the single-particle and the collective excitations discussed above are in this sense collective. This should be kept in mind when using a separation of excitations into single-particle and properly collective. It is natural to reserve the term ''collective'' for those excitations of a many-particle system which arise as a result of the quantization of its motion as a continuous medium. These excitations are manifested as a pole of the vertex function.

Collective excitations can be studied in a nonstationary SCF model. It can be shown that the nonstationary equations for the single-particle density matrix and wave function of the condensate are obtained from the stationary equations (35), (60), and (61), respectively, by the addition of the following time derivatives on the right-hand sides: $i\hbar\partial\chi/\partial t$, $i\hbar\partial\tilde{\rho}(x,x',t)/\partial t$, and $i\hbar\partial\tilde{\tau}(x,x',t)/\partial t$. Analysis of small oscillations shows that the nonstationary equations have a solution with a linear dispersion relation for $k\rightarrow 0$. The propagation velocity of these oscillations, $c_0=\sqrt{U_0 n/m}$ (n is the total particle number density), coincides with the quasiparticle velocity in the Bogolyubov theory.[20] These collective oscillations, with practically identical propagation velocities, exist in both the normal and superfluid phases. For the velocity of long-wavelength disturbances to be independent of the thermodynamic quantities, they must have a rather high frequency. These oscillations are the analog of zero sound, which was first studied in Fermi systems. At lower frequencies, in the hydrodynamic region, the sound velocity depends substantially on the thermodynamic variables. It is these excitations that form the linear part of the spectrum introduced by Landau.[10] The maxon–roton parts of this spectrum are apparently governed by single-particle excitations. On a qualitative level the problem of formation of a single spectrum from branches of excitations of different natures is discussed in Ref. 11.

As was shown in the framework of the relativistic field theory by Goldstone,[37] the breaking of the gauge symmetry gives rise to particles of zero mass. A number of papers (Refs. 38 and 39, for example) have been devoted to the generalization of the Goldstone result to nonrelativistic many-particle systems. As can be seen from the results of the present paper, in the SCF model the breaking of phase symmetry does not give rise to gapless excitations (the analog of zero-mass particles). Let us make a few remarks in this regard. We note that fields and many-particle systems are substantially different objects, and the results obtained in field theory do not automatically carry over to nonrelativistic many-particle systems. In field theory it is essentially a continuous medium that is quantized, and the particles that arise on quantization are the quanta of excitations of such a medium. In a many-particle system there are primary particles, and for this reason, as was discussed above, there are two possible types of excitations—single-particle and collective. Obviously the analog of the particles of field theory in a many-particle system are the collective excitations and not the single-particle excitations, the presence of which is due to the discrete structure of the medium, which is absent in field theory. Therefore, is appears that there are no grounds for expecting the appearance of single-particle excitations with an acoustic dispersion relation on the basis of the Goldstone result.[37] We note that in Fermi systems, too (even in the absence of the Coulomb interaction), the breaking of phase symmetry does not lead to the appearance of gapless excitations.

An essential feature of many-particle systems that does not have an analogy in quantum field theory is the noninvariance of this system with respect to the Galileo group by virtue of of the finite particle number density. The breaking of Galilean invariance is responsible for the appearance of Goldstone collective excitations—phonons. Do new Goldstone collective excitations arise in a system with a finite particle number density upon the breaking of phase symmetry? It is known that such excitations do not arise in the case of a Fermi system. Apparently, the situation is similar in many-particle Bose systems. This is also indicated by the results of experimental studies of the spectrum of excitations in ^{4}He by the method of inelastic neutron scattering. The linear part of the spectrum is found to be practically insensitive to the point of the transition of liquid ^{4}He to the superfluid state (see Ref. 11 and the literature cited therein). This same result, as we have said, follows from the nonstationary SCF equations. Let us conclude our brief discussion of this important question by noting that the generalization of the Goldstone result[37] to nonrelativistic systems has usually been done with the use of model Hamiltonians of the Heisenberg ferromagnet type. Analysis of the connection between the breaking of the symmetry and possible excitations for realistic many-particle Hamiltonians of the type (1) remains a topical problem.

CONCLUSION

The static SCF model describes the contribution of single-particle above-condensate excitations and condensate states to the thermodynamics of a many-particle system. For Fermi systems at low temperatures this contribution is the governing one. Therefore, the theory based on a single-particle description for Fermi systems can be used for studying real systems in this case. For Bose systems this is not the case, since here the contribution to the thermodynamics from single-particle excitations falls off with decreasing temperature, while the contribution of the collective excitations increases. A consistent relativistic theory of many-particle Bose systems should take into account the collective as well as the single-particle excitations. Although the static SCF model does not meet this requirement, its theoretical study is important for several reasons. First, it permits a better understanding of the structure of the state of a Bose system with broken phase invariance; in particular, it can demonstrate the substantial difference of such a state from the state of an ideal Bose gas with a condensate. Second, it allows one to find the contribution of the single-particle degrees of freedom to the observable characteristics of the system. Third, the proposed model serves as a natural initial approximation for constructing a quantum-field perturbation theory and diagram technique for Bose systems with spontaneously broken symmetries, analogous to that developed for Fermi systems in Ref. 19.

The author is grateful to I. V. Bogoyavlenskii and L. V. Karnatsevich for many helpful discussions of the experimental research on the Bose condensate and the spectrum of excitations in liquid ^{4}He by the neutron scattering method, and also to A. S. Bakai and S. V. Peletminskii for a discussion of this study.

[*] E-mail: antarasov@kipt.kharkov.ua

---

[1] D. R. Hartree, *The Calculation of Atomic Structures*, Wiley, New York (1957), Izd. Inostr. Lit., Moscow (1960).
[2] V. Fock, Z. Phys. **61**, 126 (1930).
[3] B. I. Barts, Yu. L. Bolotin, E. V. Inopin, and V. Yu. Gonchar, *The Hartree-Fock Method in the Theory of the Nucleus* [in Russian], Naukova Dumka, Kiev (1982).
[4] J. C. Slater, *The Self-Consistent Field for Molecules and Solids* [McGraw-Hill, New York (1974), Mir, Moscow (1978)].
[5] N. N. Bogolyubov, Dokl. Akad. Nauk SSSR **119**, 224 (1958) [*sic*].
[6] A. Griffin, Phys. Rev. B **53**, 9341 (1996).
[7] C. C. Bradley, C. A. Sackett, J. J. Tollett, and R. G. Hulet, Phys. Rev. Lett. **75**, 1687 (1995).
[8] K. B. Davis, M. O. Mewes, M. R. Andews, N. J. van Druten, D. S. Durfee, D. M. Kurn, and W. Ketterle, Phys. Rev. Lett. **75**, 3969 (1995).
[9] N. N. Bogolyubov and N. N. Bogolyubov Jr., *Introduction to Quantum Statistical Mechanics*, World Scientific, Singapore (1982), Nauka, Moscow (1984).
[10] L. D. Landau, J. Phys. USSR **11**, 91 (1947).
[11] Yu. M. Poluéktov and L. V. Karnatsevich, "Energetic excitations in liquid ^{4}He and their manifestation in the neutron scattering spectrum" [in Russian], Preprint KhFTI, Kharkov, 2001-1 (2001).
[12] V. V. Krasil'nikov and S. V. Peletminskiĭ, Fizika ÉChAYa **24**, 463 (1993) [Phys. Part. Nucl. **24**, 200 (1993)].
[13] A. L. Fetter, Ann. Phys. (N.Y.) **70**, 67 (1972).
[14] S. I. Shevchenko, Fiz. Nizk. Temp. **18**, 328 (1992) [Low Temp. Phys. **18**, 223 (1992)].
[15] Yu. M. Poluéktov, Fiz. Nizk. Temp. **22**, 402 (1996) [Low Temp. Phys. **22**, 313 (1996)].
[16] M. Girardeau and R. Arnowitt, Phys. Rev. B **113**, 755 (1959).
[17] P. S. Kondratenko, Theor. Math. Phys. **22**, 278 (1975).
[18] I. V. Bogoyavlenskiĭ, L. V. Karnatsevich, Zh. A. Kozlov, and A. V. Puchkov, Fiz. Nizk. Temp. **16**, 139 (1990) [Sov. J. Low Temp. Phys. **16**, 77 (1990)].
[19] Yu. M. Poluéktov, Vestnik Kharkovskogo Universiteta Ser. Fiz.: "Yadra, Chastitsy, Polya" **522**, 3 (2001).
[20] N. N. Bogolyubov, Izv. AN SSSR Ser. Fiz. **11**, 77 (1947).
[21] A. Bijl, Physica **7**, 869 (1940).
[22] G. Wentzel, Phys. Rev. **120**, 1572 (1960).
[23] M. Luban, Phys. Rev. **128**, 965 (1962).
[24] V. V. Tolmachev, Dokl. Akad. Nauk SSSR **135**, 825 (1960) [Sov. Phys. Dokl. **5**, 1267 (1960)].
[25] N. M. Hugenholtz and D. Pines, Phys. Rev. **116**, 489 (1959).
[26] S. T. Belyaev, Zh. Éksp. Teor. Fiz. **34**, 417 (1958) [Sov. Phys. JETP **7**, 289 (1958)].
[27] D. Pines, *The Many-Body Problem*, Benjamin, New York (1961), Izd. Inostr. Lit., Moscow (1963).
[28] Yu. A. Nepomnyashchiĭ and A. A. Nepomnyashchiĭ, Zh. Éksp. Teor. Fiz. **75**, 976 (1978) [Sov. Phys. JETP **48**, 493 (1978)].
[29] V. N. Popov and A. V. Serednyakov, Zh. Éksp. Teor. Fiz. **77**, 377 (1979) [Sov. Phys. JETP **50**, 193 (1979)].
[30] I. A. Malkin and V. I. Man'ko, *Dynamical Symmetry and Coherent States of Quantum Systems* [in Russian], Nauka, Moscow (1979).
[31] L. D. Landau, Zh. Éksp. Teor. Fiz. **30**, 1056 (1956) [*sic*].
[32] Yu. M. Poluéktov, Fiz. Nizk. Temp. **21**, 300 (1995) [Low Temp. Phys. **21**, 228 (1995)].
[33] V. V. Krasil'nikov, S. V. Peletminskiĭ, A. A. Rozhkov, and A. A. Yatsenko,

Fizika ÉChAYa **19**, 1440 (1988) [*sic*].
[34] J. M. Ziman, *Electrons and Phonons* [Clarendon Press, Oxford (1960); Izd. Inostr. Lit., Moscow (1962)].
[35] A. J. Leggett, Rev. Mod. Phys. **47**, 331 (1975).
[36] D. Bohm and D. Pines, Phys. Rev. **92**, 609 (1953).
[37] J. Goldstone, Nuovo Cimento **19**, 154 (1961).
[38] H. Wagner, Z. Phys. **195**, 273 (1966).
[39] R. V. Lange, Phys. Rev. **146**, 301 (1966).

Translated by Steve Torstveit

LATTICE DYNAMICS

Lattice dynamics and heat capacity of a two-dimensional monoatomic crystal on a substrate

T. N. Antsygina,* I. I. Poltavsky, M. I. Poltavskaya, and K. A. Chishko

B. Verkin Institute for Low Temperature Physics and Engineering, National Academy of Sciences of Ukraine, pr. Lenina 47, 61103 Kharkov, Ukraine

(Submitted December 20, 2001; revised February 13, 2002)
Fiz. Nizk. Temp. **28**, 621–634 (June 2002)

A model is proposed which gives an analytical description of the dynamics of collective excitations of two-dimensional close-packed atomic crystal lattices (atomic monolayers on substrates). The model takes into account both the interaction between atoms of the layer and the interaction of the layer with the substrate. The phonon spectra are found for an ideal triangular lattice and for a triangular lattice with a uniform distortion along one of the close-packed directions in the plane of the layer. The temperature dependence of the heat capacity is constructed for crystalline structures of both the commensurate and incommensurate types (in relation to the substrate). The theoretical results obtained are used for a detailed discussion and interpretation of the published experimental data on the spectra of lattice excitations and the heat capacity of monolayers of rare gases, including ^{3}He and ^{4}He, on various types of substrates. © *2002 American Institute of Physics.* [DOI: 10.1063/1.1491185]

1. INTRODUCTION

Investigation of the thermodynamic properties of two-dimensional (2D) cryocrystals (solid mono- and multilayer atomic and molecular substances on substrates of various natures) is an important problem in low-temperature condensed matter physics. Low-dimensional systems, both structurally ordered and disordered, have been actively studied for many years (a review of the problematics involved with such systems and a listing of the vast literature on this topic are given in Ref. 1). Among such systems cryocrystals are a special group of objects having some unique features in their low-temperature thermodynamics and kinetics.[2]

The experimental technique has now become sophisticated enough that one can not only study the structure and thermodynamics of 2D cryocrystals but also measure directly the dispersion curves of their phonon modes even for a single layer of adatoms on a substrate. As to the theoretical description of the phonon spectra of 2D crystals, here usually either a long-wavelength approximation is used[2,3] or the calculation is done by numerical methods.[4–6] Thus the problem of obtaining the corresponding dispersion relations in analytical form is clearly a topical one; first, it would permit an unambiguous interpretation of the experimental data on the spectra, and second, it would be useful for studying the thermodynamic and kinetic properties of such systems.

The goal of the present study is to construct a theoretical model giving an analytical description of the dynamics of collective excitations and of the thermodynamics of 2D atomic crystal lattices on substrates. The phonon spectra are calculated for an ideal triangular lattice and a triangular lattice with a uniform distortion along one of the close-packing directions in the plane of the layer. The theoretical results obtained in this study are applicable for the detailed discussion and interpretation of the existing published experimental data on the spectra of lattice excitations and the heat capacity of 2D cryocrystals on graphite and metals.

2. STATEMENT OF THE PROBLEM

We consider a layer of rare gas atoms of mass M lying on a substrate and forming a triangular lattice in the $z=0$ plane. The z axis of a Cartesian coordinate system is chosen perpendicular to the layer and directed outward from the substrate, and the origin is placed at one of the lattice sites. The interaction of adsorbed atoms (adatoms) with one another, the so-called lateral interaction $V_1(\mathbf{r})$ (where $\mathbf{r}$ is the three-dimensional radius vector, $\mathbf{r}=(\mathbf{R},z)$, $\mathbf{R}=(x,y)$), can be described in the atom–atom interaction model and is a function of the interatomic distance r.[7] The potential $V_1(r)$ is assumed to be short-ranged, so that for our purposes it is sufficient to limit consideration to the nearest neighbors only (the coordination number in the layer $z_a=6$). As to the interaction of the atoms of the monolayer and atoms of the substrate, $V_2(\mathbf{r})$, its explicit form depends substantially on the substrate material. Graphite or various metals are commonly used for this purpose.

In the case of metallic substrates a substantial role in the interaction with the adsorbate is played by free electrons, so that the approximation of the atom–atom potentials for describing the adsorbate–substrate interaction in such systems is inadequate. The explicit form of $V_2(\mathbf{r})$ is the subject of active discussion in the literature (see, e.g., the review[8]). In the general case, with allowance for the periodicity of $V_2(\mathbf{r})$ in the $x0y$ plane, it can be written in the form

$$V_2(\mathbf{r})=U_0(z)+\sum_{\mathbf{G}\neq 0} U_{\mathbf{G}}(z)\exp(i\mathbf{G}\cdot\mathbf{R}), \tag{1}$$

where $\mathbf{G}$ is the 2D reciprocal lattice vector of the periodic field of the substrate. The quantity $U_0(z)$ is the so-called surface-averaged potential. Attempts to obtain an analytical expression for $U_0(z)$ have been undertaken,[8] but its explicit form has still not been conclusively established. Only its asymptotic behavior at large distances is known exactly: $U_0(z) \propto -c/z^3$ (Ref. 9), where the coefficient c depends on both the dielectric constant of the metal and the polarizability of the adsorbate atom. Calculations of the repulsive term in $U_0(z)$ have been done in Refs. 10 and 11, where it is shown that in the case of substrates of noble metals the repulsive part of $U_0(z)$ falls off exponentially with distance. At the present time the potential most often used for describing the interaction of atoms of a monolayer with a metal is the three-parameter Vidali–Cole–Klein potential,[11] which takes into account the above-mentioned features of the behavior of $U_0(z)$ at both long and short distances. As to the Fourier amplitudes $U_{\mathbf{G}}(z)$, it is known that they depend on the form of the surface and fall off very rapidly with increasing $|\mathbf{G}|$. Therefore, as a rule, only the first harmonic is taken into account in Eq. (1) (see, e.g., Refs. 6 and 12). As a result, expression (1) takes the form

$$V_2(\mathbf{r}) = U_0(z) + U_1(z) \sum_j \exp(i\mathbf{G}_j \cdot \mathbf{R}), \tag{2}$$

where the summation is done over the shortest reciprocal lattice vectors.

The interaction of adsorbate atoms with graphite is quite often described by a sum of pair potentials of the Lennard-Jones type.[13–15] Such a treatment, however, does not adequately take into account the covalence of graphite. Attempts to improve the description of this interaction have led[13] to an expression for $V_2(\mathbf{r})$ which is analogous to Eq. (2).

Still another rather widely used type of substrate is graphite or a metal coated by a sublayer of an inert element (most often argon). Studies have shown[16] that such a coating makes the adsorbing surface smoother and more uniform in comparison with the bare substrate. A remarkable property of such systems is that the behavior of an adsorbate deposited on the coated substrate does not depend on the material of the bare substrate, and even in the case when the coating is only a single layer its role in the interaction with the adsorbate turns out to be decisive.[16] Thus in considering these systems the substrate can be assumed to be insulating, and for $V_2(\mathbf{r})$ one may use a model of short-range atom–atom potentials.

It is well known that a monolayer of adatoms can form both commensurate (epitaxial) and incommensurate structures. Commensurate structures, whose periods are multiples of the lattice periods of the substrate, are formed only for certain coverage densities ρ (the number of adatoms per unit area). In this case all of the adatoms occupy positions corresponding to minima of the periodic surface potential relief $V_2(\mathbf{r})$. Thus each adatom moves in a local potential well created by the substrate, and in a description of its motion it is necessary to take into account the dependence of $V_2(\mathbf{r})$ on all three components of the vector $\mathbf{r}$.

With increasing coverage density the interaction between adatoms increases, and this interaction is what determines the structure of the monolayer. In this case close-packed incommensurate films are formed, and all of the atoms are found under different conditions, in the sense of interaction with the substrate, so that the layer "feels" the potential of the substrate as a whole, and the dependence of $V_2(\mathbf{r})$ on $\mathbf{R}$ becomes inessential. Therefore, for describing the dynamics of the layer it seems natural to use a potential averaged over the variable $\mathbf{R}$:[3,4]

$$V_s(z) = \frac{1}{S} \int_S V_2(\mathbf{r})\, d\mathbf{R}, \tag{3}$$

where S is the surface area of the substrate. For incommensurate lattices the parameters of their structure typically can be varied continuously (by varying ρ) at constant values of the lattice parameters of the substrate.

It should be noted, however, that for certain systems the formation of commensurate structure is impossible in principle, since the diameter of the adatoms exceeds the characteristic distance between the adsorption centers on the substrate. An example of this kind is xenon on graphite.

3. EXCITATION SPECTRUM OF A MONOLAYER WITH AN IDEAL TRIANGULAR LATTICE

Let us calculate the phonon excitation spectrum of a rare gas atomic monolayer on a substrate for the case when the adatoms form an ideal triangular lattice. The approach set forth below makes it possible to describe in a unified way both epitaxial (commensurate) and nonepitaxial (incommensurate) films deposited on substrates of various types and to obtain the dispersion relations for their phonon excitation in explicit form.

The Hamiltonian of the system under study is written in the harmonic approximation as

$$H = \frac{1}{2M} \sum_{\mathbf{f}} \mathbf{p}_{\mathbf{f}}^2 + \frac{\kappa_1^2}{2} \sum_{\mathbf{f},\boldsymbol{\delta}} (\boldsymbol{\delta} \cdot \mathbf{u}_{\mathbf{f},\boldsymbol{\delta}})^2 + \frac{q}{2} \sum_{\mathbf{f},\boldsymbol{\delta}} \mathbf{u}_{\mathbf{f},\boldsymbol{\delta}}^2 + \frac{\kappa_2^2}{2} \sum_{\mathbf{f}} u_{\mathbf{f}}^{\alpha} u_{\mathbf{f}}^{\alpha} + \frac{\kappa_3^2}{2} \sum_{\mathbf{f}} u_{\mathbf{f}}^{z} u_{\mathbf{f}}^{z}, \tag{4}$$

where $\mathbf{u}_{\mathbf{f}}$ is the displacement of an atom found at a site $\mathbf{f}$ from its equilibrium position, $\mathbf{u}_{\mathbf{f},\boldsymbol{\delta}} = \mathbf{u}_{\mathbf{f}} - \mathbf{u}_{\mathbf{f}+\boldsymbol{\delta}}$, $\mathbf{p}_{\mathbf{f}} = -i\partial/\partial \mathbf{u}_{\mathbf{f}}$, $\boldsymbol{\delta}$ are the unit vectors connecting the nearest neighbors in the layer, and $\alpha = x, y$. Here and below we use a system of units in which Planck's constant $\hbar$ and Boltzmann's constant k_B are equal to unity. In writing Hamiltonian (4) we have assumed that the atoms of the substrate are immobile (rigid substrate). This conventional assumption[3,4,7,17] is justified for the systems under consideration because the elastic constants of the substrate materials are much higher than those of the adsorbate.

The second and third terms in (4) are due to the interatomic interaction in the layer:

$$= \kappa_1^2 = \frac{1}{2} \left[V_1''(R_0) - \frac{V_1'(R_0)}{R_0} \right], \quad q = \frac{V_1'(R_0)}{2R_0}. \tag{5}$$

Here R_0 is the equilibrium distance between nearest-neighbor atoms of the monolayer, and the prime denotes differentiation with respect to the argument. We note that for anharmonic crystals or crystals under pressure the derivative

$V_1'(R_0)$ is nonzero even in the case of an interaction only between nearest neighbors. However, the dominant role is played by higher derivatives with respect to R_0, since the effective intermolecular potential V_1 is a rapidly varying function of R_0. The last two terms in (4) arise on account of the interaction of the atoms of the monolayer with the substrate. Here the explicit form of the coefficients κ_2 and κ_3 are determined both by the substrate material and by whether or not the structures of the monolayer and substrate are commensurate.

Let us first consider epitaxial films. Calculations for this class of systems will be done for the particular case of the so-called $(\sqrt{3}\times\sqrt{3})R30°$ structure, which is most often discussed in the literature.[1] In the case when the interaction of the atoms of the monolayer and substrate can be described in the short-range atom–atom interaction model, the coefficients κ_2 and κ_3 have the form

$$\kappa_2^2=\frac{\sigma^2}{2}V_2''(r_0),$$

$$\kappa_3^2=(z_s-\sigma^2)V_2''(r_0)=2\kappa_2^2\left(\frac{z_s}{\sigma^2}-1\right), \tag{6}$$

where r_0 is the equilibrium distance between an atom of the layer and its nearest neighbor in the substrate, determined from the equation of equilibrium $V_2'(r_0)=0$, z_s is the number of nearest neighbors in the substrate, and σ is a dimensionless geometric parameter relating R_0 and r_0: for a substrate with a hexagonal structure $z_s=6$ and $\sigma=\sqrt{2/3}(R_0/r_0)$, and for substrates with a triangular lattice $z_s=3$ and $\sigma=R_0/r_0$. In the case when the interaction with the substrate is described by expression (2), the corresponding coefficients take the form

$$\kappa_2^2=-48\pi^2\frac{U_1(0)}{R_0^2},\quad \kappa_3^2=[U_0''(z)+6U_1''(z)]|_{z=0}. \tag{7}$$

For incommensurate films the coefficients κ_2 and κ_3 can be written in a unified way for all types of interactions. Using (3), we arrive at Hamiltonian (4) in which

$$\kappa_2^2=0,\quad \kappa_3^2=V_s''(z)|_{z=0}. \tag{8}$$

After a Fourier transformation the Hamiltonian (4) becomes

$$\begin{aligned}H=&\frac{1}{2M}\sum_{\mathbf{k}}\mathbf{p}_{\mathbf{k}}\cdot\mathbf{p}_{-\mathbf{k}}+\left[\left(\frac{\kappa_1^2}{2}+q\right)z_a+\frac{\kappa_2^2}{2}\right]\\&\times\sum_{\mathbf{k}}\mathbf{u}_{\mathbf{k}}\cdot\mathbf{u}_{-\mathbf{k}}-\kappa_1^2\sum_{\mathbf{k},\boldsymbol{\delta}}\delta_\alpha\delta_\beta u_{\mathbf{k}}^\alpha u_{-\mathbf{k}}^\beta\\&\times\exp(i\mathbf{k}\cdot\boldsymbol{\delta}R_0)-q\sum_{\mathbf{k},\boldsymbol{\delta}}\mathbf{u}_{\mathbf{k}}\cdot\mathbf{u}_{-\mathbf{k}}\exp(i\mathbf{k}\cdot\boldsymbol{\delta}R_0)\\&-\frac{1}{2}(\kappa_1^2z_a+\kappa_2^2-\kappa_3^2)\sum_{\mathbf{k}}u_{\mathbf{k}}^zu_{-\mathbf{k}}^z,\quad(\alpha,\beta=x,y).\end{aligned} \tag{9}$$

Further simplification in the problem can be achieved by taking into consideration that the inverse coordination number for the neighbors in the layer, $1/z_a$ ($z_a=6$), is a rather small quantity. This allows one to replace the summation over nearest neighbors by an integration over a circle of unit radius. In other words, we shall assume that for an arbitrary function $F(\boldsymbol{\delta})$ the following relation holds:

$$\frac{1}{z_a}\sum_{\boldsymbol{\delta}}F(\boldsymbol{\delta})\to\frac{1}{2\pi}\int d\boldsymbol{\omega}F(\boldsymbol{\omega}). \tag{10}$$

The sums over $\boldsymbol{\delta}$ in Hamiltonian (9) can be evaluated using the obvious symmetry

$$\begin{aligned}\frac{1}{z_a}\sum_{\boldsymbol{\delta}}\delta_\alpha\delta_\beta\exp(i\mathbf{k}\cdot\boldsymbol{\delta}R_0)\to&\frac{1}{2\pi}\int d\varphi\exp(i\mathbf{k}\cdot\boldsymbol{\omega}R_0)\\&\times\omega_\alpha\omega_\beta=A_0n_{\mathbf{k}}^\alpha n_{\mathbf{k}}^\beta+B_0\Delta_{\alpha,\beta},\end{aligned} \tag{11}$$

where $\mathbf{n}_{\mathbf{k}}=\mathbf{k}/k$. The coefficients A_0 and B_0 are determined from the following system of equations:

$$A_0+2B_0=\frac{1}{2\pi}\int d\varphi\exp(i\mathbf{k}\cdot\boldsymbol{\omega}R_0)=J_0(kR_0),$$

$$\begin{aligned}A_0+B_0=&\frac{1}{2\pi}\int d\varphi\exp(i\mathbf{k}\cdot\boldsymbol{\omega}R_0)(\mathbf{n}_{\mathbf{k}}\cdot\boldsymbol{\omega})^2\\&=J_0(kR_0)-\frac{J_1(kR_0)}{kR_0}.\end{aligned}$$

As a result, we find

$$A_0=-J_2(x),\quad B_0=\frac{J_1(x)}{x},\quad x=kR_0, \tag{12}$$

where $J_n(x)$ is a Bessel function of the first kind. Using (11) and (12) and performing a number of manipulations, we obtain for the Hamiltonian (9)

$$\begin{aligned}H=&\frac{1}{2M}\sum_{\mathbf{k}}\mathbf{p}_{\mathbf{k}}\cdot\mathbf{p}_{-\mathbf{k}}+\frac{1}{2}\sum_{\mathbf{k}}F_1^{(0)}(x)u_{\mathbf{k}}^\alpha u_{-\mathbf{k}}^\alpha\\&+\frac{1}{2}\sum_{\mathbf{k}}F_2^{(0)}(x)(\mathbf{n}_{\mathbf{k}}\cdot\mathbf{u}_{\mathbf{k}})(\mathbf{n}_{\mathbf{k}}\cdot\mathbf{u}_{-\mathbf{k}})\\&+\frac{1}{2}\sum_{\mathbf{k}}F_3^{(0)}(x)u_{\mathbf{k}}^zu_{-\mathbf{k}}^z.\end{aligned} \tag{13}$$

Here we have introduced the notation

$$\begin{aligned}F_1^{(0)}&=\kappa_2^2+z_a(\kappa_1^2+2q)(1-2B_0)-2z_aqA_0\\&=\kappa_2^2+z_a(\kappa_1^2+2q)[1-J_0(x)]-z_a\kappa_1^2J_2(x),\\F_2^{(0)}(x)&=-2z_a\kappa_1^2A_0=2z_a\kappa_1^2J_2(x),\\F_3^{(0)}(x)&=\kappa_3^2+2z_aq(1-A_0-2B_0)\\&=\kappa_3^2+2z_aq[1-J_0(x)].\end{aligned} \tag{14}$$

Using the standard procedure for calculating the spectrum, we obtain for the longitudinal (l) and two transverse (t,z) phonon modes

$$\omega_{l,t}^2(x)=\Delta^2(\Omega^2+D)[1-J_0(x)]\pm\Omega^2J_2(x), \tag{15}$$

$$\omega_z^2(x)=\Delta_z^2+D[1-J_0(x)], \tag{16}$$

where

$$\Delta^2=\frac{\kappa_2^2}{M},\quad \Delta_z^2=\frac{\kappa_3^2}{M},\quad \Omega^2=z_a\frac{\kappa_1^2}{M},\quad D=2z_a\frac{q}{M}. \tag{17}$$

Expressions (15) and (16) have physical meaning only for $k\leqslant k_D$, where $k_D=R_0^{-1}\sqrt{8\pi/\sqrt{3}}$ is the Debye wave number. As we see from relation (17), the values of Δ and Δ_z are determined completely by the interaction parameters of the atoms of the monolayer with the substrate. In a commensurate phase, when κ_2 is nonzero, all branches of the phonon spectrum have gaps at the Brillouin zone center (at $\mathbf{k}=0$), equal to Δ for modes l and t in the plane of the layer (in-plane modes) and to Δ_z for the mode polarized perpendicular to the layer (out-of-plane mode). Here, if the interaction with the substrate $V_2(\mathbf{r})$ is described in the model of atom–atom potentials, then by virtue of Eq. (6) the values of the gaps Δ and Δ_z are related as $\Delta_z/\Delta=[2(z_s/\sigma^2-1)]^{1/2}$. In the case of a metallic substrate, when $V_2(\mathbf{r})$ is given by Eq. (2), the values of the gaps are formally independent. It follows from Eq. (8) that $\kappa_2=0$ for incommensurate monolayers, and for them the in-plane modes are acoustic (gapless), whereas the z mode, as before, has a gap. We stress that the dispersion of the z mode is determined by the coefficient D [see Eq. (17)], which is proportional to the first derivative of the potential V_1. Since, as we have said, this derivative is small, the dispersion of the out-of-plane mode is rather weak This is just the type of behavior that was observed experimentally in Refs. 5, 6, and 18.

We note that the phonon spectrum in the problem under consideration can be calculated exactly, but the expressions obtained are rather awkward and will not be given here. For illustration of the efficiency of the proposed approach we show in Fig. 1 the dependence $\omega_l(kR_1)$ determined by the relation (15) in comparison with the exact spectrum for two directions of $\mathbf{k}$. It follows from Fig. 1 that everywhere in the Brillouin zone, relation (15) gives a rather good quantitative description for the experimentally measured longitudinal mode of the phonon spectrum of a 2D triangular lattice.

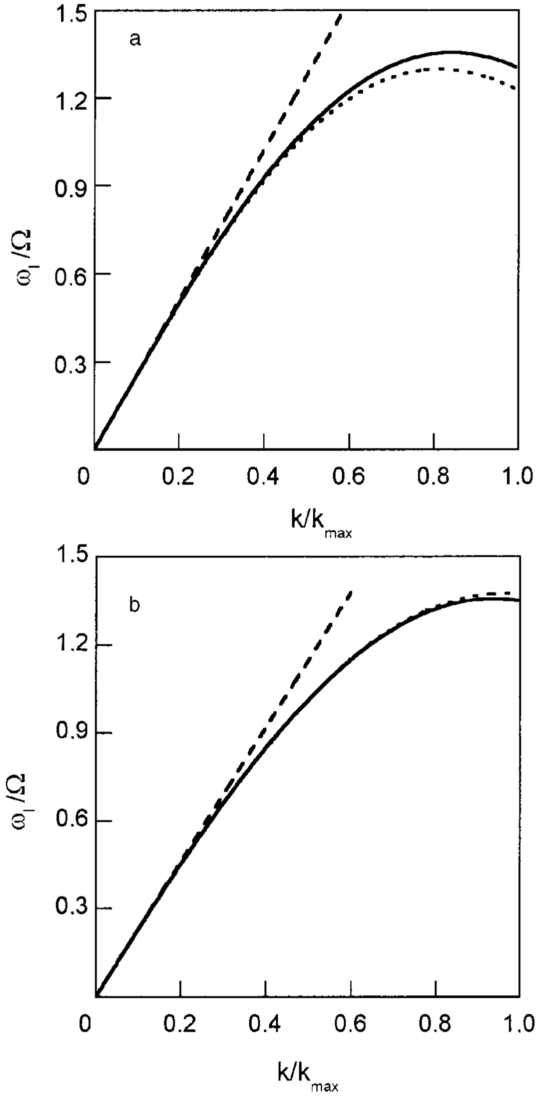

FIG. 1. Dispersion curves for the longitudinal mode, ω_l/Ω versus $k/k_{\max}$, where $k_{\max}$ is the Brillouin zone boundary ($D=0$, $\Delta=0$). The solid curves correspond to Eq. (15), the dashed curves to the exact spectrum for directions of the wave vector along the $0x$ axis (a) and at an angle of $\pi/12$ to the $0x$ axis (b); the dotted curve is the Debye approximation.

4. SPECTRUM OF EXCITATIONS IN A MONOLAYER WITH UNIFORM DISTORTION

The approach proposed above also allows one to consider the case in which the structure of the monolayer is not strictly triangular but has a slight uniform dilatation (or compression) along one of the close-packed directions of the initial ideal lattice. Such a situation arises, for example, when adatoms are deposited on a substrate formed by a cut along a non-close-packed plane of a cubic crystal.[1,18] Here a structure is formed with a quasi-triangular lattice, in which the distance to two of the nearest neighbors (for specificity we shall assume that they lie on the $0x$ axis) is equal to a, while the distance to each of the other four is a_1 (see Fig. 2), so that $|a_1-a|/a\ll 1$. Furthermore, it assumed that the area of the unit cell is unchanged by the distortion. We limit consideration to the lowest order of perturbation theory in the parameter $|a_1-a|/a$. In this case the Hamiltonian has a form analogous to (9) but with the arguments of the exponential functions changed from $\mathbf{k}\cdot\boldsymbol{\delta}R_0$ to $\mathbf{k}\cdot\mathbf{R}_\delta$, where $\mathbf{R}_\delta$ are the vectors connecting the nearest neighbors in the distorted lattice. The unit vectors $\boldsymbol{\delta}$ as before are directed to the nearest neighbors in the ideal lattice (see Fig. 2). Actually, the correction to the Hamiltonian from the increments to these vectors is a quantity of second order in the distortion and can be neglected. We also note that, in relations (5) the parameter R_0 should be replaced by $(a+2a_1)/3$.

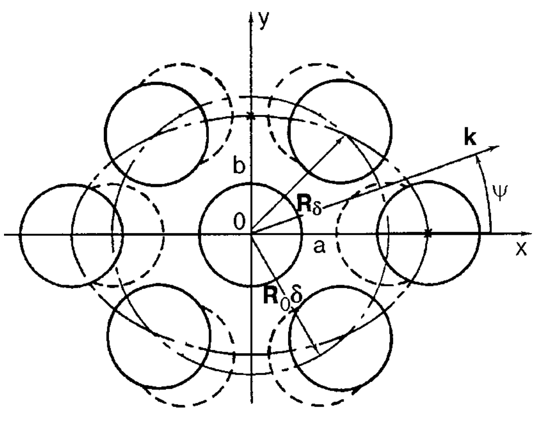

FIG. 2. Configuration of the cell of a triangular lattice with distortion.

As in the case of an ideal triangular lattice, we replace the summation over nearest neighbors by integration over an ellipse with semiaxes a and $b=a\sqrt{[4(a_1/a)^2-1]/3}$. In lowest order of perturbation theory in the parameter $\xi=(a-b)/a\ll 1$ we obtain

$$\frac{1}{z_a}\sum_{\boldsymbol{\delta}} \delta_\alpha \delta_\beta \exp(i\mathbf{k}\cdot\mathbf{R}_{\boldsymbol{\delta}}) \to A n_{\mathbf{k}}^{\alpha} n_{\mathbf{k}}^{\beta} + B\Delta_{\alpha,\beta} + Q(\Delta_{\alpha,x}\Delta_{\beta,x}-\Delta_{\alpha,y}\Delta_{\beta,y}). \tag{18}$$

Here

$$A=A_0+A_1, \quad B=B_0+B_1,$$

$$A_1=-\frac{\xi y}{4}\{J_1(y)-J_3(y)-\cos 2\psi[J_3(y)-J_5(y)]\},$$

$$B_1=-\frac{\xi}{2}\{J_2(y)+\cos 2\psi[J_2(y)-2J_4(y)]\},$$

$$Q=-\frac{\xi}{2}\{J_2(y)-J_4(y)\},$$

where $A_0(y)$ and $B_0(y)$ are given by Eq. (12), $y=kb$, and ψ is the angle between the $0x$ axis and the wave vector direction. Using the expressions obtained, we write the Hamiltonian of the system as

$$H=\frac{1}{2M}\sum_{\mathbf{k}} \mathbf{p}_{\mathbf{k}}\cdot\mathbf{p}_{-\mathbf{k}} + \frac{1}{2}\sum_{\mathbf{k}} F_1(y) u_{\mathbf{k}}^{\alpha} u_{-\mathbf{k}}^{\alpha} + \frac{1}{2}\sum_{\mathbf{k}} F_2(y) \times(\mathbf{n}_{\mathbf{k}}\cdot\mathbf{u}_{\mathbf{k}})(\mathbf{n}_{\mathbf{k}}\cdot\mathbf{u}_{-\mathbf{k}}) + \frac{1}{2}\sum_{\mathbf{k}} F_3(y) u_{\mathbf{k}}^{z} u_{-\mathbf{k}}^{z} + \frac{1}{2}\sum_{\mathbf{k}} \mathcal{F}(y)(u_{\mathbf{k}}^{x}u_{-\mathbf{k}}^{x}-u_{\mathbf{k}}^{y}u_{-\mathbf{k}}^{y}), \tag{19}$$

where F_i are related to A and B by the same expressions that relate $F_i^{(0)}$ with A_0 and B_0 [see Eq. (14)], and $\mathcal{F}(y)=-2\kappa_1^2 z_a Q$.

In the anisotropic case, as for the ideal triangular lattice, the z mode polarized perpendicular to the plane of the layer separates out. The equations of motion for the in-plane displacement components $u_{\mathbf{k}}^{x}$ and $u_{\mathbf{k}}^{y}$ become nonequivalent because Eq. (19) contains an additional [as compared to (13)] term linear in the parameter ξ, and they take the form

$$(m\omega^2 \mp \mathcal{F} - F_1)u_{\mathbf{k}}^{x,y} - F_2 n_{\mathbf{k}}^{x,y}(\mathbf{n}_{\mathbf{k}}\cdot\mathbf{u}_{\mathbf{k}})=0. \tag{20}$$

As we see from system (20), for the majority of directions of the wave vector $\mathbf{k}$ there are no solutions in the form of waves with purely longitudinal or purely transverse polarization in the plane of the layer. This situation is completely analogous to the three-dimensional case, where this circumstance is one of the main manifestations of anisotropy the crystal.[19] Because of the smallness of ξ, we can seek the solution of system (20) in the form of a sum of quasilongitudinal $\mathbf{u}_{\mathbf{k}}^{\|}$ and quasitransverse $\mathbf{u}_{\mathbf{k}}^{\perp}$ modes:

$$\mathbf{u}_{\mathbf{k}}=\mathbf{u}_{\mathbf{k}}^{\|}+\mathbf{u}_{\mathbf{k}}^{\perp},$$

$$\mathbf{u}_{\mathbf{k}}^{\|}=u_{\mathbf{k}}^{\|}(\mathbf{n}_{\mathbf{k}}+\nu\mathbf{e}_{\mathbf{k}}), \quad \mathbf{u}_{\mathbf{k}}^{\perp}=u_{\mathbf{k}}^{\perp}(\mathbf{e}_{\mathbf{k}}-\nu\mathbf{n}_{\mathbf{k}}), \tag{21}$$

where the unit vectors $\mathbf{n}_{\mathbf{k}}$ and $\mathbf{e}_{\mathbf{k}}$ satisfy the relation $(\mathbf{n}_{\mathbf{k}}\cdot\mathbf{e}_{\mathbf{k}})=0$. Substituting (21) into (20), we obtain

$$\nu=\frac{\mathcal{F}}{F_2}\sin 2\psi=\frac{\xi}{2}[1-J_4(y)/J_2(y)]\sin 2\psi, \tag{22}$$

and the corresponding dispersion relations for the quasilongitudinal (‖), quasitransverse (⊥), and z modes have the form

$$\omega_{\|,\perp}^2=\omega_{l,t}^2+\xi\{2(\Omega^2+D)\Lambda_0(y)\pm\Omega^2[\Lambda_0(y)-\Lambda_1(y)]\}, \tag{23}$$

$$\tilde{\omega}_z^2=\omega_z^2+2\xi D\Lambda_0(y), \tag{24}$$

where

$$\Lambda_n=\frac{y}{8}\{2J_{2n+1}(y)+[(-1)^n J_1(y)-J_{2n+3}(y)]\cos 2\psi\}.$$

It is easy to see that for $\xi=0$ relations (23) and (24) go over the expressions (15) and (16) for the frequencies in the isotropic case.

It follows from Eq. (22) that only in-plane excitations that propagate along axes of twofold symmetry (the $0x$ and $0y$ axes) are strictly longitudinal and transverse waves. For the other directions of the wave vector, by virtue of smallness of the parameter ν, these excitations are well-defined quasilongitudinal and quasitransverse waves. The maximum deviation of the displacement vector in the quasilongitudinal mode from the $\mathbf{k}$ direction occurs at angles $\psi=\pi(2n+1)/4$, $n=0,1,2,3$ [see Eq. (22)].

5. HEAT CAPACITY

Let us consider the case in which the adatoms form an ideal triangular lattice. The heat capacity of the monolayer per site has the form

$$\frac{C}{N}=\frac{\sqrt{3}}{4\pi}\sum_{j=l,t,z}\int_0^{k_D R_0} x\Phi\left(\frac{\omega_j(x)}{T}\right)dx,$$

$$\Phi(u)=\frac{u^2}{4}\sinh^{-2}\frac{u}{2}, \tag{25}$$

where the frequencies ω_j are given by relations (15) and (16). At arbitrary temperatures the integration in (25) can be done only by numerical methods. Analytical results can be obtained in the limit of low temperatures, where T is the smallest energy parameter of the problem. In that case the main contribution to the thermodynamics of the system is given by the long-wavelength excitations $kR_0\ll 1$. In addition, without loss of generality below we can neglect the small quantity D in the expressions for the frequencies (15) and (16). As a result, we obtain

$$\omega_l^2=\Delta^2+\frac{3}{8}\Omega^2(kR_0)^2, \quad \omega_t^2=\Delta^2+\frac{\Omega^2}{8}(kR_0)^2,$$

$$\omega_z^2=\Delta_z^2. \tag{26}$$

We recall that the gap Δ_z in the z mode is always present, and for all the real 2D systems known to us it has a value at least of the order of several degrees,[5,6,18,20] so that in the temperature region of interest to us the relation $\Delta_z\gg T$ holds. On the other hand, the in-plane branches of the spectrum, as we have said, can be gapped or gapless. In deriving the low-temperature asymptotic expressions for the heat capacity it is convenient to treat these two cases separately.

First, suppose $\Delta=0$. Then for $T\ll\Omega$ the integration in (25) can be done analytically, and we obtain for the heat capacity per site

$$\frac{C}{N}=\frac{16\sqrt{3}}{\pi}\zeta(3)\left(\frac{T}{\Omega}\right)^2+\left(\frac{\Delta_2}{T}\right)^2\exp\left(-\frac{\Delta_z}{T}\right), \qquad (27)$$

where $\zeta(x)$ is the Riemann zeta function. The first term, due to the in-plane modes, has a form analogous to that obtained in the Debye approximation for 2D crystals.[21] Here the quantity Ω is related to the Debye temperature Θ_D by the expression

$$\Omega=\left(\frac{2}{\pi\sqrt{3}}\right)^{1/2}\Theta_D\simeq 0.6063\Theta_D. \qquad (28)$$

The second term in (27) is the contribution to the heat capacity from excitations perpendicular to the plane of the monolayer, and it has the typical form for the specific heat of an Einstein oscillator system. We note that at small nonzero values of Δ the asymptotic expression (27) is also valid in the temperature region $\Delta\ll T\ll\Omega$.

In the case when the l and t modes have a gap satisfying the condition $\Delta\gg T$, the asymptotic expression for the heat capacity has the form

$$\frac{C}{N}=\frac{8}{\pi\sqrt{3}}\left(\frac{\Delta}{\Omega}\right)^2\left(\frac{\Delta}{T}\right)\exp\left(-\frac{\Delta}{T}\right)+\left(\frac{\Delta_z}{T}\right)^2\exp\left(-\frac{\Delta_z}{T}\right). \qquad (29)$$

Here, as in Eq. (27), the first term is due to the contribution from in-plane excitations, while the second is due to z-polarized phonons. We note that the excitations of the first type give a pre-exponential factor $\sim T^{-1}$ in the low-temperature heat capacity, unlike the pre-exponential factor $\sim T^{-2}$ in the second term of (29). The possibility of $T^{-1}\exp(-\Delta/T)$ behavior in the case of a 2D square lattice was also pointed out in Ref. 17.

6. DISCUSSION. COMPARISON WITH EXPERIMENT

Various aspects of the problem of interest to us have been discussed in the literature both on a theoretical level and in connection with applications to real experiments.[17,20,22–24] In particular, the question of the nature of the gaps in the excitation spectrum of a 2D crystal on a substrate and the question of how a gapped character of the spectra is manifested in the thermodynamics of a system have been examined.[2,3,17] In most of the theoretical papers the calculations of the spectrum have been done by numerical methods. The use of numerical procedures requires specializing to a concrete system, i.e., an explicit form must be specified for the potentials of the lateral interaction and the interaction with the substrate, so that one cannot obtain a relation in general form between the spectral and thermodynamic characteristics of the system and the parameters of the interaction potentials. For this reason, the experimental data on the heat capacity are usually described with the use of approximating formulas or relations obtained on the basis of phenomenological arguments,[17,20,22,25] and the interpretation of an experiment is then ambiguous.

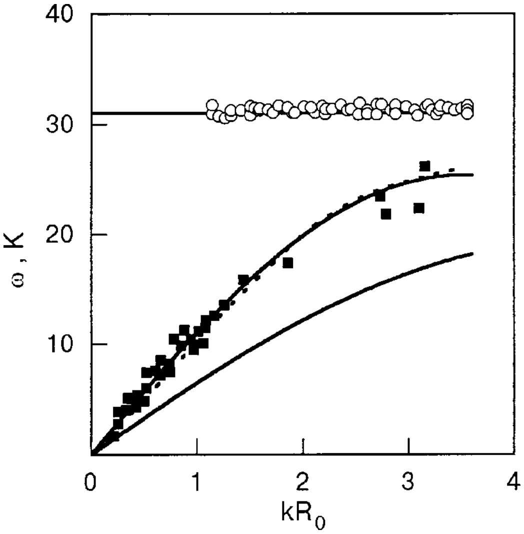

FIG. 3. Phonon dispersion curves for Xe/Cu (100): ■ and ○—experimental data[6] for the l and z modes; solid curves—the results of a calculation according to formulas (15) and (16); dashed curve—the calculation of Ref. 6.

The advantage of the analytical approach proposed in the present paper is that it allows one to find the phonon spectrum of a 2D crystal in explicit form. Here the parameters of the spectrum are expressed in terms of the parameters of the lateral interaction and interaction between the layer and substrate, the form of which, in principle, can be chosen arbitrarily. Thus it is easy to trace the connection between the character of the interactions in the system and the form of the temperature dependence of the heat capacity.

Let us now compare the results of our study with the experimental data available in the literature. We start with the dispersion relations for the phonon modes, which are directly measured by a method based on the inelastic scattering of helium atoms.[4–6,18] For example, in Refs. 5 and 6 the experimental curves of $\omega(\mathbf{k})$ were obtained for Xe monolayers adsorbed on the Cu (111) and Cu (100) surfaces. It should be noted that the experimental technique permitted measurement of only the in-plane longitudinal mode and the z mode polarized perpendicular to the plane of the layer. In the case when the Cu (100) surface was used as the substrate, so that the Xe monolayer formed an incommensurate structure, no gap was observed at the Brillouin zone center for the l mode. The z mode was found to be practically dispersionless, with a gap equal to 31 K. The authors of Refs. 5 and 6 did a numerical calculation for the corresponding modes and presented the results in graphical form. For describing the interaction with the substrate they used a potential averaged over $\mathbf{R}$, the interaction in the layer was taken into account in a nearest-neighbor approximation, and the force constants of the Xe–Xe interaction were treated as fitting parameters. Figure 3 shows a comparison of the data[5,6] for Xe/Cu (100) with the results of the present study. The fitting parameters which we used were $\Omega=18.71$ K, $\Delta_z=31$ K, and $D=0$. The force constants calculated from these fitting parameters are in good agreement with the corresponding values given in Ref. 6. Thus we see that the analytical approach based on approximation (11) correctly takes into account all of the fundamental features of the system under study.

In Refs. 5 and 6 the dispersion relations were also mea-

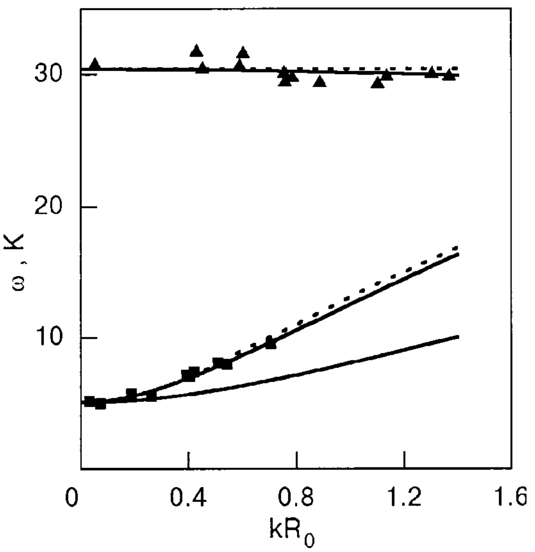

FIG. 4. Phonon dispersion curves for Se/Cu (111): ■ and ▲—experimental data[6] for the *l* and *z* modes; solid curves—the results of a calculation according to formulas (15) and (16); dashed curve—the calculation of Ref. 6.

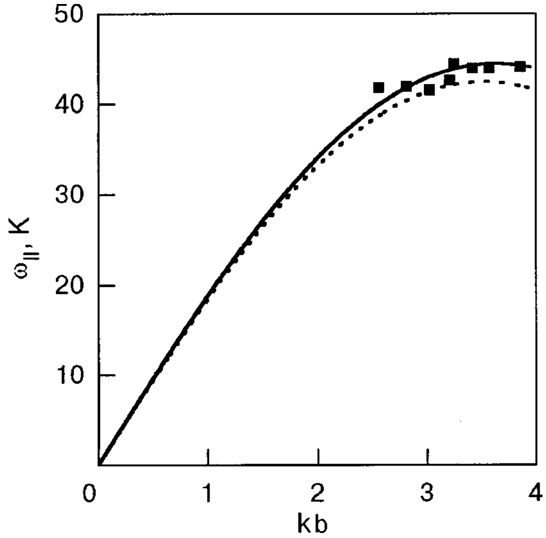

FIG. 5. Dispersion curves $\omega_\parallel(\mathbf{k})$ for Xe/Cu (110): ■—experimental data of Ref. 18; solid curve—calculation for a lattice with distortion ($\xi=0.055$); dashed curve—calculation for an ideal lattice.

sured for a commensurate $(\sqrt{3}\times\sqrt{3})R30^\circ$ monolayer of Xe on Cu(111). An important result obtained there for the first time is the presence of a gap (equal to 5.06 K) in the longitudinal mode at $\mathbf{k}=0$. As we see from the experimental data,[6] the *z* mode also has a gap at the Brillouin zone center (equal to 30.4 K) and is practically dispersionless. In the numerical calculation of the phonon spectrum, the authors of Ref. 6 as before described the Xe–Xe interaction in the nearest-neighbor approximation, and in taking into account the interaction with the substrate they considered not only the structure of the substrate but also the motion of its atoms. Figure 4 shows the data of Ref. 6 and the results of the present study. The fitting parameters which we used took the values $\Omega=20$ K, $\Delta_z=30.4$ K, $D=-35$ K^2, and $\Delta=5.06$ K. As in the incommensurate case, the force constants calculated from these fitting parameters turned out to be very close to those given in Ref. 6. This indicates that the motion of the regular atoms has hardly any effect on the character of the phonon modes of the Xe monolayer.

In Ref. 18 the phonon dispersion relations were measured in the $[1\bar{1}0]$ direction for a Xe monolayer adsorbed on Cu (110). The specifics of the geometry of the substrate in this type of system leads to distortion of the Xe monolayer, which, as a result, is found in a weakly anisotropic quasi-triangular lattice. Figure 5 shows the $\omega_\parallel(\mathbf{k})$ curves for the case of an ideal lattice ($R_0=4.31$ Å) and lattices with distortion ($a=4.42$ Å, $a_1=4.23$ Å). The lateral interaction between the Xe atoms was modeled by a Lennard-Jones potential with parameters $\epsilon=230.4$ K and $\sigma=3.84$ Å. It is seen in Fig. 5 that even though the distortion is small, it is important to take it into account in interpreting the experimental data.

It should be pointed out that in Xe/Cu systems, if the Lennard-Jones potential is chosen to describe the lateral interaction, good agreement of the theory with experiment is achieved by varying the parameter σ less than 4% in comparison with its value in the gas phase[26,27] at fixed ϵ. The same result can be obtained if the value of σ corresponding to the gaseous phase is kept fixed and the repulsive part of the potential is "softened," as was proposed in Ref. 6.

It is of interest to compare our theoretical results with the experimental data on the heat capacity. There is a vast amount of published material on the results of measurements of the heat capacity of rare gas monolayers on various substrates.[2,17,20,22,25,28–33] For monolayers of classical rare gases (Ne, Ar) an exponential dependence of $C(T)$ is observed at low temperatures in the commensurate phase.[17] This fact clearly indicates the presence of a gap in the dispersion relations for the in-plane modes. The same behavior of $C(T)$ also follows from the theoretical analysis done in the present study [see Eq. (29)]. Unfortunately, the available published experimental data for the indicated systems in the low-temperature region are presented in a form that does not permit making an accurate quantitative comparison of the theory with experiment.

Particular experimental attention has been devoted to the study of monolayer films of helium isotopes. The heat capacity of helium monolayers on graphite was first measured quite a long time ago.[2,25,28–31] Recently there has been renewed interest in these systems. For example, in Ref. 20 the $C(T)$ curves for ^{4}He monolayers on graphite were measured for 84 coverages at temperatures from 100 mK upward. Monolayers of helium isotopes have behavior quite different from that of classical rare gas monolayers: even in the commensurate phase their low-temperature heat capacity exhibits a dependence $C(T)\propto T^2$. This fact indicates the absence (or very small values $\Delta<100$ mK) of gaps for the *l* and *t* modes. In Ref. 20 it was shown that for a coverage $\rho_A=0.0637$ Å^{-2}, corresponding to the commensurate $\sqrt{3}\times\sqrt{3}$ phase, and the nearby coverage $\rho_B=0.0663$ Å^{-2}, the experimental data in the temperature region $0.3\ \mathrm{K}<T<1.5$ K are well fit by the approximating formula

$$\frac{C}{N}=\alpha+\beta T^2+(\gamma/T)^2\exp(-\Delta/T), \tag{30}$$

where $\Delta=(10.5\pm0.1)$ K, $\gamma=(12\pm1)$ K for both coverages and α and β are equal to $(19\pm2)\times10^{-4}$ and (1.75 ± 0.04)

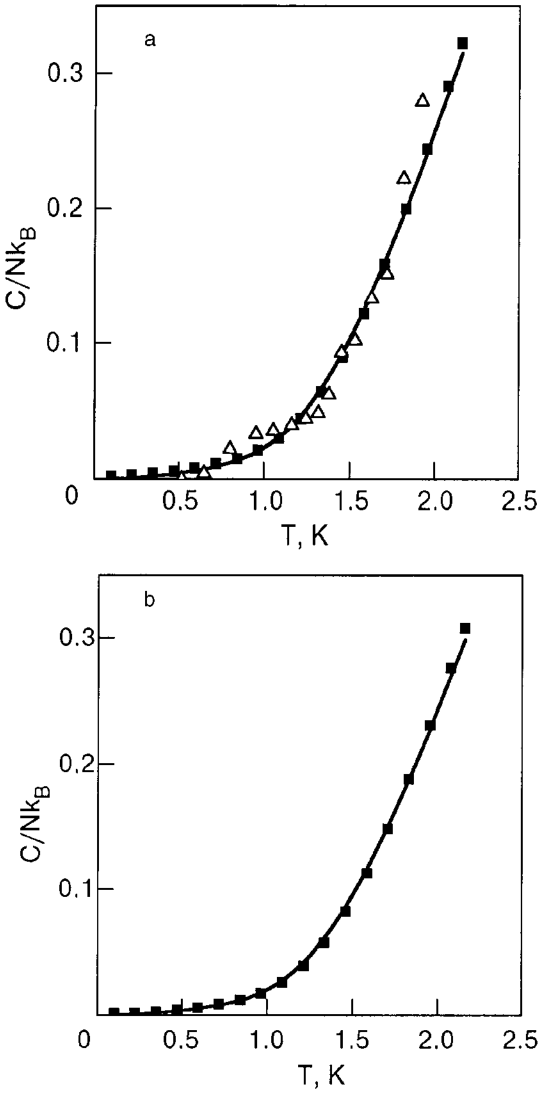

FIG. 6. Temperature dependence of the heat capacity of ^{4}He/Gr for coverages $\rho_A = 0.0637$ Å^{-2} (a) and $\rho_B = 0.0663$ Å^{-2} (b): ■—the smoothed experimental data of Ref. 20; △—the experimental data of Ref. 29; solid curve—present theory.

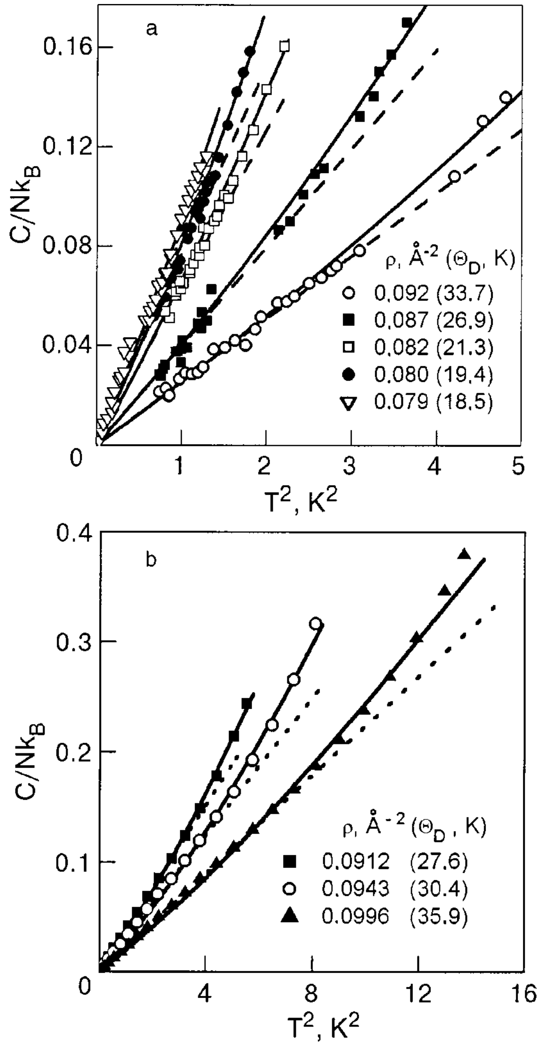

FIG. 7. Heat capacity as a function of T^2 for ^{3}He/Gr (a) and ^{4}He/Gr (b) in an incommensurate phase for different coverages ρ: the symbols in (a) are the experimental data of Refs. 28 and 29, the symbols in (b) are the smoothed experimental data of Refs. 25 and 30, the solid curves are our theory, and the dashed curves are the Debye approximation.

$\times 10^{-2}$ K^{-2}, respectively, for ρ_A and to $(6.3\pm 0.4)\times 10^{-4}$ and $(1.45\pm 0.01)\times 10^{-2}$ K^{-2} for ρ_B. The term proportional to T^2 was attributed in Ref. 20 to the contribution from a liquid phase containing approximately 3% of the atoms of the monolayer. Our results make it possible to interpret the experimentally observed behavior of the system without invoking assumptions about the presence of any additional phases besides the solid. For explaining the experiment it is sufficient to use relation (27), in which one should set $\Delta = 9.8$ K for both coverages, and $\Omega = 24.6$ and 27.0 K for ρ_A and ρ_B, respectively. Figure 6 gives a comparison of the temperature dependence of the ^{4}He/Gr heat capacity obtained by the present approach, the smoothed experimental results (30), and the data of Ref. 29.

In Refs. 2, 28, and 29 it is shown that for dense coverages ($\rho > 0.077$ Å^{-2}), at which the monolayers of helium isotopes are found to be in an incommensurate phase at low temperatures, the indicated systems behave as ideal two-dimensional crystals in the sense that the influence of the graphite substrate on their thermal properties is insignificant, and the low-temperature heat capacity of ^{3}He (^{4}He) monolayers is described quite well by the simple 2D Debye model.[21] However, the domain of applicability of the Debye approximation is extremely narrow ($T/\Theta_D \leqslant 0.07$).[2,28,29] The smallness of the influence of the substrate apparently means that the measurements were made at temperatures $T \ll \Delta_z$, at which the contribution to the heat capacity from the z mode can be neglected in expressions (25) and (27).

To interpret the experimental data[25,28–30] on the heat capacity of ^{3}He (^{4}He)/Gr in the temperature region where the deviation from the law $C \propto T^2$ is observed, we used expression (25) with the phonon frequencies $\omega_{l,t}$ given by relation (15) at $D = 0$. In Fig. 7 the heat capacity of ^{3}He and ^{4}He monolayers on graphite is plotted as a function of T^2 at high coverages. As experimental data for ^{4}He we used the fitting formula given in Ref. 30. As was noted in Ref. 30, the curves constructed with the use of this formula pass through all of the experimental points. Each value of the coverage is associated with an empirically determined Debye temperature Θ_D, which is the only fitting parameter [the frequency Ω is

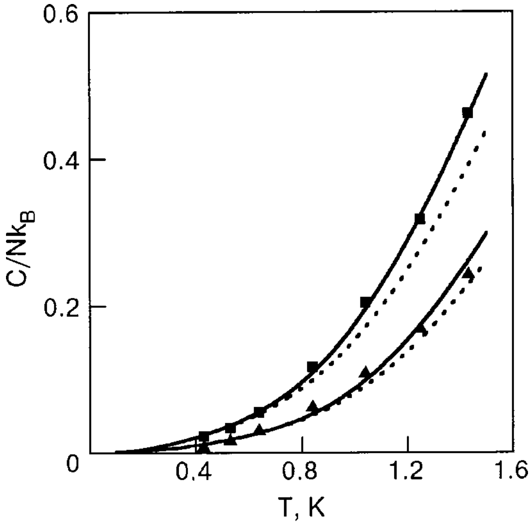

FIG. 8. Temperature dependence of the heat capacity of ^{4}He/Au. Experimental data of Ref. 22: □—$\rho=0.067$ Å^{-2}, ▲—$\rho=0.096$ Å^{-2}; the solid curves were obtained with the use of Eq. (25), the dashed curves with (27).

uniquely related to Θ_D by Eq. (28)]. For comparison the Debye relation is also shown in Fig. 7 (dashed lines). The theoretical curves clearly conform to the experimental curves not only at low temperatures but also at high temperatures, where the Debye approximation becomes ineffective.

The proposed model also permits interpretation of the experimental data on the heat capacity of helium monolayers on metal substrates. In comparison with the graphite substrates the metal ones are smoother and more uniform, and the adsorbate–substrate interaction in them can be described with the averaged potential (2). Furthermore, it is known that the adsorbate–metal interaction is weaker than the adsorbate–graphite interaction. Because of the first of these circumstances the l and t modes in such systems are acoustic $(\Delta=0)$, and the second circumstance means that the value of the gap Δ_z in the case of metal substrates is smaller than the corresponding value for systems on graphite. Thus the contribution to the heat capacity from the z mode begins to be manifested at rather low temperatures. We made a comparison of the theoretical and experimental data[22] on the heat capacity of ^{4}He monolayers adsorbed on gold for coverages $\rho=0.067$ and 0.096 Å^{-2} see Fig. 8. The theoretical curves (solid lines) were obtained from relation (25) with the dispersion of the z mode neglected $(D=0)$. The values of the fitting parameters giving the best agreement with experiment were found to be: $\Delta_z=7.8$ K and $\Omega=9.07$ K for $\rho=0.067$ Å^{-2}, and $\Delta_z=8.5$ K and $\Omega=12.65$ K for $\rho=0.096$ Å^{-2}. The dashed lines show the heat capacities found with the use of the asymptotic formula (27) for the same values of the parameters. It is seen in Fig. 8 that the asymptotic expression does not allow one to describe the experiment in the entire temperature range in which measurements were made, and an adequate interpretation of the behavior of $C(T)$ is possible only with the use of the exact spectrum (15), (16).

An attempt to calculate Ω and D for helium monolayers using the well-known atom–atom potentials with parameters obtained from measurements in the gaseous phase does not lead to physically meaningful values of these quantities. This result, which is well known for three-dimensional helium crystals,[34] is not unexpected. Indeed, the helium crystal is a quantum crystal, in which the large rms displacements of the atoms cause the equilibrium interatomic distance in the crystal to be considerably larger than the value corresponding to the minimum of the He–He pair interaction potential. On the other hand, the fact that the values of the fitting parameters Ω and D obtained in a comparison of theory and experiment turn out to be reasonable means that the Hamiltonian (4) can be used for describing the dynamics of monolayers of helium isotopes if the coefficients in it are not taken to be simply the derivatives of the atom–atom potentials but are determined in a self-consistent way.[34] Finding the relation between these coefficients and the parameters of the He–He interaction potential is a separate problem that is beyond the scope of this paper. We mention only that for solving it one can apparently use the well-developed methods employed for three-dimensional quantum crystals.[34,35]

The quantum character of helium monolayers might also be responsible for the above-mentioned absence (or essential smallness) of gaps in the spectra of l and t excitations of the commensurate phase. Indeed, the amplitude of the zero-point vibrations of the helium atoms in the plane of the layer is large, and in their motion they "feel" the fields not only of the nearest neighbors but also of more distant neighbors in the substrate. As a result, an effective "averaging" of the substrate field occurs and the gaps of the in-plane modes vanish (or decrease substantially), ultimately leading to a low-temperature heat capacity behavior $C(T)\propto T^2$, as is observed in experiment.

Let us conclude with one more remark on the model used here. Following the conventional ideas,[1,3,4,7,17] we assumed that the 2D crystal lies on a substrate whose atoms are immobile. This approximation is justified for the following reasons. First, the class of objects studied was created specifically for the purpose of studying the physical properties of two-dimensional systems. Therefore the substrate material on which the layer was deposited was chosen specially so that its influence on the properties of the 2D crystal would be as small as possible.

Nevertheless, the question of the mutual influence of the phonon modes of the substrate and adsorbate is of independent interest for the experimental study of the thermodynamics of such systems, since the heat capacity of the monolayer is found as the difference between the total heat capacity of the system and the heat capacity of an empty calorimeter, which is expected to be known precisely. In Ref. 17 detailed calorimetric measurements were made which showed that the influence of helium, neon, and argon monolayers on the heat capacity of copper substrates is unimportant within the limits of experimental error.

As to the influence of the substrate on the vibrational modes of 2D cryocrystals, a detailed theoretical analysis of this problem was carried out in Ref. 36, where analytical results were obtained in a model that treats the substrate as a semi-infinite elastically isotropic continuum, and numerical calculations were done for substrates of finite thickness. The main results of this analysis consist in the following. In the case of an incommensurate structure the motion of the substrate atoms does not affect the l and t modes of the monolayer because the sound velocity is much higher in the substrate than in the monolayer. The interaction with modes of the substrate occurs only for the dispersionless branch polarized perpendicular to the layer. Here the main effect comes from the crossing of the z mode of the layer with the Rayleigh branch of the substrate spectrum, which occurs near the center of the Brillouin zone. However, the hybridization of the modes occurs in such a narrow interval of wave vectors that this effect has long resisted attempts to observe it experimentally. The interaction is manifested only in the appearance of an additional weak dispersion of the z mode and in the broadening of the spectral lines of the layer on account of the energy transfer from the adsorbate to the substrate. At the same time, as was noted in Refs. 7 and 36, observation of these last two effects will require techniques having extremely high resolution. We also note that in the case of commensurate structures, when the l and t modes of the adsorbate are gapped, their crossing with modes of the substrate occurs at very small values of $\mathbf{k}$, although no related effects have as yet been observed experimentally.

It is clear that the motion of the substrate atoms cannot be reflected to any substantial degree in such integral characteristics of the monolayer as the heat capacity. Therefore the rigid-substrate model is entirely adequate for describing the behavior of the systems discussed in this paper.

[*] E-mail: antsygina@ilt.kharkov.ua

---

[1] I. F. Lyuksyutov, A. G. Naumovets, and V. L. Pokrovskiĭ, *Two-Dimensional Crystals* [in Russian], Naukova Dumka, Kiev (1988).

[2] J. G. Dash, Fiz. Nizk. Temp. **1**, 839 (1975) [Sov. J. Low Temp. Phys. **1**, 401 (1975)].

[3] A. D. Novaco, in *Monolayer and Submonolayer Helium Films*, edited by J. Daunt and E. Lerner, Plenum Press, New York (1973), p. 75.

[4] K. D. Gibson, S. J. Sibener, B. M. Hall, D. L. Mills, and J. E. Black, J. Chem. Phys. **83**, 4256 (1985).

[5] J. Braun, D. Fuhrmann, A. Siber, B. Gumhalter, and Ch. Wöll, Phys. Rev. Lett. **80**, 125 (1998).

[6] A. Siber, B. Gumhalter, J. Braun, A. P. Graham, M. F. Bertino, J. P. Toennis, D. Fuhrmann, and Ch. Wöll, Phys. Rev. B **59**, 5898 (1999).

[7] B. Hall, D. L. Mills, P. Zeppenfeld, K. Kern, U. Becher, and G. Comsa, Phys. Rev. B **40**, 6326 (1989).

[8] G. P. Brivio and M. I. Trioni, Rev. Mod. Phys. **70**, 231 (1999).

[9] E. M. Lifshitz, Zh. Éksp. Teor. Fiz. **29**, 94 (1955) [Sov. Phys. JETP **2**, 73 (1956)].

[10] K. E. Zaremba and W. Kohn, Phys. Rev. B **15**, 1769 (1977).

[11] G. Vidali, M. W. Cole, and J. R. Klein, Phys. Rev. B **28**, 3064 (1983).

[12] W. Steele, Surf. Sci. **36**, 317 (1973).

[13] M. W. Cole, D. R. Frankl, and D. L. Goodstein, Rev. Mod. Phys. **53**, 199 (1981).

[14] F. J. Milford, in *Monolayer and Submonolayer Helium Films*, edited by J. Daunt and E. Lerner, Plenum Press, New York (1973), p. 53.

[15] M. W. Ross and M. Salazar, Surf. Sci. **441**, 270 (1999).

[16] J. G. Daunt, S. J. Hegde, and E. Lerner, in *Monolayer and Submonolayer Helium Films*, edited by J. Daunt and E. Lerner, Plenum Press, New York (1973), p. 19.

[17] G. A. Stewart and J. G. Dash, J. Low Temp. Phys. **5**, 1 (1971).

[18] P. Zeppenfeld, M. Büchel, R. David, G. Comsa, C. Ramseyer, and C. Girardet, Phys. Rev. B **50**, 14667 (1994).

[19] F. I. Fedorov, *Theory of Elastic Waves in Crystals*, Plenum Press, New York (1968), Nauka, Moscow (1965).

[20] D. Greywall, Phys. Rev. B **47**, 309 (1993).

[21] A. A. Maradudin, E. W. Montroll, and G. H. Weiss, "Dynamic theory of the crystal lattice in the harmonic approximation," in *Solid State Physics*, Suppl. 3, Academic Press, New York (1963), Mir, Moscow (1965).

[22] J. T. Birmingham and P. L. Richards, J. Low Temp. Phys. **109**, 267 (1997).

[23] M-C. Chung and I. Peschel, Phys. Rev. B **62**, 4191 (2000).

[24] J. M. Gottlieb and L. W. Bruch, Phys. Rev. B **41**, 7195 (1990).

[25] R. L. Elgin and D. L. Goodstein, Phys. Rev. A **9**, 2657 (1974).

[26] J. A. Barker, *Rare Gas Solids*, Vol. 1, edited by M. L. Klein and J. A. Venables, Academic Press, London (1976).

[27] J. O. Hirschfelder, C. F. Curtiss, and R. B. Bird, *Molecular Theory of Gases and Liquids*, Wiley, New York (1954), Izd. Inostr. Lit., Moscow (1961).

[28] S. V. Hering and O. E. Vilches, in *Monolayer and Submonolayer Helium Films*, edited by J. G. Daunt and E. Lerner, Plenum Press, New York (1973), p. 1.

[29] M. Bretz, J. G. Dash, D. C. Hickernell, E. O. McLean, and O. E. Vilches, Phys. Rev. A **8**, 1589 (1973).

[30] R. L. Elgin and D. L. Goodstein, in *Monolayer and Submonolayer Helium Films*, edited by J. G. Daunt and E. Lerner, Plenum Press, New York (1973), p. 65.

[31] M. Bretz, G. B. Huff, and J. G. Dash, Phys. Rev. Lett. **28**, 729 (1972).

[32] G. B. Huff and J. G. Dash, J. Low Temp. Phys. **24**, 155 (1976).

[33] T. T. Chung, Surf. Sci. **87**, 348 (1979).

[34] R. Guyer, Solid State Phys. **23**, 413 (1969) in *Quantum Crystals* [in Russian], Mir, Moscow (1975), p. 23.

[35] B. I. Verkin, and A. I. Prikhot'ko (eds.), *Cryocrystals* [in Russian], Naukova Dumka, Kiev (1983).

[36] B. Hall, D. L. Mills, and J. E. Black, Phys. Rev. B **32**, 4932 (1985).

Translated by Steve Torstveit

LOW TEMPERATURE PHYSICS VOLUME 28, NUMBER 6 JUNE 2002

Multidimensional and surface solitons in a nonlinear elastic medium

A. S. Kovalev* and E. S. Syrkin

B. Verkin Institute for Low Temperature Physics and Engineering, National Academy of Sciences of Ukraine, pr. Lenina 47, 61103 Kharkov, Ukraine

J. A. Maugin

Laboratoire de Modelisation en Mecanique, Universite Pierre et Marie Curie, Paris 75253, France

(Submitted January 31, 2002; revised February 11, 2002)
Fiz. Nizk. Temp. **28**, 635–647 (June 2002)

Nonlinear shear waves in two-dimensional systems (in particular, surface waves) are investigated with allowance for the spatial dispersion of the elastic medium. It is shown that the dispersion plays an important role in the structural and modulational stability of the nonlinear waves and to a large degree determines the directions of localization of phonons in a nonlinear localized wave and, in particular, the possibility of existence of elastic surface solitons. By means of an asymptotic procedure, solutions are found for small-amplitude two-dimensional elastic shear solitons of the one-parameter stationary-profile type and for envelope solitons and also for surface solitons localized near an ideal surface of an elastic half space. Localized excitations of this kind can exist only in a medium with a ‘‘focusing’’ (soft) nonlinearity and positive dispersion $\partial^2\omega/\partial k^2>0$, where $\omega(k)$ is the dispersion relation for linear waves. A procedure is proposed for finding solutions for surface envelope solitons localized near a surface covered with a layer of another substance. A comparison is made between the structures of the surface shear solitons at an ideal surface and at a surface with a film coating. © *2002 American Institute of Physics.* [DOI: 10.1063/1.1491186]

Interest in nonlinear elastic surface waves has risen in recent years in connection with the intensive development of the physics of nonlinear phenomena.[1–17] Because of the concentration of the energy of the surface wave in a thin near-surface layer, the influence of the anharmonicity of the crystal on the properties of the surface waves is considerably stronger than for volume waves. The nonlinear properties of surface waves have been observed experimentally in a large number of studies.[12–14,18–20] The first clear evidence of nonlinearity of surface elastic waves was the observation of higher harmonic generation in a surface wave near an ideal surface upon the excitation of an initial periodic sinusoidal signal.[18–20] The observable nonlinear wave is of a nonstationary character on account of the weak dispersion of this wave. At the present time it is well known in the theory of nonlinear waves that stationary nonlinear waves and solitons can exist only in the presence of competing factors: nonlinearity of the medium and dispersion of the linear waves.[21] Indeed, experiments with nonlinear surface waves of the Love type near a surface covered by a thin film[14] have demonstrated that nonlinear waves with stationary profiles can exist in that case (the film coating leads to a substantial increase in the dispersion of linear surface waves). The question of nonlinear surface waves was considered theoretically in Ref. 2 for the simplest case of purely shear waves at an ideal surface. Some specific question of the dynamics of such waves in that model were investigated in Refs. 3–5. However, the authors of Refs. 2–5 neglected to take into account the spatial dispersion of the elastic waves. Later, in Refs. 6 and 7 it was shown that for the existence of nonlinear surface waves it is extremely important to take the spatial dispersion into account. For technical applications of nonlinear surface waves (NSWs) the possibility of propagation of stable weakly-damped pulses or wave packets of NSWs is important. It is well known that such properties are possessed by dynamical solitons.[21] The possibility of propagation of surface elastic shear solitons is considered in Refs. 8 and 9, and such surface solitons are also discussed in Refs. 10, 11, and 15. However, the authors of those papers investigated surface solitons propagating along the surface of an elastic half space covered by a layer of softer material.

In this paper we consider the possibility of propagation of elastic surface shear solitons near the ideal surface of a crystal and show that they have a fundamentally different form than solitons at a surface covered by a film, and they can exist only for a completely definite combination of signs of the nonlinearity and dispersion of the medium.

The question addressed in this paper also has fundamental significance for the general theory of propagation of multidimensional solitons, since there is a connection between the problem of solitons in an infinite medium and NSWs and surface solitons in a semi-infinite medium with an ideal free boundary. A nonlinear surface wave is ‘‘half’’ of a nonlinear wave, localized in an infinite medium in the direction perpendicular to the direction of propagation of this wave. In this sense a surface soliton is equivalent to ‘‘half’’ of a three-dimensional soliton localized in all three directions, and the problem of nonlinear surface localization is similar to the problem of the nonlinear focusing of phonons.

The problem of localization of nonlinear acoustic waves in a multidimensional medium is a fundamental and nontrivial one. Until now, multidimensional solitons have been studied mainly in systems with strong spatial dispersion (e.g., in magnetically ordered media with easy-axis anisotropy,[22] i.e., in the case when the dispersion $D=\partial^2\omega_0(k)/\partial k^2$ is nonzero even in the limit $k=0$ (where k is the wave number of the linear excitations, $\omega_0(k)$ is the frequency of a linear wave, and $\omega=\omega_0(k)$ is the dispersion law of linear waves). In this case at zero group velocity $V=\partial\omega_0(k)/\partial k$ at $k=0$ the existence of immobile multidimensional, radially symmetric solitons becomes possible. In the motion of the soliton its deformation occurs only in the direction of propagationn. However, in nonlinear media with an acoustic dispersion relation (nonlinear elastic medium or a magnet with easy-plane anisotropy), in which, in the limit of small wave numbers ($k\to 0$,) there is no dispersion ($D=0$) but the group frequency remains finite, the situation is radically different. (In the case of a nonlinear wave one usually introduces a ''nonlinear dispersion relation'' $\omega=\omega(k,A)$,[21] where A is the amplitude of the wave. Then the term dispersion refers to $D=\partial^2\omega(k,A)/\partial k^2|_{A=0}$.) Because of the motion of phonons in a definite direction with nonzero group velocity, that direction and the two directions perpendicular to it become nonequivalent for soliton formation (spontaneous breaking of the symmetry of the problem), and the conditions of localization of nonlinear waves (and also the conditions for their stability) along different coordinates also become different. These conditions are determined by the signs of the dispersion D and of the nonlinearity, which will be characterized by the parameter $N=\partial\omega(k,A)/\partial A^2$ (Ref. 21). For different relationships between the signs of D and N there can be localization of the phonon flux in the phonon propagation direction or perpendicular to it (nonlinear phonon channeling) or in all three directions.

1. NONLINEAR WAVES IN AN ANHARMONIC CHAIN AND IN A MULTIDIMENSIONAL MEDIUM

The nonlinear dynamics of elastic systems has traditionally been studied for the example of one-dimensional anharmonic chains. Below we consider purely shear waves in a three-dimensional medium in the case when the displacement in the wave depends only on one spatial coordinate (x), corresponding to the so-called one-dimensional β model of Fermi, Pasta, and Ulam, which in the long-wavelength limit is described by a modified Boussinesq equation:[21]

$$mu_{tt}=\alpha a^2u_{xx}+\alpha\chi a^4u_{xxxx}+\beta a^4u_x^2u_{xx}, \tag{1}$$

where m is the mass of an atom, a is the lattice constant, α is a characteristic of the harmonic interparticle interaction, β is the anharmonic coupling constant for the nearest-neighbor interaction, and u is the transverse displacement of the atom from its equilibrium position. The second term on the right-hand side of (1) describes the dispersion of linear waves and determines the sign of the parameter D. Ordinarily the dispersion $D\approx-3\sqrt{\alpha}a^3k/\sqrt{m}$ is assumed to be negative ($\chi>0$, $D<0$). In particular, when only central forces of nearest-neighbor interaction are taken into account, one has $\chi=\chi_0=1/12>0$. However, when the bending stiffness of the one-dimensional chain is taken into account, or allowance is made for possible layering in a real three-dimensional crystal, the dispersion can also be positive ($D>0$, $\chi<0$). Examples are Nb_3Sn, Hg^{203}, MoS_2, and $MoSe_2$ (Ref. 26). The choice of the sign of the parameter β in front of the anharmonic term is important. The authors of Refs. 2–6 chose the parameter β as negative, as seems natural for transverse oscillations. However, in Refs. 10 and 11 a positive nonlinearity ($\beta>0$) was chosen, as is observed experimentally in $LiNbO_3$, in which this sign of β is apparently due to the strong piezoelectric effect. We stress once again that we are talking about anharmonic three-dimensional crystals. For studying solitonic excitations in anharmonic chains one ordinarily chooses a positive sign of the nonlinear term ($\beta>0$) in the case of negative dispersion ($\chi>0$). However, in the general case it is more justified physically (in any case, for simple anharmonic elastic media) to choose a negative (soft) nonlinearity, with $\beta<0$, as follows from the zero asymptotics of the interparticle interaction potential at large distances.

With the suitable choice of scales for the coordinate, time, and displacements, $[x]=a$, $[t]=a/c$, $[u]=\sqrt{|\beta|/\alpha}$, where $c=a\sqrt{\alpha/m}$ is the speed of sound, it is easy to rewrite (1) in dimensionless form

$$u_{tt}=u_{xx}+\chi u_{xxxx}+\delta u_x^2u_{xx}, \tag{2}$$

where $\delta=\mathrm{sgn}(\beta)$ is the sign function ($\delta=\pm 1$).

In the linear limit the spectrum of waves of the form $u=A\sin(kx-\omega t)$ has the form $\omega_0^2(k)=k^2-\chi k^4$, with a group velocity $V\approx 1-3\chi k^2/2$ and the dispersion $D\approx -3\chi k$ in the limit of small wave numbers $k\to 0$. For weakly nonlinear waves the dispersion relation is updated to the following form:[21]

$$\omega^2(k)=k^2-\chi k^4+\delta k^4A^2/4,$$
$$D\approx-3\chi k,\quad N\approx\delta k^3/8. \tag{3}$$

Consequently, the sign of the nonlinearity N is determined by the sign of the parameter β: $\mathrm{sgn}\,N=\mathrm{sgn}\,\beta$.

From the form of the ''nonlinear dispersion relation'' (3) one can assess the stability of nonlinear periodic waves with stationary profiles. According to the Lighthill criterion,[23] one-dimensional nonlinear spatially periodic waves of constant amplitude are modulationally unstable under the condition $DN<0$, i.e., $\delta\chi>0$. The growth of this instability leads to the formation of dynamical envelope solitons.

The modified Boussinesq equation (2) is not completely integrable, and usually one discusses only its exact solutions for one-parameter solitons of stationary profile, of the form $u=u(x-Vt)$, which depend only on a single parameter, the soliton velocity V. The deformation in a nonlinear excitation of this kind has the standard soliton form:[21]

$$w=\frac{\partial u}{\partial x}=\frac{\sqrt{6(V^2-1)/\delta}}{\cosh[\sqrt{(V^2-1)/\chi}(x-Vt)]}. \tag{4}$$

Obviously such solitons exist only under the conditions

$$\begin{aligned}&x>0,\quad \delta>0,\quad V>1\\ \text{or}\quad&\chi<0,\quad \delta<0,\quad V<1,\end{aligned} \tag{5}$$

i.e., for $\delta\chi>0$, in agreement with the Lighthill criterion.

The more complex solutions of the two-parameter envelope soliton type (breathers) can be obtained only approximately, in the limit of low soliton amplitude by means of some asymptotic procedure (see, e.g., Ref. 8). In our opinion, the most convenient procedure is the one which was proposed in Ref. 24 for the nonlinear Klein–Gordon equation and which was generalized in Ref. 25 to the case of the evolution equations with an acoustic dispersion relation of the type $\omega_0^2(k)=k^2-\chi k^4$. For solutions of the envelope soliton type the function $u(x,t)$ can be written in the form of the following expansion:

$$u(x,t)=\sum_{n=0}^{\infty}\{f_{2n+1}(\zeta)\sin(2n+1)\theta+\varphi_{2n+1}(\zeta)\cos(2n+1)\theta\},\tag{6}$$

where $\zeta=x-Vt$, $\theta=kx-\omega t$, and the functions f_s and φ_s and the soliton velocity V are expanded in power series:

$$f_s=\sum_{m=0}^{\infty} f_{s,s+2m}\varepsilon^{s+2m},$$

$$\varphi_s=\sum_{m=0}^{\infty}\varphi_{s,s+2m+1}\varepsilon^{s+2m+1},\tag{7}$$

$$V=V(k)+\varepsilon^2\lambda(k)+\dots,$$

where the small parameter of the expansion (which is related to the soliton amplitude) is the quantity

$$\varepsilon=\sqrt{|\omega^2-\omega_0^2(k)|},\tag{8}$$

in which the function $\omega_0(k)$ corresponds to the dispersion relation for linear waves. (The derivatives with respect to the phase ζ are of order ε in smallness: $\partial/\partial\zeta\sim\varepsilon$.) The solution for a two-parameter envelope soliton in the leading approximation and for small values of k has the form

$$u\approx\sqrt{\frac{8(\omega^2-k^2+\chi k^4)}{\delta k^4}}\times\operatorname{sech}\left[\sqrt{\frac{\omega^2-k^2+\chi k^4}{3\chi k^2}}(x-Vt)\right]\sin(kx-\omega t),$$

$$V\approx 1-\frac{3}{2}\chi k^2,\tag{9}$$

where, as the two independent dynamical parameters of the solution, one can choose the wave vector k and frequency ω of the nonlinear wave localized in the soliton. Here the soliton velocity is a single-valued function of these two parameters, $V=V(k,\omega)$. As we see from Eq. (9), in the leading approximation with respect to the amplitude of the small-amplitude soliton, the function $V=V(k,\omega)$ for the soliton has the same dependence on wave number as the group velocity of the linear wave. It follows from expression (9) that one-dimensional envelope solitons exist only under the conditions

$$\begin{array}{ll} & \chi>0,\ \ \delta>0,\ \ V<1,\ \ \omega>\omega_0(k) \\ \text{or} & \chi<0,\ \ \delta<0,\ \ V>1,\ \ \omega<\omega_0(k),\end{array}\tag{10}$$

i.e., for $\delta\chi>0$, which again agrees with the Lighthill criterion.

It follows from the form of the soliton solution (9) that in the limit of zero dispersion ($\chi\to 0$) the soliton collapses, i.e., its localization region goes to zero. Moreover, it is easy to show that the ratio of the amplitudes of the second and fundamental harmonics is given by $f_3/f_1=\varepsilon/(36k^4\chi)$, and, hence, the true parameter of the asymptotic expansion is $\varepsilon^2/(k^4\chi)$, which diverges in the dispersionless limit $\chi\to 0$. This indicates the importance of taking the spatial dispersion into account in the problem under study.

The existence conditions obtained for one-dimensional solitons of different types are easily represented on the $(\tilde{\omega},V)$ plane, where V is the soliton velocity and $\tilde{\omega}=\omega-kV$ is the frequency of the internal oscillations of the envelope soliton in a coordinate system moving with velocity V. (Here the two independent parameters of the soliton solution are not k and ω but V and $\tilde{\omega}$.) In the linear limit (for linear waves) the dispersion relation $\omega_0^2(k)=k^2-\chi k^4$ implies the following dependence of $\tilde{\omega}_0=\tilde{\omega}_0(V)$:

$$\tilde{\omega}_0\approx\left(\frac{2}{3}\right)^{3/2}\frac{1}{\sqrt{\chi}}(1-V)^{3/2},\tag{11}$$

where V is the group velocity of the linear wave.

In Fig. 1 these parabolas are shown by the fine lines. The shaded regions near them in Figs. 1a and 1b correspond to the small-amplitude envelope solitons considered here, which depend on a single spatial variable. The heavy lines (Figs. 1a and 1b) correspond to small-amplitude one-parameter solitons of stationary profile, which depend on a single spatial variable. The shaded region in Fig. 1c corresponds to the channeling of phonons or to nonlinear surface waves.

The solutions discussed above describe solitons in a three-dimensional medium in the case when they are localized only in one direction—the direction of propagation of the nonlinear wave (along the x axis). Below we show that there can be situations in which the nonlinear wave is localized in one or two directions perpendicular to the propagation or in all three directions in a three-dimensional space. We restrict discussion to a cubic anharmonic crystal in which a wave is propagating along one of the principal crystallographic directions, when a purely shear wave is split off from waves with other polarizations. Nonlinear surface waves in such a crystal were considered for the first time in Refs. 2, 3, and 5, but without taking the spatial dispersion of the waves into account. This dispersion was taken into account in Refs. 6 and 7, where nonlinear shear waves were investigated in the framework of the following equation, which is the three-dimensional generalization of equation (2):

$$\begin{aligned}u_{tt}={}&u_{xx}+u_{zz}+u_{yy}+\chi(u_{xxxx}+u_{zzzz}+u_{yyyy}+\mu u_{xxzz}\\&+\mu u_{xxyy}+\mu u_{yyzz})+\delta\{u_x^2u_{xx}+u_z^2u_{zz}+u_y^2u_{yy}\\&+\lambda[(u_x^2u_z)_z+(u_z^2u_x)_x+(u_x^2u_y)_y+(u_y^2u_x)_x\\&+(u_z^2u_y)_y+(u_y^2u_z)_z]\}=0.\end{aligned}\tag{12}$$

In what follows we shall mainly be considering the propagation of waves with a horizontal shear polarization and with displacements that depend on two spatial coordinates, and only in one case (in a discussion of three-dimensional solitons localized in all three dimensions) will they depend on all three coordinates. The geometry of the problem is is as follows: a wave is propagating along the x axis, the displacements of the atoms are directed along the y axis, the plane of the structure (in the case of surface waves

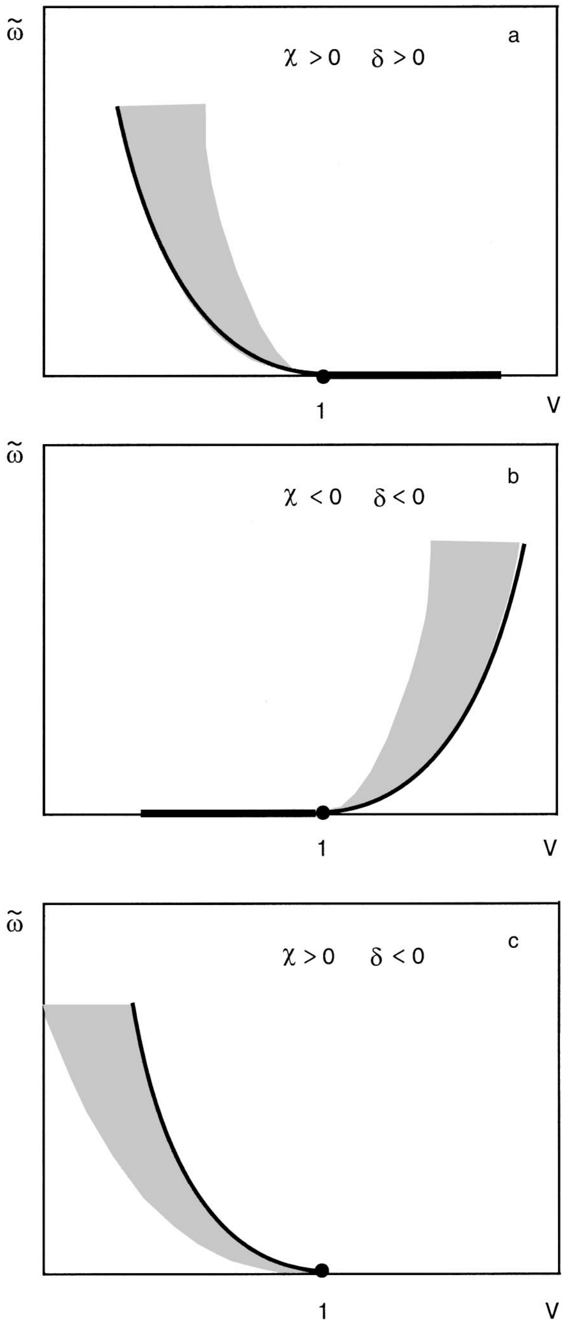

FIG. 1. Dispersion relations for linear waves (fine lines), the existence region of small-amplitude one-dimensional envelope solitons (the shaded regions in parts "a" and "b"), and the curves corresponding to one-parameter solitons of stationary profile (heavy lines) of the modified Boussinesq equation: $\chi>0$, $\delta>0$ (a); $\chi<0$, $\delta<0$ (b), $\chi>0$, $\delta<0$ (c). The shaded region in part "c" corresponds to phonon channeling or nonlinear surface waves.

and surface solitons) is the xy plane, perpendicular to the direction of the z axis, and the amplitude of the wave depends on the x and z coordinates (in the majority of the cases considered) but not on the y coordinate (see Fig. 4b). Then $\partial/\partial y=0$, and Eq. (12) is simplified considerably. If the wave is propagating along the x axis and is uniform in the direction of the z axis, then its nonlinear dispersion relation as before will have the form in Eq. (3). However, now the question of the stability of the nonlinear wave will be posed in a broader sense. The Lighthill criterion $DN<0$ $(\delta\chi>0)$ determines only the modulational instability of the uniform wave with respect to longitudinal fluctuations (along the x axis). The question of the transverse stability (in the directions of the z and y axes) is easily solved in the particular case when $\mu=2$ and $\lambda=1/3$. Then the frequency depends only on the modulus of the wave vector, and the nonlinear dispersion relation remains of the form (3), where $k=\sqrt{k_x^2+k_z^2+k_y^2}$. Here, as was noted in Ref. 23, the uniform nonlinear wave is unstable with respect to transverse disturbances for $N<0$ $(\delta<0)$. Thus for $\chi<0$ and $\delta>0$ the uniform nonlinear wave is stable in all directions and it cannot be localized. For $\chi>0$ and $\delta>0$ the wave is localized in its propagation direction, and the one-dimensional solitons described above can exist in a three-dimensional space. For $\chi>0$ and $\delta<0$ the wave is localized in the direction perpendicular to its propagation, and stable surface nonlinear waves can exist and phonon channeling can occur. Finally, a uniform wave is unstable in all directions when the inequalities $N<0$ and $D>0$ are both met simultaneously. Therefore, one expects that the two- and three-dimensional acoustic solitons can exist only in media with positive dispersion and soft nonlinearity (for $\chi<0$ and $\delta<0$).

Above we have considered the localization of a nonlinear wave in the direction of its propagation. We now turn to a study of excitations localized in one or two transverse directions.

2. PHONON CHANNELING, SURFACE WAVES, AND TWO-DIMENSIONAL SOLITONS

Let us first consider a system with negative dispersion and soft nonlinearity: $D<0$ $(\chi>0)$ and $N<0$ $(\delta<0)$. This is the most natural situation for shear waves. Here the nonlinear wave is modulationally stable in the direction of its propagation but unstable in the transverse directions; this leads to localization of phonons in these directions. This effect can be called phonon channeling. Here it is necessary to seek a solution of equation (12) which is periodic along the propagation direction (the x axis) and localized in the directions of the z and y axes. We limit consideration to the case when the solution is independent of y. Of course, ultimately the development of a transverse instability will lead to localization of the wave in the direction of the y axis as well, but we shall not consider that question here. In the small-amplitude limit the solution is found with the aid of the following asymptotic expansion:[6]

$$u(x,z,t)=\sum_{n=0}^{\infty}\sum_{m=0}^{\infty} f_{2n+1,2n+2m+1}(z)\varepsilon^{2n+2m+1}\times\sin(2n+1)\theta, \tag{13}$$

where $\theta=kx-\omega t$ and $\varepsilon=\sqrt{\omega_0^2(k)-\omega^2}$, and in the leading approximation has the form[6]

$$u\approx\sqrt{\frac{8(k^2-\chi k^4-\omega^2)}{k^4}}\times\operatorname{sech}\left[\sqrt{\frac{k^2-\chi k^4-\omega^2}{1-\chi\mu k^2}}z\right]\sin(kx-\omega t), \tag{14}$$

where k and ω are two arbitrary parameters of the soliton solution.

This expression outwardly resembles solution (9) but has a different existence region on the plane of parameters

$(\tilde{\omega},V)$: the frequencies of such channeled phonons at a fixed wave vector or group velocity lie below the frequencies of the linear waves (the shaded region in Fig. 1c). In the dispersionless limit $\chi\to 0$ solution (14) agrees with the result obtained in Ref. 2, but it is easy to show that the ratio of the amplitudes of the harmonics in expansion (13) is of order $f_{s+1,s+1}/f_{s,s}\sim\varepsilon/\chi k^2$. Consequently, the solution (14) has meaning (the asymptotic series converges) only when the dispersion of the medium in the region $k^2-\chi k^4-\omega^2 \ll \chi^2 k^4$ is taken into account.

Up till now we have been talking only about the channeling of nonlinear phonons in an infinite three-dimensional elastic medium. However, solution (13), (14) also describes nonlinear surface shear waves near an ideal surface of a semi-infinite crystal. Indeed, the boundary condition that follows from Eq. (12) at the free boundary $z=0$ has the form

$$[u_z(1+\delta u_z^2/3+\delta\lambda u_x^2)+\chi u_{zzz}+\chi\mu u_{xxz}]_{z=0}=0, \tag{15}$$

and the solution (14) clearly satisfies it. (In this article we will not be discussing the fundamental question of the necessity of formulating additional boundary conditions for Eq. (12), which contains higher spatial derivatives up to and including the fourth. They actually reduce to the requirement that the conditions for a long-wavelength treatment hold.)

Finally, let us investigate the question of multidimensional and surface solitons localized in three dimensions. As we have said, nonlinear excitations of this kind can exist only in the case of a medium with positive spatial dispersion and soft nonlinearity ($\chi<0$, $\delta<0$). The second inequality is natural for shear waves and should be satisfied in the majority of substances. The first inequality is unusual, since in the majority of materials the dispersion of linear waves is negative. Nevertheless, crystals with positive dispersion at low frequencies do exist (see Ref. 26).

Let us begin by studying three-dimensional envelope solitons localized in two directions (x and z). They correspond to the shaded region in Fig. 1b (which coincides with the existence region of two-dimensional envelope solitons of the modified Boussinesq equation). The small-amplitude solutions for multidimensional envelope solitons can be sought in the form of an expansion (6)–(8) with $\varepsilon=\sqrt{\omega_0^2(k)-\omega^2}$, assuming now that the functions f_{rs} and φ_{rs} depend not only on the phase $\zeta=x-Vt$ but also on the coordinate z. A complication in this case is that even at the first step of the asymptotic procedure a nonlinear partial differential equation arises which can only be solved numerically (accordingly, all the subsequent steps can only be carried out numerically as well). In the leading (resonance) approximation we have to accuracy ε

$$u\approx\varepsilon f_{11}(\zeta,z)\sin\theta\equiv\varepsilon f(\zeta,z)\sin\theta, \tag{16}$$

where the function $f(\zeta,z)$ depends weakly on its "slow" variables. In the case of longitudinal localization of the nonlinear wave the decay of its amplitude is governed by the small parameter ε: $\partial/\partial\zeta\sim\varepsilon$, as follows from Eq. (9). For transverse localization of the wave, on the other hand, it follows from Eq. (14) that the localization region is also determined by this small parameter: $\partial/\partial z\sim\varepsilon$. It is therefore natural to assume that in the case of a two-dimensional envelope soliton (16) the dependence of the function $f(\zeta,z)$ on its arguments will be determined by the same parameter ε. Then, keeping in Eq. (12) the leading terms of order ε^3 ($f\sim\partial/\partial\zeta\sim\partial/\partial z\sim\varepsilon$), we obtain the following equation for the function f:

$$f_{\zeta\zeta}(3\chi k^2)-f_{zz}+\varepsilon^2 f-\varepsilon^2 k^4 f^3/4=0. \tag{17}$$

(In the coefficient of the first term we have made the approximate substitution $V^2\approx 1-3\chi k^2$, and in the coefficient of the second term we have set $1-\chi\mu k^2\approx 1$.) As it followed before from a stability analysis of the uniform nonlinear waves, it follows from Eq. (17) that multidimensional localized envelope solitons exist only under the conditions $\chi<0$, $\delta<0$, and $\omega<\omega_0(k)$. Introducing a convenient scale for the coordinates and field amplitude,

$$\varepsilon\zeta/\sqrt{3|\chi|k^2}=\xi,\quad \varepsilon z=\eta,\quad fk^2/2=g, \tag{18}$$

we write Eq. (17) in the radially symmetric dimensionless form

$$g_{\xi\xi}+g_{\eta\eta}-g+g^3=0. \tag{19}$$

The radially symmetric solutions of this equation have been studied in detail by both qualitative[27] and numerical[28,29] methods. (The analogous centrosymmetric solutions of the corresponding equations in three space are also well known; there the two-dimensional Laplacian in (19) is replaced by its three-dimensional counterpart, and the solution depends on the coordinate y as well). There is an infinite set of these symmetric solutions parametrized by the number of zeros of the field as a function of the radial coordinate. The lowest energy belongs to a solution for which the field g falls off monotonically with the coordinate $r=\sqrt{\xi^2+\eta^2}$. The field amplitude at the center of the two-dimensional soliton is $g(z=x-Vt=0)=2.2$. (In the three-dimensional envelope soliton the degree of localization is higher, and the amplitude at the center of the soliton at this same frequency and velocity will be larger: $g_{3\mathrm{D}}(0)\approx 4.5$.) The profile of the two-

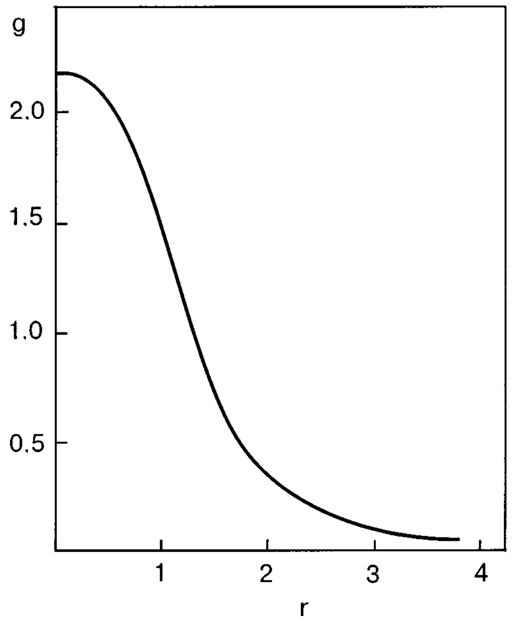

FIG. 2. Profile of the envelope of a two-dimensional dynamical two-parameter soliton of elastic shear displacements (in dimensionless variables).

dimensional envelope soliton $g=g(\xi)$ is shown in Fig. 2. In the original variables the solution for the two-dimensional soliton has the form

$$u=\frac{2\varepsilon}{k^2}g\left(\varepsilon\frac{x-Vt}{\sqrt{3|\chi|k^2}},\varepsilon z\right)\sin(kx-\omega t), \tag{20}$$

where the soliton velocity V depends on the parameters k and ω and in the leading approximation corresponds to the group velocity of linear waves with the same value of k. It follows from (20) that the localization regions of the soliton in different directions (Δx and Δz) have different values:

$$\frac{\Delta x}{\Delta z}\sim k\sqrt{|\chi|}. \tag{21}$$

As we see from this expression, in the long-wavelength limit we have $\Delta x\ll\Delta z$, and the soliton is highly flattened in the direction of its propagation (see Fig. 4a). This figure also illustrates the situation when the soliton is localized in all three directions and is described by Eq. (19) with the three-dimensional Laplacian.

Since solution (20) satisfies condition (15), it also describes a surface-shear-wave envelope soliton localized near an ideal surface. Since surface waves are usually excited by strip radiators, and a finite time is required for development of the transverse instability, the two-dimensional surface solitons considered here (localized only in one direction in the plane of the surface) are completely observable. We note that in Ref. 13, where surface solitons apparently were first observed experimentally, it is stated that the conditions of the experiment corresponded to the signs which we took for the dispersion and nonlinearity ($D>0$, $N<0$).

It should be emphasized that in the given case the localization of the nonlinear wave in the plane of the surface and near it has the same physical cause: nonlinearity of the elastic medium.

Let us turn to an analysis of the two-dimensional and surface one-parameter solitons of stationary profile, i.e., the two-dimensional analogs of solution (4). As before, we shall consider waves propagating along the x axis with a frequency V, i.e., solutions of the form $u=u(x-Vt,z)$. As it turned out, such states can exist for $\chi<0$, $\delta<0$, and $V^2\leqslant1$ (see Fig. 1b). From solution (4) for one-dimensional solitons it follows that in the limit $1-V^2\ll1$ the solution becomes small-amplitude and weakly localized:

$$u_x\sim\sqrt{1-V^2}\ll1,\quad \partial/\partial x\sim\sqrt{1-V^2}\ll1.$$

Here the terms $u_{tt}-u_{xx}$ and χu_{xxxx} and $\delta u_x^2u_{xx}$ in Eq. (12) become quantities of the same order: $\sim(1-V^2)^2$. We assume that the dependence on the coordinate z is also weak ($\partial/\partial z\ll1$) and keep only the leading term in the derivatives with respect to the coordinate z, viz., u_{zz}. Then this term will be of order $(1-V^2)^2$, and the derivative with respect to the coordinate z will be of order $\partial/\partial z\sim1-V^2$. Then the terms that have been dropped in Eq. (12) will be of order $(1-V^2)^3$ and $(1-V^2)^4$. In the leading approximation, Eq. (12) reduces to the following:

$$(1-V^2)u_{xx}+u_{zz}-|\chi|u_{xxxx}-u_x^2u_{xx}=0. \tag{22}$$

It is convenient to use the following new coordinates and displacements:

$$\xi=\frac{\sqrt{1-V^2}(x-Vt)}{\sqrt{|\chi|}},\quad \eta=\frac{(1-V^2)z}{\sqrt{|\chi|}},\quad \varphi=\frac{u}{\sqrt{6|\chi|}}, \tag{23}$$

in terms of which the equation for an arbitrary deformation $w=\varphi_\xi$ takes the form

$$w_{\xi\xi}+w_{\eta\eta}-w_{\xi\xi\xi\xi}-2(w^3)_{\xi\xi}=0. \tag{24}$$

We see that this equation has a different structure than Eq. (19) for the two-dimensional envelope solitons. It is reminiscent of the stationary version of the Kadomtsev–Petviashvili equation,[30] only with the quadratic nonlinearity of the latter changed to cubic: $(w^2)_{\xi\xi}\rightarrow(w^3)_{\xi\xi}$. The soliton solution of the Kadomtsev–Petviashvili equation is well known.[31] It has a completely different form than the two-parameter soliton (20). First, its asymptotic behavior is not exponential, as in one-dimensional solitons, but power-law. Furthermore, in the direction of motion the field falls off nonmonotonically with distance from the center of the soliton. These properties are preserved in the elastic shear solitons of stationary profile described by Eq. (24). Formally this equation is the same as the equation for small-amplitude nonlinear waves of stationary profile in a two-dimensional easy-plane ferromagnet, obtained and studied in Ref. 32. Therefore the profile of the soliton solution (24) can be determined from a comparison with the data of a numerical simulation of the magnetic dynamics of an easy-plane magnet at velocities of nonlinear excitations close to the velocity of the spin waves recently recorded by S. Komineas (private communication). The distribution of the longitudinal deformation in the soliton is shown in Fig. 3 in the form of two cross sections: along the motion, $w(\xi,\eta=0)$, and in the perpendicular direction, $w(\eta,\xi=0)$. We see that this solution has qualitatively the same form as the Kadomtsev–Petviashvili soliton: in the direction of propagation the profile as a nonmonotonic character. In spite of the fact that the minima in Fig. 3 are small compared with the central peak, because of the slow fall-off of the deformation with distance, the role of the regions of negative deformation is very large. Apparently, as in the

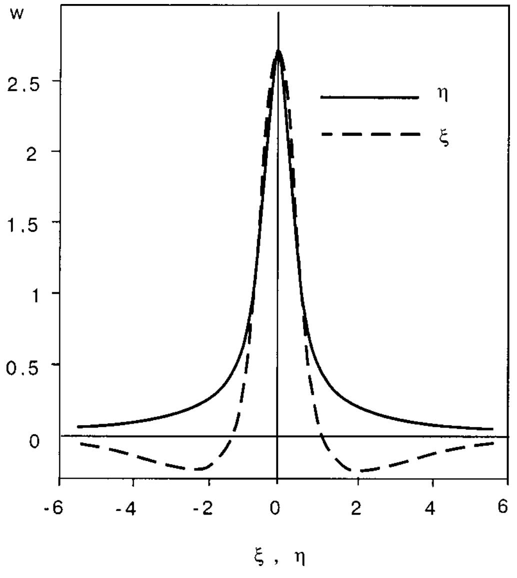

FIG. 3. Distribution of deformation in a two-dimensional soliton of stationary profile (in dimensionless variables).

Kadomtsev–Petviashvili equation, in our case the total deformation in the soliton is equal to zero: $\int w d\xi d\eta = 0$. In any case a calculation of the total magnetization in a moving magnetic soliton in the limit of large soliton velocities (when the magnetic and elastic systems are practically equivalent) shows that this quantity become anomalously small, which corresponds to an anomalously small total deformation in the acoustic soliton. We recall that in the one-dimensional case in the motion of a soliton of stationary profile (4) the total deformation is nonzero: $\int w dx = \sqrt{24\chi/\delta} \neq 0$. It may be that the properties listed above for a one-parameter two-dimensional soliton are general for systems with an acoustic spectrum of linear excitations. For example, the surface Rayleigh solitons[16,17] have a form qualitatively similar to that shown in Fig. 3.

If we change back to the original variables in the soliton solution, its characteristic size in the direction of propagation will be $\Delta x \sim 1/\sqrt{1-V^2}$, while the size in the perpendicular direction will be substantially larger: $\Delta z \sim 1/(1-V^2) \gg \Delta x$ (see Fig. 4a). However, now the flattening of the soliton in the direction of propagation is determined not by the wave vector (as in the envelope soliton) but by the velocity of the soliton of stationary profile.

Since the soliton solution obtained is symmetric with respect to the axis $z=0$, it describes, as in the previous cases, surface shear solitons (in this case, of stationary profile) localized in the x and z directions and propagating along an ideal surface of a three-dimensional elastic half space.

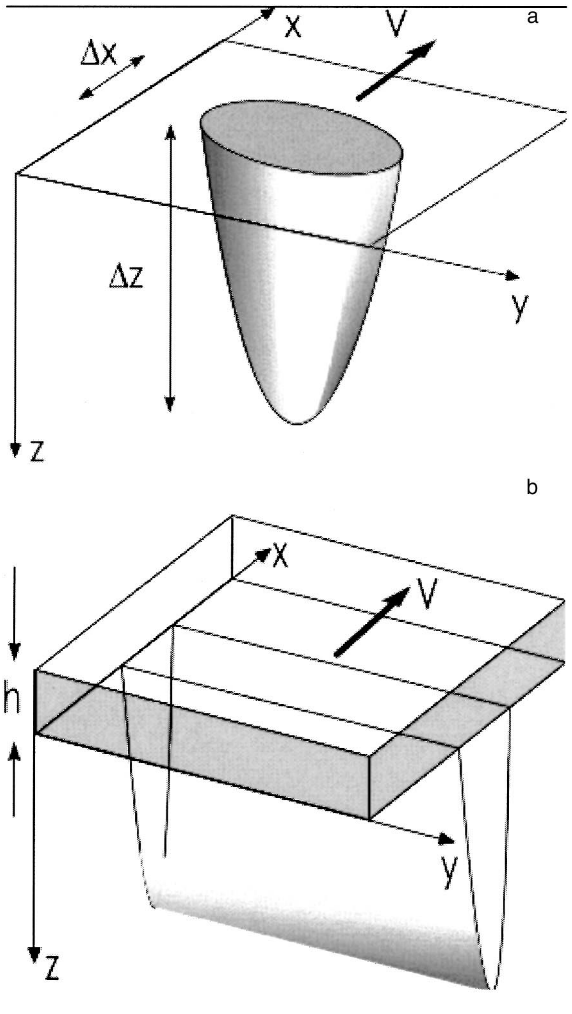

FIG. 4. Profile of a surface soliton localized near an ideal surface (a) and around a surface coated with a film of a different material (b).

3. SOLITONS LOCALIZED NEAR A SURFACE WITH A FILM COATING AND NEAR A PLANAR DEFECT

In the previous Section we considered solitons of different kinds in a three-dimensional elastic medium and near an ideal surface of a half space, and we gave the conditions for their existence (a combination of the signs of the nonlinearity and dispersion of the medium). However, if the surface an an anharmonic crystal is coated with a film of a different material (or in the presence of a planar defect in the crystal), the conditions for the existence of surface solitons or solitons localized near a defect plane can change. The possibility of existence of these shear surface solitons was first pointed out in Refs. 10 and 11. In such a statement of the problem the experimental observation of solitons near the surface and near a planar defect is more probable, since for a thickness $h \gg a$ of the coating layer or of the interface between two media, the dispersion of linear waves localized near the surface or defect can be substantially higher than the ''intrinsic'' dispersion of bulk elastic waves. As a result, the nonlinear stationary wave or soliton is formed in substantially less time (when damping may still be ignored) and the deformation in the stationary wave decreases; this justifies a long-wavelength treatment of the problem. However, while in the previous Section the localization of the wave in two directions was due to nonlinearity, now the nonlinearity leads to localization only in the direction of propagation of the soliton, while the localization in the transverse direction is due to the presence of a planar defect or surface layer (i.e., it exists in the linear limit). Here for localization of a linear wave it is necessary that its frequency lie below the spectrum of bulk transverse waves; this imposes conditions on the characteristics of the defect layer and leads to negative effective dispersion of the surface shear waves, contrary to the positive dispersion considered in the previous Section. Moreover, as was shown in Refs. 10 and 11, in this case the solitons exist only in the case of a ''hard'' nonlinearity of the medium $(N>0)$. This condition is opposite to the condition for the existence of solitons in a homogeneous medium or near an ideal surface. Indeed, now we are considering a nonlinear Love wave.[33] Since the nonlinearity causes localization of the wave only in the longitudinal direction, the properties of the solitons that arises are of a specific nature. Although in the previous Section we considered two-dimensional solutions but (as was pointed out) in a three-dimensional medium, nonlinearity leads to localization in all three directions. In the case under consideration here, the wave is localized near the surface, while in the plane of the surface it is localized only in the direction of propagation. Thus in the three-dimensional case the solitons remain two-dimensional (see Fig. 4b).

For comparison of the surface solitons of different types, let us first give a way of obtaining a simple qualitative solution in a medium with a film coating. We consider a half space covered by a thin film (of thickness h) of a material differing only in density from that of the bulk. It is clear that in the case of a planar defect the symmetric localized excitations will be described by the same solutions as in a half space coated by a film if the thickness of the planar defect is equal to $2h$. It is known[33] that Love waves exist in a linear medium only in the case when the density ρ_0 in the film is greater than the density ρ of the material in the bulk ($\rho_0/\rho=s>1$), and the dispersion relation of such waves at small wave numbers has the form

$$\omega_0^2=k^2-h^2\nu^2k^4, \tag{25}$$

where $\nu=s-1$ is a characteristic of the capillary effects; as above, the speed of sound in the bulk is assumed equal to unity. We see that linear Love waves have negative dispersion ($D=-3h^2\nu^2k<0$). This dispersion relation is determined by the decay of the amplitude of the surface wave with distance from the surface: $u\sim\exp(-\gamma z)$, where $\gamma\approx hk^2\nu\sim D^2$. In the long-wavelength limit ($hk\ll1$) we have $\gamma/k\approx hk\nu\ll1$, i.e., the change in field along the coordinate z occurs much more slowly than along the coordinate x: $\partial/\partial z\ll\partial/\partial x$. Therefore, in a treatment of small-amplitude nonlinear localized Love waves which are independent of the coordinate y, we can neglect all the nonlinear terms in Eq. (12) which contain derivatives with respect to the coordinate z, keeping only the leading term $\sim u_x^2u_{xx}$. Furthermore, in this equation we can drop all of the "internal" dispersional linear terms on account of the presence of the effective dispersion due to the film. As we see from Eq. (25), its presence is determined by the dispersion term $\sim h^2\nu^2u_{xxxx}$, which for $h\nu\gg a$ exceeds the largest dispersion term $a^2\chi u_{xxxx}$ in Eq. (12), which is due to the intrinsic dispersion of the bulk waves. Thus instead of (12) we can limit consideration in the bulk to the equation

$$u_{tt}=u_{xx}+u_{zz}+\delta u_x^2u_{xx},\quad z>0, \tag{26}$$

which should be supplemented by an effective boundary condition. This is most easily obtained by integrating the equation analogous to (26) for the film over its thickness ($-h<z<0$):

$$hsu_{tt}=hu_{xx}+u_z+h\delta u_x^2u_{xx},\quad z=0. \tag{27}$$

This approach gives the correct result for the spectrum of Love waves in the case of long wavelengths, $k\ll1/h$: in the linear limit, Eqs. (26) and (27) imply the dispersion relation

$$\omega_0^2=k^2-h^2(s\omega_0^2-k^2)^2, \tag{28}$$

which for $k\ll1/h$ agrees with the exact expression for the dispersion relation of Love waves and with expression (25). Formally this same dispersion relation can be obtained in the following way. In the linear approximation, it follows from Eq. (27) that in the region near the boundary of the medium and film

$$\frac{\partial}{\partial z}\approx h\left(s\frac{\partial^2}{\partial t^2}-\frac{\partial^2}{\partial x^2}\right). \tag{29}$$

(The relation $\partial/\partial z\sim\partial^2/\partial x^2$ for surface waves was mentioned above.) Now substituting the operator (29) into the linearized equation (26), we again arrive at the spectrum of Love waves (28). However, if such a substitution is done in the nonlinear equation (26), then we obtain a modified Boussinesq equation (2) with an effective dispersion $\chi=h^2\nu^2$:

$$u_{tt}=u_{xx}+h^2\nu^2u_{xxxx}+\delta u_x^2u_{xx}. \tag{30}$$

Since now the dispersion is negative ($D<0$) the soliton solutions exist only for a "hard" nonlinearity ($\delta>0$, $N>0$), i.e., the conditions for the existence of a soliton are directly opposite to the conditions near an ideal surface. The solution (30) itself has the form of expression (9) with $\chi=h^2\nu^2$. Having used the z dependence typical for linear Love waves, $u\sim\exp(-\gamma z)$ with $\gamma=\sqrt{k^2-\omega^2}\approx h\nu k^2$, we have a final approximate solution for surface solitons near a surface with a film coating:

$$u\approx\frac{2\sqrt{2}\varepsilon}{\sqrt{\delta}k^2}\operatorname{sech}\left(\frac{\varepsilon(x-Vt)}{\sqrt{3}h\upsilon k}\right)\times\sin(kx-\omega t)\exp(-h\upsilon k^2z), \tag{31}$$

where $\varepsilon=\sqrt{\omega^2-k^2+h^2\nu^2k^4}$ and $V\approx1-3h^2\nu^2k^3/2$. From solution (31) and the exact expression for the localization parameter γ of the Love wave we see that the soliton frequencies for a fixed value of k lie in the interval $k^2-h^2\nu^2k^4<\omega^2<k^2$. The above derivation of the soliton solution is of a qualitative character. A rigorous method of finding the soliton solutions is given in Appendix.

It follows from (31) that the localization region in the plane of the surface $\Delta x\sim h\nu k/\varepsilon$ is determined by the same expression as in the case of an ideal surface, but with an effective dispersion parameter. However, the size of the soliton in the direction of the z axis is now given by the quantity $\Delta z\sim1/(h\nu k^2)$, which is completely different from the case of the ideal surface ($\Delta z\sim1/\varepsilon$). The ratio of the sizes of the soliton in different directions,

$$\frac{\Delta x}{\Delta z}\sim kh\upsilon\,\frac{k^2h\upsilon}{\varepsilon} \tag{32}$$

differs from its counterpart in the case of the ideal surface by the factor $k^2h\nu/\varepsilon$, which can be arbitrary.

Thus we see that multidimensional shear solitons in a homogeneous medium and in a medium with a planar defect and surface solitons near an ideal surface and a surface covered with a thin film can have substantially different structures.

APPENDIX

Here we consider the system of equations (26), (27) for the displacements $u(x,z,t)$ in the bulk of an anharmonic crystal and on its surface, $u(x,z=0,t)=U(x,t)$. For small-amplitude weakly localized surface solitons in the "resonance" approximation, solution (26), (27) can be written in the form

$$u=a(x-Vt,z)\sin(kx-\omega t)+b(x-Vt,z)\cos(kx-\omega t), \tag{A1}$$

$$U=A(x-Vt)\sin(kx-\omega t)+B(x-Vt)\cos(kx-\omega t), \tag{A2}$$

where the frequency differs only slightly from the frequency of Love linear surface waves, $\omega_0(k)$: $\omega^2-\omega_0^2(k)=\varepsilon^2\ll1$; the dependence of the functions a, b, A, and B on the argument ($x-Vt$) is slow: $\partial/\partial x\sim\varepsilon$, while the order of each of the functions a, b, A, and B is as follows: $a\sim A\sim\varepsilon$, $b\sim B\sim\varepsilon^2$. (The dependence on the coordinate z is now unrelated to the small parameter ε.) We introduce the characteristic deviation of the frequency from the dispersion relation for bulk linear waves $\gamma=\sqrt{k^2-\omega^2}$. Substituting expansions (A1) and (A2) into Eqs. (26) and (27) and equating the terms in $\sin(kx-\omega t)$ and $\cos(kx-\omega t)$ to zero, we obtain the following system of equations accurate to ε^3:

$$a_{zz}-\gamma^2 a=(V^2-1)a_{xx}+2(k-V\omega)b_x+\delta k^4 a^3/4, \tag{A3}$$

$$b_{zz}-\gamma^2 b=-2(k-V\omega)a_x, \tag{A4}$$

$$h(sV^2-1)A_{xx}+h(k^2-s\omega^2)A+2h(k-sV\omega)B_x$$
$$+h\delta k^4 A^3/4-a_z(z=0)=0, \tag{A5}$$

$$h(k^2-s\omega^2)B-2h(k-sV\omega)A_x-b_z(z=0)=0. \tag{A6}$$

Writing the functions a and b in the form of expansions in powers of the small parameter ε: $a=a_1\varepsilon+a_3\varepsilon^3+\ldots$, $b=b_2\varepsilon^2+b_4\varepsilon^4+\ldots$ and writing out the terms with to order ε^3, we obtain a system of equations for finding the values of a_1, a_3, and b_2:

$$\varepsilon:\quad a_{1zz}-\gamma^2 a_1=0, \tag{A7}$$

$$\varepsilon^2:\quad b_{2zz}-\gamma^2 b_2=-2(k-V\omega)a_{1x}, \tag{A8}$$

$$\varepsilon^3:\quad a_{3zz}-\gamma^2 a_3=(V^2-1)a_{1xx}+\delta k^4 a_1^3/4$$
$$+2(k-V\omega)b_{2x}. \tag{A9}$$

The solution of this system of equations for waves localized near the surface has the obvious form:

$$a=f(x)\mathrm{e}^{-\gamma z}-f_{xx}\left\{\frac{(k-V\omega)^2}{2\gamma^2}z^2+\frac{(k-V\omega)^2}{2\gamma^3}z\right.$$
$$\left.+\frac{(V^2-1)}{2\gamma}z\right\}\mathrm{e}^{-\gamma z}+\frac{\delta k^4}{32\gamma^2}f^3\mathrm{e}^{-3\gamma z}, \tag{A10}$$

$$b=f_x\frac{(k-V\omega)}{\gamma}ze^{-\gamma z}. \tag{A11}$$

From here, finding the values of a, a_x, a_{xx}, a_z, b, b_x, and b_z at $z=0$ and substituting them into equations (A5) and (A6), we obtain the following two equations for finding the function $f(x)$ and the parameter V:

$$\varepsilon^3:\quad \left[h(sV_2-1)+\frac{(k-V\omega)^2}{2\gamma^3}+\frac{(V^2-1)}{2\gamma}\right]f_{xx}$$
$$+[\gamma+h(k^2-s\omega^2)]f+\frac{\delta k^4}{32}\left[\frac{h(k^2-s\omega^2)}{\gamma^2}+8h+\frac{3}{\gamma}\right]f^3=0, \tag{A12}$$

$$\varepsilon^2:\quad [2h(k-sV\omega)+(k-V\omega)/\gamma]f_x=0. \tag{A13}$$

From Eq. (A13) we obtain the relation $V(k,\omega)$ for the velocity of surface solitons:

$$V=\frac{k}{\omega}\,\frac{1+2h\sqrt{k^2-\omega^2}}{1+2hs\sqrt{k^2-\omega^2}}. \tag{A14}$$

In the limit of linear surface waves, by equating the coefficient of f in Eq. (A12) to zero we obtain the dispersion relation (25). It then follows from (A14) that $V\approx 1-3h^2k^2\nu^2/2=\partial\omega_0(k)/\partial k$, i.e., the soliton velocity is equal to the group velocity of linear surface waves. Taking these relations into account, we rewrite Eq. (A12) in the leading approximation as

$$(\sqrt{3}hk\upsilon)^2 f_{xx}-\varepsilon^2 f+\delta k^4 f^3/8=0. \tag{A15}$$

Thus in a consistent treatment of the problem, the solution for the surface shear solitons has the form

$$u(x,z,t)\approx\frac{4\varepsilon}{\sqrt{\delta}k^2}\operatorname{sech}\frac{\varepsilon(x-Vt)}{\sqrt{3}h\upsilon k}\,\mathrm{e}^{-h\upsilon k^2 z}\sin(kx-\omega t), \tag{A16}$$

where $\omega^2=k^2-h^2\nu^2k^4+\varepsilon^2$ and $V=1-3h^2k^2\nu^2/2$. This solution differs by a factor of $\sqrt{2}$ in the amplitude from the qualitative result given in the main text.

The authors thank Stavros Komineas for kindly providing the data of a numerical simulation of the dynamics of two-dimensional magnetic solitons in an easy-plane ferromagnet.

This study was supported by the INTAS program under Grant No. 99-0167.

[*] E-mail: kovalev@ilt.kharkov.ua

---

[1] A. P. Mayer, Phys. Rep. **256**, 237 (1995).
[2] V. G. Mozhaev, Phys. Lett. A **139**, 333 (1989).
[3] V. I. Gorentsveĭ, Yu. S. Kivshar', A. M. Kosevich, and E. S. Syrkin, Fiz. Nizk. Temp. **16**, 1472 (1990) [Sov. J. Low Temp. Phys. **16**, 833 (1990)].
[4] Yu. S. Kivshar and E. S. Syrkin, Phys. Lett. A **146**, 156 (1991).
[5] Yu. A. Kosevich, Phys. Lett. A **146**, 529 (1990).
[6] A. S. Kovalev and E. S. Syrkin, Zh. Éksp. Teor. Fiz. **102**, 522 (1992) [JETP **75**, 277 (1992)].
[7] A. S. Kovalev and E. S. Syrkin, Surf. Sci. **346**, 337 (1996).
[8] K. Bataille and F. Lund, Physica D **6**, 95 (1982).
[9] A. A. Maradudin, in *Physics of Phonons*, edited by T. Paszkievich, Springer, New York (1987), p. 82
[10] G. A. Maugin and H. Hadouaj, in *Frontiers in Nonlinear Acoustics*, edited by M. F. Hamilton and D. T. Blackstock, Elsevier, London (1990), p. 565; Phys. Rev. B **44**, 1266 (1991).
[11] H. Hadouaj and G. A. Maugin, C. R. Acad. Sci., Paris, **2–309**, 1877 (1989); J. Phys. (Paris), Colloq. **51**, C2-57 (1990); Wave Motion **16**, 115 (1992).
[12] Y. Nakagawa, Jpn. J. Appl. Phys. **22**, 157 (1985).
[13] M. Planat and M. Hoummady, Appl. Phys. Lett. **55**, 103 (1989).
[14] V. I. Nayanov, JETP Lett. **44**, 314 (1986).
[15] G. A. Maugin, H. Hadouaj, and B. A. Malomed, Phys. Rev. B **45**, 9688 (1992).
[16] C. Eckl, A. P. Mayer, and A. S. Kovalev, Phys. Rev. Lett. **81**, 983 (1998).
[17] C. Eckl, J. Schollmann, A. P. Mayer, A. S. Kovalev, and G. A. Maugin, Wave Motion **34**, 35 (2001).
[18] L. K. Zarembo and V. A. Krasil'nikov, Usp. Fiz. Nauk **102**, 549 (1970) [Sov. Phys. Usp. **14**, 216 (1971–72)].
[19] V. I. Nayanov and I. A. Vasil'ev, Fiz. Tverd. Tela (Leningrad) **25**, 2490 (1983) [Sov. Phys. Solid State **25**, 1430 (1983)].
[20] M. K. Balakirev, A. L. Belostotskiĭ, and L. A. Fedyukhin, Fiz. Tverd. Tela (Leningrad) **25**, 339 (1983) [Sov. Phys. Solid State **25**, 191 (1983)].
[21] A. M. Kosevich and A. S. Kovalev, *Introduction to Nonlinear Physical Mechanics* [in Russian], Kiev, Naukova Dumka (1989).
[22] A. M. Kosevich, B. A. Ivanov, and A. S. Kovalev, *Nonlinear Magnetization Waves. Dynamical and Topological Solitons* [in Russian], Kiev, Naukova Dumka (1983).
[23] V. N. Karpman, *Non-Linear Waves in Dispersive Media*, Pergamon Press, Oxford (1975), Nauka, Moscow (1973).
[24] A. M. Kosevich and A. S. Kovalev, Zh. Éksp. Teor. Fiz. **67**, 1793 (1974) [Sov. Phys. JETP **40**, 891 (1975)].
[25] A. S. Kovalev, Author's Abstract of Doctoral Dissertation [in Russian], Kharkov (1989).
[26] H. G. Smith and N. Wakabayashi, in *Phonons in Dynamics of Solids and*

Liquids, Vol. 3, edited by S. W. Lovesay and T. Springer, Springer, Berlin (1977), p. 98.
[27] Z. K. Yankauskas, Radiofizika **9**, 417 (1966).
[28] R. Y. Chiao, E. Garmire, and C. H. Townes, Phys. Rev. Lett. **13**, 479 (1964).
[29] J. I. Rasmussen and R. Rypdal, Phys. Scr. **33**, 481 (1986).
[30] B. B. Kadomtsev and V. I. Petviashvili, Dokl. Akad. Nauk SSSR **192**, 753 (1970) [Sov. Phys. Dokl. **15**, 539 (1970–1)].
[31] L. A. Bordag, A. R. Its, and W. B. Matveev, Phys. Lett. A **63A**, 205 (1977).
[32] N. Papanicolaou and P. N. Spathis, Nonlinearity **12**, 285 (1999).
[33] S. V. Biryukov, Yu. V. Gulyaev, V. V. Krylov, and V. P. Plesskiĭ, *Surface Acoustic Waves in Inhomogeneous Media* [in Russian], Nauka, Moscow (1991).

Translated by Steve Torstveit

LOW TEMPERATURE PHYSICS VOLUME 28, NUMBER 6 JUNE 2002

Thermal conductivity of a GaAs single crystal grown in microgravity

A. I. Ivanov and A. N. Luk'yanov

S. P. Korolev "Energiya" Rocket and Space Corporation, 141070 Korolev, Moscow District, Russia

B. A. Merisov, A. V. Sologubenko, and G. Ya. Khadjai*

V. N. Karazin Kharkov National University, pl. Svobody 4, 61077 Kharkov, Ukraine

(Submitted February 28, 2002)
Fiz. Nizk. Temp. **28**, 648–652 (June 2002)

A comparative study of the thermal conductivity in the temperature interval 2–300 K is carried out for single-crystal GaAs samples grown on Earth and grown under analogous conditions in microgravity on the manned space station Mir. It is found that the heat transfer in the samples is due to phonons. A consistent processing of the temperature dependence of the thermal conductivity of the Earth-grown and space-grown samples is carried out in the framework of the Debye model of the phonon spectrum with allowance for boundary and resonant scattering and for scattering on "planar defects" and phonon–phonon *U*-processes. The difference in the behavior of the thermal conductivity space-grown and Earth-grown samples is due to the presence of excess arsenic in the Earth-grown sample, resulting in both resonant scattering and scattering on planar defects, which may be clusters of arsenic atoms. © *2002 American Institute of Physics.* [DOI: 10.1063/1.1491187]

INTRODUCTION

Gallium arsenide is one of the most important semiconductor materials, used for fabricating fast and radiation-resistant microelectronic devices. A study of the influence of the growth technology and conditions on the degree of perfection of GaAs single crystals is a subject of ever-present interest.

The experimental study of the thermal conductivity of such materials, especially at low temperatures, with the results described in terms of the existing theoretical models makes it possible to establish the spectrum of defects in the samples and to estimate the change of their concentrations as a result of treatment procedures.

This paper is devoted to a comparative study of the low-temperature thermal conductivity of GaAs samples grown by the same technique on Earth and in a microgravity environment on the manned space station Mir.

EXPERIMENT

The gallium arsenide single crystal investigated is a single monolith consisting of two parts: a single crystal grown on Earth under laboratory conditions, and a single crystal obtained by recrystallization under conditions of microgravity in space on the Gallar furnace.

The choice of this two-part single crystal as the object of study was deemed optimal for a comparative analysis, since the laboratory-grown single crystal is not only the seed but also the initial object for obtaining the gallium arsenide single crystal from the melt by the method of directed crystallization under conditions of microgravity.

The initial single crystal prepared for the space experiment was a cylinder 22.2 mm in diameter and 85 mm long. The length of the part of the sample remelted in space was 50 mm. After the space experiment, ingot sections 25 and 15 mm long were cut from the Earth and space samples, and then samples were cut from them by oriented cutting technology.

The elemental composition of the samples was determined on an ÉMAL-2 laser energy–mass analyzer. The measures of the analysis are presented in Table I.

Analysis of the structure of the gallium arsenide samples with the use of a URS-60 apparatus and a URS-50 IM diffractometer and also by standard methods of x-ray structural analysis showed that these samples are single crystals. The growth direction coincides quite precisely with the [100] crystallographic direction. In both samples a macroblock structure is obtained. The average density of dislocations was 9.9×10^4 cm^{-2} in the Earth-grown sample and 7.8×10^4 cm^{-2} in the space-grown sample. The impurity concentration was determined by spark mass spectrometry on a JMS-01-BM2 mass spectrometer. The level of most impurities in both samples was less than 10^{-8} by mass. The impurities of fluorine, magnesium, sulfur, calcium, and zinc were at the level of 10^{-7} by mass. The concentration of sodium, potassium, phosphorus, iron, and chromium in the space-grown crystal were lower. Considering the level of sensitivity of the methods employed, we can state that no phase segregates or elemental precipitates larger than 1 μm were present and that the concentration of light elements was no

TABLE I. Elemental composition of the samples.

Element	Concentration, at. %	
	Earth-grown	Space-grown
As	50.044	49.974
Ga	49.944	49.976
O	0.012	0.05

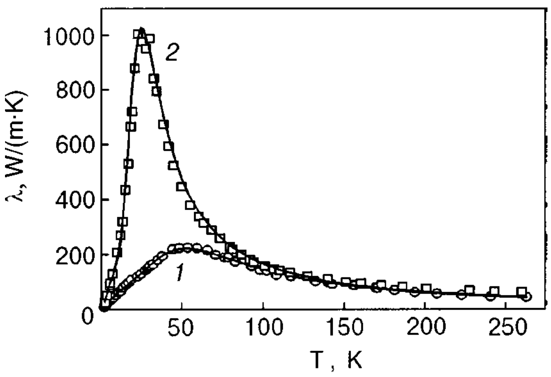

FIG. 1. Temperature dependence of the thermal conductivity λ of a GaAs single crystal: Earth-grown sample (*1*); the space-grown sample, which has been remelted in a microgravity environment (*2*).

greater than 10^{-4} by mass and that of heavy elements no greater than 10^{-5} by mass.

The thermal conductivity of the samples was measured using a steady uniaxial heat flux in the temperature interval 2–300 K. The heat flux was directed along the [100] crystallographic direction. The temperature was monitored with Cu–Au+Fe thermocouples. To eliminate heat loss to radiation at $T>100$ K we used an active antiradiation shield.

RESULTS AND DISCUSSION

1. The temperature dependence of the thermal conductivity λ of the two GaAs samples is shown in Fig. 1. The maximum value of the thermal conductivity of the "space-grown" sample is approximately 5 times as high as the analogous value for the "Earth-grown" sample. The maximum of the thermal conductivity of the space-grown sample is shifted to lower temperatures.

Measurements of the temperature dependence of the electrical conductivity showed that for both samples the electronic contribution to the thermal conductivity can be neglected in the entire temperature interval studied. We note that the electrical conductivity of the Earth-grown sample is approximately twice as high as that of the space-grown sample.

2. The temperature dependence of the thermal conductivity of the samples was described by the well-known phonon scattering mechanisms.

Extremely complicated formulas are often used for calculating the temperature dependence of the thermal conductivity of GaAs (see, e.g., Refs. 1–6), which take into account the nonlinear dispersion of the phonon spectrum, the difference in the phonon–phonon interaction for the longitudinal and transverse phonons, etc. This complication of the model inevitably leads to an increase in the number of parameters to be calculated, often without improving the fit but only increasing the uncertainty in the parameters and the time required to do the calculations. It is therefore natural to try to use the simplest model that corresponds to the process to be described.

The temperature dependence of the thermal conductivity of the Earth-grown and space-grown samples were calculated in the framework of the Debye model of the phonon spectrum[7] (the Debye temperature $\Theta=344$ K; the value sound velocity $V_s=3265$ m/s; Ref. 8):

$$\lambda(T)=\frac{k}{2\pi^2 V_s}\left(\frac{k}{h}\right)^3 T^3\int_0^{\Theta/T}\tau(x)\frac{x^4e^x}{(e^x-1)^2}dx, \qquad (1)$$

$$x=h\omega/kT,$$

$$\tau^{-1}(x)=\sum_i \tau_i^{-1}(x). \qquad (2)$$

Initially the following processes were taken into account in the calculation of the inverse relaxation time $\tau^{-1}(x)$: scattering on boundaries, resonant scattering with allowance for damping, Rayleigh scattering on point defects, phonon–phonon U- and N-processes, and also scattering on "planar" defects.

However, it was found in the fitting that the coefficients for the terms describing the N-processes and Rayleigh scattering are equal to zero within the error limits. Taking the damping of the resonance into account also failed to improve the fit. Therefore, these terms were not taken into account in the subsequent calculations. The boundary scattering parameter was not varied, but the values of the transverse dimensions of the samples were used.

Thus the expression for the inverse relaxation time has the form

$$\tau^{-1}(\omega)=V/a_1+a_2\omega^2/(a_6^2-\omega^2)^2+a_3\omega^2 + a_4\omega^2 T\exp(-\Theta/Ta_5). \qquad (3)$$

Here the first term describes the boundary scattering, the second and third terms describe resonant scattering and scattering on "planar" defects,[9–11] and the last term describes

TABLE II. Parameters of the temperature dependence of the thermal conductivity of GaAs according to Eqs. (1)–(3).

Scattering mechanism	Coefficient	Sample		Relative change on going from the Earth-grown to the space-grown sample
		Earth-grown	Space-grown	
On boundaries	a_1,m	$3.36\cdot10^{-3}$	$1.94\cdot10^{-3}$	–
Resonant	a_2, s^{-3}	$29.9\cdot10^{33}$	$3.122\cdot10^{33}$	8.6
	a_6, s^{-1}	$10.065\cdot10^{12}$	$6.068\cdot10^{12}$	0.7
On "planar" defects	a_3, s	$96.83\cdot10^{-19}$	$2.016\cdot10^{-19}$	47.0
phonon-phonon	a_4, s/k	$1.172\cdot10^{-18}$	$1.156\cdot10^{-18}$	0.01
	a_5	2.820	3.272	−0.14

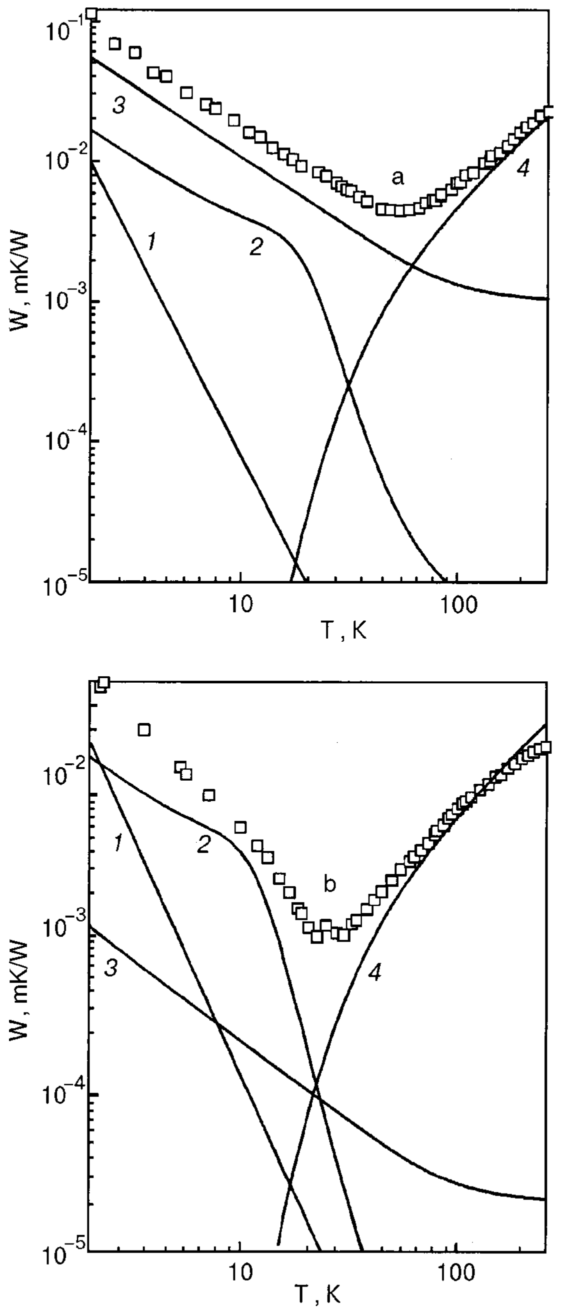

FIG. 2. Phonon scattering mechanisms for the Earth-grown (a) and space-grown (b) samples. The contribution of the different scattering mechanisms to the overall thermal resistance process: *1*—boundary scattering, *2*—resonant scattering, *3*—scattering on ''planar'' defects, *4*—phonon–phonon scattering; □—experiment.

phonon–phonon *U*-processes. The coefficients a_2–a_6 were varied. Values of the coefficients ensuring an approximation error of not worse than 4% are given in Table I. It is seen from Table II that the coefficients a_4 and a_5 for the two samples are close in value, as expected, since the parameters of the phonon–phonon scattering should not depend on the heat treatment.

The contributions of the individual scattering mechanisms to the total thermal resistivity of the Earth-grown and space-grown samples are illustrated in Fig. 2.

The difference in the behavior of the space-grown and Earth-grown samples is entirely due to the presence of defects. On going from the Earth-grown to the space-grown sample the coefficients characterizing the resonant scattering (a_2) and the ''planar'' defects (a_3) decrease. Both of these terms are proportional to the concentration of the corresponding defects.

An elemental analysis (see Table I) showed that the main difference between the samples is the presence of nonstoichiometric (excess) arsenic (0.1 at. %) in the Earth-grown sample. In the space-grown sample the concentration of excess arsenic is about 20 times lower and is right at the limits of error. This change in the concentration of excess arsenic is correlated with the relative changes of the coefficients a_3 and a_2.

Thus the presence of excess arsenic is the only possible cause of both the resonant scattering and the scattering on ''planar'' defects. The latter could be clusters of arsenic atoms. The slight shift of the resonance frequency (the coefficient a_6) may be due to relaxation of the internal stresses caused by the presence of ''planar'' defects. It was shown in Ref. 12 that the resonance frequencies can be smeared out and shifted in the presence of internal stresses in the sample. These stresses are probably larger in the Earth-grown sample.

The approximating curve of the thermal conductivity of the space-grown sample at high temperatures deviates on the low side from the experimental values. This may be due to the appearance of photonic heat conduction in the sample.[13]

CONCLUSION

In summary, the results of measurements of the temperature dependence of the thermal conductivity have shown that excess arsenic contained in the Earth-grown sample forms clusters that sharply increase both the resonant scattering and scattering on ''planar'' defects. Elimination of the excess arsenic leads to appreciable growth of the thermal conductivity in the low-temperature region—in the region of the maximum the thermal conductivity of the space-grown sample was 5 times higher than the thermal conductivity of the Earth-grown sample.

[*] E-mail: george.ya.khadjai@univer.kharkov.ua

---

[1] M. D. Tiwari, D. N. Talwar, and B. K. Agrawal, Solid State Commun. **9**, 995 (1971).
[2] M. C. Al Edani and K. S. Dubey, Phys. Status Solidi B **87**, K47 (1978).
[3] M. C. Al Edani and K. S. Dubey, Phys. Status Solidi B **86**, 741 (1978).
[4] K. S. Dubey and G. S. Verma, Phys. Rev. B **4**, 4491 (1971).
[5] S. Singh and G. S. Verma, Phys. Rev. B **19**, 1069 (1979).
[6] C. M. Bhandari and G. S. Verma, Phys. Rev. **140**, A2101 (1965).
[7] R. Berman, *Thermal Conduction in Solids* [Clarendon Press, Oxford (1976); Mir, Moscow (1979)].
[8] C. W. Garland and K. C. Parks, J. Appl. Phys. **33**, 759 (1962).
[9] P. L. Vuillermoz, A. Laugier, and P. Pinard, Solid State Commun. **17**, 413 (1975).
[10] P. L. Vuillermoz, J. Jouglar, A. Laugier, and H. R. Winteler, Phys. Status Solidi A **41**, 561 (1977).
[11] P. L. Vuillermoz, A. Laugier, and C. Mai, J. Appl. Phys. **46**, 4623 (1975).
[12] V. Adolf, D. Fortier, J. H. Albany, and K. Suzuki, Phys. Rev. B **21**, 5651 (1980).
[13] B. M. Mogilevskiĭ and A. F. Chudnovskiĭ, *Thermal Conductivity of Semiconductors* [in Russian], Nauka, Moscow (1972).

Translated by Steve Torstveit

LOW-TEMPERATURE PHYSICS OF PLASTICITY AND STRENGTH

Kinetics of the low-temperature structural transformation in the In–4.3 at. % Cd solid solution

S. V. Lubenets, V. D. Natsik, L. N. Pal-Val, P. P. Pal-Val,* and L. S. Fomenko

B. Verkin Institute for Low Temperature Physics and Engineering, National Academy of Sciences of Ukraine, pr. Lenina 47, 61103 Kharkov, Ukraine

(Submitted February 27, 2002)
Fiz. Nizk. Temp. **28**, 653–666 (June 2002)

The reversible structural transformation of the hysteretic type observed previously by the authors in the In–4.3 at. %Cd alloy on low-temperature thermocycling is investigated further. In the hysteresis region (150–290 K) a pronounced instability of the macroscopic characteristics of the alloy is observed, which is manifested as time dependence of the dynamic Young's modulus and resistivity of the samples at a constant temperature fixed during the cooling or heating run. The kinetic effects are investigated in detail near the boundaries of the hysteresis, where they are most clearly expressed. Less clear signs of the structural transformation are observed on the temperature dependence of the microhardness of the alloy. It is found that the structural transformation is governed by thermally activated processes with several characteristic relaxation times: the analytical form of the kinetic curves and the temperature dependence of the relaxation times are substantially different for the direct (on cooling) and reverse (on heating) transformations. Similarities and differences between this transformation and the known structural rearrangement processes in the physics of alloys are discussed. The structural transformation investigated here is also discussed in relation to the phase diagram of the In–Cd system. © *2002 American Institute of Physics.* [DOI: 10.1063/1.1491188]

INTRODUCTION

In–Cd substitution solid solutions with cadmium concentrations 4 at. %$<c<$5.9 at. % on cooling undergo a reversible structural transformation of the martensitic type, at which the high-temperature fcc phase goes over to a low-temperature phase with the fct lattice inherited from indium.[1–4] The temperature of the transformation M_s strongly depends on the cadmium concentration c and decreases from $M_s\approx 421$ K at $c=4$ at. % to $M_s\approx 293$ K at $c=5.9$ at. %. The transformation occurs in a temperature interval of the order of 10 K. As far as we know, the phase diagram below room temperature has not been studied before and it is labeled as provisional in the literature.[1–4]

We recently showed[5,6] that the martensitic phase is unstable at low temperatures. Thus the alloy In–4.3 at. % Cd in low-temperature thermocycling at a finite rate of change of the temperature undergoes a reversible structural transformation which is accompanied by hysteresis and is clearly discerned in measurements of the acoustic, micromechanical, and resistive properties. The temperature boundaries of the hysteresis depend on the rate of thermocycling and are approximately 130–290 K according to the data of acoustic measurements, and 175–290 K according to the resistometric data. The transformation has a pronounced isothermal character: within the hysteresis loop both in the direct transition (during cooling) and in the reverse transition (during heating) the Young's modulus and the resistivity depend substantially on the hold time of the sample at a fixed temperature. The microscopic picture of this structural transformation remains unclear at the present time.

The goal of this study was to make a detailed investigation of the kinetics of the transition process in the martensitic phase of the In–4.3 at. % Cd solid solution from a metastable to an equilibrium state in the region of the hysteresis loop, particularly near its boundaries. The kinetics of the relaxation to equilibrium is studied by measuring the time dependence of the dynamic Young's modulus and resistivity. These data are supplemented with measurements of the temperature and concentration dependences of the microhardness of In–Cd solid solutions with cadmium concentrations $c<5.9$ at. %. These results are needed for analysis of the microscopic processes that govern the low-temperature structural instability of In–Cd solid solutions. In addition, they may be useful for refining the low-temperature, In-rich side of the state diagram of the In–Cd system.

1. EXPERIMENTAL PROCEDURE

The binary alloys In–c at. % Cd ($c=1.5$, 3, and 4.3) were obtained by fusion of weighed portions of 99.999% pure indium and cadmium in air in an alundum crucible. The melt, overheated to about 20 °C above the melting temperature, was poured onto the surface of a steel or ceramic slab. The ingot was a large-grained polycrystal (average grain diameter ~0.3 mm). The cadmium concentration in the ingot was determined by chemical analysis.

Part of the ingot was forged and rolled into bars of square cross section (~2×2 mm or ~0.9×0.9 mm), from which samples of the necessary size were cut. For the acoustical measurements we used samples with dimensions of $2\times2\times7.5$ mm, with ends that had been lapped perpendicular to the long axis of the sample on a steel slab with a fine abrasive. The samples for the resistance measurements had dimensions of $0.9\times0.9\times23$ mm. The surface of the samples for the micromechanical measurements was polished in a solution of hydrochloric acid and hydrogen peroxide. The other details of the sample preparation and the measurement of the temperature dependence of the microhardness can be found in Ref. 7.

A study of the morphology of the grains of the martensitic phase showed that they consist of thin domains, the interfaces between which are twin boundaries. This sort of microstructure and crystallographic misorientation of the domains, as a rule, makes for a number of interesting features of the inelastic deformation of the alloy, in particular, superelasticity, high damping of mechanical vibrations, etc.

The acoustical properties (the logarithmic decrement δ of vibrations and the dynamic Young's modulus E) were studied by the two-component composite vibrator method[8] at a longitudinal standing wave frequency of $\sim$75 kHz at a constant amplitude of the acoustic strain $\varepsilon_0=2\times10^{-7}$ in the amplitude-independent region.

The resistivity ρ was measured in direct current using a standard four-probe method. The power dissipated in the sample did not exceed 2×10^{-5} W. To eliminate the influence of parasitic emf's, the measurements were made for two opposite directions of the transport current. To establish the temperature boundaries of the structural instability of the alloy, we studied the temperature dependences of δ, E, and ρ, which were obtained during an isochronal thermocycling in the temperature interval 320–5.5–320 K with an average cooling (heating) rate of 0.25–1 K/min. The temperature of the sample was changed by using a "standard" two-step procedure: first the temperature was lowered (raised) at a rate of 0.5–2 K/min, then held steady for 10–2.5 min; after the hold, the measurements of δ, E, and ρ were made.

For studying the kinetics of the transition from one structural state to another we measured the isothermal time dependences of the dynamic Young's modulus and the resistivity at fixed temperatures within the boundaries of the hysteresis loop. For studying the kinetics of the "direct" transformation from the high-temperature to the low-temperature state the samples were cooled at an average rate of 2 K/min from room temperature to one of the measurement temperatures (250, 240, 230, 220, 210, 205, 200, 190, and 175 K). For studying the kinetics of the "reverse" transformation the samples were first held for six hours at a temperature of 200 K to establish the equilibrium low-temperature structural state, and then were heated at an average rate of 1 K/min to one of the measurement temperatures (265, 275, and 280 K).

The Vickers microhardness H_V was measured in the temperature interval 77–300 K with a load of 0.046 N on the indenter and an indentation time of 10 s. For studying the temperature dependence of H_V the sample temperature was changed at a rate of 1 K/min or stabilized for a certain time at the chosen temperature points. In the latter case 10 indentations were made and the average value of the diagonal of the indentation (and, hence, of the hardness) was determined at the given temperature, while in the "ramp" mode each temperature corresponded to one indentation, and the lengths of the diagonals (hardness values) were averaged over a temperature interval $\Delta T=5$ K. The values obtained were assigned to the temperature at the midpoint of the interval.

2. EXPERIMENTAL RESULTS

2.1. Temperature dependence of the acoustic attenuation (internal friction) and the dynamic Young's modulus

The typical temperature dependence of the logarithmic damping decrement δ and dynamic Young's modulus E, obtained in the temperature interval 300–5.5–300 K on isochronal thermocycling of a sample of the alloy In–4.3 at. % Cd at an average rate of 0.5 K/min is shown in Fig. 1. The large values of the decrement ($\delta>5\times10^{-3}$) over a rather wide interval of low temperatures attest to the fact that this alloy should be classed as a high damping material. The $\delta(T)$ curve exhibits nonmonotonic behavior (Fig. 1a): the decrement decreases sharply with decreasing temperature from 300 to 200 K, reaches a minimum at $T\approx125$ K, and then increases, reaching a maximum at $T\approx12$ K, after which a decrease can be noticed. On heating, the $\delta(T)$ curve does not completely retrace the curve obtained on cooling: in the temperature interval 200–270 K the decrement is higher on heating. The maximum size of the hysteresis loop in the vertical direction is observed at 250 K and reaches approximately 25% of the value of the attenuation measured on increasing temperature.

The temperature dependence of the dynamic Young's modulus E is also nonmonotonic and exhibits a wide hysteresis with boundaries of 130–290 K (Fig. 1b). In the hysteresis region the Young's modulus, like the decrement, has a

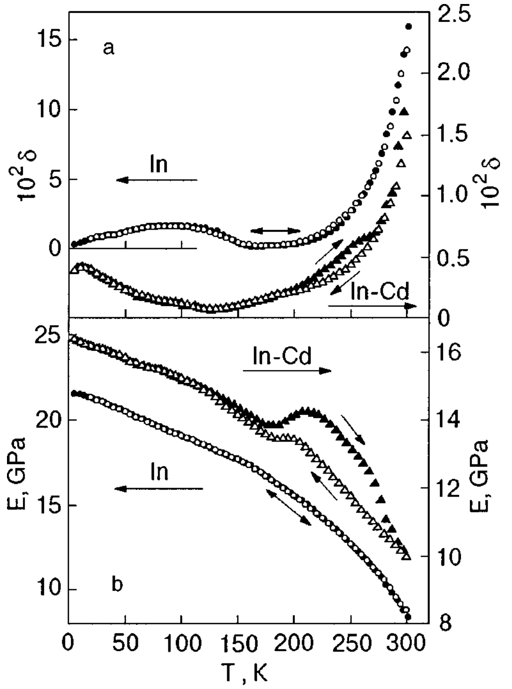

FIG. 1. Temperature dependence of the decrement δ (a) and dynamic Young's modulus E (b) for a single isochronal thermocycling at an average rate of 0.5 K/min: (△,▲)—In–4.3 at. % Cd, (○,●)—pure In; the unfilled symbols are data taken on cooling of the samples, the filled symbols, on heating.

higher value on heating: the maximum difference is reached at $T \approx 250$ K and amounts to about 10%, which is an appreciable effect for the elastic modulus. The $E(T)$ curves both on cooling and on heating exhibit a pronounced anomaly near 190 K in the form of a smeared step with a positive derivative dE/dT.

The hysteresis loops on $\delta(T)$ and $E(T)$ are completely reproduced when the samples are heated to room temperature and the thermocycling is repeated.

The acoustic characteristics of a polycrystalline sample of pure indium do not exhibit hysteresis on thermocycling in this temperature interval (see Fig. 1) and do not change during an isothermal hold.

2.2. Instability and kinetics of the change of the Young's modulus in the hysteresis region

By repeating the isochronal thermocycling several times in the vicinity of the lower boundary of the hysteresis loop, in the temperature interval 175–230 K, the sample can be brought to a stable low-temperature state, which exhibits higher values of the Young's modulus in the entire temperature interval—all the way down to liquid helium temperature. The total increase of the Young's modulus at 250 K has a value of the order of 22%. Figure 2a shows a schematic illustration of the change of the Young's modulus on successive thermocycles I, II, and III, constructed from the experimental measurements (see also Figs. 3–5 of Ref. 5). A feature of the limiting stable low-temperature state is the absence of any anomalies on the temperature dependence of the Young's modulus on thermocycling in the temperature interval 250–5.5 K.

The temporal instability of the Young's modulus is apparently due to the occurrence of a structural transformation in the sample. An interesting feature of the reaction of the Young's modulus to a variation of the temperature in the vicinity of the lower boundary of the hysteresis loop is that the value of E measured during both cooling and heating first falls sharply to values corresponding to the lower curve in Fig. 2a (the "unrelaxed" modulus E_U) and then grows, and by the end of a five-minute isothermal hold it has reached values corresponding to the upper curve (the partially "relaxed" modulus E_R). These transitions are illustrated schematically in Fig. 2a by the sequences $1 \rightarrow 2' \rightarrow 2$ (cooling) and $3 \rightarrow 4' \rightarrow 4$ (heating). In the real experiments the points *3*, *4* and *1*, *2* are the values of E_R corresponding to the temperatures T and $T \pm 5$ K (the "+" for heating and the "−" for cooling) and are separated in time by 10 min (the 5 min during which the temperature was changed at a rate of 1 K/min, and the 5 min of the isothermal hold prior to the measurements). The points $2'$ and $4'$ correspond to the "dip" values E_U measured at the instant the given temperature is reached.

The transition from a low-temperature hardened state to the initial high-temperature state occurs near the upper boundary of the hysteresis loop, in the interval 260–290 K (Fig. 2a), with a decrease of the modulus both during heating to the temperature of the isothermal hold and during the hold itself (the points $5 \rightarrow 6' \rightarrow 6$).

Thus we can conclude that below room temperature there are the two limiting branches $E_U(T)$ and $E_R(T)$ of the temperature dependence of the Young's modulus of the alloy In–4.3 at.% Cd (Fig. 2b): the branch $E_U(T)$ is realized for extremely rapid variation of the temperature, and the branch $E_R(T)$ for extremely slow. On thermocycling at a finite rate the Young's modulus in a time $t = 10$ min "ranges through" the values of E lying within the shaded loops in Fig. 2a, between the two successively measured values of the partially relaxed modulus (on subsequent thermocycles II and II the vertical range of the loops decreases, and they are not shown on the diagram). The value of the intermediate "dip" of the modulus near the low-temperature boundary of the hysteresis could not be established precisely. The fall of the modulus gave way to a rapid increase immediately after the temperature variation was stopped, and in the cases registered amounted to not less than 10% of the measured value of E. The kinetic curves of $E(t)$ characterizing the structural changes in the alloy were recorded after cooling from room temperature to one of four temperature points (205, 200, 190, and 180 K), which correspond to the smeared step on $E(T)$. The relaxation of the Young's modulus to its equilibrium value corresponds rather well to a first-order reaction (Fig. 3):

$$\Delta E(t) = E(t) - E(0) = \Delta E_{\max}[1 - \exp(-t/\tau_E)], \qquad (1)$$

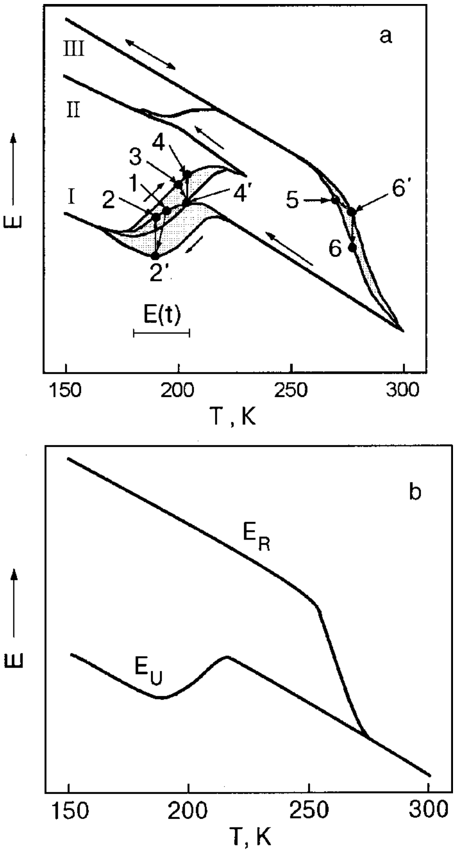

FIG. 2. Temperature dependence of the dynamic Young's modulus E during multiple thermocycling within the boundaries of the hysteresis loop (schematic): I,II,III—successive thermocycles; points *1, 3,* and *5* correspond to the values of the elastic modulus before the change in temperature, the points $2'$, $4'$, $6'$ are unrelaxed values of the elastic modulus at the time when the measurement temperature is reached; points *2, 4, 6* are partially relaxed values of the elastic modulus 5 min after the specified temperature was established. The temperature interval in which the $E(t)$ isotherms were measured is in the lower part of panel (a); the temperature dependence of the completely unrelaxed E_U and relaxed E_R Young's modulus (b).

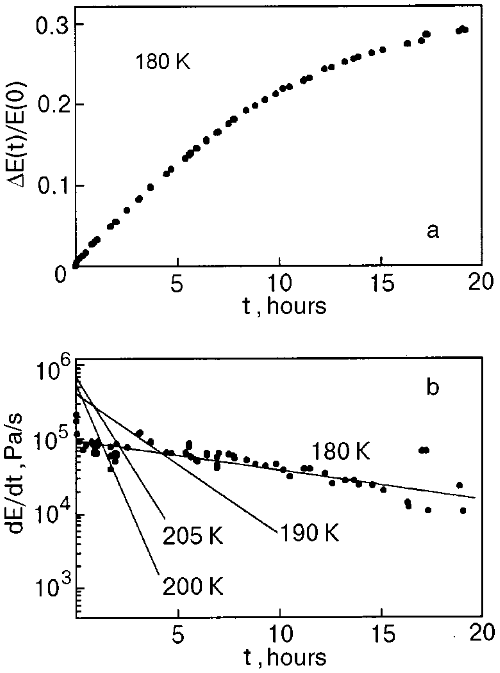

FIG. 3. Isothermal change of the Young's modulus after cooling of the alloy from 300 K to the specified temperature. The kinetic curve $\Delta E(t)/E(0)$ measured at 180 K (a); the logarithm of the rate of change of the Young's modulus versus the time at different temperatures; the straight lines are linear approximations obtained by the least-squares method; the experimental points are shown only for $T=180$ K (b).

where $t=0$ is the time at which the measurement of the Young's modulus begins. Here, however, we should mention the presence of small initial segments on the $E(t)$ curves where the increase of E is more rapid; clearly approximation (1) is not valid for those regions (see Fig. 3b). The relaxation time τ_E determined for the slope of the straight line in Fig. 3b has a substantial dependence on temperature (Fig. 4).

2.3. Temperature dependence of the resistivity

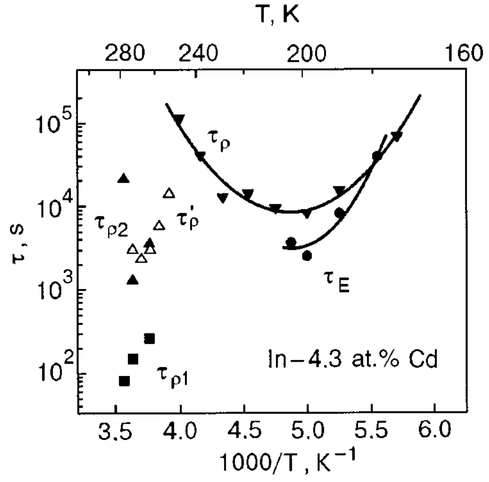

FIG. 4. Arrhenius plot for the relaxation times of the Young's modulus, τ_E (●), and of the resistivity, τ_ρ (▼) on cooling from 300 K, and also for two relaxation times of the resistivity: on heating of samples stabilized at 200 K, $\tau_{\rho 1}$ (▲) and $\tau_{\rho 2}$ (■), and on isothermal annealing with a step of $\Delta T=5$ K, τ'_ρ (△).

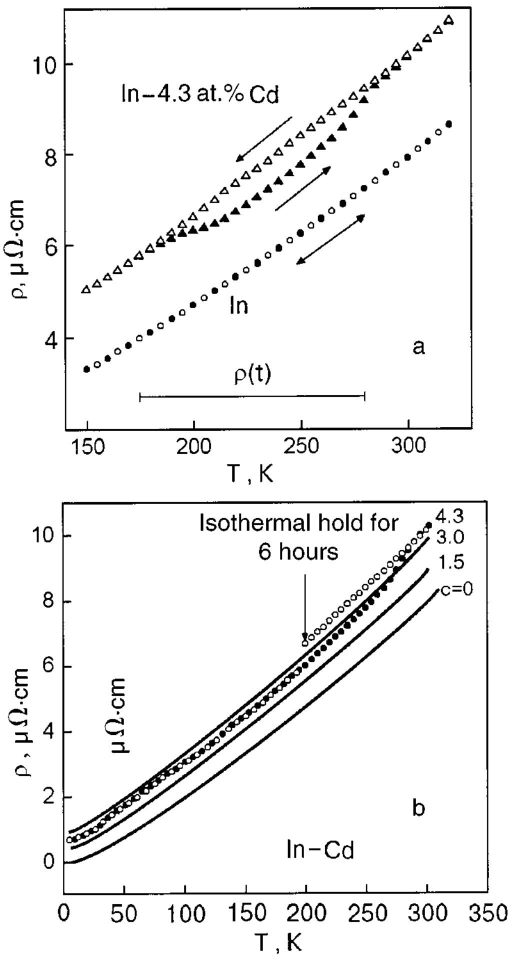

FIG. 5. Temperature dependence of the resistivity of pure In and of In–Cd alloys; the curves were obtained during single thermocycling at an average rate of 0.25 K/min. The temperature interval of the measurement of the time dependence of ρ is indicated in the lower part of panel (a); a 6-hour hold was made at 200 K during cooling of the alloy In–4.3 at. %Cd (b).

A more detailed study of the reversible structural transformation observed here was done by a resistometric method. The resistivity is one of the most sensitive indicators of the structure state of a material.[9,10] In Fig. 5 we show the temperature dependence of the resistance ρ of an In–4.3 at. % Cd alloy and of pure indium, obtained during thermocycling at a cooling (heating) rate of 0.25 K/min in the interval 320–150–320 K. For the pure indium the direct and reverse runs of $\rho(T)$ coincide completely, while for the alloy $\rho(T)$ exhibits a hysteresis loop with temperature boundaries of about 175–290 K, somewhat narrower than the hysteresis loop of the dynamic elastic modulus. In the central part of the hysteresis loop the resistance is 9% lower on heating than on cooling.

In the experiments we also recorded the temperature dependence of the resistivity ρ on cooling and heating for intermediate concentrations of cadmium in the alloy. It is seen in Fig. 5b that in the alloys with concentrations of 1.5 and 3 at. % Cd there is no hysteresis. This attests to the stability of the structure of these alloys in the low-temperature region.

In the hysteresis region a substantial temporal instability of the resistivity is observed for the In–4.3 at. % Cd alloy. The kinetic effects are most pronounced in the vicinity of the boundary of the hysteresis: an isothermal hold near $T\approx 190$ K is accompanied by a decrease of the resistivity, and one near $T\approx 270$ K by an increase (during heating of the

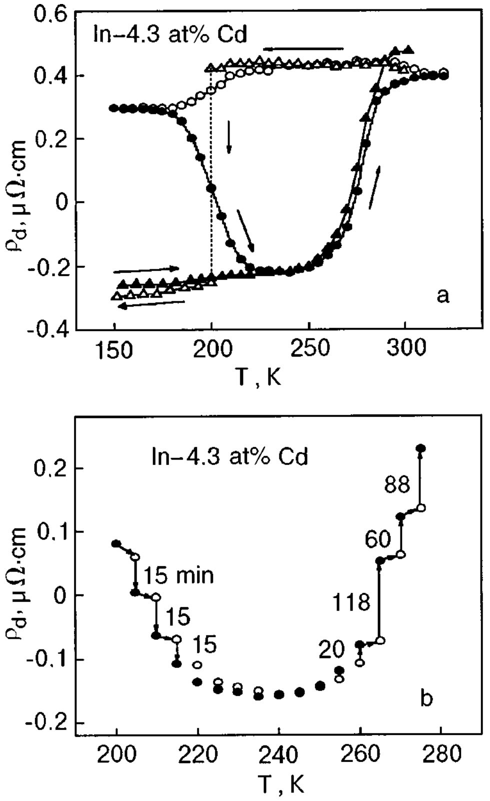

FIG. 6. Hysteresis of the reduced residual resistivity $\rho_d=\rho_{4.3}-\rho_3$ (see text) during isochronal thermocycling at a rate of 0.25 K/min (○,●) and during thermocycling with an intermediate isothermal hold at 200 K (△,▲) (the unfilled symbols are data taken on cooling of the samples, the filled symbols, on heating) (a). The unrelaxed (○) and partially relaxed (●) values of ρ_d during isothermal annealing with a step $\Delta T=5$ K (the numbers indicate the annealing time). The measurements were begun after a hold of 2.5 hours at 200 K (b).

sample). After thermocycling four times through the temperature interval 175–230 K as well as after a long hold of the sample at a fixed temperature within this interval (at $T=200$ K for the example shown in Fig. 6a), the value of the resistivity stabilizes, indicating that the transition to the low-temperature structural state has gone to completion. Heating to $T\approx310$ K completely restores the resistivity to its initial (higher) values, which correspond to the high-temperature structural state of the samples.

2.4. Instability of the resistivity in the hysteresis region

It is seen in Fig. 5 that the hysteresis effect in the temperature dependence of the resistivity of the alloy In–4.3 at. % Cd is observed against the background of a rather strong temperature dependence due to the electron–phonon interaction. This background can be subtracted from the experimental $\rho(T)$ curve under conditions such that Matthiessen's rule is valid in the range of Cd concentrations studied. In Ref. 1 it was shown that in alloys of the In–Cd system at concentrations $c>2$ at. % Cd, Matthiessen's rule holds rather well, at least for $T\geqslant293$ K. Our data also attest to the validity of Matthiessen's rule. Since the temperature dependence of the resistivity for a Cd concentration of 3 at. % shows no anomalies in the temperature region of interest to us, for further analysis we can consider the temperature dependence of the difference $\rho_d(T)=\rho_{4.3}(T)-\rho_3(T)$ as the differential analog of the change of the residual resistivity of the alloy In–4.3 at. % Cd on thermocycling. This allows us to see more clearly the hysteresis effects and instability effects caused by the structural rearrangements in the alloy under study, since the residual resistivity has a particularly high sensitivity to the change in structural parameters of the crystal.

Figure 6a shows a plot of $\rho_d(T)$ obtained both during isochronal thermocycling at a rate of 0.25 K/min (cf. Fig. 5) and as a result of thermocycling at the same rate of change of the temperature in the interval 300–5.5–303 K but with an intermediate isothermal hold for 6 hours at $T=200$ K. It is seen that at the chosen rate of cooling, the start of the noticeable decrease of ρ_d is observed near 210 K. We note that the limiting minimum value of the residual resistivity, which characterizes the low-temperature state of the sample, does not depend on how this state is reached.

As in the case of the hysteresis of the acoustical properties, a rapid change of temperature corresponds to the unrelaxed branch of the temperature dependence of the resistivity, whereas a slow change in temperature corresponds to the relaxed branch of the temperature dependence. Figure 6b shows $\rho_d(T)$ for two different degrees of relaxation, corresponding to the final stage of the transition of the alloy to the low-temperature stable state, and to the initial stage of the reverse transition to the high-temperature stable state. For the chosen regime of temperature variation the two runs cross at $T\approx245$ K. A prolonged hold at this temperature does not lead to any noticeable change in the resistivity.

2.5. Kinetics of the transition of the alloy to the low-temperature state

Figure 7 shows the time dependence of the resistivity measured at fixed temperatures. Plotted on the vertical axis is the quantity $\Delta\rho(t)=\rho(t)-\rho(0)$, where $t=0$ is the time at the start of the measurements. It is seen that at all temperatures the transformation reaction begins slowly and then, after some time, it speeds up, its rate reaching a maximum and then gradually declining. We note that at $T=240$ K the start of the transformation is accompanied even by a slight increase in the resistivity (Fig. 7b).

In contrast to the relaxation of the dynamic Young's modulus, the kinetic curves of $\Delta\rho(t)$ are S-shaped and are not described by a first-order reaction equation (1). The kinetic curves shown in Fig. 7 are approximated rather well by a simple expression which was proposed by Avrami for describing the kinetics of isothermal transformations governed by processes of nucleation and growth of the particles of the new phase:[11–13]

$$\Delta\rho(t)=\Delta\rho_{\max}\left\{1-\exp\left[1-\left(\frac{t}{\tau_\rho}\right)^n\right]\right\},\qquad(2)$$

where τ_ρ is the effective relaxation time of the alloy to equilibrium at the given temperature. For $n=1$ this equation describes a first-order reaction, but for the curves shown in Fig. 7a the exponent n varies in the range 1.5–1.8 (with an average value of 1.57) and this parameter shows no systematic dependence on temperature. The temperature dependence of the relaxation time $\tau_\rho(T)$ in Arrhenius coordinates is shown in Fig. 4. This is a rather symmetric curve with a minimum at

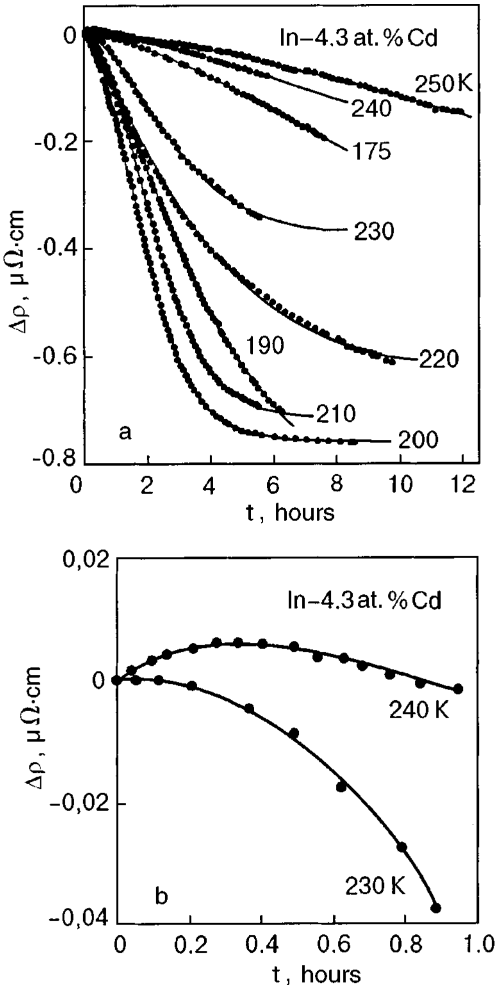

FIG. 7. Kinetic curves of the isothermal change of the resistivity of the alloy In–4.3 at. %Cd at the transition to the low-temperature structural state; the solid curves show the functions [Eq. (2)] approximating the experimental data (a); the initial parts of the kinetic curves at 230 K and 240 K (b).

$T = 200$ K: the relaxation time increases substantially when the temperature is decreased or increased from this value. It is seen from Fig. 4 that the transformation is characterized by long relaxation times (the minimum value is $\tau_\rho = 2.2$ hours at $T = 200$ K).

The maximum value of the rate of change of the resistance depends substantially on the temperature (see Fig. 8): $\max|d\rho/dt|$ initially increases with decreasing temperature of the isothermal hold in the interval 250–200 K and then decreases on going to 190 and 175 K. The minimum time for an experiment to follow the approach of the resistivity to a value close to its equilibrium value $\rho_\infty = \rho(t \to \infty)$ also depends importantly on the temperature: it is ~ 5.5 hours at $T = 200$ K and a considerably longer 24 hours at temperatures of 250 and 175 K.

2.6. Kinetics of the transition of the alloy to the high-temperature state

This transition was studied in less detail. We measured three $\rho(t)$ isotherms in the region of the high-temperature boundary of the hysteresis, 260–290 K (Fig. 9a). The reverse structural transition is accompanied by an increase in the resistivity to the values which were obtained at the start of the thermocycling.

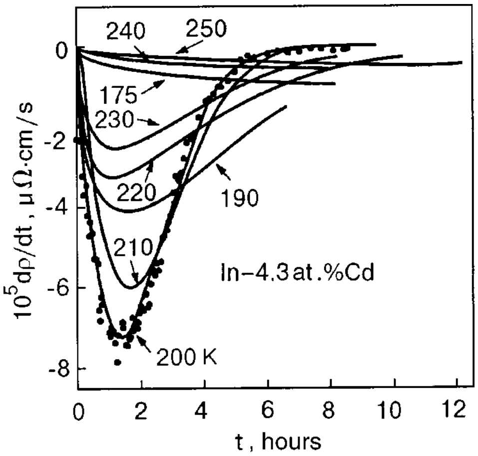

FIG. 8. Time dependence of the rate of isothermal relaxation of the resistivity in the cooling stage: the solid curves are the time derivatives of the approximating functions [Eq. (2)] corresponding to different temperatures (see Fig. 7).

The presence of two linear segments with different slopes on the plots of $\ln(d\rho(t)/dt)$ versus time (Fig. 9b) shows that the reverse transition process in this experimental setup corresponds to a heterogeneous first-order reaction with two substantially different characteristic relaxation times $\tau_{\rho 1}$ and $\tau_{\rho 2}$. The experimental points in Fig. 9a are well approximated by the expression

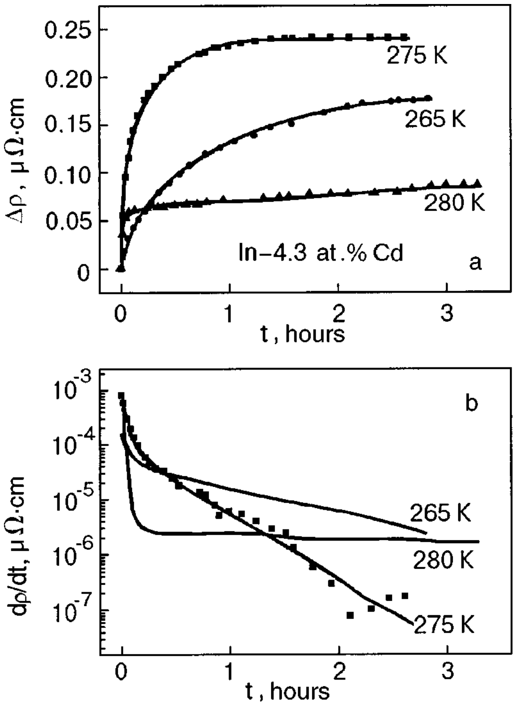

FIG. 9. Kinetic curves of the relaxation of the resistivity of an alloy on heating of the sample from 200 K; the solid curves show the approximating functions [Eq. (3)] (a). Logarithm of the rate of change of the resistivity, $\ln(d\rho/dt)$, versus time for different temperatures; the solid curves show the time derivatives of the approximating functions (3) corresponding to the different temperatures (b).

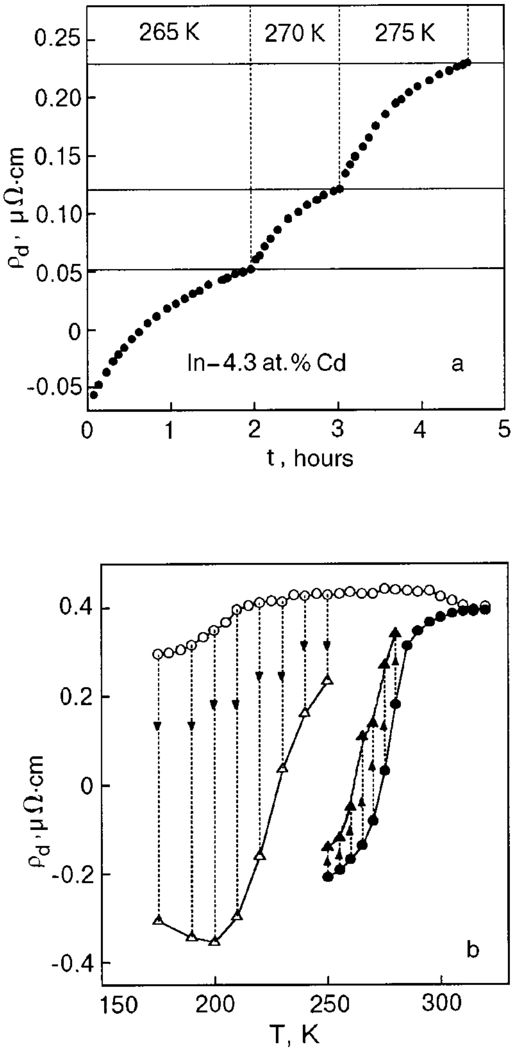

FIG. 10. Kinetic curves of the change of the reduced residual resistivity ρ_d during isothermal annealing with a step $\Delta T = 5$ K (a); the limiting values of ρ_d on cooling (△) and heating (▲) of the sample, obtained by extrapolating the corresponding kinetic curves to $t\rightarrow\infty$ with the aid of Eqs. (2) and (3); (○,●)—the direct and reverse branches of the $\rho_d(T)$ curve during thermocycling at an average rate of 0.25 K/min (see Fig. 6a) (b).

$$\Delta\rho(t) = \Delta\rho_{\max}^{(h)}\left\{ m\left[1-\exp\left(-\frac{t}{\tau_{\rho 1}}\right)\right] + (1-m)\left[1-\exp\left(-\frac{t}{\tau_{\rho 2}}\right)\right]\right\}, \tag{3}$$

where m is the relative contribution of the faster process. The ratio $m/(1-m)$ is equal to 0.21 at 265 K, 0.92 at 275 K, and 1.02 at 280 K.

The values obtained for the relaxation times $\tau_{\rho 1}$ and $\tau_{\rho 2}$ are shown in Fig. 4. It is seen that the relaxation to the initial high-temperature state occurs considerably faster than the transition to the low-temperature state.

If the isothermal annealing of the low-temperature state is done with a small temperature step, $\Delta T = 5$ K (see Fig. 10a), the transformation occurs uniformly in time in accordance with the first-order reaction

$$\Delta\rho_d(t) = \Delta\rho_{d\,\max}[1-\exp(-t/\tau'_\rho)]. \tag{4}$$

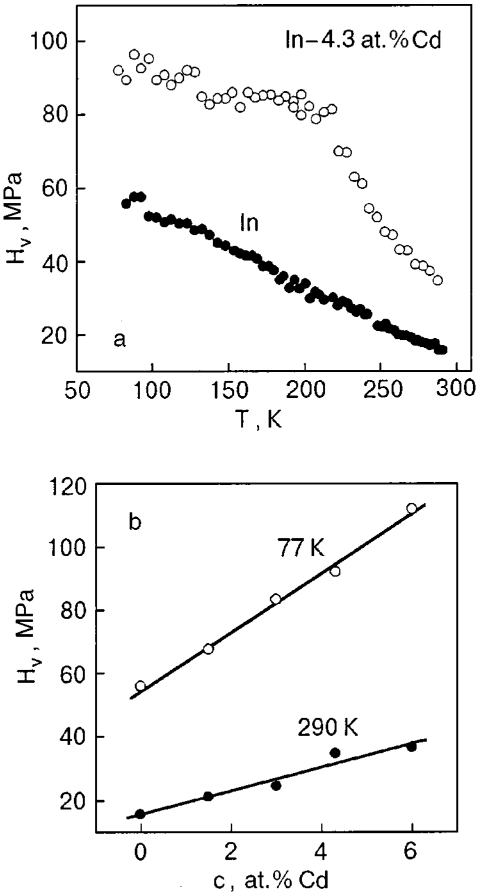

FIG. 11. Temperature dependence of the microhardness of the alloy In–4.3 at. %Cd (○) and pure In (●) (a); the concentration dependence of the microhardness of In–Cd alloys at temperatures of 290 K and 77 K (b).

The relaxation time τ'_ρ here is close to the relaxation time of the slower process (see Fig. 4). In that experiment the three successive anneals were interrupted long before the structure of the alloy reached its equilibrium state at the given temperature, and so the initial state of the sample at each successive temperature was not an equilibrium state.

2.7. Dependence of the microhardness of In–Cd alloys on the temperature and cadmium concentration

As in the acoustical and and resistance experiments, signs of the structural instability of the alloy In–4.3 at. % Cd are also clearly observed in the temperature dependence of the microhardness (Fig. 11a) measured in the temperature "ramp" mode as the sample is cooled. The microhardness of pure indium increases linearly as the temperature is lowered. The microhardness of the alloy is substantially higher at the same temperatures and varies nonlinearly. The hysteresis region on $E(t)$ and $\rho(t)$ corresponds to an interval of strong temperature dependence of the microhardness. However, at the accuracy achievable in our experiments, the recorded microhardness did not reveal any hysteresis of $H_V(T)$ or instability effects: the value of $H_V(T)$ is independent of the isothermal hold time of the sample, regardless of whether it was under a loaded indenter or not, and is also independent of the direction of the temperature change.[5]

The impurity hardening of indium under doping by cadmium atoms is illustrated by Fig. 11b, which shows the concentration dependence of the microhardness $H_V(c)$ at temperatures of 293 and 77 K, corresponding to the high- and low-temperature structural states of the alloy In–4.3 at.% Cd. As we have said, the solid solutions with cadmium concentrations $c<4$ at.% do not have phase transitions, while the alloys with 4 at.% $<c<5.9$ at.% Cd have a phase transition of the martensitic type on cooling. This feature is not reflected in any way on the $H_V(c)$ curve, which at both temperatures remains linear in the entire range of cadmium concentrations.

We note that this sort of behavior is a sign that the mobility of dislocations in the alloy is being affected by the diffusion of impurity atoms. Indeed, for the standard stable solid solutions in the low-temperature region, where the diffusion of impurity atoms is ruled out, a power-law dependence of the yield stress of the alloy on the impurity concentration, with an exponent of 1/2 or 2/3, is observed.[14] Since the microhardness, as a rule, is proportional to the yield stress, it can be assumed that for stable alloys the $H_V(c)$ curve should have a similar form in the absence of impurity diffusion.

3. DISCUSSION OF THE RESULTS

3.1. Hysteresis properties of the alloy during thermocycling

Analysis of the experimental data obtained in the present study shows that the cause of the temporal instability of a number of physical properties of the alloy In–4.3 at.% Cd in the temperature interval 170–290 K is a spontaneous reversible low-temperature structural transformation of a hysteretic type. The width of the hysteresis depends on the rate of isochronal thermocycling, but even when the rate is made infinitesimally slow, the width cannot be reduced to zero but retains a significant residual value. Figure 10b shows a plot of the values obtained when the $\rho_d(t)$ curves measured at different temperatures are extrapolated to $t\to\infty$. Also shown in this figure for comparison are the direct and reverse branches of $\rho_d(T)$ measured during isochronal thermocycling at an average rate of 0.25 K/min. It follows from Fig. 10b that at such a rate of thermocycling, the structure of the alloy is far from equilibrium both on cooling and heating of the sample. In the first case the largest deviation from the equilibrium values of ρ_d is observed near 200 K, and in the second case, near 275 K. In addition, it is seen that even in the limiting case $t\to\infty$ the forward and reverse branches of ρ_d do not coincide with each other, and the maximum residual hysteresis in temperature is $\sim$30 K. The cause of this wide residual hysteresis may be the circumstance that in the indicated temperature interval the formation of new-phase nuclei is hindered (or eliminated altogether), possibly because, for example, the decrease of the free energy at the phase transition is small compared to the elastic energy (the effective driving force of the process is negative[11]). The presence of residual hysteresis attests to the lack of a one-to-one correspondence between the structure of the samples and the temperature of the measurement during thermocycling. This might explain why the $\rho_d(T)$ curves did not display a segment of equilibrium values of the residual resistivity, which is ordinarily registered during the isochronal annealing of quenched alloys which undergo a transition to an ordered state.[15] On such a segment the equilibrium value of ρ_d is uniquely related to the equilibrium structure of the alloys at the given temperature and is independent of the direction of temperature change during the isochronal thermocycling.

3.2. Kinetics of formation of the low-temperature state

The low-temperature structural state is characterized by higher values of the elastic modulus and a higher microhardness. In this sense it can be called a hardened state. The kinetics of the transition to a hardened state can be judged from the time dependence of the resistivity, which has a characteristic S-shaped form. The initial stage of the transformation begins essentially from a zero rate on all the kinetic curves. At $T=240$ K one even observes an initial increase in the resistivity (Fig. 7b). As time goes on, the rate of the process increases, reaches a maximum value, and then rapidly falls off (Fig. 8). At temperatures of 175, 240, and 250 K the measurement periods used permitted observation of only the initial stage of the process. The maximum rate of the process in the fast stage of the transformation depends nonmonotonically on temperature and, on the whole, correlates with the temperature dependence of the relaxation time τ_ρ of the process: the shortest relaxation time, at 200 K, corresponds to the highest value of the maximum rate of the transformation (cf. Figs. 4 and 8).

The above-described form of the time dependence of the resistivity curves $\rho(T)$ for samples cooled from room temperature (i.e., from a temperature in the existence region of the stable high-temperature phase) is typical of processes of nucleation and growth of particles of a new phase and is similar, for example, to the kinetics of the resistivity in the transformation of the disorder–order type in the alloy Cu_3Au (Ref. 16). The value of the exponent n ($\approx$1.5–1.8) in the Avrami equation (2) corresponds to the early stage of the diffusional growth of the nuclei of small sizes, with a declining rate of their nucleation (see Table 1 in Ref. 11). The initial increase of the resistivity at 240 K in this case may mean that in the early stage of the transformation the size of the nuclei is comparable to the mean free path of the charge carriers, and the nuclei are therefore efficient scattering centers for conduction electrons. The subsequent growth of the nuclei of the ordered phase decreases the contribution of this mechanism to the resistivity of the alloy.

In the general case, when the rates of nucleation and growth are governed by thermally activated processes, the rate of isothermal transformation is a nonmonotonic function of temperature. With decreasing temperature the nucleation rate increases rapidly in connection with the increase of the driving force of the transformation. At the same time, the rate of growth decreases with decreasing temperature, since it is limited by the activation energy of atomic rearrangements, which itself is almost independent of temperature.[11] Therefore, with decreasing temperature the rate of transformation of the high-temperature phase into the low-temperature phase initially increases (the relaxation time decreases) and then decreases (the relaxation time increases) on account of a competition between two factors: the increasing driving force of the transformation and the simultaneous slowing of the rate of thermally activated processes. One notices the similarity of our results to the analogous data

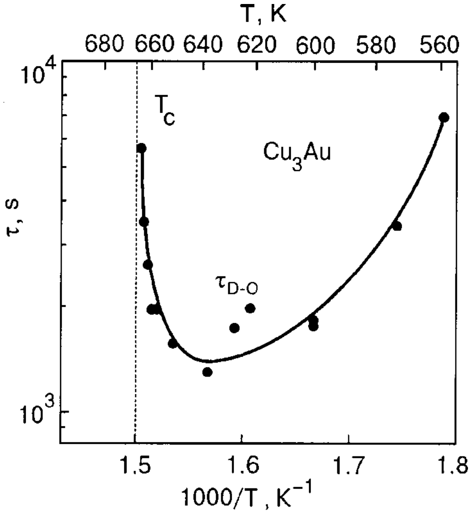

FIG. 12. Arrhenius plot for the relaxation times τ_{D-O} of transformations of the disorder–order type after quenching of the alloy Cu_3Au from $T>T_c$ (Ref. 16).

obtained in Ref. 16 in a study of the kinetics of the disorder–order transformation in Cu_3Au (the data of Ref. 16, processed according to formula (2), are presented in Fig. 12). The main difference of the results is the marked asymmetry of the $\tau_\rho(1/T)$ curve, which is due to the presence of a critical temperature T_c for long-range ordering in Cu_3Au. In the alloy In–Cd, as is shown in Fig. 10b, the transition to the low-temperature structural state has a width $\Delta T = 50-70$ K, and this can explain the nearly symmetrical shape of the $\tau_\rho(1/T)$ curve.

3.3. Kinetics of the transition to the high-temperature structural state

As in the case of the direct transformation, the kinetics of the formation of the high-temperature structural state depends substantially on the temperature of the isothermal hold of the alloy. Furthermore, it is in large measure determined by the structural state of the samples at the time when the specified measurement temperature is reached. When samples with the stable low-temperature structure reached after a long hold at 200 K are heated comparatively rapidly to a temperature above ~250 K, the kinetics of the reverse transition to the initial high-temperature (softened) state is determined by the simultaneous occurrence of at least two thermally activated relaxation processes, one relatively rapid and one relatively slow, with the specific contribution of the faster process increasing with increasing temperature [see expression (3)]. During isothermal annealing with a small temperature step $\Delta T = 5$ K (Fig. 10a) the transformation occurs in accordance with a first-order reaction. The relaxation time here is close to the relaxation times of the slower of the two processes, which governs the kinetics of the change of the resistivity during an isothermal hold of a sample stabilized at 200 K (Fig. 4).

3.4. Relationship of the low-temperature structural transformation to the state diagram of the alloy

Let us consider the possible connection between the observed structural instability and the state diagram of the alloy. According to the equilibrium phase diagram, the In–Cd system has a eutectoid point at a Cd concentration of 5.9 at.% and a temperature of 293 K.[1–4] As we have said, the phase diagram has not been studied at temperatures below the eutectoid point, and in the published sources known to the authors a possible phase boundary has been shown provisionally (the dotted line *1* in Fig. 13). Presumably, as the temperature is lowered the tetragonal phase α_t with a concentration $c<5.9$ at.% Cd suffers a decomposition, with the formation of a small amount of cadmium-enriched solid solution in the matrix of the α_t phase, and the temperature of the decomposition decreases with decreasing cadmium concentration. If the low-temperature instability of the α_t phase observed by us for the solid solution In–4.3 at.% Cd is due to this structural transformation, the phase boundary should pass between the low- and high-temperature branches of the residual hysteresis, corresponding to the direct and reverse transformations in the alloy with the given Cd concentration (dotted line *2* in Fig. 13). Granted, in this case one would expect manifestations of instability of the acoustical and resistive properties of the alloys with Cd concentrations of 1.5 and 3 at.% in a lower temperature region. The absence of anomalies in those alloys may be a consequence of a decrease of the driving force of the process as the Cd concentration decreases or of a significant decrease of the rate of thermally activated processes when the alloys are cooled to the corresponding temperatures (150–160 K for $c = 1.5$ at.% Cd and 190–200 K for $c = 3$ at.% Cd). This assumption will require further experimental study on alloys with cadmium concentrations $3\ \text{at.\%} < c < 5.9$ at.%.

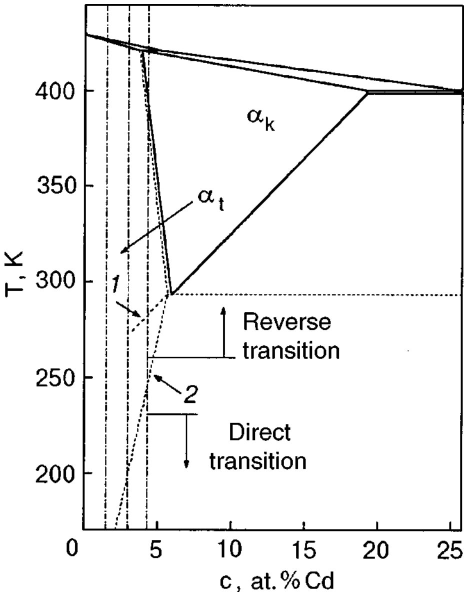

FIG. 13. State diagram of the alloy In–Cd from the In side: α_k is a solid solution with an fcc structure, α_t is a solid solution with an fct structure; the dot-and-dash vertical lines correspond to Cd concentrations investigated in this study. *1*—phase boundary provisionally identified in Refs. 1–4; *2*—position of the phase boundary corresponding to the results obtained in the present study (see text).

Of course, experiments done with the use of indirect structurally sensitive methods (acoustic, resistive, and micromechanical) do not permit one to establish conclusively the specific microscopic mechanisms that govern the observed low-temperature structural transformation in the alloy In–4.3 at.% Cd. However, a number of signs indicate that the given structural transformation has a more complex nature than the known mechanisms for changes in the mutual arrangement of atoms in solid solutions (short-range or long-range ordering, clustering, decomposition of a supersaturated solution, etc.). Among these signs we mention the following:

— The presence of a segment with a positive derivative on the curve of the Young's modulus $E(T)$ of the metastable high-temperature phase in precisely that temperature interval in which the effects of structural instability are most pronounced, and the complete absence of such a segment on the $E(T)$ curve in the stable low-temperature phase.

— An unusual reaction of the elastic modulus of a sample in the metastable high-temperature phase to a change in temperature in the critical temperature region: regardless of the sign of the change in temperature (decreasing or increasing) a dip of the modulus is always observed, which goes away when the temperature is stabilized. Such behavior may be due to a loss of stability of the crystal lattice, which ordinarily occurs near a phase transition temperature.

— Appreciable residual hysteresis of the properties of the alloy during thermocycling, which cannot be reduced to zero for arbitrarily slow rates of change of the temperature.

— Anomalously large values of the relative increase of the Young's modulus ($\sim 27\%$) and decrease of the resistivity ($\sim 11\%$) at the transition from the high- to the low-temperature stable structural state.

A conclusive explanation of the nature of the observed effects will require further study, mainly by the methods of structural analysis. The close values of the scattering factors of the In and Cd atoms makes it difficult to study this alloy by x-ray diffraction methods. The high plasticity and low melting temperature of the samples make it practically impossible to use the method of high-voltage transmission electron microscopy. The most suitable method in this case is neutron diffraction. Useful information can also be obtained from dilatometric and thermophysical experiments.

CONCLUSIONS

1. A reversible low-temperature structural transformation of the hysteretic type is observed in polycrystals of the solid solution In–4.3 at.% Cd; it is registered in the acoustical, resistometric, and micromechanical measurements in the temperature interval 175–290 K.

2. The transition to the low-temperature structural state is spontaneous, smeared in temperature, and features a large residual hysteresis. This transition is governed in a complex way by thermally activated processes of nucleation and growth of particles of the low-temperature ordered phase, as is attested to by the S-shaped form of the kinetic curves of the resistivity and the nonmonotonic temperature dependence of the relaxation time.

3. The low-temperature structural state observed as a result of the transformation is characterized by considerably higher values of the Young's modulus (E increases by $\sim 27\%$) and microhardness and by a considerably lower residual resistivity (ρ_d decreases by approximately 30%).

4. Further study, mainly by methods of direct structural analysis, will be needed to explain the detailed microscopic picture of this structural transformation.

This study was supported in part by the Swiss National Science Foundation, Grant No. 7UKPJ048645. The authors thank Prof. G. Kostorz and Dr. Yu. A. Pokhil for helpful discussions of the results.

*E-mail: palval@ilt.kharkov.ua

---

[1] Th. Heumann and B. Predel, Z. Metallkde. **53**, 240 (1962).

[2] F. A. Shunk, *Constitution of Binary Alloys*, Second Supplement, McGraw-Hill, New York (1971), Metallurgiya, Moscow (1973).

[3] A. E. Vol and I. K. Kagan, *Structure and Properties of Binary Metal Systems* [in Russian], Vol. 3, Nauka, Moscow (1976).

[4] T. B. Massalski (ed.), *Binary Alloy Phase Diagrams*, Vol. 2, 2nd ed., ASM International, Materials Park, OH 44073, USA (1990).

[5] S. V. Lubenets, V. D. Natsik, P. P. Pal-Val, L. N. Pal-Val, and L. S. Fomenko, Mater. Sci. Eng., A **256**, 1 (1998).

[6] S. V. Lubenets, V. D. Natsik, P. P. Pal-Val, L. N. Pal-Val, and L. S. Fomenko, Izv. Ross. Akad. Nauk Ser. Fiz. **64**, 1718 (2000).

[7] B. Ya. Farber, N. S. Sidorov, V. I. Kruglov, Yu. A. Iunin, A. N. Izotov, G. A. Emel'chenko, V. S. Bobrov, L. S. Fomenko, V. D. Natsik, and S. V. Lubenets, Sverkhprovodimost' **4**, 2394 (1991) [Superconductivity **4**, 2296 (1991)].

[8] V. D. Natsik, P. P. Pal-Val, and S. N. Smirnov, Akust. Zh. **44**, 640 (1998) [Acoust. Phys. **44**, 553 (1998)].

[9] G. T. Meaden, *Electrical Resistivity of Metals*, Plenum Press, New York (1965).

[10] B. G. Livshits, V. S. Kraposhin, and Ya. L. Linetskiĭ, *Physical Properties of Metals and Alloys* [in Russian], Metallurgiya, Moscow (1980).

[11] J. W. Christian, in *Physical Metallurgy*, edited by R. W. Cahn, North-Holland, Amsterdam (1965), Mir, Moscow (1968).

[12] J. W. Christian, *The Theory of Transformations in Metals and Alloys*, Pergamon Press, Oxford (1975), Mir, Moscow (1978).

[13] R. D. Doherty, in *Physical Metallurgy*, Vol. 2, edited by R. W. Cahn and P. Haasen, North-Holland, Amsterdam (1983), Metallurgiya, Moscow (1987).

[14] I. N. Kidin and M. A. Shtremel', Fiz. Met. Metalloved. **11**, 641 (1961).

[15] W. Pfeiler, J. Opt. Mater. **5**, 14 (2000).

[16] F. R. Burns and S. L. Quimby, Phys. Rev. **97**, 1567 (1955).

Translated by Steve Torstveit

LOW TEMPERATURE PHYSICS VOLUME 28, NUMBER 6 JUNE 2002

SHORT NOTES

Features of the magnetization of an antiferromagnet with single-ion anisotropy of the easy-plane type and with ion spins $S=1$

V. M. Kalita

Institute of Physics of the National Academy of Sciences of Ukraine, pr. Nauki 46, 03028 Kiev, Ukraine

I. M. Ivanova

Taras Shevchenko National University, pr. Glushkova 6, 03022 Kiev, Ukraine

V. M. Loktev*

N. N. Bogolyubov Institute of Theoretical Physics, National Academy of Sciences of Ukraine, ul. Metrologicheskaya 14,b, 03143 Kiev, Ukraine

(Submitted January 18, 2002)
Fiz. Nizk. Temp. **28**, 667–670 (June 2002)

A theory is proposed for the two-step phase transition from the singlet to a ferromagnetic state in systems of the ABX_3 type. It is shown that the transition is due to a substantial rearrangement of the single-ion spectrum. The critical fields and magnetic susceptibility are calculated. © *2002 American Institute of Physics.* [DOI: 10.1063/1.1491189]

INTRODUCTION

Recently there has been considerable interest in many-sublattice hexagonal antiferromagnets (AFMs) of the ABX_3 type with the $CsNiCl_3$ lattice, in which the spins of the magnetic ions B^{2+} form AFM chains along the C_6 axis, on the one hand, and triangular structures in the basal plane, on the other (see reviews[1,2]). A triangular easy-plane Loktev structure in the cryocrystal β-O_2 (Ref. 3) has been quite well studied, but in that system the intramolecular anisotropy constant is much less than the exchange constant, and so it cannot be classed with the quantum magnets. The latter have anisotropy of a single-particle origin, the value of which is comparable to or greater than the exchange interactions.[4] The necessary relations are fulfilled for the AFM $CsFeBr_3$, in which, at a value of the pseudospin of the Fe^{2+} ion $S=1$, the single-ion anisotropy constant $D\approx 20-30$ K, while the exchange interactions J_{ch} for the nearest-neighbor ions belonging to the two adjacent planes are equal to 3–5 K and for the same ions in the basal planes $J_{pl}\approx 0.3-0.4$ K.[5–8] At these values of the parameters a singlet spin state is realized in the AFM. In other words, of the three possible single-ion spin states with projections on the C_6 axis of $S_z=\pm 1$ and 0, the last state is the lowest, so that the crystal is actually nonmagnetic.

When such an AFM is placed in a magnetic field $\mathbf{H}$, a change of the sequence of levels occurs, and one of the triplet states with nonzero spin projection the lowest (ground) state. Here the magnetic field causes a transition from a nonmagnetic to a magnetic phase.

The available information about the nature of this transition, which was discussed in Ref. 5 for the case $\mathbf{H}\parallel C_6$, is contradictory. In Refs. 9 and 10 it is classed as second-order, while in Refs. 11–13 it is identified as first-order. While the experiment done in Ref. 5 does not permit one to reach an unambiguous conclusion, it is the goal of the present paper is to do a comprehensive study the behavior of the $CsFeBr_3$ crystal in a longitudinal magnetic field. The magnetization curves given in Ref. 5 indicate a sequence of two second-order phase transitions: from the singlet state to a canted phase (CF) and from the latter to a ferromagnetic (FM) phase. In this paper we consider a theoretical model describing these phase transitions and determine the conditions under which they occur. In contrast to Ref. 5, the theory considered here contains variational parameters that pertain to physically observable quantities—the sublattice spins and their canting angles.

MODEL

We limit consideration to bilinear isotropic exchange interactions, single-ion anisotropy, and the Zeeman contribution. In this case the Hamiltonian can be written in the form

$$H=\frac{1}{2}\sum_{\mathbf{n}\alpha,\mathbf{m}\beta} J_{\alpha\beta}\mathbf{S}_{\mathbf{n}\alpha}\mathbf{S}_{\mathbf{m}\beta}+D\sum_{\mathbf{n}\alpha}(S^z_{\mathbf{n}\alpha})^2-h\sum_{\mathbf{n}\alpha}S^z_{\mathbf{n}\alpha}, \quad (1)$$

where α and β ($\alpha\neq\beta$) label the magnetic sublattices, of which there are six; $\mathbf{n}$ and $\mathbf{m}$ are vectors specifying the positions of the spin in the sublattices; the constant D is positive, corresponding to anisotropy of the easy plane type. The field $h=\mu_\beta g H$ is given in energy units and is directed perpendicular to the easy axis along the axis $Z\parallel C_6$. For such an orientation of the field the spins of the sublattices differing with respect to the Z axis will be canted in the same way relative to this axis. In the $CsFeB_3$ crystal the exchange interaction is anisotropic in space, i.e., it depends on the position of the spins in the lattice. For example, J_{pl} in the easy plane differs in value from the exchange interaction J_{ch} in the direction of the hard axis (the direction of the chains).

1063-777X/2002/28(6)/3/$22.00

When the features of the structure are taken into account, the exchange parameter J_{ch} in the direction of the hard axis tends to establish an antiparallel orientation of the nearest-neighbor spins in adjacent planes, and J_{pl} orients the spins nearest to the easy plane at an angle of $2\pi/3$.

Our analysis of Hamiltonian (1) will be done using the self-consistent field approximation, in which the effect of spin–spin fluctuations is ignored, and the average of a product of spin operators is equal to the product of their averages. In this case the ground-state energy E_{gr} per unit cell (for spins belonging to different sublattices—three in one plane and three in the neighboring planes) will be equal to

$$E_{\mathrm{gr}}=\frac{1}{2}\sum_{\alpha\beta} J_{\alpha\beta}z_{\alpha\beta}\mathbf{s}_\alpha\mathbf{s}_\beta+D\sum_\alpha Q_\alpha-h\sum_\alpha s_\alpha^z, \tag{2}$$

where $\mathbf{s}_\alpha$ is the average value of the spins of the ions of the sublattices, $z_{\alpha\beta}$ is the number of nearest neighbors, which is equal to three for spins of the same plane and equal to two for spins from two neighboring planes, and we have also introduced the average values of the squares of the z projections of the spin operators, which are customarily referred to in the literature as the components of the quadrupole spin moment Q_α.

For the spins of each sublattice the proper coordinate systems ξ_α, η_α, ζ_α are such that the direction of the average spin of the αth sublattice is oriented along the ζ_α axis, while the ξ_α axis lies in the $Z\zeta_\alpha$ plane. Then in the proper coordinate system the wave function of the the spin ground state of the sublattice with index α will have the form[4]

$$\Psi=\cos\phi_\alpha|1\rangle+\sin\phi_\alpha|-1\rangle, \tag{3}$$

where $|\pm 1\rangle$, $|0\rangle$ are the eigenfunctions of the operator $S^{\zeta}_{\mathbf{n}\alpha}$. With allowance for Eq. (3) we calculate the mean values of the spin and the components of the quadrupole spin moment

$$s=\cos 2\phi,\quad Q^{\zeta\zeta}=1,\quad Q^{\xi\xi}=\frac{1}{2}(1+\sin 2\phi). \tag{4}$$

In the expressions for the averages (4) we have dropped the sublattice indices, since in the chosen approach the given quantities are independent of α. The energy (2) with the use of (4) takes the form

$$\begin{aligned}E_{\mathrm{gr}}={}&9J_{\mathrm{pl}}\cos^2 2\phi(3\cos^2\theta-1)+6J_{\mathrm{ch}}\cos^2 2\phi(2\cos^2\theta\\&-1)+6D\left(\cos^2\theta+\frac{\sin^2\theta}{2}(1+\sin 2\phi)\right)\\&-6h\cos 2\phi\cos\theta,\end{aligned} \tag{5}$$

where θ is the angle between sublattice spins and the magnetic field $\mathbf{H}$ and is equal to the angle between the crystallographic axis and the proper axes ζ_α. We note that in Ref. 5 the ground-state energy of the crystal is also found and minimized. However, the wave functions chosen in Ref. 5, unlike (3), are written in a general form referring to the crystallographic rather than the proper coordinate system and so contain the parameters of the rotation of the vectors $|\pm 1\rangle$ and $|0\rangle$ in Hilbert space, and that makes it hard to interpret the relationship between the observable and calculated (variational) parameters.

EQUATIONS OF STATE AND THEIR ANALYSIS

The spin configurations that determine the ground state in the different possible phases and their interconversion in a magnetic field are determined from the equations obtained by minimizing the energy (5) with respect to ϕ and θ:

$$\begin{aligned}&-\cos 2\phi\sin 2\phi[6J_{\mathrm{pl}}(3\cos^2\theta-1)+4J_{\mathrm{ch}}(2\cos^2\theta\\&\quad-1)]+D\sin^2\theta\cos 2\phi+2h\sin 2\phi\cos\theta=0,\end{aligned} \tag{6}$$

$$\begin{aligned}&-\cos\theta\sin\theta[(9J_{\mathrm{pl}}+4J_{\mathrm{ch}})\cos^2 2\phi+D(1-\sin 2\phi)]\\&\quad+h\cos 2\phi\sin\theta=0.\end{aligned} \tag{7}$$

These equations can be reduced to the equations for determining the ground state which were obtained by Ostrovskiĭ and one of the present authors,[4] by using an artificial self-consistency procedure. Although Eqs. (6) and (7) give the same solutions as before, they are nevertheless preferable, since they can be used to determine the stability of the phases.

Let us analyze the solutions of the system of equations (6), (7). The first of them corresponds to a FM state and is realized for $\sin\theta=0$, $\sin 2\phi=0$. In this case the spins of the sublattices are directed along the field, their magnitudes are maximum: $s=S=1$. This is the so-called paraphase, in which the longitudinal magnetic susceptibility χ_{zz} is equal to zero.

The second solution corresponds to a three-sublattice state in the plane of the AFM, with the Loktev structure.[3] It obtains for $\cos\theta=0$ and $\sin 2\phi=-D/(6J_{\mathrm{pl}}+4J_{\mathrm{ch}})$. This solution can exist only in the absence of magnetic field.

In the corresponding 120° structure the values of the spins are equal and contracted: $s=\sqrt{1-D^2/(6J_{\mathrm{pl}}+4J_{\mathrm{ch}})^2}$.

The third solution pertains to a canted phase in which again $s\leqslant 1$. From Eq. (7) we find directly that the angle between the sublattice spin and $\mathbf{H}$ depends nonlinearly on the value of the field:

$$\cos\theta=\frac{h\cos 2\phi}{(9J_{\mathrm{pl}}+4J_{\mathrm{ch}})\cos^2 2\phi+D(1-\sin 2\phi)}. \tag{8}$$

With increasing field the canting of the spins toward the field increases and, accordingly, the value of s increases.

The field of the transition from the canted phase to a state in which all the spins flip to a perpendicular orientation with respect to the easy plane is determined by substituting the values $\cos\theta=1$ and $\cos 2\phi=1$ into expression (8) for the canting angle. We obtain $h_{\mathrm{flip}}=9J_{\mathrm{pl}}+4J_{\mathrm{ch}}+D$, which agrees with the expression for the spin-flip field given in Ref. 5. We see that the value of the spin-flip field is additive with respect to the values of the anisotropy and exchanges, although the physical mechanisms of their action are different.

Taking expressions (4) for the sublattice spins into account, we obtain the magnetic susceptibility in the canted phase in the proper coordinate systems:

$$\chi_{zz}=-2\sin 2\phi\cos\theta\frac{\partial\phi}{\partial h}-\cos 2\phi\sin\theta\frac{\partial\theta}{\partial h}. \tag{9}$$

Here the derivatives with respect to field in (9) can be calculated using Eqs. (6) and (7).

At the beginning of the spin canting process upon the introduction of small magnetic fields $h \to 0$, when the second solution is the ground state, the value of χ_{zz} in the canted phase will be determined by the expression

$$\chi_{zz}|_{h=0} = \frac{(6J_{\mathrm{pl}}+4J_{\mathrm{ch}})^2-D^2}{(9J_{\mathrm{pl}}+4J_{\mathrm{ch}})(6J_{\mathrm{pl}}+4J_{\mathrm{ch}})^2-3J_{\mathrm{pl}}D^2+D(6J_{\mathrm{pl}}+4J_{\mathrm{ch}})^2}. \tag{10}$$

We see from Eq. (10) that in the case of a large value of D under the condition $D>6J_{\mathrm{pl}}+4J_{\mathrm{ch}}$ the value of χ_{zz} becomes negative. Consequently, for such a relationship of the constants of the Hamiltonian the antiferromagnetic 120° phase loses stability.

The fourth and last possible solution is specified by the relations $\cos\theta=0$ and $\cos 2\phi=0$. It can be realized both at nonzero magnetic fields and for $h=0$. The contraction of the spins in this state is maximum ($s=0$), and here $\sin 2\phi\approx -1$. This is the so-called singlet state,[14] in which the magnetic order is characterized by a spin quadrupole moment. In the singlet state the average values of the spin quadrupole moment are the same for all directions in the easy plane, and because of the vanishing of s the direction of the axes of quantization become indeterminate in the plane. Since the energy of this state is independent of the value of h, the magnetic susceptibility in it, determined in the direction along the field, will also be zero.

Indeed, let us calculate the second derivatives of the energy (5) for the singlet state. We find that $\partial^2E_{\mathrm{gr}}/\partial\phi^2 = -12(6J_{\mathrm{pl}}+4J_{\mathrm{ch}})+12D$, $\partial^2E_{\mathrm{gr}}/\partial\theta^2=12D$, $\partial^2E_{\mathrm{gr}}/\partial\phi\partial\theta = 12h$, and the boundary of the region of its stability is determined from the condition that the expressions for $\partial^2E_{\mathrm{gr}}/\partial\phi^2$ and the Jacobian vanish:

$$\frac{\partial^2E_{\mathrm{gr}}}{\partial\phi^2}\frac{\partial^2E_{\mathrm{gr}}}{\partial\theta^2}-\left(\frac{\partial^2E_{\mathrm{gr}}}{\partial\phi\partial\theta}\right)^2 = 144(D^2-D(6J_{\mathrm{pl}}+4J_{\mathrm{ch}})-h^2)=0. \tag{11}$$

Ultimately we arrive at the finding that the stability of the singlet state is preserved when $D>6J_{\mathrm{pl}}+4J_{\mathrm{ch}}$ and the field h is less than a critical field h_{QP}, where

$$h_{QP}=\sqrt{D^2-D(6J_{\mathrm{pl}}+4J_{\mathrm{ch}})}. \tag{12}$$

The susceptibility (9) in the canted phase, determined at zero field for $D\geqslant 6J_{\mathrm{pl}}+4J_{\mathrm{ch}}$, changes sign, indicating a loss of stability. It can be shown that for $D>6J_{\mathrm{pl}}+4J_{\mathrm{ch}}$ in a field equal to h_{QP}, a second-order phase transition occurs from the quadrupolar spin state to the canted phase. Here the value of the field h_{QP} is lower than the spin-flip field h_{flip}, and the magnetization of the system for $h=h_{QP}$ changes continuously. In fields $h\geqslant h_{QP}$ the magnetization, starting from zero, increases continuously as the field increases. In the field region $h\geqslant h_{\mathrm{flip}}$ it reaches a maximum possible value and stops growing. Thus, in fields $h\leqslant h_{QP}$ and $h\geqslant h_{\mathrm{flip}}$ the susceptibility will equal zero in the canted phase and have a nonzero value in the field interval $h_{QP}\leqslant h\leqslant h_{\mathrm{flip}}$. At the points of the second-order phase transition from the quadrupolar spin state to the canted phase and from the canted phase to the FM state the susceptibility χ_{zz} changes in a jump. It is this behavior of the magnetization and susceptibility that was observed experimentally in Ref. 5. If the quantity $D-(6J_{\mathrm{pl}}+4J_{\mathrm{ch}})$ is positive and not small, then the theoretical treatment becomes complicated and requires numerical analysis. Here the possibility of a first-order phase transition from the singlet phase to the canted phase or directly to the FM phase cannot be ruled out. Examples of this will be considered separated.

This study was supported in part by the Foundation for Basic Research of Ukraine (Project F7/514-2001).

*E-mail: vloktev@bitp.kiev.ua

---

[1] M. F. Collins and O. A. Petrenko, Can. J. Phys. **75**, 605 (1997).
[2] B. S. Dumesh, Usp. Fiz. Nauk **170**, 403 (2000).
[3] V. M. Loktev, Fiz. Nizk. Temp. **5**, 295 (1979) [Sov. J. Low Temp. Phys. **5**, 142 (1979)].
[4] V. M. Loktev and V. S. Ostrovskiĭ, Fiz. Nizk. Temp. **20**, 983 (1994) [Low Temp. Phys. **20**, 775 (1994)].
[5] Y. Tanaka, Y. Tanaka, and T. Ono, Preprint cond-mat/0104287 (2001).
[6] B. Dorner, D. Visser, U. Stiegenberger, K. Kakurai, and N. Steiner, Z. Phys. B: Condens. Matter **72**, 487 (1988).
[7] D. Visser and A. Harrison, J. Phys. (Paris), Colloq. **49, C 8**, 1467 (1988).
[8] A. Harrison and D. Visser, J. Phys.: Condens. Matter **4**, 6977 (1992).
[9] Y. Kawamura, J. Phys. Soc. Jpn. **61**, 1299 (1992).
[10] Y. Kawamura, J. Phys.: Condens. Matter **10**, 4707 (1998).
[11] Y. Kadowaki, S. M. Shapiro, T. Inami, and Y. Ajiro, J. Phys. Soc. Jpn. **57**, 2640 (1998).
[12] Y. Ajiro, T. Nakashima, Y. Uno, Y. Kadowaki, M. Mekata, and N. Achiwa, J. Phys. Soc. Jpn. **57**, 2648 (1988).
[13] T. E. Mason, B. D. Gaulin, and M. F. Collins, Phys. Rev. B **39**, 586 (1989).
[14] A. K. Zvezdin, V. M. Matveev, A. A. Mukhin, and A. I. Popov, *Rare-Earth Ions in Magnetically Ordered Crystals* [in Russian], Nauka, Moscow (1985).

Translated by Steve Torstveit